Photonic conversion of sol-gel organometallic precursors into inorganic thin films

CHRISTINA KOUTSIAKI

A thesis submitted in partial fulfilment of the requirements of

Nottingham Trent University for the degree of Doctor of Philosophy.

School of Science and Technology

Nottingham Trent University

March 2023

Copyright Statement

The copyright in this work is held by the author. You may copy up to 5% of this work for private study, or personal, non-commercial research. Any re-use of the information contained within this document should be fully referenced, quoting the author, title, university, degree level and pagination. Queries or requests for any other use, or if a more substantial copy is required, should be directed to the author.

Abstract

Large area electronics manufacturing has been emerged over this last decade to become an exciting and yet challenging field of interest. The realisation of large-scale fabrication of high-performance electronics is achieved *via* a solution-processing based manufacturing scheme that is compatible to high-throughput fabrication systems. Metal oxides (MOs) constitute an attractive, highly promising candidate towards delivering trend-of-future applications, with their enhanced electronic properties, mechanical stability and optical transparency establishing them as a unique tool. The realisation of MO thin films *via* the solution processes such as "sol-gel" is employed through the conversion of metalorganic precursor films into MOs. To tackle the demanding post-deposition annealing treatments of precursor films in high-temperatures, laser annealing (LA) has been proposed as a propitious alternative, as its unique characteristic of localised, high-temperature induction that is able to deliver a successful precursor conversion within a few nanoseconds. This research sought to tackle two principal challenges that accompany the fabrication of MO thin films *via* sol-gel and LA: the first challenge concerned the difficulty of monitoring the conversion process of ultra-thin films (~ 10 nm) with non-invasive characterisation tools and was overcome using infrared spectroscopic ellipsometry (IRSE). To the best of our knowledge, this work comprised the pioneering investigation of the potential of IRSE in delivering a detailed overview of the conversion steps by detecting the associated by-products. More importantly, the challenge implied by the low film thickness, as required for electronic devices, was tackled by enhancing IRSE sensitivity using highly reflective substrates as well as proposing a comprehensive tool for testing the substrate sensitivity that is inherently tailored for each material of interest. The IRSE study thus provided vital information on the formation of In_2O_3 and ZnO films, which constituted the "seed" materials for overcoming the second core challenge of this research: the introduction of LA to the sol-gel process. LA was employed towards the fabrication of solution processed In_2O_3, $IGZO$, and ZnO thin films and their pre- and post-processed properties were analysed through their role as an active layer in TFT devices. SiO_2 was employed as the device dielectric, with various SiO_2 thicknesses constituting an additional parameter of study due to the thickness effect on the irradiation absorption for the surface films. This research objective was realised by expanding the material palette of laser processed and sol-gel fabricated MOs into dielectric films. Focus was given to the study of ZrO_2, a promising dielectric candidate that had as-of-yet stood untested with LA. The manufacturing schemes of the resultant ZrO_2 thin films were investigated, followed by their use as dielectrics in MO capacitor devices. Finally, all the attained knowledge was aggregated and applied it towards the fabrication of TFTs based entirely on laser-processed, sol-gel fabricated, and heterogeneously metal oxide dielectric and semiconductor thin films.

Acknowledgements

First and foremost, I would like to thank my Director of Studies, Dr. Demosthenes Koutsogeorgis, for giving me the opportunity to conduct this research. His endless support, guidance and insights have greatly contributed to my development as a researcher along with my achievements during this study. Apart from his academic guidance, Demos has also been one of my greatest supports since I started this academic journey, leaving my home country and moving to the UK. I am deeply grateful for our scientific brainstorming sessions, our conversations about life and his support during hard times. To my second supervisor, Dr. Nikolaos Kalfagiannis, I would like to start by expressing my sincere gratitude for his continuous insights during this work. It's a blessing to work with people that constantly transmit so much knowledge, even in a 5-minute chat across the lab corridor. His encouragement, guidance and insights during this research study were essential. Apart from his vital role in this work, Nikos has also been a great friend, who I am grateful to have.

My gratitude also extends to our collaborators across the world, without whom this research would not have been possible: Associate Prof. Christopher Mellor at the University of Nottingham – UK for providing access and supervision for the use of NIR-VIS-UV spectroscopic ellipsometry (SE) system, Prof. Thomas Anthopoulos at KAUST, for our fruitful collaboration which resulted in one of my happiest moments in this work. I would also like to thank the experts in ellipsometry at J. A. Woollam for their provision on the CompleteEase™ software beta with IR capabilities.

I would also like to show my sincere appreciation to my colleagues at iSMART and MTIF: Dr. Jacob Spear, Dr. Magda Patel, Josh Barkby, Dr. Gary Mudd and Ryan Toms. To Dr. Dominic Craske, thank you for your guidance and input on the AFM measurements and analysis, as well as for making me laugh during my most stressful moments. To Jodie West, it was a pleasure to share this journey with you, thank you for all the moments we shared our achievements and struggles and thank you for recommending "Fleabag" to me back in 2019. To Luke Blyth, the sunshine of the group, our days in the lab (and our Friday dinners) will be amongst my favourite moments of this adventure. To Thomas Howe, thank you for always bringing the calm and bright energy everywhere you go. It's been a pleasure to work with you. And finally, to Matthew Spink, who has been more than a colleague. Matt, you are a true friend, my support and one of my favourite people. Thank you for our excellent collaboration during this scientific adventure, but mostly thank you for everything else. You know what these are.

Acknowledgements

To my partner in crime, Dr. James Hillier, what a journey has it been! I will always be thankful to this work for taking me to that place, that December, with you. The best is yet to come.

To my friends in NL, I am so lucky to be surrounded by such bright and fun people like you. Thank you for all those Friday nights when you gave me strength while I was (again) stressed. Thank you for all the laughs, the fun Fridays, and the long board game nights, all of which have been my favourite moments of the week. Most importantly, thank you for offering me a new “home” since day one.

To my parents, none of these would have happened without you. Being so far away from you for so long has been quite a challenge, but we made it. Thank you for your endless, pure love, I always carry it with me.

To my best friends, my chosen family, thank you for always being there. To Thodoris, thank you for being always there for me, no matter how far we are (only geographically). To Thanos, your love and support has been the power I needed when I thought I could not make it. Sometimes it’s difficult to express with words my gratitude because it’s just too much. This is one of these moments. To my bestie, Zwi, thank you for always transmitting this excitement for life (even in the darkest moments) and for giving me the wisest advice I could ever ask for. I always keep them in my heart. To my bestie, Despoina, thank you for being the most genuinely good person I’ve ever met. Being around you makes me see life in a romantic, pure and peaceful perspective that I love. Also, thank you for all the times you have supported me in the UK and for those fantastic movie nights in Derby. Unforgettable. To my bestie, Christina, it’s the third time in my life that I am thanking you in an acknowledge session, but it always feels like it’s not enough. For our endless talks and support, I cannot thank you enough. I am lucky to call you my best friend, without you I wouldn’t have made it. You’re always there to share the happiness and to lift me up when I need it the most. For 12 years now. All I can say is, thank you, you add so much colour in my life, especially when it’s just black and white. I love you.

To my twin sister, Marilou, being away from you has been the most difficult part of this journey. I might be away, but a part of my heart stays always with you. Thank you for being the best sister and best friend anyone would ask for. Always and forever.

List of publications

- Yarali, E., **Koutsiaki, C**., Faber, H., Tetzner, K., Yengel, E., Patsalas, P., Kalfagiannis, N., Koutsogeorgis, D. C., Anthopoulos, T. D., Recent Progress in Photonic Processing of Metal-Oxide Transistors. *Adv. Funct. Mater.* 2020, 30, 1906022. https://doi.org/10.1002/adfm.201906022.

- **C. Koutsiaki,** D.C. Koutsogeorgis, N. Kalfagiannis, Physicochemical Analysis of Nanoscale Metal Oxide Thin Film Precursors via Infrared Spectroscopic Ellipsometry, *J. Phys. Chem. C* 2023, 127, 32, 15876–15886.

- **Koutsiaki, C.**, Kalfagiannis, N., Koutsogeorgis, D., The role of oxide thickness in Laser Annealing-assisted conversion of In_2O_3 thin films through the scope of TFT device performance, *Materials:* Special Issue *"Thin-Film Transistors: Devices for the Next Generation Large Area Electronics"*, to be submitted by October 2023.

List of Conference Presentations

- **C. Koutsiaki**, N. Kalfagiannis and D.C. Koutsogeorgis, Excimer Laser Annealing of sol-gel Metal-Oxide thin films, *IOP PGS Conference: Printing for the future* (04 April 2019).

- **C. Koutsiaki**, D.C. Koutsogeorgis and N. Kalfagiannis, Excimer Laser Annealing of Sol-Gel metal oxide thin films, 2019 MRS Fall meeting and Exhibit, Boston, 1-6 December 2019,

- **C. Koutsiaki**, D.C. Koutsogeorgis and N. Kalfagiannis Excimer Laser Annealing of Sol-Gel metal oxide thin films, Innovations in Large Area Electronics (innoLAE) Conference, 21-22 January 2020, Welcome Genome Campus, Cambridge, UK

- **C. Koutsiaki**, D.C. Koutsogeorgis and N. Kalfagiannis The use of Infra-Red Spectroscopic Ellipsometry (IRSE) to determine the formation of metal oxide ultra-thin ($<10\ nm$) films *via* sol gel precursors, 2021 E-MRS Fall Meeting Virtual Conference,20-23-September 2021.

- **C. Koutsiaki**, D.C. Koutsogeorgis and N. Kalfagiannis The use of Infra-Red Spectroscopic Ellipsometry (IRSE) to determine the formation of metal oxide ultra-thin ($<10\ nm$) films *via* sol gel precursors, 2021 MRS Fall Meeting and Exhibit, Boston, Massachusetts, 29 November 2-December 2021.

- **C. Koutsiaki**, D.C. Koutsogeorgis and N. Kalfagiannis, Unravelling the chemical conversion of ultra-thin metal oxide thin film precursors: An IRSE study, TCM-TOEO 2022, 16-21 October 2022, Hersonissos, Crete, Greece.

Table of Contents

Copyright Statement ii
Abstract iii
Acknowledgements iv
List of publications vi
List of Conference Presentations vii
Table of Contents viii
List of Symbols x
List of Abbreviations xii
List of Figures xiii
1. Introduction 1
1.1. Motivation and Challenges 1
1.2. Novelty and Impact 5
1.3. Research Aim 6
1.4. Research Objectives 6
1.5. Overview of Research Methodology 7
1.6. Structure of Thesis 8
2. Background and Literature Review 9
2.1. Optical Properties of Solids 9
2.2. Introduction to Metal Oxides (MOs) 13
2.3. History and properties of MO semiconductors 14
2.4. Metal Oxide Dielectrics 16
2.5. Sol-gel Chemistry 18
2.6. Electrical Characterisation 22
2.7. Solution Processed Metal Oxide TFTs: Advances and Challenges 33
2.8. UV-Assisted Metalorganic Conversions 34
2.9. Brief History of Laser Annealing 36
3. Experimental Methods 37
3.1. Thin Film Fabrication 37
3.2. Excimer Laser Annealing 42
3.3. Characterisation 49

4. IRSE Investigation on Indium Oxide and Zinc Oxide Ultra-Thin Films 61
4.1. Infrared Transmission of $In(NO_3)_3$ and $Zn(CH_3COO)_2$ 62
4.2. Ellipsometric Results and Analysis 65
4.3. IRSE and IRT Simulations 80
4.4. Concluding Remarks 86
5. Laser Annealed Sol-Gel Thin Film Transistors 88
5.1. Materials of Interest and Reference Devices 89
5.2. Sol-gel Laser Annealed of In_2O_3 TFTs 92
5.3. Sol-gel Laser Annealed IGZO TFTs 110
5.4. Comparison Between In_2O_3 and IGZO 112
5.5. Sol gel LA ZnO TFTs 118
5.6. Concluding Remarks 126
6. Laser Annealed Sol-Gel Thin Film Capacitors 128
6.1. IRSE Analysis of ZrO_2 Precursor-Temperature Effect 129
6.2. Electrical Performance of ZrO_2 MOS Capacitors 132
6.3. Electrical Characterisation of TFTs Based on a Sol-Gel Laser Annealed Dielectric and Semiconductor 144
6.4. Concluding Remarks 154
7. Conclusions and Future Perspectives 157
7.1. Conclusions 157
7.2. Future Perspectives 159
8. References 161
9. Appendix 177

List of Symbols

Symbol	Description
D	Electric displacement
B	Magnetic induction
Ξ	Electric field
H	Electric field
R	Space vector
Q	Charge density
J	Current density
P	Electric polarisation
E_0	Free space permittivity
M	Magnetisation
M_0	Free space permeability
K	Wavevector
Ω	Angular frequency
E	Relative permittivity
M	Relative permeability
E	Dielectric constant
Σ	Conductivity
$\tilde{E}(\Omega)$	Complex permittivity
E_1	Real part of complex permittivity
E_2	Imaginary part of complex permittivity
$\underline{\hat{E}}$	Unit vector
$\tilde{N}(\Omega)$	Complex refractive index
N	Refractive index
K	Extinction coefficient
$V(\omega)$	Phase velocity
$A(\omega)$	Absorption coefficient
Λ	Wavelength
R	Electron displacement
Γ	Damping coefficient
E	Electron charge
M_e^*	Effective mass of electron
K	Spring constant
Ω_0	Oscillator frequency
X_e	Electron susceptibility
N_l	Number of Lorentzian oscillators per unit volume
E_∞	High frequency permittivity
A_l	Oscillator amplitude
$\hbar$	Planck's constant
N	Free carrier concentration
E_g	Energy bandgap
E_f	Fermi energy level
K	Dielectric constant
Φ_μ	Work function
E_c	Conduction band energy
E_{vacuum}	Vacuum energy
X_{ox}	Electron affinity of insulator
X_s	Electron affinity of semiconductor
E_i	Fermi energy of intrinsic semiconductor
V_g	Gate voltage
Δq	Charge difference
E_v	Valence band energy
N_e	Electron density in semiconductor
N_i	Electron density in intrinsic semiconductor
T	Temperature
Φ_s	Surface potential
$\Delta\varphi_{ox}$	Potential drop across oxide layer
$\mathcal{E}(x)$	Electric field across the depletion region in semiconductor
N_d	Doping concentration
X_d	Depletion length
E_s	Dielectric permittivity of semiconductor
$\mathcal{E}_{ox}$	Electric field across the oxide
E_{ox}	Dielectric permittivity of oxide

T_{ox}	Thickness of oxide layer
C_{ox}	Parallel plate capacitance per Unit area of oxide
Q_{ss}	Surface charge density of oxide
Q_{i}	Surface charge density due to Semiconductor implant dopants
V_{t}	Threshold voltage
Q_{inv}	Inversion charge
V_{ds}	Source-drain voltage
V_{gs}	Source-gate voltage
Q_{ch}	Total charge per channel area
W	Channel width
L	Channel length
M_{n}	Electron mobility in the channel
Υ_{d}	Electron drift velocity
I_{ds}	Source-drain current
T_{ds}	Average electron time from Source to drain
$I_{ds,sat}$	Saturation current
$M_{lin} = M_{fe}$	Linear (field effect) mobility
M_{sat}	Saturation mobility
$I_{on/off}$	On-off ratio
V_{on}	On voltage
I_{on}	On current
I_{off}	Off current
H_{f}	Thin film thickness obtained after spin coating
H	Thickness of fluid layer
T	Rotating time
P	Density of liquid
H	Viscosity
R_{rms}	Root-mean-square roughness
R_{a}	Arithmetic roughness
Z_{i}	Surface height at a given point
$\overline{Z}$	Arithmetic mean of the surface height
R_{f}	Fresnel reflection coefficient
T_{f}	Fresnel transmission coefficient
Θ_{i}	Angle of incidence
Θ_{t}	Refracted angle
Θ_{r}	Reflected angle
$R(e)$	Frequency-dependent reflectance
$T(e)$	Frequency-dependent transmittance
I_{s}	Intensity of reflected light
I_{d}	Dark intensity
R_{al}	Reflectivity of al mirror
Ψ	Psi (ratio of outcoming to incoming light amplitude)
Δ	Delta (phase difference upon p-s polarisation)
Γ_{n}	Broadening of gaussian oscillator
T_{opt}	Optical scattering time
P_{opt}	Optical resistivity
Ω_{p}	Plasma frequency
V_{dep}	Depletion voltage
Y_{d}	Width of depletion layer
D_{s}	Semiconductor thickness
K_{th}	Thermal conductivity
$I_{\tilde{n}_F N_a}$	Interface matric from air to film
$P_{\tilde{n}_F L_{tot}}$	Propagation matrix in the film
$I_{\tilde{n}_{Sub} \tilde{N}_F}$	Interface matrix from film to substrate
E_{evap}	Solvent evaporation rate
F	Total laser fluence
P_{m}	Mass density
S	Poynting vector

List of Abbreviations

2-ME	2-methoxyethanol
AFM	Atomic force microscopy
ALD	Atomic layer deposition
AZO	Aluminium zinc oxide
BGTC	Bottom gate top contact
CB	Conduction band
CBM	Conduction band minimum
CNT	Classical nucleation theory
CPU	Central processing unit
CVD	Chemical vapor deposition
DC	Direct current
DRAM	Dynamic random-access memory
EBE	Electron beam evaporation
ELA	Excimer laser annealing
FTIR	Fourier transform infra-red
FWHM	Full-width Half-maximum
G	Gate
IoT	Internet of Things
IPA	Isopropanol
IR	Infrared
IRSE	Infrared spectroscopic ellipsometry
IRT	Infrared transmission
ITO	Indium tin oxide
KrF	Krypton fluoride
LA	Laser annealing
MEA	Monoethanolamine
MOs	Metal oxides
MOS	Metal oxide semiconductor
MOSFET	Metal oxide semiconductor field effect transistor
MSE	Mean square error
OLED	Organic light emitting diode
ORS	Optical reflection spectroscopy
p-Si	P-doped Silicon
PVD	Physical vapor depositions
R2R	Roll-to-Roll
RH	Relative humidity
S-D	Source-drain
SE	Spectroscopic ellipsometry
TA	Thermally annealed
TCO	Transparent conductive oxide
TE	Transverse electric
TEM	Transmission electron microscopy
TFTs	Thin film transistors
TM	Transverse magnetic
UV	Ultraviolet
VASE	Variable angle spectroscopic ellipsometry
VB	Valence band
VBM	Valence band maximum
VIS	Visible
XPS	X-ray Photoelectron Spectroscopy

List of Figures

Figure 2.1. Real (blue) and Imaginary (red) permittivity of a Lorentz oscillator (Page **13**)

Figure 2.2. Illustration of simplified band structure of a metal oxide semiconductor. (Page **15**)

Figure 2.3. Graphical representation of sol-gel processing steps towards M – O – M network formation. (Page **21**)

Figure 2.4. Energy band diagrams as per material of a metal-oxide-semiconductor (MOS) capacitor. (Page **23**)

Figure 2.5. MOSFET structure, representing the main device components. (Page **27**)

Figure 2.6. Linear region operation in a MOSFET. (Page **28**)

Figure 2.7. MOSFET channel alteration due to gradual increase in VDS. (**29**)

Figure 2.8. Pinch-off operation region in a MOSFET. The channel formation is depicted as a black dotted area between source and drain. (Page **30**)

Figure 2.9. Drain current (IDS) versus drain voltage (VDS) in a) linear (Field Effect), b) pinch off and c) saturation regime. (Page **30**)

Figure 2.10. Typical a) transfer and b) output characteristic of an n-type Thin Film Transistor (TFT). (Page **31**)

Figure 2.11: Misinterpretation of Threshold Voltage VT in accord to changes in VGS range. (Page **32**)

Figure 2.12. Typical structure of MOSFET (centre) and TFT architectures. (**33**)

Figure 2.13: Photochemical phenomena conducted during ultraviolet irradiation of sol-gel metal oxide precursor films. (Page **35**)

Figure 3.1: Steps comprising spin coating process. (Page **38**)

Figure 3.2: Illustration of evaporation system employed in Al deposition. (Page **41**)

Figure 3.3: A typical laser annealing experimental setup. (Page **43**)

Figure 3.4: Important parameters associated with the laser annealing process. (**43**)

Figure 3.5. Principles and operation of AFM. (Page **50**)

Figure 3.6. Schematic of light refraction and reflection at a boundary between two materials with different refractive indexes, ni and nt. (Page **51**)

Fig. 3.7. Schematic of the reflectance measurement set-up. (Page **54**)

Figure 3.8: Illustration of the Ellipsometry main principle. (Page **55**)

Figure 3.9: Illustration of the Mark II IR-VASE. (Page **57**)

Figure 3.10: Equipment setup used for electrical characterisation in this work. (Page **59**)

Figure 4.1: IR transmittance intensity measurements. (Page **61**)

Figure 4.2: Imaginary part of the dielectric permittivity of 2-ME (red), (b) $In(NO_3)_3$ in 2-ME solution (green), (c) $Zn(CH_3COO)_2$ in 2-ME solution (blue), (d) $In(NO_3)_3$ dried film (orange) and (e) $Zn(CH_3COO)_2$ dried film (magenta). (Page **63**)

Figure 4.3: Measured Ψ (red lines) and Δ (green lines) for stabilised (step 1) $In(NO_3)_3$ thin films on top of (a) Si, (b) TiN, (c) Al and (d) Au and $Zn(CH_3COO)_2$ thin films on top of (e) Si, (f) TiN, (g) Al and (h) Au. (Page **68**)

Figure 4.4: Measured Ψ (red lines) and Δ (green lines) for thermally annealed (step 2: $300\ °C$, $60\ min.$) $In(NO_3)_3$ thin films on top of (a) Si, (b) TiN, (c) Al and (d) Au and $Zn(CH_3COO)_2$ thin films on top of (e) Si, (f) TiN, (g) Al and (h) Au. (Page **69**)

Figure 4.5: Imaginary part of complex permittivity ($\varepsilon_2(\omega)$) for stabilised $In(NO_3)_3$, as extracted from Ψ and Δ fit of $In(NO_3)_3$ films on top of (a) Si, (b) TiN, (c) Al and (d) Au, after step 1 (150℃,15 min). (Page **71**)

Figure 4.6: Imaginary part of the complex permittivity ($\varepsilon_2(\omega)$) for stabilised $Zn(CH_3COO)_2$, as extracted from Ψ and Δ fit of $Zn(CH_3COO)_2$ films on top of (a) Si, (b) TiN, (c) Al and (d) Au, after step 1 ($150\ °C$, $15\ min.$). (Page **72**)

Figure 4.7: Imaginary part of the complex permittivity for thermally annealed $In(NO_3)_3$, as extracted from Ψ and Δ fit of of $In(NO_3)_3$ films on top of (a) Si, (b) Al, (c) TiN and (d) Au, after step 2 ($300\ °C$, $60\ min.$). (Page **74**)

Figure 4.8: Imaginary part of the complex permittivity (ε2(ω)) for thermally annealed $Zn(CH_3COO)_2$, as extracted from Ψ and Δ fit of of $Zn(CH_3COO)_2$ films on top of (a) Si, (b) Al, (c) TiN and (d) Au, after step 2 (300℃,60 min). (Page **76**)

Figure 4.9: Imaginary part of the complex permittivity of the thermally annealed (450℃, step 3) (a) $Zn(CH_3COO)_2$ and (b) $In(NO_3)_3$ films on top of Al. Each panel presents each peak in colour, labelled with its interpretation. (Page **78**)

Figure 4.10: IR Reflectivity of Al (red), Au (orange), TiN (yellow), Si (light green), p-Si (petrol blue), (p/n) Si++ (blue and purple), as well as ITO (magenta). Light blue and grey shaded regions denote the areas where $In(NO_3)_3$ and $Zn(CH_3COO)_2$ spectral features are detected. (Page **80**)

Figure 4.11: MSE of generated optical model of stabilised $In(NO_3)_3$ on various substrates that are described by a Drude oscillator, with respect to simulated optical resistivity ρopt and scattering time τopt (coloured lines) of the substrate. (Page **82**)

Figure 4.12: MSE of generated optical model of stabilised $Zn(CH_3COO)_2$ on various substrates that are described by a Drude oscillator, with respect to simulated optical resistivity ρopt and scattering time τ_{opt} (coloured lines) of the substrate. (Page **83**)

Figure 4.13: Simulation- process flow. The substrate optical constants (extracted experimentally or theoretically) constitute the seed to obtain simulated Ψ values (a), while noise constitutes an additional simulation parameter (b). Generated data (c) include Ψ values describing the optical response of the entire structure of study: thin film (of interest) on top of substrate (simulated data). (Page **84**)

Figure 4.14: Simulated transmittance values of $Zn(CH_3COO)_2$ (a-c) and $In(NO_3)_3$ (b-d) on top of Si (substrate). Simulation of Si transmittance includes the addition of 15% noise and is shown in black. Simulated transmitted values of $Zn(CH_3COO)_2$ and $In(NO_3)_3$ thin films on top of Si are presented in colour, with thin film thicknesses ranging from 0-90 nm. (Page **85**)

Figure 4.15: (a) Emission intensity of IR source used in IRSE and IRT measurements, (b) measured Ψ and Δ values of stabilised $In(NO_3)_3$ thin film on top of Au, (c) Simulated Ψ and Δ values of stabilised $In(NO_3)_3$ thin film on top of Au. Simulations in (c) include the addition of 15% noise. Blue shaded regions in (a), (b) and (c) represent the area where emission intensity drops, thus causing a rapid increase on the noise levels in measured Ψ and Δ. (Page **87**)

Figure 4.16: Simulated Ψ (red) and Δ (green) values of Au substrate, with noise levels ranging from 0 to 160%. Ψ and Δ values of 1 nm film of stabilised $In(NO_3)_3$ on top of Au (generated data) are also presented in each panel, for comparison to bare Au. At low noise levels, the generated (black) data present a clear distinction from simulated values of Au, while at increased noise levels the distinction between generated data ($In(NO_3)_3$ on Au) and simulated (bare Au) is increasingly difficult or even unattainable. (Page **88**)

Figure 5.1: 3D structure and optical microscopy image of TFT device geometry. (**90**)

Figure 5.2: Transfer (red) and output (blue) characteristics of BGTC TFT devices based on thermally annealed (300 °C,60 min) sol-gel In_2O_3 (a,d), IGZO (b,e) and ZnO (c,f) thin films. Thermally grown SiO_2 (200 nm) and n-Si were employed as a device dielectric and substrate respectively. (Page **91**)

Figure 5.3: AFM images of stabilised (a-c) and thermally annealed (d-f) In_2O_3, IGZO and ZnO thin films. Stabilisation and thermal annealing conditions involved hot plate treatment at 150 °C (15 min) and 300 °C (60 mins), respectively. (Page **93**)

Figure 5.4: a) Numerical simulation of In_2O_3 absorption coefficient in various SiO2 thicknesses and irradiation wavelengths. White line shows the extinction coefficient of In_2O_3 , k. b) absorption of In_2O_3 at irradiation wavelength of 248 nm, for various SiO_2 thicknesses. Magenta stars denote the absorption for 100, 200 and 400 nm of SiO_2, which are thicknesses that were used in this work. c) schematic illustration of the structure used during the modelling. (Page **94**)

Figure 5.5: Transfer characteristics of sol-gel Laser Annealed In2O3 TFT devices, treated with 100 (a), 150 (b) and (c) 200 mJ/cm^2. Green, red, and blue lines represent devices treated with 1,5 and 10 laser pulses, respectively. Dotted lines show the corresponding I_{GS} current - same colour code applied as in I_{DS}. V_{DS} is set at 5V to obtain a linear region operation. (Page **96**)

Figure 5.6: Field Effect mobility μ_{FE} and $I_{ON/OFF}$ values for LA sol-gel In_2O_3 TFTs with 100 nm SiO_2 as dielectric. Black lines display μ_{FE} and $I_{ON/OFF}$ values of devices treated at 100 mJ/cm^2, while red and blue lines correspond to 150 and 200 mJ/cm^2, respectively. (Page **97**)

Figure 5.7: Output characteristics of LA sol-gel In_2O_3 TFTs with 100 nm SiO_2 as dielectric, annealed at 1 pulse at (a) 100 mJ/cm^2, (b) 150 mJ/cm^2 and (c) 200 mJ/cm^2. Gate voltage VGS ranged from -20 to 50 V, with a step of 10 V. VDS is dually swept at $0 < V_{DS} < 40$ V. A clear transition from linear to saturation region is shown in (a), while saturation is not obtained at (b) and (c). For devices treated at 200 mJ/cm^2, current values exceeded 10 mA – the top current limit of the measurement setup. (Page **98**)

Figure 5.8: Transfer characteristics of sol-gel Laser annealed In_2O_3 TFT devices with 200 nm SiO_2 as a dielectric, treated at (a) 100, (b) 150, (c) 200 and (d) 250 mJ/cm^2. Green, red, and blue lines represent devices treated with 1,5 and 10 pulses, respectively. Dotted lines show the corresponding I_{GS} current- same colour code applied as IDS. Arrows display the current direction during VGs dual sweep at $-60 < V_{GS} < 60$ V. V_{DS} is set at 5V to obtain a linear region operation. (Page **99**)

Figure 5.9: (a) Field Effect mobility μ_{FE}, (b) V_{ON} and (c) $I_{ON/OFF}$ values of LA sol-gel In_2O_3 TFTs with 200 nm SiO_2 as a dielectric. Black, red, blue, and green lines represent values extracted from devices treated at 100,150,200 and 250 mJ/cm^2 respectively. (Page **100**)

Figure 5.10: Output characteristics of LA sol-gel In_2O_3 TFTs with 200 nm SiO_2 as dielectric, annealed at 150 $mJ/cm^2$with (a) 1 pulse, (b) 5 pulses and (c) 10 pulses. Gate voltage V_{GS} ranged from -20 to 60 V, with a step of 10 V. V_{DS} is dually swept at $0 < V_{DS} < 50$ V. A clear transition from linear to saturation region is shown in (a) and (b), while saturation is not obtained at (c), with this corresponding device remaining in ON mode. Note the I_{DS} scales are different. (**101**)

Figure 5.11: Transfer characteristics of sol-gel Laser annealed In_2O_3 TFT devices with 400 nm SiO_2 as a dielectric, treated at (a) 100, (b) 150, (c) 200 and (d) 250 mJ/cm^2. Green, red, and blue

lines represent devices treated with 1,5 and 10 pulses, respectively. Dotted lines show the corresponding I_{GS} current- same colour code applied as IDS. Arrows display the current direction during VGS dual sweep at $-60 < V_{GS} < 60$ V. V_{DS} is set at 5V to obtain a linear region operation. (Page **102**)

Figure 5.12: (a) Field Effect mobility μ_{FE}, (b) V_{ON} and (c) I_{ONOFF} values of LA sol-gel In_2O_3 TFTs with 400 nm SiO_2 as a dielectric. Black, red, blue, and green lines represent values extracted from devices treated at 100,150,200 and 250 mJ/cm^2 respectively. (Page **103**)

Figure 5.13: Output characteristics of LA sol-gel In_2O_3 TFTs with 400 nm SiO_2 as dielectric, annealed at 150 $mJ/cm^2$with (a) 1 pulse, (b) 5 pulses and (c) 10 pulses. Gate voltage VGS ranged from -20 to 60 V, with a step of 10 V. V_{DS} is dually swept at $0 < V_{DS} < 50$ V. For devices treated at 1 pulse (a), red area denotes the presence of hysteresis along with abnormal current collection during the return sweep (see blue arrows for forward and reverse bias). (Page **104**)

Figure 5.14: Transfer characteristics of sol gel LA In_2O_3 TFT (200 nm SiO_2 dielectric) exposed in ambient conditions. I-V measurements were conducted every 7 months to explore the air - In_2O_3 interaction. Dotted arrows highlight the transfer evolution over time. Laser Annealing conditions ($250\ mJ/cm^2$, 5 pulses) were purposely chosen to obtain a highly conductive semiconductor layer. Measurement dates are shown in figure legend, along with their corresponding colours. (Page **106**)

Figure 5.15: Transfer characteristics of sol-gel Laser annealed In_2O_3 TFT devices with 200 nm SiO2 as a dielectric, treated at (a) 100, (b) 150, (c) 200 and (d) 250 mJ/cm^2. Solid lines represent devices where 60 mg/ml of $In(NO_3)_3$ solution was deposited, and laser processed while dotted lines represent corresponding devices where 30 mg/ml $In(NO_3)_3$ solution was employed. Green, red, and blue lines represent devices treated with 1,5 and 10 pulses, respectively. Arrows display the change in IOFF during VGS dual sweep at $-60 < V_{GS} < 60$ V. V_{DS} is set at 5V to obtain a linear region operation. (Page **108**)

Figure 5.16: N and band diagrams at $V_{GS} = 0$ V (unbiased gate) for different semiconductor thicknesses ds; (a) high; (b) medium; (c) small. (Page **110**)

Figure 5.17: (a-d) Transfer characteristics of sol-gel Laser annealed IGZO TFT devices with 200 nm SiO_2 as a dielectric, treated at (a) 100, (b) 150, (c) 200 and (d) 250 mJ/cm^2. Green, red, and blue lines represent devices treated with 1, 5 and 10 pulses, respectively. Dotted lines show the corresponding I_{GS} current- same colour code applied as I_{DS}. Arrows display the current direction during V_{GS} dual sweep at $-60 < V_{GS} < 60$ V. V_{DS} is set at 5 V to obtain a linear region operation. (Page **112**)

Figure 5.18: Output characteristics of LA sol-gel IGZO TFTs with 200 nm SiO_2 as dielectric, annealed at 150 mJ/cm^2 with a) 1 pulse, b) 5 pulses and c) 10 pulses. Gate voltage V_{GS} ranged from -20 to 60 V, with a step of 10 V. V_{DS} is dually swept at $0 < V_{DS} < 50$ V. (Page **113**)

Figure 5.19: AFM images of sol-gel Laser Annealed (b-d) In_2O_3 and (f-h) IGZO thin films, treated at 150 mJ/cm2 with 1 (b and f), 5 (c and g) and 10 (d and h) pulses. AFM images of stabilised In_2O_3 (a) and IGZO (e) precursor films are displayed for comparison. (Page **115**)

Figure 5.20: Field Effect mobility μ_{FE} (a), V_{ON} (b) and $\frac{I_{ON}}{OFF}$ (c) values of sol-gel Laser Annealed In_2O_3 and IGZO TFTs, treated at 100 (black line), 150 (blue line), 200 (red line) and 250 mJ/cm^2 (green line). IGZO and In_2O_3 parameters are displayed in solid and dotted lines, respectively. (Page **117**)

Figure 5.21: Mobility evolution versus gate voltage V_{GS} in Laser Annealed (In_2O_3 and (b) IGZO TFTs. Devices are treated at 150 mJ/cm^2 under 1 (green), 5 (red) and 10 (blue) pulses. Colour-shaded areas represent VGS window where mobility starts to increase. Colour-coded arrows and colour-coded dotted vertical lines also highlight the corresponding VGS threshold, above this point mobility starts to increase. Blue and pink shaded circles reveal areas of mobility decline. (Page **119**)

Figure 5.22: Transfer characteristics of laser annealed sol-gel ZnO TFT devices, treated at (a) 250 mJ/cm2, (b) 300 mJ/cm^2 and (c) 350 mJ/cm^2. V_{DS} was set at 5 V to ensure operation at the linear region. (Page **121**)

Figure 5.23: Field effect mobility μ_{FE} (solid lines) and VON values (dotted lines) of sol-gel ZnO TFTs, Laser annealed at 250 (black), 300 (red) and 350 mJ/cm^2 (blue). (Page **122**)

Figure 5.24: AFM images (a-d), transfer (e-h) and output (i-l) plots of thermally (300 °C,60 min) and Laser Annealed ZnO TFTs, treated at 300 mJ/cm^2, at 5,15 and 20 pulses. (Page **123**)

Figure 5.25: Re-crystallisation mechanism of ZnO films due to Laser Annealing effect. As Number of pulses increases, ZnO grains (a) agglomerate into larger grain structures (b), gradually forming a dense (c) film including large ZnO grains. Yellow arrows indicate the electron path during V_{GS} sweep. (**125**)

Figure 6.1: IRSE (Ψ and Δ) measurements, at 600 and 700 of incidence, of stabilised (150°C,15 min) and thermally annealed (300°C,60 min) $Zr(AcAc)_4$ thin films. Ψ values are presented in red (stabilised) and light pink lines (thermally annealed). Δ is displayed in blue (stabilised) and cyan (thermally annealed). Alongside Ψ and Δ, the corresponding fitting is shown in black solid lines. The fitted values are associated to the corresponding opto-geometric model that includes a stack of Si substrate, a native SiO_2 and $Zr(AcAc)_4$. (Page **130**)

Figure 6.2: Real and imaginary parts of complex permittivity of stabilised (150°C,15 min) and thermally annealed (300°C,60 min) $\mathrm{Zr(AcAc)_4}$. ε_1 and ε_2 of stabilised $\mathrm{Zr(AcAc)_4}$ are presented in red and blue lines, while ε1 and ε2 of thermally annealed $\mathrm{Zr(AcAc)_4}$ is shown in light pink and cyan, respectively. The extraction of ε_1 and ε_2 was conducted *via* fitting of Ψ and Δ, shown in Figure 6.2 1 in black lines. The graph is divided in 4 colour-coded regions: yellow area where Zr-O associated phonon modes are detected, green area for acetate-associated phonons modes, lilac area for hydroxyl (-OH) phonon modes and white area where no spectral features are detected. (Page **131**)

Figure 6.3: Thickness values of LA sol-gel $\mathrm{ZrO_2}$ thin films, based on 1, 2 and 3-layered stacks. The solution concentration was kept constant at 0.1 M, with $\mathrm{Zr(AcAc)_4}$ as metal oxide precursor and 2-ME as a solvent. Films were deposited *via* spin coating (4000 rpm,30 s). As LA parameters, 3 sets of laser fluence (200,250,275 $\mathrm{mJ/cm^2}$) and number of pulses (1,2 and 3) were used. Stars denote thicknesses of TA samples (TA-1L, TA-2L and TA-3L correspond to thermally annealed 1,2 and 3 layered films). (Page **133**)

Figure 6.4: Capacitance- voltage (C-V) measurements of MOS-Capacitor devices, with sol-gel Laser Annealed $\mathrm{ZrO_2}$ as a dielectric. The solution concentration was chosen at 0.1 M. C-V characteristics are divided in 3 panels, corresponding to the number of deposited precursor ($\mathrm{Zr(AcAc)_4}$) layers *via* spin coating deposition. Laser fluences varied from 200-275 $\mathrm{mJ/cm^2}$. The number of pulses selected for each laser fluence was set to 1,2 and 3. Highly doped Silicon (p-Si++) is used as a substrate to $\mathrm{ZrO_2}$ films, therefore, accumulation region is formed in negative voltage values. The Voltage sweep window was set at -3 <V<1 V to examine the device operation regions. Thermally evaporated Al constitutes the bottom and top electrode material. Device performance of thermally annealed (TA) $\mathrm{ZrO_2}$ dielectric films is also depicted in navy blue. (Page **135**)

Figure 6.5: Capacitance- frequency measurements of MOS-Capacitor devices, with LA $\mathrm{ZrO_2}$ as a dielectric. The solution concentration was chosen at 0.1 M. C-V measurements are divided in 3 panels, corresponding to the number of deposited precursor ($\mathrm{Zr(AcAc)_4}$) layers *via* spin coating deposition. Laser fluences varied from 200-275 $\mathrm{mJ/cm^2}$. The number of pulses selected for each laser fluence was set to 1, 2 and 3. Frequency is swept from 1 kHz to 1 MHz while stress voltage is kept at -3 V. Each panel contains a shaded area where the highest Capacitance – frequency dispersion is detected. For C-f measurements corresponding to 2 Layers of deposited $\mathrm{ZrO_2}$ precursor (b), the shaded area is presented in blue to highlight the improved device performance in comparison to (a) and (c). (Page **136**)

Figure 6.6: Dielectric constant values (k) along with the corresponding frequency dependence of MOS-Capacitor devices with Laser annealed $\mathrm{ZrO_2}$ as a dielectric. The solution concentration

was chosen at 0.1 M while the number of layers was chosen at 2. Three colour coded regions are presented. Region 1 (light yellow) corresponds to devices with low k and high frequency dispersion, region 3 (light blue) includes the optimum capacitor behaviour and region 3 (lilac) corresponds to devices exhibiting high k alongside high frequency dispersion. In region 2, black arrows on left and right highlight the change in k with frequency increase. (Page **137**)

Figure 6.7:(a-c) Capacitance – Voltage (C-V) and (d-f) Capacitance- Frequency (C-f) measurements of MOS-Capacitor devices, with LA $\mathrm{ZrO_2}$ as a dielectric. The solution concentration was chosen at 0.15 M. C-V and C-f measurements are divided in 3 panels, corresponding to the number of deposited precursor ($\mathrm{Zr(AcAc)_4}$) layers *via* spin coating deposition. Laser fluences varied from 200-250 $\mathrm{mJ/cm^2}$. The number of pulses selected for each laser fluence was set to 1, 2 and 3. Frequency is swept from 1 kHz to 1 MHz while stress voltage is kept at -3 V. Thermally annealed (TA) measurements are also presented in navy blue. (**138**)

Figure 6.8: Thickness values of LA sol-gel $\mathrm{ZrO_2}$ thin films, based on 2 and 3-layered stacks. The solution concentration was kept constant at 0.15 M, with $\mathrm{Zr(AcAc)_4}$ as metal oxide precursor and 2-ME as a solvent. Films were deposited *via* spin coating. As LA parameters, 3 sets of fluence (200,225,250 $\mathrm{mJ/cm^2}$) and number of pulses (1,2 and 3) were used. (Page **139**)

Figure 6.9: Dielectric constant values (k) along with the corresponding frequency dependence of MOS-Capacitor devices with Laser annealed $\mathrm{ZrO_2}$ as a dielectric. The solution concentration was chosen at 0.15 M while the number of deposited layers varied between 2 and 3. (Page **140**)

Figure 6.10: Dielectric breakdown of 2 and 3-layered LA $\mathrm{ZrO_2}$ thin films, treated at 200, 225 and 250 $\mathrm{mJ/cm^2}$, under 1 (black), 2 (red) and 3 (blue) pulses. Green line also represents the performance of reference (TA) samples. The extrapolation of breakdown region into the associated breakdown field ($\mathrm{MV/cm}$) is represented by corresponding dotted lines. (Page **142**)

Figure 6.11: Atomic Force Microscopy (AFM) analysis of 2 and 3-layered $\mathrm{ZrO_2}$ thin films, treated at 225 $\mathrm{mJ/cm^2}$, under 1, 2 and 3 pulses. The corresponding TA samples are also presented for reference. (Page **144**)

Figure 6.12: I-V and C-V characterisation of TFT devices based on sol-gel thermally (a-d) and Laser annealed (e-h) $\mathrm{ZrO_2}$ and $\mathrm{In_2O_3}$ thin films. The thermal annealing conditions chosen here are 3000C,60 mins. Panels (e-h) represent devices annealed at two stages; $\mathrm{ZrO_2}$ is annealed at 225 $\mathrm{mJ/cm^2}$ (1 pulse), followed by $\mathrm{In_2O_3}$ precursor deposition and additional annealing at 150 $\mathrm{mJ/cm^2}$ (1 pulse). (Page a and e) represent the transfer curves, (b-f) leakage currents, (c-g) output curves and (d-h) C-V measurements of thermally and laser annealed TFT devices, respectively. $\mathrm{V_{DS}}$ Output curves (c-g) are extracted at $-0.25 < \mathrm{V_{GS}} < 2$ V. Arrows in e indicate the IDS direction during VGS sweep. (Page **147**)

Figure 6.13: I-V and C-V characterisation of TFT devices based on sol-gel thermally (a-d) and Laser annealed (e-h) Al_2O_3 and In_2O_3 thin films. The thermal annealing conditions chosen here are 300°C,60 mins. Panels (e-h) represent devices annealed at two stages; Al_2O_3 is annealed at 175 mJ/cm^2 (1 pulse), followed by In_2O_3 precursor deposition and additional annealing at 150 mJ/cm^2 (1 pulse). a) and e) represent the transfer curves, (b-f) leakage currents, (c-g) output curves and (d-h) C-V measurements of thermally and laser annealed TFT devices, respectively. Output curves (c-g) are extracted at $-0.25\ V < V_{GS} < 2\ V$. Arrows in e) indicate the I_{DS} direction during V_{GS} sweep. Drain voltage values at e) range from 0.3V to 0.6 V, to prevent device from damage due to dielectric malfunction. (Page **149**)

Figure 6.14: I-V and C-V characterisation of TFT devices based on one step sol-gel Laser annealed ZrO_2/In_2O_3 (a-d) and Al_2O_3/In_2O_3 (e-h) thin films. Dielectric precursor solutions were initially spin coated and stabilised (150℃,15 min), followed by the corresponding In_2O_3 precursor deposition and stabilisation; A single laser annealing step (150 mJ/cm^2,1 pulse) was afterwards conducted. (Page a-e) represent the transfer curves, (b-f) leakage currents, (c-g) output curves and (d-h) C-V measurements, of thermally and laser annealed TFT devices, respectively. Output curves (c-g) are extracted at $-0.25V < V_{GS} < 2\ V$. (Page **151**)

Figure 6.15: I-V and C-V characterisation of TFT devices based on ALD fabricated Al_2O_3 with sol-gel thermally annealed In_2O_3 (a-d) and ALD fabricated Al_2O_3 with sol-gel LA In_2O_3 (e-h) thin films. (Page a-e) represent the transfer curves, (b-f) leakage currents, (c-g) output curves and (d-h) C-V measurements of thermally and laser annealed TFT devices, respectively. Output curves (c-g) are extracted at $-0.25V < V_{GS} < 2\ V$. Arrows in e) indicate the I_{DS} direction during V_{GS} sweep. Drain voltage values at a) and e) range from 1.6V to 2V. (**152**)

Figure 6.16: C-V characteristics of LA ZrO_2/In_2O_3 TFTs. LA was employed in a two-step process; initially, ZrO_2 was formed *via* LA of $Zr(AcAc)_4$ at 225 mJ/cm^2. Afterwards, $In(NO_3)_3$ precursor deposition was conducted, following LA at conditions shown in figure legend (150-250 mJ/cm^2, 1-3 pulses). (Page **154**)

1. Introduction

Over the last decade, the introduction of novel materials and techniques into electronics manufacturing has led to the evolution of a new technological era, consisting of a plethora of novel applications such as flexible displays [1], high sensitivity/responsivity sensors [2,3], memory devices [4], energy generation [5]. Fundamentally, these applications are based on high performance devices such as organic light emitting Devices (OLED), thin film transistors (TFT) and photovoltaics (PV) [6–10]. Considering them as trends-of-future, these applications principally comprise metal-oxides (MOs) due to their unique characteristics (optical transparency, high carrier mobility, mechanical stability) that render them superior candidates, especially compared to conventional technologies based on silicon (Si) and/or organic materials [11,12]. MO-based thin film devices (such as TFTs and capacitors) form an emerging scientific point of interest. Their ability to be readily integrated in complementary metal oxide semiconductor (CMOS) technologies is of paramount importance to achieving the delivery of the Internet-of-Things (IoT). An exciting recent development in the field explore the introduction of solution processing techniques into the existing manufacturing scheme of electronics [13–16]. This constitutes a potential step change (as a disruptive technology) in the realisation of the IoT, with potential to provide cost-effective, high throughput fabrication of devices with enhanced optoelectronic performance. A key point into implementing the pioneering progress delivered in the scheme of solution-processed metal oxide thin film fabrication in flexible substrates is the introduction of nanosecond Laser Annealing (LA) as an integral part of the process flow, in order to effectively achieve the formation of high-quality metal oxide thin films thus enabling the possibility of high-performance electronics. This annealing technique is superior to the conventional thermal annealing approach, as it surpasses the manufacturing limitations that originate from incompatibility of flexible substrates with high temperatures during thermal annealing. The research presented in this PhD thesis investigates the underlying mechanism behind metal oxide thin film formation *via* a combination of sol-gel and LA process steps, as well its implementation into development of TFTs and metal oxide capacitor devices.

1.1. Motivation and Challenges

Metal-oxide based electronics undoubtedly allows for a broad spectrum of innovative and high importance application fields, combining the “three pylon characteristics” of the ideal materials: transparency, tuneable optoelectronic properties, and stability [17]. Further expansion of this technology presents a tremendous dependency on its fabrication cost and scalability. A key bottleneck in delivering cost and scalability gain is the reliance on conventional deposition techniques such as vacuum based processes. These techniques offer high-quality MO thin films, but their high fabrication costs and energy consumption hinder their applicability to affordable,

large-scale electronics. Solution processed MO thin films offer several advantages in comparison to conventional approaches such as operation at atmospheric pressures, low raw material costs, and low operating costs. Furthermore, solution processes are, generally, more environmentally friendly by producing less waste) than conventional techniques. The steady realignment of material fabrication research towards solution processes acts as a complementary feature that enables metal oxides to better deliver on their promise for low-cost and high-performance electronic devices. The introduction of metal oxides into solution processes is achieved *via* a specific process that is commonly referred to as “sol-gel”. This process provides an easy route towards the preparation of MO thin films. Starting from metalorganic precursor salts (powders), an oxide network is obtained *via* inorganic polymerisation reactions [18,19]. These reactions occur by dissolving precursor salts into solvents thus forming solutions to be deposited on the substrates of interest [20]. Therefore, the term “sol-gel processing” is used to describe the synthesis of MOs by “wet chemistry” methods. The sol-gel process is low-cost and possesses essential advantageous features such as composition tuning and ambient processing conditions, allowing for a more straightforward approach to the synthesis of “tailor-made” materials [21–23]. Nevertheless, mastery of the sol-gel process requires accurate control over the entirety of chemical steps occurring during sol-gel process.

Amongst the wide set of available MO semiconductors, indium oxide ($\mathrm{In_2O_3}$) has recently attracted an increasing interest owing to its large electron mobility [24–26], high optical transparency [27,28], as well as its role as a transparent conducting oxide (TCO) host [29–32]. Zinc oxide (ZnO) has been routed as a favourable material in the scene of high-standard contemporary research due to its wide range of properties such as chemical [33–35] and mechanical stability [36,37]. Along with the semiconductors, metal oxide dielectrics (such as $\mathrm{Al_2O_3}$ and $\mathrm{ZrO_2}$) have emerged as excellent materials for optoelectronic applications such as active waveguide sensors and dielectric layer in TFTs, due to their high dielectric constant, wide bandgap, and high refractive index. Metal oxides, through the scope of sol-gel, have the potential to enable a high throughput manufacturing scheme of devices with remarkable performance, based on the use of ultra-thin MO films ($\sim 10\ \mathrm{nm}$). To achieve this, accurate monitoring over thin film manufacturing *via* sol-gel is key. Importantly, $\mathrm{In_2O_3}$ and ZnO constitute solution processible materials, with sol-gel chemistry allowing for the fine tuning of their optoelectronic properties. Various precursor salt types have been used towards the formation of metal oxide thin films, including nitrates, acetates, perchlorates and more [38]. Importantly, the salt types are accompanied by their corresponding chemical reaction pathways towards MO formation, thus demanding treatment in specific temperatures and atmospheric conditions.

The chemical complexity accompanying the formation of sol-gel MO thin films has provoked the interest of various scientific studies over the past years, that seek to elucidate the chemical make-up of thin film MOs with conventional characterisation techniques such as Fourier transform infrared spectrometry (FTIR) [39,40] and X-ray photoelectron spectroscopy (XPS) [24,41,42]. These studies have massively contributed towards a deeper understanding of the chemical pathways involved in sol-gel process, enabling the establishment of sol-gel metal oxide thin films implementation in a plethora of applications such as sensors and TFTs. However, conventional characterisation techniques such as FTIR present a diminishing sensitivity as the film thickness decreases, hindering their applicability for ultra-thin (~ 10 nm) film-based applications. Also, the high-cost and time requirements of X-Ray Photo Spectroscopy (XPS) alongside its invasive character (*e.g.*, Argon etching for depth-profile XPS) allows only for final product analysis, restricting the possibility of in situ monitoring during fabrication. Therefore, the implementation of non-invasive, characterisation pathways with nm-scale resolution amenable to in-line monitoring of thin film production systems (*e.g.* R2R)[43] could realise the introduction of sol-gel metal oxide thin films in high throughput manufacturing.

Alongside the challenges involved in the characterisation of ultra-thin MO films, the introduction to large-area manufacturing of electronics is still restricted by the conventional but rather restrictive post-deposition, high-temperature, thermal annealing treatment. Specifically, after the deposition of the MO precursor solution *via* wet-chemical techniques (sol-gel) there are steps that drive the chemical transition into the desirable MO accompanied by film densification and condensation. These steps require an induced amount of energy, which is currently delivered by an intense thermal treatment. For this step, high temperatures (> 250 ℃) at prolonged processing times (1 hour or more) are mandatory, in order to obtain the optimal film properties such as chemical homogeneity, desirable stoichiometry and crystal structure. This conventional scheme of MO film manufacturing suffers from various disadvantages, including high energy consumption and loss, high thermal budget, and most importantly the prohibition of plastic and other flexible substrate integration. Therefore, substitution of thermal annealing by novel routes is essential. Reflecting on the outlined present state of sol-gel MO thin film technology, one can identify two major challenges preventing the proliferation of the large-scale electronics and the IoT:

1. Unravelling of MO formation mechanism *via* characterisation techniques that present both high sensitivity to ultra-thin films and compatibility with high throughput manufacturing systems.
2. Substitution of prolonged and high-temperature thermal annealing with ultra-fast surface annealing methods that preserve the substrate properties.

As such, seeking solutions to overcome these challenges comprise the main objectives of this work. To address the first challenge, this work introduces the use of infrared spectroscopic ellipsometry (IRSE) in the characterization "agenda" of sol-gel ultra-thin films. The non-destructive, self-referencing, and highly sensitive (sub-nm scale) nature of IRSE has placed it amongst the top-rated optical characterisation techniques. To this end, IRSE has been employed in MO-based studies, providing vital information about the structural (vibrational modes), optoelectronic (carrier mobility), and geometrical (thickness, roughness) features of MO thin films. However, to the best of our knowledge, IRSE has not as-of-yet been implemented for the optical characterisation of ultra-thin sol-gel MO films. In this work, IRSE was employed in the detection and analysis of metal-oxide sol-gel formation process of two principal metal oxide materials that were extensively investigated in this thesis, namely $\mathrm{In_2O_3}$ and ZnO, based on the thermal conversion of indium nitrate ($\mathrm{In(NO_3)_3}$) and zinc acetate ($\mathrm{Zn(CH_3COO)_2}$) precursors, respectively. We extracted information about the absorption spectra during each conversion step by detecting the presence of vibrational modes and associating them with conversion by-products. To activate the potential of implementation in device manufacturing, the challenge of ultra-thin film analysis was addressed, with thicknesses ranging from $7-15\ \mathrm{nm}$. To this end, this work focused on the role of substrates towards the accurate detection of vibrational modes in thermally processed ultra-thin $\mathrm{In(NO_3)_3}$ and $\mathrm{Zn(CH_3COO)_2}$ films. The use of conductive substrates is implemented, as a comparison to moderately doped $\mathrm{n\text{-}Si}$, to enhance the sensitivity of IRSE. Finally, the substrate's electronic properties (conductivity) are correlated with the detectability out of the spectral features of $\mathrm{In_2O_3}$ and ZnO precursor films.

To tackle the second challenge, various cost and time effective strategies have been proposed in order to replace high-temperature thermal treatment for sol-gel precursor transition[44,45]. In detail, several studies have recently reported the successful fabrication of sol-gel MO thin films *via* photonic curing, such as deep ultra-violet (DUV) lamp irradiation[46–48], flash lamp [49–53] and, substantially fewer, laser annealing (LA) attempts [54]. Overcoming the demand of prolonged exposure time and patterning masks in the case of DUV and flash lamps, LA constitutes a novel tool towards MO film manufacturing, gathering multiple advantages such as rapid energy transfer and fast processing times alongside a fine tuning of the resultant thin film (corresponding to the exact set of the multiple laser annealing parameters) [55]. In addition, the high spatial resolution of LA offers the opportunity of precise control over the area of interest, thus enabling accurate patterning of the deposited film without the use of time and material-consuming lithography steps [56]. Finally, the selective energy delivery and precise absorption depth allow for the control of energy absorption only in the MO film, leaving the substrate intact. This establishes the compatibility of LA with flexible substrates, rendering

it as one of the most promising candidates into commercialization of MO-based device manufacturing.

1.2. Novelty and Impact

This work proposes a novel material processing strategy that combines solution-processing and laser annealing, in order to establish two important attributes that are currently absent from the state-of-the-art commercial technologies: scalable manufacturing and photonic assisted annealing *via* ultra-fast laser post-processing. Due to the temporal nature of the laser-annealing step (typically nanoseconds), efficient conversion of the printed metal oxide precursor can be achieved even when the layer is deposited atop temperature-sensitive substrates such as plastic. There is currently no other method that combines these two highly attractive attributes (scalability and short processing time) while being compatible with existing manufacturing processes. Therefore, this research is hugely timely for the relevant scientific and commercial sector due to its close relevance to numerous emerging technologies that rely on MOs for TFT technologies. The feasibility of the proposed approach has already been demonstrated [24], so it is now timely to proceed with developing an in-depth understanding of the mechanisms involved. Building such an understanding will enable optimisation of the process and tight control of the resultant materials' properties, facilitating the expansion to more complex device architectures (multilayer structures involving dielectrics and semiconductors). Additionally, the implementation of IRSE as a principal characterisation route towards deconvoluting the LA effect on sol-gel metal oxide ultra-thin film introduces a versatile, non-destructive, and highly accurate approach towards the study and optimisation of MO thin film properties. The combination of the above-mentioned fabrication and characterisation techniques could drive new research to better understand sol-gel and MOs, which will further boost the adoption of LA into a new technological era of high throughput device realisation.

1.3. Research Aim

The primary aim of this thesis is to establish a deeper understanding behind the laser annealing mechanism of solution processed MOs and further to utilize this understanding for the fabrication of electronic devices based on solution processed MO thin films.

1.4. Research Objectives

The realisation of the research aim came to fruition through the following objectives:

1. Elucidation of the metalorganic conversion mechanism into MO through the scope of IRSE: Formation of indium oxide ($\mathrm{In_2O_3}$) and zinc oxide (ZnO) ultra-thin films ($7-15\ \mathrm{nm}$) *via* solution processing was investigated with IRSE, including measurements and analysis of 3 thermal annealing steps. The influence of the substrate on the enhancement of IRSE sensitivity was additionally studied, accompanied by the development of a universal approach towards extracting an optoelectronic profile of ultra-thin films *via* IRSE. To the best of our knowledge, this is the report where IRSE is employed for such purpose.
2. Determination of the influence of LA parameters on the photochemical conversion of solution processed metalorganic precursors towards TFT fabrication: The effect of various LA parameters (*e.g.*, laser energy density, number of pulses) on the photochemical conversion of $\mathrm{In_2O_3}$,Indium Gallium Zinc Oxide (IGZO) and ZnO was thoroughly investigated, building a database of laser processing recipes and attainable thin film properties. The LA-induced photochemical conversion mechanism was investigated through study and analysis of TFT device performance, with LA sol-gel semiconductors $\mathrm{In_2O_3}$, ZnO, IGZO as active device elements. The response of $\mathrm{In_2O_3}$ and ZnO precursors with respect to thermal processing (extracted from IRSE analysis) constituted the starting point of reference.
3. Utilisation of the above-mentioned data and expanding towards MO dielectrics, MO thin film capacitors and fully solution processed MO TFTs: The in-depth understanding and optimisation of sol-gel MO semiconductor thin films enabled us to proceed into investigating sol-gel MO dielectrics ($\mathrm{ZrO_2}$, $\mathrm{Al_2O_3}$) and deliver MO thin film capacitor (TFC) devices. The optimisation of dielectrics allowed for attempting fabrication of TFT devices based on sol-gel and laser processed MO thin films for both the semiconductor and dielectric layers. Hereby, the incorporation of LA and solution processing is presented as a novel, versatile, and superior route to TFT manufacturing.

1.5. Overview of Research Methodology

This work involves the use of solution processes (spin coating) and LA to fabricate MO thin films that constitute active elements of TFTs and TFCs. The spin coating process starts with preparation of solution to be deposited, which involves dilution of the desired material (typically precursor salts for sol-gels) in a solvent. The solution is subsequently dispensed on the substrate surface, followed by substrate spinning. The thickness of the film is determined by the solution viscosity (associated to molar concentration) spinning speed, and surface tension. The solvent is removed partly during the spinning process due to evaporation and partly by subsequent annealing at temperatures close to the solvent's boiling point (to ensure solvent removal). This technique results in a relatively planar surface and is the most widely adopted solution process for research and industrial applications, largely due to the ability to finely control the deposition parameters. In addition, this technique is often used for planarization purposes as well as photoresist deposition in lithography systems. In the case of sol-gels, spin coating of precursor salts followed by the solvent removal results in the gel solidification which subsequently forms a dense and uniform solid thin film [57].

The formation of MO thin films *via* sol-gel routine presently demands a post-deposition thermal annealing step of the precursor film in order to promote its conversion into an MO. However, the TA process is cumbersome and requires long dwell times (hours) to remove any precursor-related by-products and achieve a complete conversion. In addition, the use of high TA temperatures ($> 500^0\mathrm{C}$) demanded by sol-gel chemistries hinder their compatibility with electronic manufacturing technologies based on flexible substrates. To overcome these limitations, LA was adopted as the principal post-deposition processing technique which promotes the photochemical precursor conversion. The short processing times, along with the technique's ability to process small areas across a shallow depth, constitute LA as a promising annealing pathway. In LA, the laser photons with energy higher than the material's band gap irradiate and are absorbed by the annealed material. The photon energy is rapidly converted into a highly localised heating with a thermal gradient between the surface and underlying layers [58,59]. LA is often performed at atmospheric conditions (pressure and composition), while fine tuning of LA parameters such as laser fluence and number of pulses is performed.

1.6. Structure of Thesis

This thesis is composed of seven chapters organised as follows:

1. **Chapter 1** presents the research aims and objectives and motivation as well as a brief overview of the research methodology and novelty of this work. The chapter is completed with an outline of the thesis structure.
2. **Chapter 2** elaborates on the background literature and fundamentals associated to the results of this work. It involves the basics on optical properties of solids as well as the fundamental principles of TFT operation. Also, an outline to sol-gel chemistries is provided, to engage the reader into the basic process flow of thin film fabrication utilised in this project. Also, an overview on metal oxides is presented, focusing on the unique features of metal oxide semiconductors and dielectrics, as well as their association with photonic processing. A brief introduction to laser annealing is also conducted, including its origin and applications.
3. **Chapter 3** provides extensive detail into all the fabrication and characterisation techniques employed in this work.
4. **Chapter 4** presents the results on IRSE analysis of ultra-thin sol-gel $\mathrm{In_2O_3}$ and ZnO films, including associated simulations which – along with the experimental findings – contribute to building a deep understanding of the MO precursor conversion through the scope of IRSE, as well as proposing a model to associate the substrate's optoelectronic properties to IRSE sensitivity.
5. **Chapter 5** reports the results on TFT devices based on sol-gel LA MO semiconductor layers, with respect to changes in LA annealing parameters (laser fluence and number of pulses). Specific attention is paid on the role of dielectric thickness as a parameter defining the photochemically assisted conversion of the upper (semiconductor) layer. Based on the findings of **Chapter 4** (which highlight differences amongst $\mathrm{In_2O_3}$ and ZnO thin film formation), a deep analysis of the electrical performance of the corresponding TFTs is conducted.
6. **Chapter 6** presents new insights into the electrical performance of MO capacitors, based on sol-gel MO LA thin film dielectrics ($\mathrm{ZrO_2}$ and $\mathrm{Al_2O_3}$). In addition, the performance of fully solution processed LA TFTs is reported.
7. **Chapter 7** remarks the conclusions and key outcomes of this work along with suggestions on future work on solution processed LA MO based electronic devices.

2. Background and Literature Review

This chapter provides the background information on the fundamentals of the optical properties of solids alongside the operation of thin film transistors (TFTs). In addition, an overview of sol-gel chemistry is presented, along with key features of metal oxides (MOs), focusing on the materials of interest in this work. Finally, the laser annealing (LA) of MOs is briefly discussed, aiming to reinforce the motivation behind this work.

2.1. Optical Properties of Solids

2.1.1. Electromagnetism Fundamentals

Since this work investigates the formation of MO materials through the scope of an optical characterisation technique, namely infrared spectroscopic ellipsometry (IRSE), the fundamentals regarding the optical properties of solids, upon which the conducted analysis is based, must be underlined. All descriptions of optical properties stem from the solutions to the fundamental equations of Maxwell, which describe the interaction of electromagnetic radiation and matter. In differential form and SI units, they are written as [60,61]:

$$\nabla \cdot \mathrm{D}(\mathrm{r},\mathrm{t}) = \mathrm{q}(\mathrm{r},\mathrm{t}) \tag{2.1}$$

$$\nabla \cdot \mathrm{B}(\mathrm{r},\mathrm{t}) = 0 \tag{2.2}$$

$$\nabla \times \Xi(\mathrm{r},\mathrm{t}) = \frac{\delta \mathrm{B}(\mathrm{r},\mathrm{t})}{\delta \mathrm{t}} \tag{2.3}$$

$$\nabla \times \mathrm{H}(\mathrm{r},\mathrm{t}) = \frac{\delta \mathrm{D}(\mathrm{r},\mathrm{t})}{\delta \mathrm{t}} + \mathrm{j}(\mathrm{r},\mathrm{t}) \tag{2.4}$$

where D represents the electric displacement, B is the magnetic induction, Ξ is the electric field, and H is the magnetic field. D, B, Ξ, and H constitute functions of time, t, and space vector, r. Charge and current density are represented by q and j. D and H are also described as:

$$\mathrm{D}(\mathrm{r},\mathrm{t}) = \varepsilon_0 \Xi(\mathrm{r},\mathrm{t}) + \mathrm{P}(\mathrm{r},\mathrm{t}) \tag{2.5}$$

$$\mathrm{H}(\mathrm{r},\mathrm{t}) = \frac{1}{\mu_0}\mathrm{B}(\mathrm{r},\mathrm{t}) - \mathrm{M}(\mathrm{r},\mathrm{t}) \tag{2.6}$$

where $\mathrm{P}(\mathrm{r},\mathrm{t})$ defines the electric polarisation (average electric dipole moment per unit volume), ε_0 is the permittivity of free space ($\varepsilon_0 = 8.854 \times 10^{-12}\ \mathrm{Fm}^{-1}$), $\mathrm{M}(\mathrm{r},\mathrm{t})$ is the magnetisation (average magnetic dipole moment per unit volume) and μ_0 is the permeability of free space ($\mu_0 = 1.257 \times 10^{-6}\ \mathrm{Hm}^{-1}$). In order to describe the response of matter to fields described by the above equations (assuming an isotropic and linear medium without external charges and currents), D and B are supplemented with the constitutive relations [60,62], which are combined with **Eqs. 2.3** and **2.4** (following an assumption of a time-harmonic field) to give:

$$\mathrm{D}(\mathrm{k},\omega) = \varepsilon_0 \varepsilon(\mathrm{k},\omega)\Xi(\mathrm{k},\omega) \tag{2.7}$$

$$\mathrm{B}(\mathrm{k},\omega) = \mu_0 \mu(\mathrm{k},\omega)\mathrm{H}(\mathrm{k},\omega) \tag{2.8}$$

$$\mathrm{j}(\mathrm{k},\omega) = \sigma(\mathrm{k},\omega)\Xi(\mathrm{k},\omega) \tag{2.9}$$

where k and ω are the wavevector and angular frequency, respectively. $E(k, \omega)$ and $\mu(k, \omega)$ are the relative permittivity and permeability of a material, respectively. ε is also often reffered to as the dielectric constant, while $j(k, \omega)$ is the current density and $\sigma(k, \omega)$ is the conductivity of the material. **Eqs. 2.7** and **2.9** display a dependence of ε, μ and σ on the wavevector and angular frequency. For wavelengths much smaller than the material dimensions, the wavevector dependence is neglected. The frequency dependence of $\varepsilon(\omega)$ is referred to as the dielectric function or the material's permittivity and it is a fundamental point of interest on the material's optical response. In the case of uniform, isotropic and non-magnetic materials ($\mu(\omega) = 0$), the Helmholtz wave equation can thus be extracted [63]:

$$\nabla^2 \Xi_\omega(r) + \frac{\omega^2}{c^2}\, \varepsilon(\omega) \Xi_\omega(r) = 0 \qquad 2.10$$

In the case of a material where current sources are considered, the Helmholtz wave equation is then described as:

$$\nabla^2 \Xi_\omega(r) + \frac{\omega^2}{c^2} \left(\varepsilon(\omega) + i \frac{\sigma(\omega)}{\omega \varepsilon_0} \right) \Xi_\omega(r) = 0 \qquad 2.11$$

By comparing the forms of Helmholtz equation before and after the addition of current sources, one observes the transformation of permittivity into a complex value:

$$\varepsilon(\omega) \rightarrow \varepsilon(\omega) + i \frac{\sigma(\omega)}{\omega \varepsilon_0} \qquad 2.12$$

Therefore, the frequency-dependent properties of a material can be described by the complex permittivity:

$$\tilde{\varepsilon}(\omega) \rightarrow \varepsilon_1(\omega) + i\varepsilon_2(\omega) \qquad 2.13$$

where $\varepsilon_1(\omega)$ and $\varepsilon_2(\omega)$ are the real and imaginary parts of complex permittivity, $\tilde{\varepsilon}(\omega)$.

2.1.2. Description of Electromagnetic Waves

In order to study the propagation of the electromagnetic waves within a material (medium), one must first define them (here assuming their simplest form as plane waves) [61]:

$$\Xi(r, t) = \Xi_o e^{i(k \cdot r - \omega t)} \qquad 2.14$$

$$H(r, t) = H_o e^{i(k \cdot r - \omega t)} \qquad 2.15$$

where Ξ_o and H_o are the complex vectors representing the electric and magnetic field amplitudes, respectively. $\tilde{k} = k_1 + ik_2$ is also complex. In the case of a homogeneous electromagnetic plane wave with $\tilde{k} = (k_1 + ik_2)\underline{\hat{e}} = \tilde{k}\underline{\hat{e}}$, where $\underline{\hat{e}}$ is a real unit vector in the direction of the wave propagation and there is no charge or current density ($j = 0$), one derives:

$$\varepsilon(\omega) k \cdot \Xi_o = 0 \qquad 2.16$$

$$k \cdot H_o = 0 \qquad 2.17$$

$$k \times \Xi_o = \omega \mu_0 H_o \qquad 2.18$$

$$k \times H_o = -\omega \varepsilon_0 \tilde{\varepsilon}(\omega) \Xi_o \qquad 2.19$$

Eqs. 2.14 and **2.15** show the presence of a transverse wave, as k is perpendicular to Ξ_o and H_o. The combination of 2.16 and 2.17 thus leads to the dispersion relation:

$$k(\omega) = \sqrt{\varepsilon(\omega)}\frac{\omega}{c} = \tilde{n}(\omega)\frac{\omega}{c} \qquad 2.20$$

where $\tilde{n}(\omega)$ is the complex refractive index:

$$\tilde{n}(\omega) = \sqrt{\varepsilon(\omega)} = n(\omega) + i\kappa(\omega) \qquad 2.21$$

while $n(\omega)$ is the usual refractive index and $\kappa(\omega)$ is the extinction coefficient. n determines the phase velocity, $v(\omega) = c/n(\omega)$, where c is the speed of light in vacuum. κ defines the attenuation of a wave propagating through the medium, giving the absorption coefficient $\alpha(\omega)$:

$$\alpha(\omega) = 2\frac{\omega}{c}\kappa(\omega) = \frac{4\pi\kappa(\omega)}{\lambda} \qquad 2.22$$

where λ is the wavelength. n and κ can thus be used to define the real and imaginary part of the complex permittivity, $\varepsilon_1(\omega)$ and $\varepsilon_1(\omega)$, respectively:

$$E_1(\omega) = n^2(\omega) - \kappa^2(\omega) \qquad 2.23$$

$$\varepsilon_2(\omega) = 2n(\omega)\kappa(\omega) \qquad 2.24$$

$$n^2(\omega) = \frac{1}{2}\sqrt{\varepsilon_1^2(\omega) + \varepsilon_2^2(\omega)} + \frac{\varepsilon_1(\omega)}{2} \qquad 2.25$$

$$\kappa^2(\omega) = \frac{1}{2}\sqrt{\varepsilon_1^2(\omega) + \varepsilon_2^2(\omega)} - \frac{\varepsilon_1(\omega)}{2} \qquad 2.26$$

In this work, $\varepsilon_1(\omega)$ and $\varepsilon_2(\omega)$ were extensively used to define the material's properties, mostly focusing on $\varepsilon_2(\omega)$, as it is highly indicative of the absorption as a function of the photon energy.

2.1.3. Lorentzian Oscillator

To describe an optical absorption at a specific photon frequency, a set of various oscillators are implemented that describe the physical mechanism behind this light-matter interaction. The most broadly used oscillator, the Lorentz model, describes the bond amongst a negatively charged electron and a positively charged ion (*i.e.,* a hydrogen atom), presented in **Figure 2-1**. This oscillator model is analogous to a classic damped oscillator with a restoring force that is characterised by a resonant frequency, ω_0, as well as any bound dipoles. The equation of motion for the electron in response to an external electric field can be derived from Newton's laws, while including damping, driving and spring forces [64]:

$$F_{acceleration} = m\frac{d^2r}{dt^2} = F_{Driving} + F_{Damping} + F_{Spring} \qquad 2.27$$

By using Hooke's law to describe the spring force [65], Coulomb's Law for driving force due to external electric field $\Xi(t)$ [66], and assuming that damping is linearly proportional to mass velocity (with a damping constant γ), one derives:

$$\frac{d^2r(t)}{dt^2} + \gamma\frac{dr(t)}{dt} + \omega_0^2 r(t) = \frac{e}{m_e^*}\Xi(t) \qquad 2.28$$

where $r(t)$ is the electron displacement at a time t, γ is the damping coefficient, e is the electron charge and m_e^* is the electron's effective mass. According to Hooke's law, the spring constant K is associated to the oscillator frequency, ω_0 *via* $\omega_0 = \sqrt{K/m_e^*}$. Also, for $\Xi(t) = \Xi_0(\omega)e^{-i\omega t}$ and seeking a solution in the form of $r(t) = r_0(\omega)e^{-i\omega t}$ gives that:

$$r_0(\omega) = \frac{e}{m(\omega_0^2 - \omega^2 - i\gamma\omega)}\Xi_0(\omega) \quad 2.29$$

Given the electric dipole moment, $\mu_0(\omega) = er_0(\omega)$, the polarisation vector (density of dipole moments per volume), $P = N\mu_0(\omega) = Nqr_0(\omega)$ [67], and by also noting that $P(\omega) = \varepsilon_0\chi_e(\omega)\Xi_0(\omega)$, one obtains the complex permittivity:

$$\tilde{\varepsilon}(\omega) = 1 + \frac{N_L e^2}{\varepsilon_0 m_e^*} \cdot \frac{1}{\omega_0^2 - \omega^2 - i\gamma\omega} \quad 2.30$$

where N_L is the number of Lorentzian oscillators per unit volume. To consider all other transitions which take place in a real material, the electric displacement is divided into two parts: the resonant part: $P(\omega) = \varepsilon_0(\tilde{\varepsilon}(\omega) - 1)\Xi(\omega)$ and the background part, $P_b(\omega) = \varepsilon_0(\varepsilon_\infty - 1)\Xi(\omega)$. The resonant part represents the Lorentzian oscillator whereas the background contributions are represented by a high frequency permittivity, ε_∞. The complex permittivity can therefore be written as [68]:

$$\tilde{\varepsilon}(\omega) = \varepsilon_\infty + \frac{f_L^2}{\omega_0^2 - \omega^2 - i\gamma.\omega} \quad 2.31$$

where $f_L^2 = N_L e^2/\varepsilon_0 m_e^*$ is the oscillator amplitude, A_L. In the resonant condition ($\omega = \omega_0$):

$$\varepsilon_2(\omega = \omega_0) = A_L = \frac{f_L^2}{\gamma\omega_0} \quad 2.32$$

such that $\tilde{\varepsilon}(\omega)$ can be then written as:

$$\tilde{\varepsilon}(\omega) = \varepsilon_1(\omega) + i\varepsilon_2(\omega) = \varepsilon_\infty + \frac{A_L\gamma\omega_0}{\omega_0^2 - \omega^2 - i\gamma\omega} \quad 2.33$$

with:

$$\varepsilon_1(\omega) = \varepsilon_\infty + \frac{(A_L\gamma\omega_0)(\omega_0^2 - \omega^2)}{(\omega_0^2 - \omega^2)^2 + (\gamma\omega)^2} \quad 2.34$$

and:

$$\varepsilon_2(\omega) = \frac{(A_L(\gamma^2\omega_0\omega)}{(\omega_0^2 - \omega^2)^2 + (\gamma\omega)^2} \quad 2.35$$

Figure 2-1 presents the typical shape of the real and imaginary parts of a Lorentzian oscillator, where $\varepsilon_\infty = 1$, $A = 10$, $\gamma = 0.1$ eV, and $E_0 = \hbar\omega_0 = 3$ eV. E_2 is represented as a bell-shaped curve which is defined by the amplitude, A, and full-width half-maximum (FWHM), γ, centred on E_0. Also, $\varepsilon_2 \to 0$ when $E \to 0$ or $E \to \infty$. The lineshape of ε_1 is divided into two regions: the normal dispersion region (increasing E from left to right), where ε_1 increases, reaching a maximum value at $\approx E_0 - \gamma$. The anomalous dispersion region follows, where ε_1

rapidly decreases at $E_0 - \gamma < E < E_0 + \gamma$. When $E > E_0 + \gamma$, a re-entry in the normal dispersion region is obtained, with an increase in ε_1 as it trends towards ε_∞. Note the importance of Lorentzian oscillator description in this part of the thesis, as it provides the background knowledge of absorption representation during IRSE analysis.

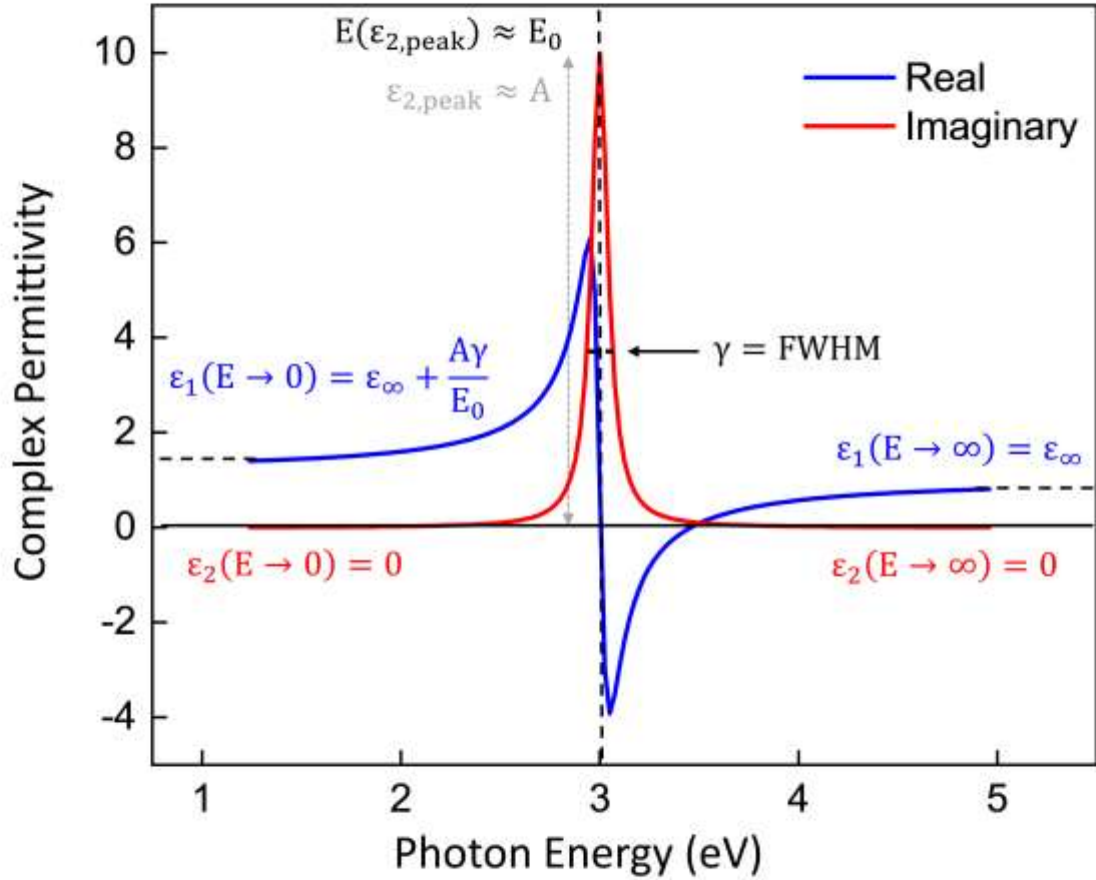

Figure 2-1. Real (blue) and Imaginary (red) permittivity of a Lorentz oscillator with $\varepsilon_\infty = 1, A = 10, \gamma = 0.1$ eV, and $E_0 = \hbar\omega_0 = 3$ eV.

2.2. Introduction to Metal Oxides (MOs)

The emergence of thin film-based electronics has set the foundation of a revolutionary device ecosystem, namely the Internet of Things (IoT) [69]. This incorporates the realisation of an expanded palette of applications in energy saving [70–73], flexible displays [74–77], and smart windows [78–82]. Each are expected to have a tremendous impact on our quality of life. Thin film transistors (TFTs) [83–85], solar cells [86–88], and sensors [89,90] constitute only a fraction of thin film-based devices that have shaped a socio-technological synergy over the last decades. The current thin film technology is mostly dominated by traditional silicon (Si) microchip-based electronics [91,92], based on conventional vacuum-based processing techniques [93]. However, the economic and technological constrains imposed by Si technology (*e.g.,* limited charge carrier mobility, high manufacturing cost, and incompatibility with flexible substrates) [94–98] demand a radical change in the choice of materials, as well as manufacturing technologies. To

tackle these challenges, metal oxides (MOs) [99–102] have emerged as the ideal alternative due to their outstanding electrical and optical properties (high mobility [103] and transparency [17]) and mechanical stability [104]. Their assembly into low dimensional metal oxide heterostructures [105–107] has been shown to result in even higher mobilities rivalling those of poly-Si [108–110]. In addition, MOs offer a unique processing versatility as they can be grown *via* both vapour-and solution-phase techniques [111–114]. Henceforth, their superiority is reinforced as they create a new industry path in electronics, characterised by up-scalable and high-throughput manufacturing [115].

2.3. History and properties of MO semiconductors

A comparison amongst metal oxides and various material categories reveals the superiority of the former due to their unique combination of properties: high optical transparency in the visible range along with tuneable conductivity, σ. Metals, for instance, are considered excellent conductors due to the high conductivity values they exhibit. However, the high concentration of free carriers N renders them opaque at visible wavelengths. On the other hand, ceramics are distinguished in optical applications due to their typically wide bandgap, $\mathrm{E_g}$, which renders them transparent. Their insulating behaviour does, however, hinder their use as active materials in electronic devices. Nevertheless, a fraction of ceramic materials, referred to as MO semiconductors in this work, exhibit both optical transparency ($\mathrm{E_g} > 3\ \mathrm{eV}$) and high carrier concentrations ($\mathrm{N} > 10^{19}$). These properties establish them as excellent candidates for optoelectronic applications. Indium oxide ($\mathrm{In_2O_3}$), zinc oxide (ZnO), and tin oxide ($\mathrm{SnO_2}$) constitute some of the most widely used MO semiconductors. Due to their lower mobility values (compared to single crystalline Si where $\mu > 400\ \mathrm{cm^2/vs}$), these materials are often degenerately doped to achieve high values of σ. This doping is usually achieved by the introduction of extrinsic substitutional elements in the host crystal structure (for example Sn doping in $\mathrm{In_2O_3}$ which leads to the formation of indium-tin-oxide (ITO)), as well as intrinsic defects such as oxygen vacancies. This versatility in doping is directly associated to large deviations from formation of stoichiometric MO semiconductors (also depending on the deposition process), which constitutes the principal reason for the electrical conductivity of these materials: to maintain charge neutrality, the abovementioned defects give rise to free carrier generation, depending on the dopant's energy level with respect to $\mathrm{E_g}$ of the "seed" oxide. Most MO semiconductors display an n-type behaviour. However, the importance of p-type oxides is increasingly highlighted due to their significant role in fabrication of complementary logic circuits. With NiO constituting the first p-type oxide ever reported in 1993 [116]. $\mathrm{Cu_2O}$ and its doped forms ($\mathrm{CuAlO_2}$, $\mathrm{SrCuO_2}$ and $\mathrm{CuGaO_2}$) have also emerged as p-type oxides of great importance. According to Kawazoe *et al.* [117] the strategy towards p-type oxides

with good optical transparency and electrical conductivity is the design of materials with tetrahedral coordination where cations have a closed shell with comparable energy to the 2p levels of oxygen anions, followed by a decrease in the dimension of crosslinking of cations. Despite the tremendous progress achieved in p-type oxides, further investigation is still required in order to achieve conductivity and optical transparency comparable to n-type oxides [118].

Typically, an n-type oxide, such as $\mathrm{In_2O_3}$ and ZnO, contains metallic cations with $\mathrm{ns^0}$ and oxide anions with $\mathrm{2s^2 2p^6}$ valence electron configurations. The conduction band minimum (CBM) is composed by the empty metallic s-orbitals whereas the filled oxygen $\mathrm{2p}$-orbitals constitute the valence band maximum (VBM), as depicted in **Figure 2-2**. In the case of stoichiometric oxides, the Fermi Energy level ($\mathrm{E_F}$) lies in the middle of the energy bandgap, $\mathrm{E_g}$. However, the presence of intrinsic or extrinsic defects shifts $\mathrm{E_F}$ near or within CBM. The form of the CBM, which is associated to large radii and spherical s-orbitals, allows for the formation of an easy electron pathway due to the overlap of the neighbouring cations. Particularly for $\mathrm{In_2O_3}$ and ZnO, optical bandgaps above $3\ \mathrm{eV}$ are exhibited, in accordance with transparent materials. Regarding the carrier mobility, μ, in the case of $\mathrm{In_2O_3}$ and ZnO single crystals, similar values are exhibited amongst $\mathrm{In_2O_3}$ and ZnO. This lies on the fact that $\mathrm{In_2O_3}$ has larger 5s-orbitals which provide a better overlapping in comparison to 4s-orbitals of ZnO, however the higher metal-atom number densities and shorter metal-metal distances of the latter tend to balance the overall electrical properties achieved in these single-crystal semiconductors. Also, the transition from a single crystal to an amorphous/polycrystalline form (mostly defined by the chosen deposition route) has a dramatic effect on the carrier mobility, due to the introduction of grain boundary scattering, which reduces μ [119,120].

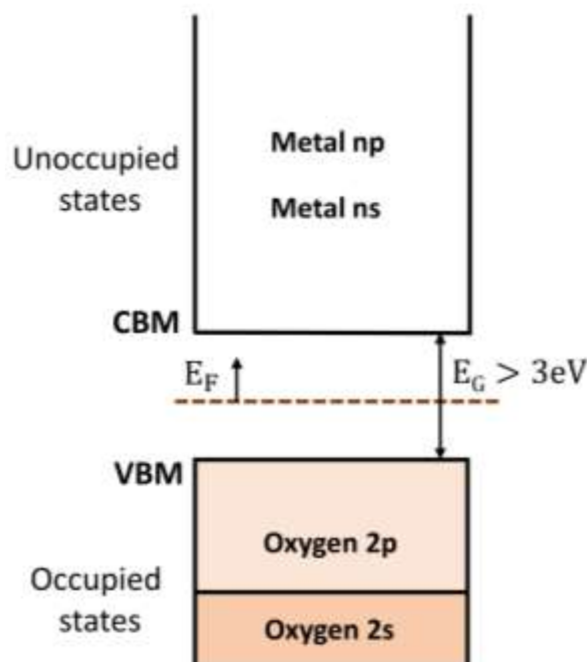

Figure 2-2. Illustration of simplified band structure of a metal oxide semiconductor.

Despite the superiority of MOs in comparison to conventional semiconductor materials, their optoelectronic properties are highly dependent upon their corresponding crystal structure, which is defined by the deposition technique and conditions. As most conventional thin film fabrication techniques lead to polycrystalline oxides, the introduction of grain boundaries is inevitable. This marks a decrease in carrier mobility. Conversely, to achieve oxides with high crystallinity orders, deposition in high temperatures is demanded. This precludes increased cost and time requirements. The trade-off between cost, industrialisation, and material performance constitutes a challenge, such that a deeper investigation on the comparison between amorphous and crystalline semiconductors is mandatory. a-Si is considered a well common example on successful implementation of an amorphous semiconductor, despite its deteriorated electrical performance in comparison to poly-Si.

For oxide semiconductors (like $\mathrm{In_2O_3}$) low processing temperatures lead to amorphous structure. However, in contrast to Si, the electrical properties of amorphous and polycrystalline MOs may appear similar. This observation was initially conducted by Bellingham *et al.* in 1990 [121], where ionised impurity scattering was presented as the principal carrier transport mechanism amongst amorphous and polycrystalline $\mathrm{In_2O_3}$ thin films. A few years later, the pioneering work of Hosono's group introduced a novel point of view towards amorphous oxide semiconductors [122]. A new compositional design was demonstrated, where multicomponent oxides composed of post-transition cations with a $(\mathrm{n}-1)\mathrm{d}^{10}\mathrm{s}^{0}$ electronic configuration displayed an amorphous nature with concurrent mobility values similar to polycrystalline materials. This establishment of dissociation amongst crystallinity and electrical performance can be explained by comparing the CBM structures of ionic (oxide) versus covalent (Si) semiconductors: In crystalline Si, the CBM is principally constructed by strongly directive and anisotropic sp^3 orbitals. Therefore, transition from crystalline to amorphous Si is accompanied by significant changes in bond angles, leading to highly localised stated with energy levels inside the bandgap. This change has a tremendously negative effect in the carrier transport, which is now achieved by carrier hoping amongst localised tail-states without achieving band conduction. In the case of MOs, large spherical isotropic ns orbitals (originating from metal cations) are forming the CBM. For $\mathrm{n} > 4$, an overlap amongst neighbouring orbitals is achieved, regardless of the disorder posed by amorphicity. This overlap secures a well-defined carrier path in the CBM, leading to higher μ values [123,124].

2.4. Metal Oxide Dielectrics

2.4.1. Device Requirements

A "dielectric" is an electrically insulating material that becomes polarised in the presence of electric field. Dielectric materials are characterised by absence of free carrier paths within them.

Instead, localised charges are slightly shifted from their equilibrium positions within the cell, leading to the formation of dielectric polarisation. This redistribution in charge counteracts the imposed external electric field. The formation of net dipoles at a specific location is described by the vector summation of each charge-displacement product from the superposition principle [125]. Dielectric materials have been widely used in the TFT industry in the role of insulators, in which a rapid reorientation and relaxation is demanded when a high frequency alternating current (AC) signal is used. This prerequisite is associated with the behaviour of various dielectric material upon specific frequency regions, which also define the operation of corresponding electronic devices. Usually, in a bottom gate, top Contact (BGTC) TFT structure, the dielectric layer is placed between a "gate" and the semiconductor. The carrier transport between "source" and "drain" electrodes is controlled by gate bias that polarises the gate dielectric. As the role of gate insulator principally defines the operation of a TFT device, several critical requirements are in place for the choice of dielectric layers, such as:

1. High dielectric constant, k, and decreased film thickness, which leads to low power consumption.
2. Low surface roughness and surface matching with (top) semiconductor layer, as the dielectric-semiconductor interface is relevant to the channel formation where carrier transport is conducted. The presence of carrier trap sites due to structural/morphological defects on the interface might deteriorate carrier mobility.
3. High thin film density to minimise leakage currents.
4. Minimisation of structural defects within the dielectric layer, the presence of which might affect the dielectric polarisation process.

In addition to the abovementioned features, the high bandgap $(\mathrm{E_g})$ is yet another point of attention for high-k dielectrics. Insulators with high bandgap values can block the charge injection to and from electrodes, due to the more effective reduction of parasitic electrical conduction. However, there is a difficulty in finding materials with high $\mathrm{E_G}$ and high k values, with no presently known dielectric presenting an ideally high dielectric constant (*i.e.,* $\mathrm{k} > 30$) and large energy band gap (*i.e.,* $\mathrm{E_g} > 8\ \mathrm{eV}$).

2.4.2. Metal Oxide Dielectrics as Insulating Layers

As the semiconductor industry has been continuously putting effort into minimisation of device dimensions (scale down), the dielectric layer thickness arises as one of the major associated challenges. In Si technology, $\mathrm{SiO_2}$ is typically used as the dielectric layer, due to the perfect $\mathrm{Si/SiO_2}$ interface formation. This effect is directly associated to the origin of $\mathrm{SiO_2}$ fabrication, as it is not deposited but rather formed by thermal oxidation of Si. However, recent device scaling down demands for dielectrics with thicknesses lower than $10\ \mathrm{nm}$, resulting in the use of

SiO_2 facing its critical limit from gate leakages that are dramatically increased due to tunnelling effects. To overcome this challenge, the implementation of high-k dielectrics in current device technologies is required. Since their first report in 1962 [126], MO dielectrics have extensively gathered interest mostly due to their high-k values [127–129], mechanical and chemical stability [130,131], as well as high optical transparency [17,132]. A plethora of high-k MO dielectrics have also been utilised as substitutions to SiO_2 in various microelectronic applications, such as central processing units (CPUs) and dynamic random-access memory (DRAM) [133,134]. In detail, many MO dielectrics present an inherently k that is significantly larger than SiO_2 (*i.e.,* $k = 3.9$). Also, regardless of the fabrication process (vacuum or solution-based), metal oxide dielectrics exhibit robustness and mechanical stability, which renders them ideal candidates for thin film thicknesses below $50\ nm$ while keeping the leakage currents minimised. The decreased thickness along with high k synergistically contribute to decreasing the demanded operating voltages in TFT devices, an important factor that is associated to low power consumption. This feature enables the transition towards the development of portable integrated electronics where low power consumption is mandatory.

Regarding the fabrication routes, considerable progress has been achieved towards developing high-performance metal oxide dielectric films *via* solution processes. Amongst the most prominent sol-gel dielectrics, AlO_x and ZrO_x have been widely investigated [16,54,135–139] due to the plethora of available precursors (*e.g.,* nitrates, acetylacetonates, chlorides, and alkoxides), high-k values ($Al_2O_3 \approx 15,\ ZrO_2 \approx 25$), and environmental stability. In addition, both AlO_x and ZrO_x maintain their amorphous phase even when processed at high temperatures [54,140], a feature that tremendously affects the insulator/semiconductor interface, as well as prohibits the formation of crystalline states which might lead to increase in leakage currents [141]. As this work focuses on MO thin films solely based on solution processing techniques, the fundamentals of sol-gel chemistry are going to be presented, with particular focus on MO formation.

2.5. Sol-gel Chemistry

The fabrication of inorganic refractory materials lies on the progress of complex technological systems that involve high temperature and long-lasting solid-state reactions. The introduction of materials like ceramics, MOs, and glasses has been defined by these schemes for thousands of years, based on natural raw materials. Following the evolution of thin film technologies, the integration of MO thin films in industrial device fabrication systems has been well established, while the use of temperature constitutes an integral part of the thin film formation processes such as deposition, melting and annealing. In general, the fabrication pathways of MO thin films can be divided into two principal groups:

i. Methods based on physical processes such as sputtering, physical vapor deposition (PVD), and electron beam evaporation (EBE), to name a few.
ii. Methods based on chemical reactions such as sol-gel chemistry, chemical vapour deposition (CVD), atomic layer deposition (ALD), to name a few.

The principle of the physical methods is a top-down approach where a bulk counterpart of the material of interest is employed. During the physical deposition processes, a gradual depletion of the bulk counterpart is conducted. This is in contrast to chemical methods where a bottom-up approach is followed and the assembly of atoms or molecules to form a network which gradually transforms into the thin film of interest [142]. Sol-gel technologies have been broadly explored over the past 50 years, as they constitute a remarkable alternative to produce MOs, as well as ceramics and glasses, at significantly lower temperatures. A sol-gel based system represents a solution where different polymerisation and polycondensation processes lead to the formation of a solid phase network [143].

The formed solution is at first subjected to a series of operations: gelling, pressing, drawing, and casting, which results in various structural and phase transformations. This permits formation of powders, fibres, coatings, and bulk monolithic products (*etc*.) from the same initial composition. In 1845, Ebelman became the first to report the formation of a transparent material as a result of slow hydrolysis of an ester of the silicic acid [144]. Since then, a large amount of reports, publications and conferences were dedicated to sol-gel technologies, presenting a wide range of investigations comprising all nuances in the corresponding field [145]. This solid-state chemistry alternative offers some superior advantages, centred on the ability to produce a solid-state material based on the conversion of a homogeneous precursor [21]. Amongst the various advantages of this chemical processing route, a remarkable control of dimension, composition and structure of the associated films is achieved. This is a critical factor in the evolution of various applications such as catalysis, optoelectronic devices, and sensing technologies. In addition, the development of sol-gel technologies has recently been combined with alternative thermal treatment approaches and less demanded energy for carrying out the thin film formation, establishing this route as vastly more economical compared to physical methods [142]. By ensuring atomic level mixing of reagents during solution formation, one should be able to produce complex inorganic materials such as ternary and quaternary oxides at lower processing temperatures and shorter synthesis times. The basic principle of sol-gel chemistry is the formation of inorganic polymers or ceramics and MOs from solution *via* the use of associated precursor solutions which transform into a "sol" and eventually to a network structure, "gel". The "sol" step is conducted *via* hydrolysis and condensation of metalorganic precursors [21]. The steps leading to MO thin film formation based on sol-gel chemistry are displayed in **Figure 2-3**, and are discussed below.

Step 1: Synthesis of the 'sol' from hydrolysis: This step involves hydrolysis of the precursors diluted in water or alcohols. For the synthesis of thin films based on the precursor conversion, oxygen is necessary. This is provided by water or other organic solvents (*e.g.,* alcohols). If water, H_2O, is used as a solvent, it is known as aqueous sol–gel method; and use of organic solvent as reaction medium for sol–gel process is termed as nonaqueous sol–gel route. In addition to water and alcohol, an acid or a base can also help in the hydrolysis of the precursors. Hydrolysis process can thus be described as [142]:

$$M - OR + H_2O \rightarrow MOH + ROH \qquad \text{(Hydrolysis)}$$

where M is the metal and R is the alkyl group (C_nH_{2n+1}). The quantity of water has a direct impact during the formation of gel; a higher water content facilitates the formation of a higher ratio of bridging to nonbridging oxygens, thus yielding a more polymerised and more branched structure during the condensation [142,146].

Step 2: Formation of the gel *via* polycondensation to form metal–oxo–metal or metal–hydroxy–metal bonds: During this step, condensation of adjacent molecules is conducted, along with removal of water and alcohol molecules. The formation of metal oxide linkages is employed, and polymeric networks grow to colloidal dimensions in the liquid state. Condensation occurs *via* two processes "olation" and "oxolation". During Olation, a hydroxyl (–OH–) bridge is formed between two metal centres (metal–hydroxy-metal bonds). During oxolation, an oxo (–O–) bridge is formed between two metal centres (metal–oxometal bonds) [142]. The progression of condensation depends on the degree of hydrolysis that has already occurred. Multiple condensation steps result in small, highly branched agglomerates in the 'sol' which eventually crosslink to form a colloidal gel [21]. In sol-gel syntheses, pre-condensation reactions are initiated in solution to control film morphology and ensure atomic-level mixing of multi-metal systems [147].

Condensation process can be described as:

$$M - OH + XO - M \rightarrow M - O - M + XOH \text{ (Condensation)}$$

where M is the metal and $X = H$ or alkyl group (C_nH_{2n+1}). During Condensation or polycondensation, the viscosity of solvent gradually increases; a porous structure is formed while the liquid phase is maintained - this state is defined as a gel. Also, solution parameters such as pH or type of precursor will ultimately define the size of the agglomerates comprising the gel [142,148–150].

Step 3: Gel drying: During this step, the gel is dried in order to form a dense "xerogel" [21]. The drying process is complicated because water and organic components are detached to form the gel, disturbing the structure of the gel network. There are different drying processes: atmospheric/thermal drying, supercritical drying, and freeze-drying, each one having different implications on the gel structure. Heating the deposited gel at elevated temperatures causes densification and promotes solvent evaporation, thus leading to the formation of a thin film. A critical parameter during the drying process is relative humidity (RH). The RH directly affects the stability and performance of nanomaterials. Particularly, nanofilms dried at lower RH are more stable than those which have been dried at higher RH [142,151].

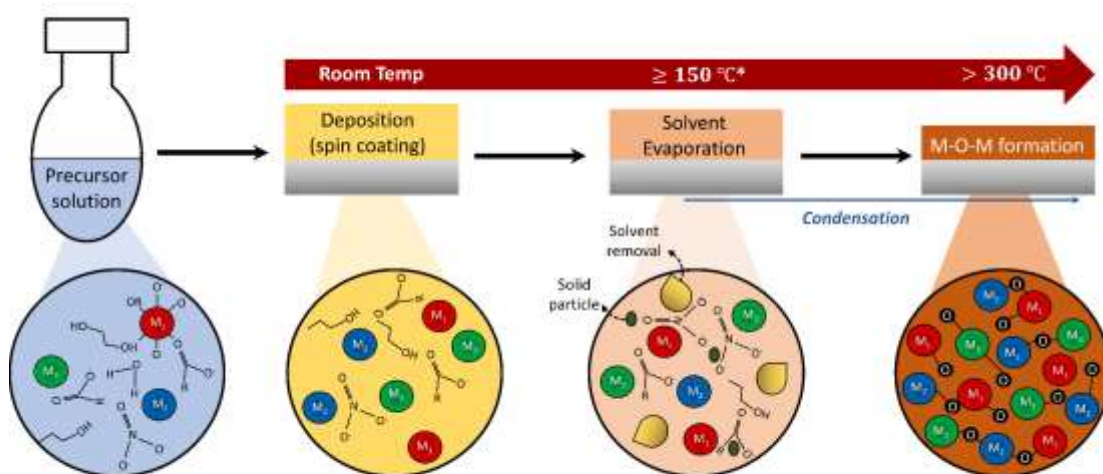

Figure 2-3. Graphical representation of sol-gel processing steps towards $\mathrm{M-O-M}$ network formation. Adapted from [152].

Steps 2 and 3 strongly depend on the temperature gradient involved during the deposition process. Specifically, the gel formation starts by a solvent evaporation that begins the drying process. This is achieved during solution deposition on top of the substrate *via* various solution processing techniques such as spin coating. During coating, the rapid substrate rotation and subsequent heating cause a concentrated gel film to be adhered to the substrate. To convert the gel into an MO thin film, solvent removal must be conducted along with decomposition of precursor-related by-products. In addition, metal-hydroxide groups must be condensed to form the metal-oxide network ($\mathrm{M–O–M}$). All these steps require energy input which is provided *via* the form of thermal annealing. Usually, to obtain the desirable MO thin film, the annealing occurs in two stages: a mild thermal annealing associated to solvent removal and gel formation and an extensive annealing at elevated temperatures. A noteworthy category of MO precursors is metal nitrates ($\mathrm{M(NO_3)_x}$). Amongst various salt precursors (*e.g.,* acetates or chlorides), metal nitrates have been often considered the optimal choice [147]. Importantly, the conversion of metal nitrates into oxides can be realised under lower annealing temperatures, due to higher volatility of the by-products formed during precursor decomposition [153,154]. This feature of

metal nitrates renders them as more compatible to “low temperature” processing techniques such as ultra-violet (UV) irradiation [55], photolysis [155], or water-vapor annealing [156] In addition, treatment at $< 250\ °C$ allows for use of plastic substrates, thus enabling the development of transparent and flexible electronic devices. For the abovementioned reasons, metal nitrates have been extensively employed in the formation of semiconductor [157–159], dielectric [160–162], or TCO [163,164] thin films [147].

2.6. Electrical Characterisation

2.6.1. Metal-Oxide-Semiconductor (MOS) Capacitor

A MOS capacitor is a structure that defines the origin of a MOS-field effect transistor (MOSFET) device. Therefore, analysis of a MOS capacitor operation is essential towards the extraction of MOSFET-related formulas. The main structure of a MOS Capacitor involves the use of three materials: a semiconductor (the bulk), an insulator (usually referred to as oxide due to the wide use of high-k metal oxide dielectrics) and a conductive layer (the gate). Various materials can be employed as a gate, with metals being the most prominent choice. The isolated energy band diagrams of the MOS capacitor materials with an n-type semiconductor layer are presented in **Figure 2-4**. The work function, Φ_{M}, represents the required energy needed to release an electron from the metal conduction band energy, $\mathrm{E_C}$, to the vacuum energy, $\mathrm{E_{vacuum}}$. The electron affinity, χ_{ox}, of the insulator represents the energy difference between the conduction band of the insulator and the vacuum energy. The electron affinity of the semiconductor, χ_{S}, is, accordingly, the difference between the conduction band of the semiconductor and the vacuum energy. Since the electron affinity of a semiconductor, χ_{S}, is an intrinsic property of the material (*i.e.,* it does not depend on the relative location of the Fermi level thus the doping level of a material), the use of χ_{S} is preferable to the work function, Φ_{S}, as the latter is related to χ_{S} by $\Phi_{\mathrm{S}} = \chi_{\mathrm{S}} + \mathrm{E_C} - \mathrm{E_f}$. Therefore, χ_{S} is related to the semiconductors doping level. $\mathrm{E_I}$ represents the Fermi Energy for the intrinsic semiconductor. In an MOS capacitor, the abovementioned types of material are combined within a single structure. In the absence of an applied gate voltage ($\mathrm{V_G} = 0$), the energy band diagram is presented in **Figure 2-4a**. When $\mathrm{V_G} = 0$, no electric charge is formed in the O-S interface. Therefore, energy bands remain flat. This steady state is defined as the flat-band condition (see **Figure 2-4a**). Under a non-zero gate voltage, the Fermi level of the metal, $\mathrm{E_{f,M}}$, is instead shifted (**Figure 2-4b-d**). Therefore, the application of $\mathrm{V_G} \neq 0$ will shift the relative height of the fermi levels, as follows:

$$\mathrm{qV_G} = \mathrm{E_{f,M}} - \mathrm{E_{f,S}} \quad 2.36$$

where q is the elementary charge. When $\mathrm{V_G} > 0$, positive charges will accumulate to the metal-oxide interface due to Gauss’s law (when excess charge is placed on a solid conductor (metal) at rest, it accumulates entirely on the metal/oxide (M-O) interface, $+\Delta\mathrm{Q}$) [165]. This will cause an

increase the electron density within the semiconductor, $-\Delta Q$, with a subsequent band bending of E_C, E_V, and E_I of the semiconductor in the vicinity of the O-S interface. (**Figure 2-4b**) reveals the "shift" of E_c towards $E_{f,S}$ in the vicinity of the O-S interface, as it gets farther from E_i. The density of electrons, n_e, in a semiconductor is given by:

$$n_e = n_i e^{\frac{E_{f,S}-E_i}{kT}} \quad 2.37$$

where n_I represents the density of electrons in the intrinsic semiconductor, k is the Boltzmann constant, and T is the temperature (in Kelvin). In the O-S interface, $(E_{f,S} - E_i)$ increases (**Figure 2-4b**). Therefore, electrons will accumulate towards the O-S interface (increasing n). This operating condition is referred to as accumulation. When a small negative voltage ($V_G < 0$) is applied, negative charges will accumulate at the edge of the metal (metal-oxide interface), therefore a positive charge must be formed in the O-S interface, to maintain charge neutrality.

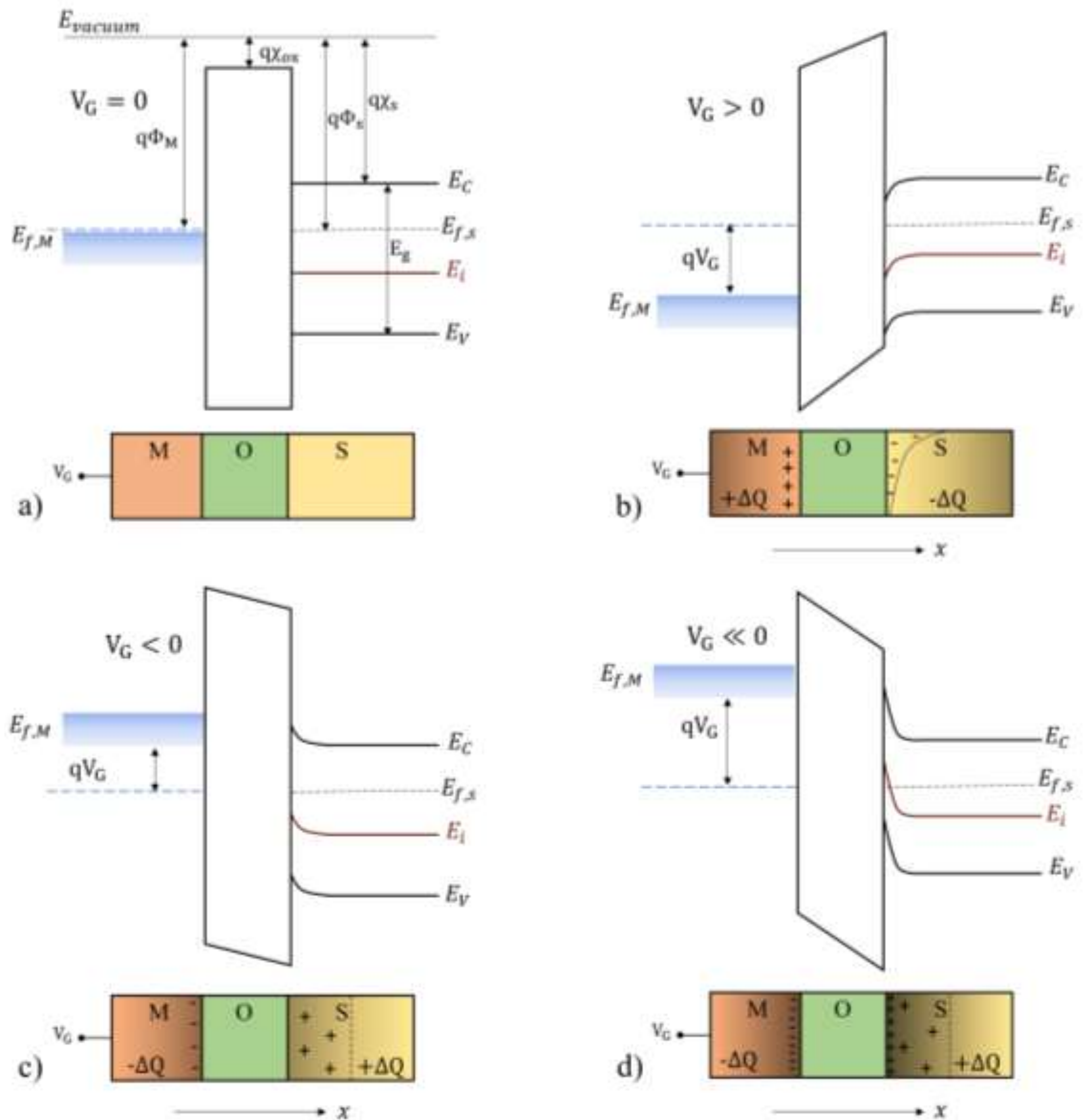

Figure 2-4. Energy band diagrams as per material of a metal-oxide-semiconductor (MOS) capacitor.

This is implemented by repelling the negative carriers (electrons) inside the semiconductor and in the vicinity of the O-S interface, forming an electron-depleted region. Within this “depletion region”, the presence of positive ions ($+\Delta Q$) balances the negative charges at the metal-oxide interface ($-\Delta Q$). The corresponding band diagram is presented in **Figure 2-4c**, where E_f is getting closer to E_i. In the case that $V_G \ll 0$, E_f and E_I intercept in the vicinity of the O-S interface (**Figure 2-4d**) for a specific value of V_G (to be defined later). A further reduction of V_G will lead to a band diagram in which $E_{f,S}$ will be below E_I (**Figure 2-4d**). At this stage ($E_{f,S} > E_i$), the number of positive carriers (holes) in the O-S interface will be higher than n (electrons), with the semiconductor effectively converting into p-type close to the O-S interface. This condition is called “inversion”, referring to the change of the type of carriers in the material. A weak inversion occurs for small differences between $E_{f,S}$ and E_i. However, a further decrease of V_G into more negative values is fuelling the increase of ($E_{f,S} - E_i$) and the subsequent increase of induced holes in the O-S interface. When:

$$\underbrace{\left|E_{f,S} - E_i\right|}_{O-S\ \text{interface}} = \underbrace{\left|E_i - E_{f,S}\right|}_{\text{bulk semiconductor}} \tag{2.38}$$

the density of holes in the interface is equal to the density of electrons in the bulk region. This value defines the initiation of strong inversion. During the inversion stage, the already-formed depletion region has a threshold length, above which it cannot extend any further with the increase of a negative V_G into more negative values. Therefore, the charge balance towards ($-\Delta Q$) is achieved *via* the formation of a thin layer of holes close to the O-S interface. The origin of these holes in an isolated MOS capacitor, where no external charge addition takes place, depends on thermal equilibrium phenomena (generation-recombination of electron-hole pairs in the bulk region). It is, therefore, a slow process. In order to define the point of strong inversion, we first need to determine the relation between V_G and surface potential φ_s (step 1) and then define φ_s at strong inversion (step 2) [166]. Starting from Step 1:

$$V_G = \varphi_s + \Delta\varphi_{ox} \tag{2.39}$$

where $\Delta\varphi_{ox}$ is the potential drop across the oxide layer. The electric field across the depletion region in the semiconductor, $\mathcal{E}(x)$, is given by:

$$\mathcal{E}(x) = \frac{qN_D}{\varepsilon_s}(x - x_d) \tag{2.40}$$

where N_D is the doping concentration of the semiconductor, x is the distance from the O-S interface, x_d is the depletion length and ε_s is the dielectric permittivity of the semiconductor. The potential $\varphi(x)$ across the semiconductor is, then, given by:

$$\varphi(x) = -\int_{x_d}^{x} \mathcal{E}(x) = -\frac{qN_D}{\varepsilon_s}\int_{x_d}^{x}(x - x_d) = \frac{qN_D}{2\varepsilon_s}(x - x_d)^2 \tag{2.41}$$

The potential at the interface ($x = 0$), φ_s, is:

$$\varphi_s = \frac{qN_D}{2\varepsilon_s} x_d^2 \qquad 2.42$$

and the electric field across the oxide, $\mathcal{E}_{ox}$, will be constant due to the absence of net charge:

$$\mathcal{E}_{ox} = \Delta\varphi_{ox} t_{ox} \Rightarrow \Delta\varphi_{ox} = \frac{\mathcal{E}_{ox}}{t_{ox}} \qquad 2.43$$

Due to boundary conditions across the interface, the electric displacement vector, D, should be continuous across the interface. Therefore:

$$D_{ox} = D_s \Rightarrow \varepsilon_{ox}\mathcal{E}_{ox} = \varepsilon_s \mathcal{E}_s \qquad 2.44$$

where ε_{ox} is the dielectric permittivity of the oxide. $\mathcal{E}_s$ and $\mathcal{E}_{ox}$ are the electric fields at the interface inside the semiconductor and the oxide, respectively.

$$\Delta\varphi_{ox} = \frac{\varepsilon_s}{\varepsilon_{ox}} \mathcal{E}_s t_{ox} \qquad 2.45$$

where t_{ox} is the thickness of the oxide layer. The gate voltage V_G (**Eq. 2.39**) can then be expressed as:

$$V_G = \varphi_s + \frac{\varepsilon_s}{\varepsilon_{ox}} \mathcal{E}_s t_{ox} \qquad 2.46$$

where:

$$\mathcal{E}_S = \frac{qN_D}{\varepsilon_s} x_d \qquad 2.47$$

and:

$$\varphi_s = \frac{qN_D}{2\varepsilon_s} x_d^2 \Rightarrow x_d = \sqrt{\frac{2\varepsilon_s \varphi_s}{qN_D}} \qquad 2.48$$

Combining **Eq. 2.46** and **Eq. 2.48** gives:

$$V_G = \varphi_s + \frac{\varepsilon_s}{\varepsilon_{ox}} t_{ox} \sqrt{\frac{2qN_D}{\varepsilon_s} \varphi_s} = \varphi_s + \gamma\sqrt{\varphi_s} \qquad 2.49$$

where $\gamma = \sqrt{2q\varepsilon_s N_D}/C_{ox}$ and $C_{ox} = \varepsilon_{ox}/t_{ox}$ is the parallel plate capacitance per unit area of the oxide. Step 2 defines the point of strong inversion. To describe this, a relation between φ_s and φ_f is (arbitrarily) chosen, where $q \cdot \varphi_{f,S} = E_{f,S} - E_I$ (at the point of strong inversion initiation) as the energy difference between E_I and $E_{f,S}$, where $\varphi_f = (kT/q)\ln(N_D/n_i)$. Hence:

$$\varphi_s = 2\varphi_f = \frac{2kT}{q} \ln\left(\frac{N_D}{n_i}\right) \qquad 2.50$$

The voltage initiating the strong inversion is referred to as “threshold voltage”, V_{TO}, and is defined by (**Eq. 2.49**) as:

$$V_{TO} = 2\varphi_f + \gamma\sqrt{2\varphi_f} \qquad 2.51$$

At this point, correction factor corresponding to a “flat band” assumption must be included, according to which the work functions of the semiconductor and metal are equal (at $V_G = 0$). For that reason, a “correction” factor, φ_{ms}, is introduced:

$$\varphi_{ms} = \frac{1}{q}(\Phi_M - \Phi_S) = \frac{1}{q}(\Phi_M - \chi_s - E_c + E_f) \tag{2.52}$$

In addition to φ_{ms}, another correction factor must be also included in the initial analysis, corresponding to the presence of charge density in the O-S interface. The origin of this may be related to impurities of the oxide material, as well as by threshold-adjust implant dopants in the semiconductor.[92] Consequently, a “flat band” voltage factor, V_{FB}, is extracted:

$$V_{FB} = \varphi_{ms} - \frac{Q_{SS}}{C_{ox}} - \frac{Q_i}{C_{ox}} \tag{2.53}$$

where Q_{SS} represents the surface charge density of the oxide, Q_I is the surface charge density due to semiconductor implant dopants and C_{ox} is the parallel plate capacitance per unit area of the oxide. Therefore, the corrected threshold voltage, V_T (**Eq. 2.51**), can be written as:

$$V_T = V_{FB} + 2\varphi_f + \gamma\sqrt{2\varphi_f} \tag{2.54}$$

Any voltage above V_T will linearly increase the inversion charge, Q_{inv}:

$$Q_{inv} = C_{ox}(V_G - V_T) \tag{2.55}$$

The abovementioned analysis covers the main principles of a MOS capacitor, which will later constitute the key for the extraction of the mostly used mathematical formulas of MOSFETs.

2.6.2. Metal Oxide Semiconductor Field Effect Transistors (MOSFETs)

Metal oxide thin film transistors (MOSFETs) constitute the foundation of electronics, providing a plethora of applications due to their versatile structure. The transition from a MOS capacitor (2-terminal) to a MOSFET (3-terminal) device includes the addition of 2 highly doped semiconductor areas in the oxide-semiconductor interface (**Figure 2-5**). The doping of these areas, namely the source (S) and drain (D) must be opposite to the bulk semiconductor (n-type for a p-type semiconductor and vice-versa). First consider a MOSFET comprised of a p-type semiconductor layer. Source and drain regions must be n-doped. Under zero bias between source and drain ($V_{DS} = 0$), the structure is similar to a MOS capacitor but with one key difference; that during inversion, the source and drain can also contribute to the generation of free carriers (electrons for the case of a p-type semiconductor). Therefore, the carrier generation is achieved very quickly (compared to a simple MOS capacitor). For simplicity, we exclude the application of an extra voltage source, V_{SB} (the body effect) [167]. For $V_{DS} \neq 0$, the electron cloud formed in the O-S interface through inversion will be accelerated from source to drain through the MOSFET channel, being collected to the latter terminal (a process that also marks the terminals as source and drain).

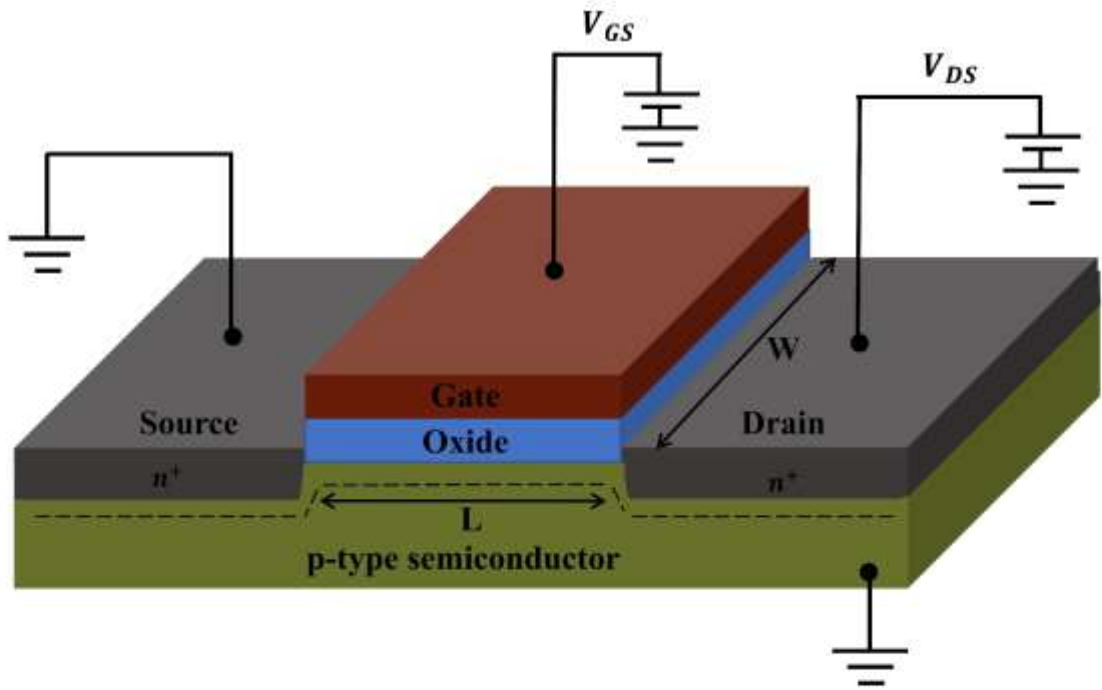

Figure 2-5. MOSFET structure, representing the main device components. Si substrate (semiconductor layer) is displayed in green, oxide dielectric in blue, gate electrode in dark red and source/drain electrodes in grey. Channel width (W) and length (L) are also shown.

To investigate the relation between the applied voltages, V_{GS} and V_{DS}, the collected current, I_{DS}, and the geometrical MOSFET features, channel width (W) and length (L) (see Figure 2-5), it is important to define two distinct operation regions during inversion ($V_{GS} \geq V_T$). These operation regions, namely the linear and the saturation region, are discussed further below. Starting from small values of V_{DS} ($V_{DS} < V_{GS} - V_T$), the inversion charge is uniformly distributed across the MOSFET channel with the total charge per channel area, q_{ch}, given by:

$$q_{ch} = W \cdot L \cdot Q_{inv} = W \cdot L \cdot C_{ox}(V_{GS} - V_T) \qquad 2.56$$

The average time needed for an electron to accelerate from source to drain is:

$$\tau_{DS} = \frac{L}{\upsilon_d} = \frac{L}{\mu_n E} = \frac{L}{\mu_n V_{DS} L^{-1}} = \frac{L^2}{\mu_n V_{DS}} \qquad 2.57$$

where μ_n is the electron mobility in the channel and υ_d is the electron drift velocity. The source-drain current, I_{DS}, is then defined as:

$$I_{DS} = \frac{q_{ch}}{\tau_{DS}} = \frac{W \cdot L \cdot C_{ox}(V_{GS} - V_T)}{\frac{L^2}{\mu_n V_{DS}}} \Rightarrow I_{DS} = \frac{W \cdot \mu_n \cdot C_{ox}}{L}(V_{GS} - V_T) \cdot V_{DS} \qquad 2.58$$

Eq. 2.58 and Figure 2-9a show the linear relation of I_{DS} to V_{DS}. Under this operating condition ($V_{DS} < V_{GS} - V_T$), the device functions as a resistor (Ohm's Law), whose resistivity value is proportional to V_{GS}. This operation region is referred to as the "linear" region (Figure 2-6). At this stage, the V_{GS}-controlled channel, also referred to as "the field effect channel", comprises the origin of the "MOSFET" term.

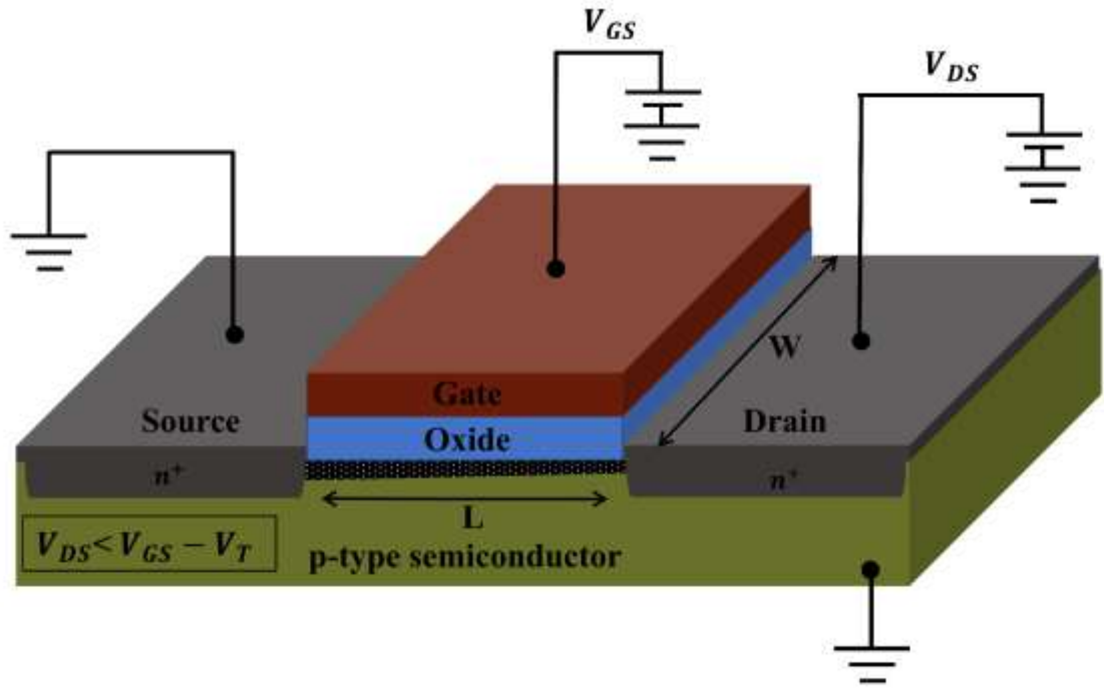

Figure 2-6. Linear region operation in a MOSFET. The channel formation is depicted as a black dotted area between source and drain.

As V_{DS} increases, the inversion charge density will be altered around the drain area, due to the interference of V_{DS} with V_{GS}. To further explore this effect, the channel is assumed to comprise a set of infinitesimal MOS transistors in series. This assumption allows one to express V_{DS} as the summation of infinitesimal voltage drops dV across an infinitesimal distance dx (

Figure **2-7**). Considering one MOS transistor with voltage drop dV across dx and an incremental inversion charge, dq, Eq. 2.56 becomes:

$$dq = W \cdot C_{ox} \cdot dx \cdot [V_{GS} - V(x) - V_T] \qquad 2.59$$

where $V(x)$ is the channel voltage at x. Due to conservation of charge, the drain current, I_D, in every MOS transistor across the channel should be the same as the current through the entire transistor, and is:

$$I_D = \frac{dq}{d\tau} = W \cdot C_{ox} \cdot dx \cdot \frac{[V_{GS} - V(x) - V_T]}{(dx^2/\mu dV)} = \mu C_{ox} W [V_{GS} - V(x) - V_T] \frac{dV}{dx} \qquad 2.60$$

Integrating across the channel gives:

$$I_D = \int_0^{V_{DS}} dx = \mu CoxW \int_0^{V_{DS}} [V_{GS} - V(x) - V_T] dV \qquad 2.61$$

Therefore:

$$I_D = \frac{\mu C_{ox} W}{L} \left[(V_{GS} - V_T) V_{DS} - \frac{V_{DS}^2}{2} \right] \qquad 2.62$$

The above equation is only valid when the channel extends across the entire source-drain area. However, if $V_{DS} = V_{GS} - V_T$, the inversion charge across the drain ($V(x) = V_{DS}$) will equal zero (Eq. 2.59). Therefore, the channel will become narrower (Figure 2-8).

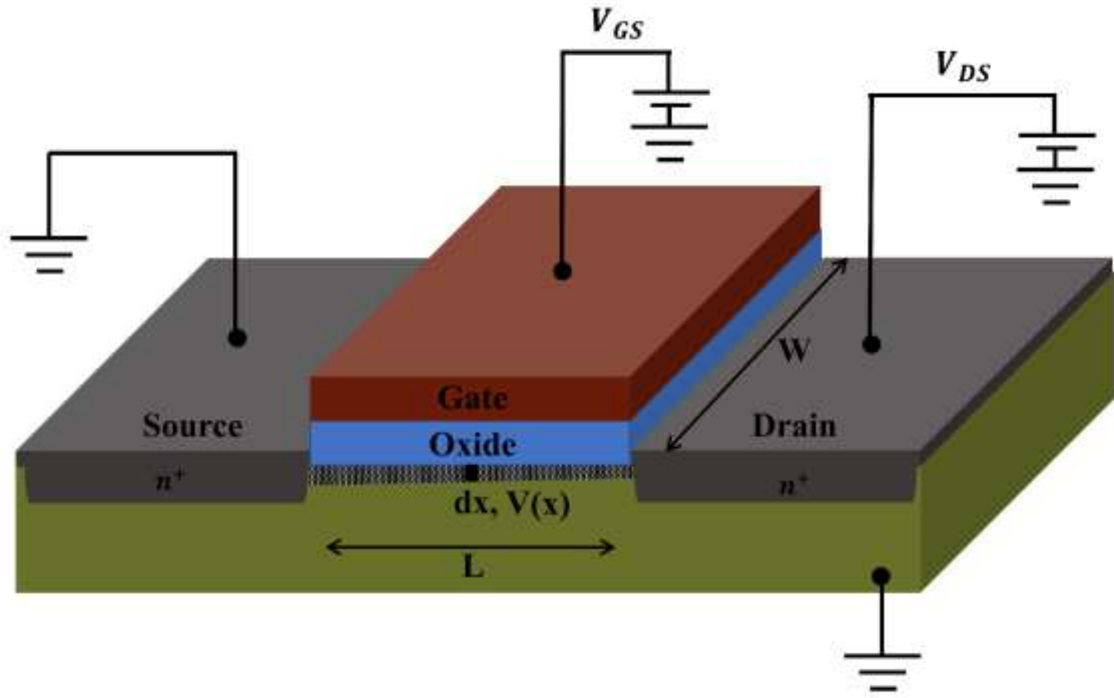

Figure 2-7. MOSFET channel alteration due to gradual increase in V_{DS}.

This operation point is called "pinch-off". During pinch-off, the voltage at the edge of the channel will remain $V_{GS} - V_T$, as this is the voltage initiating the strong inversion that forms the channel. As $V_{DS} \geq V_{GS} - V_T$, the pinch-off point moves to the left (Figure 2-8). At higher V_{DS}, this voltage is applied across the shorter channel. The electrons are brought into pinch-off through drift and are collected in the drain by the electric field. The voltage drop across this effective channel is $V_{GS} - V_T$ and does not depend on V_{DS}. Therefore, the current does not increase with V_{DS} and remains constant (Figure 2-9c). This operation regime is called the saturation region. The current at the boundary condition (pinch-off) of $V_{DS} = V_{GS} - V_T$ (Figure 2-9b) is referred to as saturation current, $I_{DS,sat}$, and is given by:

$$I_{DS,sat} = \frac{\mu C_{ox} W}{2L}(V_{GS} - V_T)^2 \qquad 2.63$$

Eq. 2.63 is valid when $V_{DS} \geq V_{GS} - V_T$ and is extracted from Eq. 2.62 using a channel length of L that is assumed to be constant. This analytical approach is defined as the "gradual channel approximation" model [168]. However, the effective channel length in the post pinch-off regime ($V_{DS} \geq V_{GS} - V_T$) is smaller than L (a parameter not included in the model) [129].

Table 2-1. Operation modes of a MOSFET device.

V_{DS}, V_{GS}, V_T	$V_{GS} - V_T \geq V_{DS}$	$V_{GS} - V_T < V_{DS}$
$V_{GS} < V_T$	Off $I_D = 0$	Off $I_D = 0$
$V_{GS} \geq V_T$	Resistor (Ohm's Law) $I_{DS} = \frac{\mu C_{ox} W}{L}\left[(V_{GS} - V_T)V_{DS} - \frac{V_{DS}^2}{2}\right]$	Saturation $I_D = \frac{\mu C_{ox} W}{2L}(V_{GS} - V_T)^2$

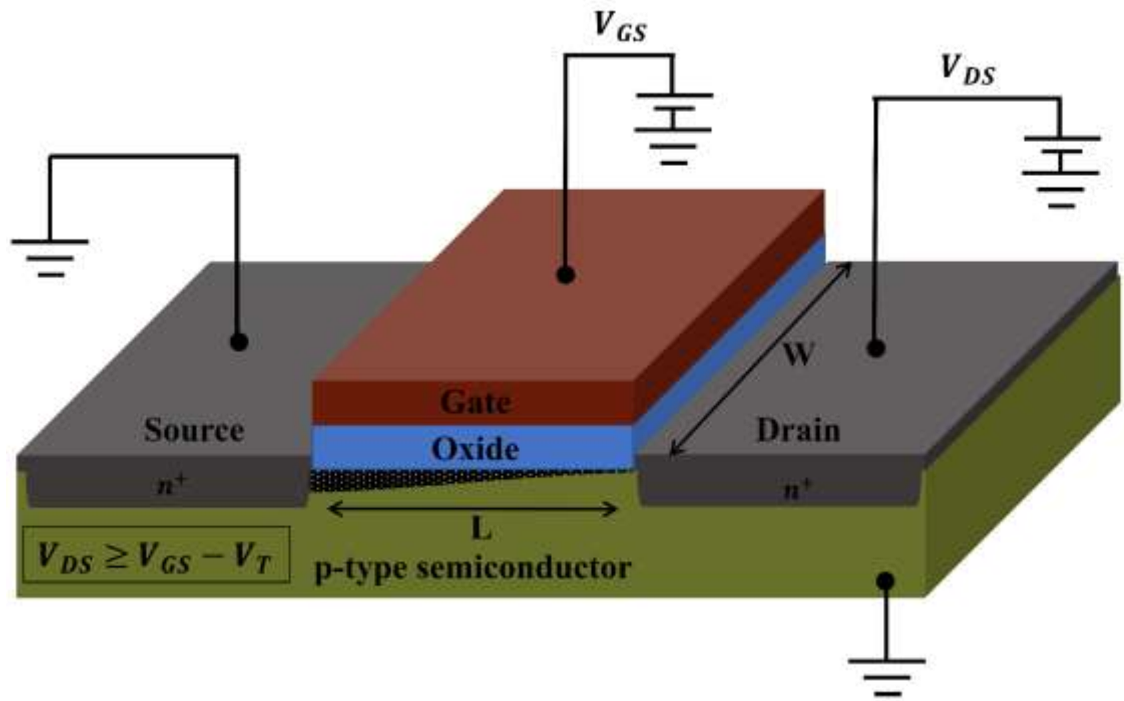

Figure 2-8. Pinch-off operation region in a MOSFET ($V_{DS} \geq V_{GS} - V_T$). The channel formation is depicted as a black dotted area between source and drain.

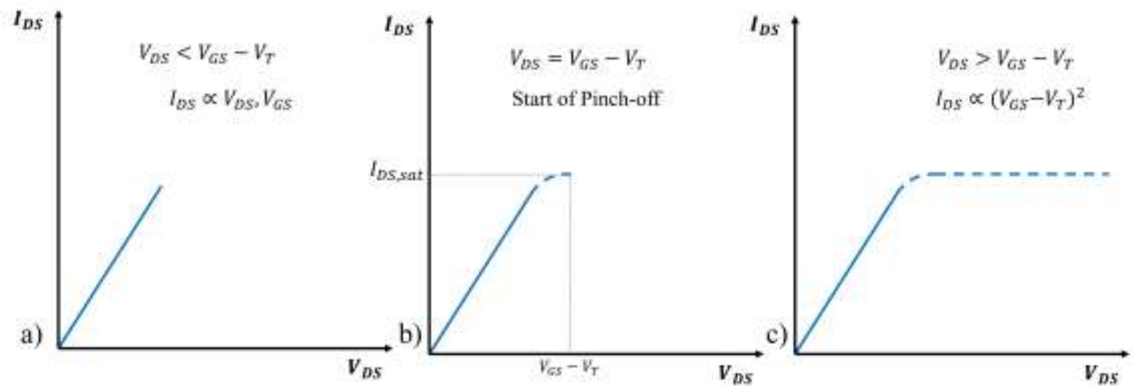

Figure 2-9. Drain current (I_{DS}) versus drain voltage (V_{DS}) in a) linear (Field Effect), b) pinch off and c) saturation regime.

Mobility

The most prevalent methods used to extract the mobility, μ, values in a MOSFET device involve the use of I_D-related expressions that describe each operation region. For the linear region (Field Effect), Eq. 2.58 is employed:

$$I_{DS} = \frac{W \cdot \mu_{lin} \cdot C_{ox}}{L} (V_{Gs} - V_T) \cdot V_{DS}$$
$$\Rightarrow \quad \frac{\partial I_{DS}}{\partial V_G} = \frac{W \cdot \mu_{lin} \cdot C_{ox}}{L} \frac{\partial (V_{Gs} - V_T)}{\partial V_G} V_{DS} \tag{2.64}$$
$$\Rightarrow \quad \mu_{lin} = \frac{L}{W \cdot C_{ox} V_{DS}} \frac{\partial I_{DS}}{\partial V_G}$$

Similarly, in the pinch-off regime, the saturation mobility, μ_{sat}, is extracted by **Eq. 2.63** (the gradual channel approximation):

$$I_{DS,sat} = \frac{\mu_{sat} \cdot C_{ox} \cdot W}{2L}(V_{GS} - V_T)^2$$
$$\Rightarrow \quad \frac{\partial^2 I_{DS,sat}}{\partial V_G^2} = \frac{\mu_{sat} \cdot C_{ox} \cdot W}{2L}\frac{\partial^2[(V_{GS} - V_T)^2]}{\partial V_G^2} \qquad 2.65$$
$$\Rightarrow \quad \mu_{sat} = \frac{L}{C_{ox}W}\frac{\partial^2 I_{DS,sat}}{\partial V_G^2}$$

Threshold Voltage and On-Off Ratio

The threshold voltage, V_T, corresponds to V_G for which a carrier channel between source and drain is formed within the semiconductor, close to the O - S interface. V_T is commonly determined *via* the linear extrapolation of the $I_{DS} - V_{GS}$ in the transfer curve (for low V_{DS} values) or of the $I_{DS}^{1/2} - V_{GS}$ (for higher V_{DS} values). The on-off ratio, $I_{ON/OFF}$, is the maximum to minimum I_{DS}, defined in a transfer curve. The minimum I_{DS} is usually given by the noise level of the measurement, while the maximum I_{DS} depends on the semiconductor material properties, as well as on the effectiveness of capacitive injection by the field effect [129]. All the above MOSFET parameters define the device quality, as well as provide information regarding each individual layer. The extraction of these parameters depends on the accurate analysis of transfer and output characteristics, where $V_T, I_{ON/OFF}$, as well as the linear and saturation region are presented.

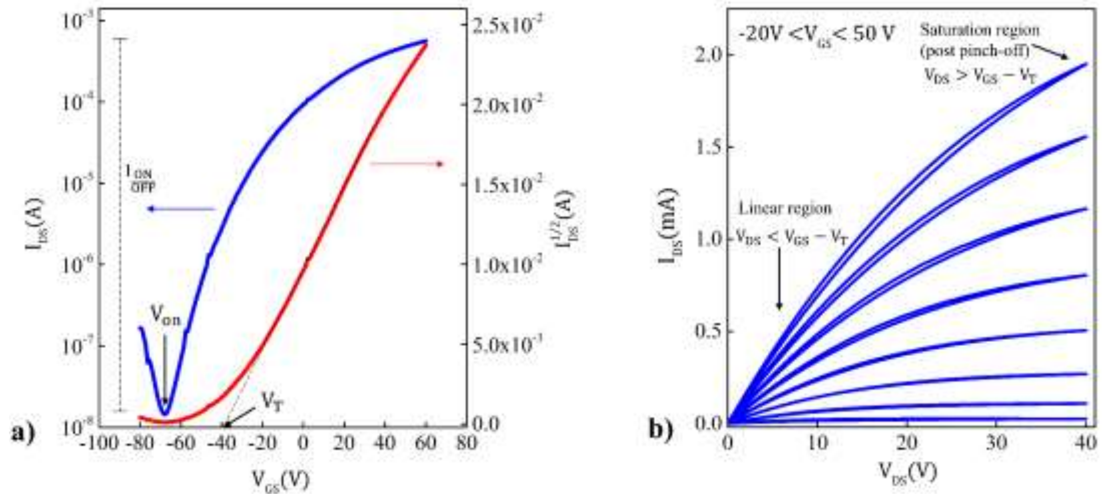

Figure 2-10. Typical a) transfer and b) output characteristic of an n-type Thin Film Transistor (TFT).

Threshold ($\mathbf{V_T}$) vs ON ($\mathbf{V_{on}}$) Voltage

Despite the plethora of reported work where the threshold voltage, V_T, is used as a parameter of study in TFT analysis, the risk of false estimation should always be considered. This lies on the estimation routine of V_T, which involves the extrapolation of the linear region in a typical

transfer curve. As presented in **Figure 2-11**, the difference in x-axis range (gate voltage (V_{GS})) may lead to variation in V_T values, which is thus associated to misinterpretation of the device operation region. To avoid this risk in this work, On Voltage (V_{ON}) is used instead, the value of which is displayed on the device Turn-On point (see **Figure 2-10a**).

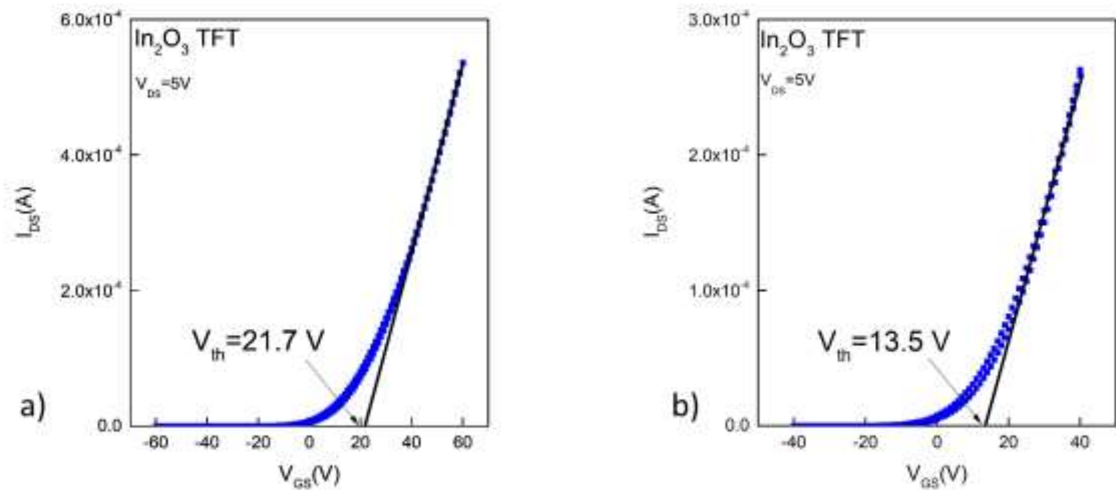

Figure 2-11. Misinterpretation of the threshold voltage V_T in accord to changes in V_{GS} range.

2.6.3. Thin Film Transistors (TFTs)

A thin film transistor (TFT) is a type of MOSFET with an ultra-thin (few nm) semiconductor layer used instead of the bulk Si layer in conventional Si-MOSFETs. Like MOSFETs, TFTs are 3-terminal devices with similar operational principles, except for two key differences:

1. MOSFET vs TFT geometry: A MOSFET structure includes a gate-oxide-Semiconductor stack, along with two highly doped areas (the source and drain) within the semiconductor body. In contrast, a TFT structure may vary, depending on the particular use of the device. The main components of a TFT, namely the gate, dielectric, semiconductor, and the source and drain, can be met in various stack combinations that are often dependent upon the film fabrication process. The source and drain layers in TFTs are represented by conductor materials (commonly metals), instead of highly doped areas within the semiconductor in a MOSFET. A comparison between typical MOSFET and TFT structures is presented in **Figure 2-12**.
2. MOSFET vs TFT operation region: A MOSFET operation is defined by the $n^+ - p^+ - n^+$ (or $p^+ - n^+ - p^+$) source-semiconductor-drain area, where a channel (Field Effect) is formed during the inversion mode. However, the channel conduction path in a TFT is simpler, following a metal (source)-semiconductor-metal (drain) structure. Therefore, TFTs are turned on in accumulation region of operation.

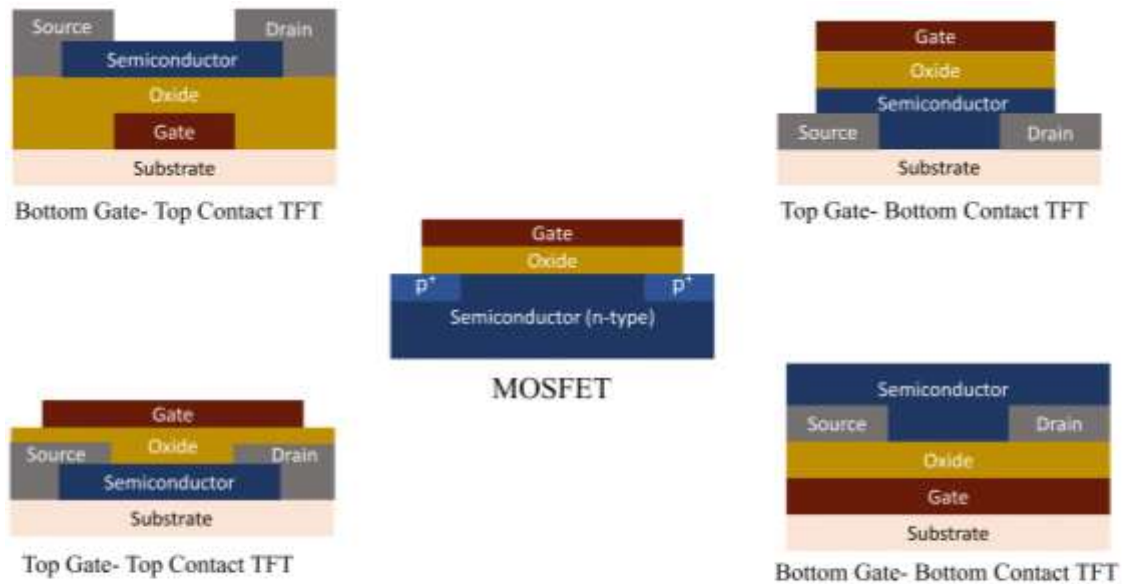

Figure 2-12. Typical structure of MOSFET (centre) and TFT architectures.

The structural versatility of TFTs constitutes a key factor towards the implementation of MOSFET technology into novel, cutting edge applications. The incorporation of a multilevel palette of materials, fabrication, and processing techniques into a single TFT device constitutes a perpetually growing scientific field. Therefore, TFTs cover a significant part of this study. Since the electrical parameters of TFTs and MOSFETs are similar, this chapter comprises a guide towards the accurate analysis of the TFT devices fabricated in this work.

2.7. Solution Processed Metal Oxide TFTs: Advances and Challenges

The transition from Si technologies to metal oxide TFTs based on conventional fabrication technologies (vacuum-based) has eloped into commercialisation over the last decades. However, the costly and time-demanding nature of this conventional approach hinders the introduction of low-cost electronics based on large-area integration systems. Solution processes have thus started to become the topic of interest regarding the next generation of metal oxide TFTs due to their simplicity, roll-to-roll compatibility as well as their low-cost nature. Starting from n-type semiconductors, the evolution of solution-processed metal-oxides has expanded into high-k MO dielectrics as well as p-type MO semiconductors, thus enabling the fabrication of TFTs solely based on solution processed layers, with device performances comparable to TFTs based on conventional technologies. There have already been reported cases where solution processed MO TFT backplanes have been developed in industrial scale, with Evonik Resource Efficiency GmbH demonstrating their large area fabrication and further integration as active elements in display technologies [169]. Despite this progress, the demand for thermal annealing at high temperature still constitutes the biggest challenge. The need for treatment temperatures above 400 °C (in conventional thermal annealing) is inevitable, as devices have shown degradation in performance when treated in temperatures below 300 °C. According to reported studies, low-

temperature processing results in incomplete formation of $\mathrm{M-O-M}$ networks, which are primarily substituted by $\mathrm{M-OH}$ [170]. Since carrier transport is hindered in metal-hydroxide lattices, the difference in device performance amongst high and low temperature processed TFTs seems tremendous [111]. Therefore, in order to fully realize all-solution-processed metal oxide flexible circuitry, it is highly desirable to establish a generalised methodology for rapid conversion of as-deposited xerogel-like oxide materials to high-quality thin-films at low temperatures, while effectively removing metal ligands, condensation by-products, and other chemical impurities during M-O-M network formation, using the various types of general MO precursors [131].

2.8. UV-Assisted Metalorganic Conversions

As analysed in 2.3-2.4, MO semiconductors and dielectrics constitute the dominant materials of use in electronics today. The reason behind this choice is based on their unique properties, which includes high optical transparency and carrier mobility, even in the amorphous state. This effect lies in the CBM of MOs, as it is composed of spatially based ns (spherical) orbitals, thus independent on orientation. As these orbitals overlap (forming an electron transport pathway), this mechanism remains unaffected by any $\mathrm{M-O-M}$ bond distortion that may be found in amorphous states. This advantage in amorphicity enables the MO processing at low temperatures ($\sim 350\ °\mathrm{C}$), which activate the potential of deposition in large areas of flexible substrates *via* sol-gel. However, the principal-imposed constraint is the inability of $\mathrm{M-O-M}$ network formation in temperatures compatible with these substrates. Therefore, the demand for low-temperature solution processing depositions is urgent. To attain solution processed amorphous MO thin films at low temperatures, two key strategies have been proposed in the literature: the first facilitates new designs in solution chemistry while the second suggest the use of UV irradiation as an alternative to conventional thermal annealing.

The first strategy incorporates the focus on careful choice of solution precursors, as well as reaction catalysts which may accelerate various sol gel steps such as condensation. This occurs *via* targeting and consuming hydroxide anions, thus assisting the formation of M-O-M networks. Furthermore, fabrication of MO thin films in low temperatures has been realised through the addition of reaction “fuels” such as acetylacetone and urea. This chemical deviation from the usual sol-gel route aims to promote the temperature increased in a localised level within the film *via* combustion reactions and has been often reported in literature [45,54,171,172]. The second strategy proposes the MO formation using of UV radiation sources that promote the rapid photochemical conversion of precursors into the films of interest. Various UV sources have been employed to facilitate the M-O-M formation, including UV lamps and laser sources [47,55,173,174]. This approach has reportedly led to high mobility values for

MO semiconductors, as well as high-k MO dielectrics. Particularly for laser irradiation, the conversion mechanism lies on the photothermal effect due to the high absorption MOs present in UV range as well as the high energy transferred in the thin film (due to high power sources) and gathered in a small area. This effect can induce local increase in temperature at a level of thousands of °C at the film surface, promoting a complete precursor conversion without any need for additional heating procedures. In addition, the low penetration depths found in UV light sources are compatible with flexible substrates, as the temperature increase remains at the film surface without penetrating the substrate. These large amounts of energy can promote the dissociation of various by-product related bonds, dissociate molecules, and ultimately modify the molecular network of the gel layer. The underlying mechanism of UV irradiation effect on $M-O-M$ is presented in **Figure 2-13**. At first, irradiation promotes the bond cleavage of photosensitive organic compounds that originate from the precursor. Also, strong oxidant species such as O_3 and $O(1d)$ are created and contributes to the removal of surface by-products. Specifically, for O_3, its strong oxidant character promotes the bond dissociation by ozonolysis of the organic remaining by-products. Afterwards, metal-oxygen bonds start forming an amorphous M-O-M network, which densifies as condensation evolves. Stoichiometry is also dynamically altered, as atomic oxygen can react with oxygen vacancies (V_O), thus altering the metal-to-oxygen ratio [152]. Also, the presence of various reactive species such as $-OH$ and $-H$ contributes to the condensation rate as well as enhance the crystallisation of the film. This delicate process can also be affected by various external controlled factors, such as the environmental stoichiometry, addition of reaction "fuels", and the UV irradiation conditions.

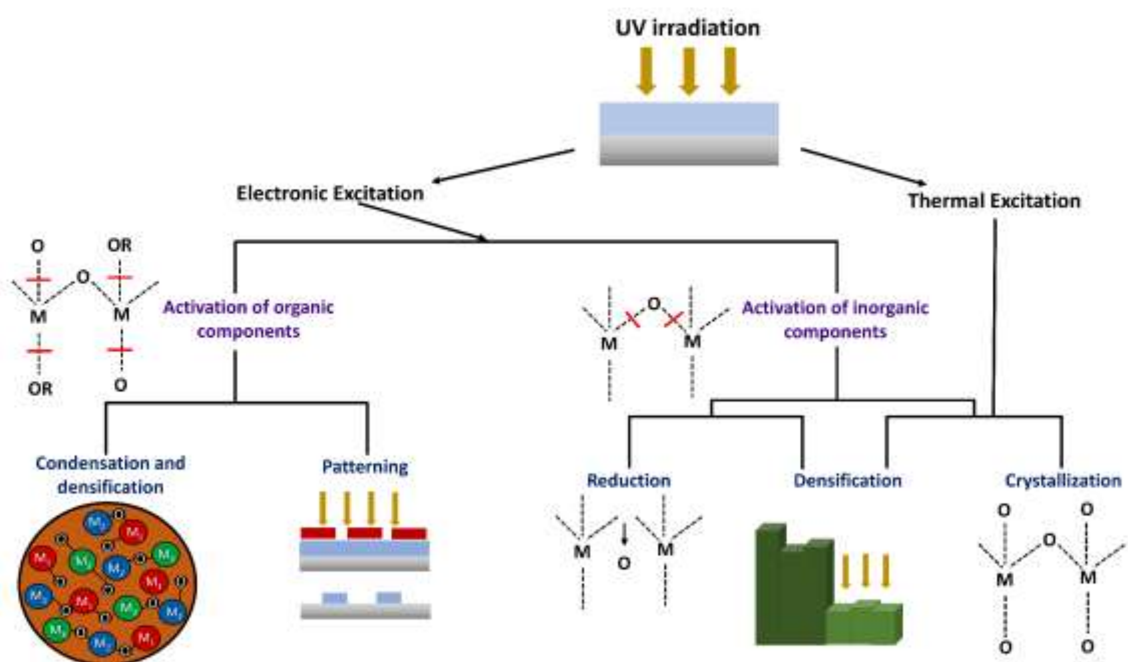

Figure 2-13. Photochemical phenomena conducted during ultraviolet irradiation of sol-gel metal oxide precursor films.

2.9. Brief History of Laser Annealing

Based on the existing, well-established, research regarding its effect on conventional materials [175–180], the implementation of laser annealing into MO treatment has been continuously accompanying the evolution of novel materials and fabrication techniques over the last decades [181–183]. The remarkable characteristics of this promising annealing method match perfectly with the high energy demand during MO thin film manufacturing, along with multiple advantageous characteristics such as decreased processing time, compatibility with Roll-to-Roll systems, low processing temperatures, and selective patterning [24,184,185]. Therefore, the introduction of laser annealing into MO-based applications has been boosting the technological regime into a next generation of opto-electronical characteristics, comprising of enhanced performance TFTs, OLEDs, sensors, memory devices and photovoltaics [6–8,10]. From MO semiconductors to dielectrics and conductors, the essential role of laser annealing onto their transition into high quality films has been thoroughly investigated [186,187]. The parallel evolution of manufacturing techniques, mainly focusing on solution processes (sol-gels) has triggered a new era of large-scale fabrication of metal-oxide film-based devices that now demands a time and cost-efficient way of inducing the required photochemical transition of the precursors into high quality MOs. Therefore, laser annealing, by fulfilling the abovementioned requirements as well as being compatible with flexible substrate utilisation (especially UV laser annealing with its low penetration depth), comprises the most promising candidate for MO electronics. Nevertheless, the route into achieving the optimised film characteristics, demands special attention into determining the parameters of laser annealing. Thus, multiple studies have been focusing on the correlation between these parameters and the exact mechanism of MO film formation, successfully exhibiting remarkable film characteristics and enhanced device performance [55,188,189].

3. Experimental Methods

The current thin film technology is mostly dominated by traditional silicon microchip electronics [91,92], based on conventional vacuum deposition techniques [93]. However, the economic and technological constrains imposed by Si technology (limited charge carrier mobility, high manufacturing cost, incompatibility with flexible substrates) demand a radical change in the choice of materials, as well as manufacturing technologies [94–98]. To tackle these challenges, metal oxides (MOs) [99–102] have emerged as the ideal alternative due to their outstanding electrical and optical properties (high mobility [103] and transparency [17]) and mechanical stability [104]. In addition, MOs offer a unique processing versatility as they can be grown *via* both vapour-and solution-phase techniques [111–114]. Henceforth, their superiority is reinforced as they create a new industry path in electronics, characterised by up-scalable and high-throughput manufacturing [115].

While MO films based on solution processing fabrication techniques accommodate a plethora of advantages, an essential step towards the formation of high-quality films remains a challenge to this day. This key step is the drying process. For Mos especially, the transition from the as deposited to a denser film is accompanied by an additional complexity, as the route to MO films demands the use of metalorganic precursor solutions. Such solutions are converted into MO films after drying (annealing) at high temperatures. As the global electronic market gradually favours the transition towards a silicon-free and vacuum-less device schemes, dominated by plastic substrates, the use of high annealing temperatures (> 500 °C) deems incompatible. Therefore, this work incorporates the use of an alternative annealing routine which involves the use of photonic-based annealing *via* the use of an excimer laser. This process is called excimer laser annealing (LA). This chapter presents a detailed view on the fabrication routine of MO thin films *via* solution processing routes (spin coating) along with their post-deposition LA processing technique. The fundamentals of thermal evaporation process (used to deposit electrodes) are highlighted. Finally, the complete set of optical and electrical characterisation techniques employed in this work is analysed in detail.

3.1. Thin Film Fabrication

3.1.1. Spin Coating

Spin coating is a commonly used solution processing technique, whose advantage lies on the formation of uniform and ultra-thin films atop of piecemeal, usually disk shaped, substrates. This process involves the deposition of a thin film evenly across the surface of the substrate of interest by subsequently or simultaneously rotating the substrate. During this process, a thin axisymmetric film of Newtonian fluid is spread on a planner substrate which rotates with

constant angular velocity. Spin coating is broadly used in deposition of polymer films, photoresist deposition in microelectronic applications as well as MO thin films based on sol-gel chemistry. The rapid radial solvent evaporation which occurs during the high speed substrate rotation results in film thinning and solidification by drying [190]. Parameters such as rotating speed and spin duration, solvent's boiling point, and solution viscosity each play a role in defining the eventual quality, uniformity, and thickness of the as-spun film. **Figure 3-1** displays the principal steps involved during spin coating deposition.

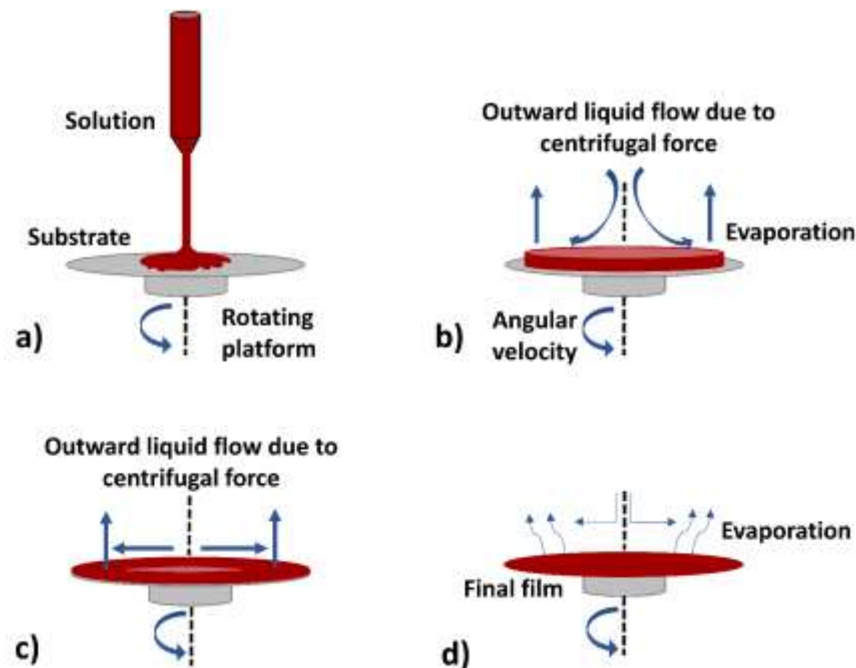

Figure 3-1. Steps comprising spin coating process: (a) The solution is dispensed on top of the substrate, followed by the rotation initiation. (b) Immediately afterwards, the solution is spread across the substrate, due to centrifugal force. (c) As rotation time progresses, the film thickness decreases, with concurrent solvent evaporation mainly in the film edges (where the film is thinner). (d) Towards the rotation completion, evaporation occurs across the whole sample, leading to the solid thin film formation.

Thickness equation

The general rule that defines the film thickness is described as:

$$h_f \propto \omega^{-1/2} \qquad 3.1$$

where h_f represents the obtained film thickness and ω is the angular substrate velocity (rotating speed). As seen in **Eq. 3.1**, film thickness is inversely proportional to the square root of ω. However, since this deposition process entails further parameters, there have been various scientific approaches to derive a more precise thickness determination. The first attempt was conducted by Emslie, Bonner and Peck in 1958 [191]. This analysis incorporated various approximations such as excluding the case of a non-Newtonian behaviour as well as ignoring the solvent evaporation parameter. This model is well described by the following equation:

$$\frac{\partial h}{\partial t} + \frac{\rho\omega^2 r}{\eta} h^2 \frac{\partial h}{\partial r} = -\frac{2\rho\omega^2 h^3}{3\eta} \tag{3.2}$$

where h is the thickness of the fluid layer (not the dried film), t is the rotating time, ρ is the liquid density, r is the distance to the rotation centre, and η is the viscosity. Here $\partial h/\partial t$ represents the dynamic thickness change and $\partial h/\partial r$ the spreading rate. In the case of an initial uniform liquid film deposition, the fluid film thickness can be described as:

$$h = \frac{h_0}{\left(1 + \frac{4\rho\omega^2}{3\eta} h_0^2 t\right)^{1/2}} \tag{3.3}$$

where h_0 displays the uniform film thickness at $t = 0$. This model does not include parameters representing the solvent evaporation. Therefore, it cannot be used to estimate the thickness of the final dried film and a more precise model is required.

Meyerhofer model

In 1978, Meyerhofer reported another theoretical approach to calculate the dried film thickness, this time involving a parameter representing the solvent evaporation rate:

$$\frac{\partial h}{\partial t} = \frac{\rho\omega^2 h^3}{3\eta} - E_{evap} \tag{3.4}$$

where E_{evap} is the solvent evaporation rate in evaporated solvent volume per unit area per unit time. According to the model, flow dominates the film thinning process (spin off) in the early stages of spin coating. As the process continues, the principal thinning mechanism is defined by solvent evaporation. If the transition from spin-off to film thinning due to solvent evaporation is rapid, the film thickness of the dried film can be calculated analytically. The critical point where spin off transitions to thinning by solvent evaporation can be described as:

$$E = \frac{(1 - C)2\omega^2\rho h_0^3}{3\eta} \tag{3.5}$$

where h_0 is now the film thickness at the transition point and C is the volume fraction of solute in the film. The dried film thickness becomes:

$$h_f = \left(\frac{3\eta_0 E}{2(1 - C_0\rho\omega^2}\right)^{1/3} \tag{3.6}$$

Here, C_0 represents the initial solution concentration and $\eta_0 = \eta(C_0)$. It is assumed that the solution concentration remains C_0 until the critical point. Meyerhofer also calculated the final film thickness excluding the evaporation parameter by assuming that air flow remains constantly laminar during spin coating. The final film thickness becomes:

$$h_f = \left(\frac{3}{2}\right)^{\frac{1}{3}} k^{\frac{1}{3}} C_0 (1 - C_0)^{-\frac{1}{3}} \rho^{-\frac{1}{3}} \eta_0^{\frac{1}{3}} \omega^{-\frac{1}{2}} \tag{3.7}$$

where k represents a solvent-dependent constant. This equation aligns with **Eq. 3.1** where $h_f \propto \omega^{-1/2}$. This shows that the proportionality constant includes several parameters such as viscosity, solution concentration and density.

Spin speed

The rotating speed during spin coating constitutes the principal factor which defines the final film thickness and quality. It can be easily altered, ranging from $600 - 7000$ rpm. The speed choice is also associated by the solution properties (viscosity) as well as substrate size and shape (low speed can easily lead to edge effects in non-spherical substrates). Since the rotating speed can change by a factor of 10 (approximately 600 rpm to 6000 rpm), the film thickness can thus be altered by a factor of $\sqrt{10} \approx 3.2$. Solution concentration can also have an impact on the final film uniformity, as higher concentrations may lead to unequal solution distributions in the substrate edges, especially when low rotating speeds are employed. In this work, rotating speed (and rotation time) was mostly kept constant at 4000 rpm, for 30 s. Spin coating constitutes the principal deposition technique involved in this work. The formation of MO thin films was based on sol-gel chemistry. A detailed overview of this process is presented in **Chapter 2**. Amongst the advantages of using the sol-gel process is the conduction of experiments at room temperature (as followed in this work). This allows one to produce a wide range of novel and functional materials with potential applications in different areas. Room temperature deposition is attractive compared to other methods, due to its low production costs.

As mentioned in **Chapter 2**, sol-gel synthesis involves the dissolution of a compound (*e.g.* a salt) in a solvent to obtain the desirable material (thin film / nanoparticles). In order to define the product's properties, various parameters must be tailored accordingly. Such parameters include precise stoichiometry, use of crosslinkers or mix of various salts. To prepare the In_2O_3 and ZnO thin films, the following precursors were used: indium nitrate hydrate ($In(NO_3)_3{\cdot}xH_2O$, Thermo-Fisher) and Zinc Acetate Dihydrate ($Zn(CH_3COO)_2{\cdot}2H_2O$, Merck). The precursor salts were dissolved in 2-Methoxy-Ethanol (2-ME) (30 mg/ml). Both solutions were stirred overnight, thus obtaining a clear form. Monoethanolamine (MEA, Acros) was added to zinc acetate solution (1: 1 molar ratio), in order to enable the precursor salt dissolution in 2-ME. The addition of MEA was performed with a pipette, to ensure the accuracy of the quantity of MEA. The typical volumes of solutions fabricated prior to each experiment were 15 ml.

Regarding IGZO solution fabrication, Indium nitrate hydrate ($In(NO_3)_3{\cdot}xH_2O$), Zinc Nitrate Hexahydrate ($Zn(NO_3)_2{\cdot}6H_2O$) and Gallium Nitrate Hydrate ($Ga(NO_3)_3{\cdot}xH_2O$) were used as precursor salts. Each salt was separately mixed with the solvent (2-ME), forming a solution of 30 mg/ml. After the formation of separate solutions, the formation of

IGZO precursor solution was formed by mixing the individual solutions in a molar ratio of 5:3:1 (In:Zn:Ga).

The precursor thin films were then deposited onto 4 substrates of choice: Aluminium (Al; thermal evaporation onto n-Si), Au (RF-magneton sputtering onto n-Si), TiN (RF-magneton sputtering onto n-Si) as well as bare n-Si. The bare n-Si was moderately doped to achieve a resistivity of $1-10\ \Omega\text{cm}$ and is referred to as simply 'Si' throughout the remainder of this study). Prior to thin film deposition, the substrates were cleaned by sequential ultrasonication in deionised water, acetone, and IPA (10 min. for each step). Substrates were subsequently exposed to an atmospheric pressure UV/ozone lamp treatment for 1 hr. at room temperature, aiming to increase the substrate's wettability. The precursor solutions were deposited *via* spin coating (Laurell Technologies,model WS-650MZ-23NPPB) at 4000 rpm, 30 s, in an ambient environment. After deposition, 3 thermal treatment steps were followed. During step 1, the films were thermally stabilised on a hot plate (150 ℃, 15 min.) to remove the excess solvent. During step 2 a further thermal treatment was employed (300 ℃, 60 min.), aiming to induce the thermally assisted precursor conversion into In_2O_3 and ZnO films [24,54]. Step 3 involved the final thermal treatment (450 ℃, 60 min.) following step 2, in order to further promote the MO formation. During all spin coating depositions conducted in this work, the spin coater was placed inside a fume hood. The presence of Relative Humidity (RH) constituted an issue to be resolved, since high RH values (RH>70%) caused de-wetting phenomena during spin coating. To overcome this, a dehumidifier was placed inside the fume hood, aiming to control the % RH during deposition. Therefore, the addition of dehumidifier led to constant RH values (45-50%) amongst spin coating depositions, which also eliminated the de-wetting problems.

3.1.2. Aluminium Deposition *via* Thermal Evaporation

Thermal evaporation constitutes a widely known physical vapor deposition (PVD) technique which promotes thin film formation of various materials (typically metals). Thermal evaporation began to be developed in earnest after the work of John Strong on the aluminization of astronomical mirrors in the mid-1930s [192]. The technique is based on the evaporation of a material under vacuum conditions due to the high temperature. A schematic representation is displayed in **Figure 3-2**.

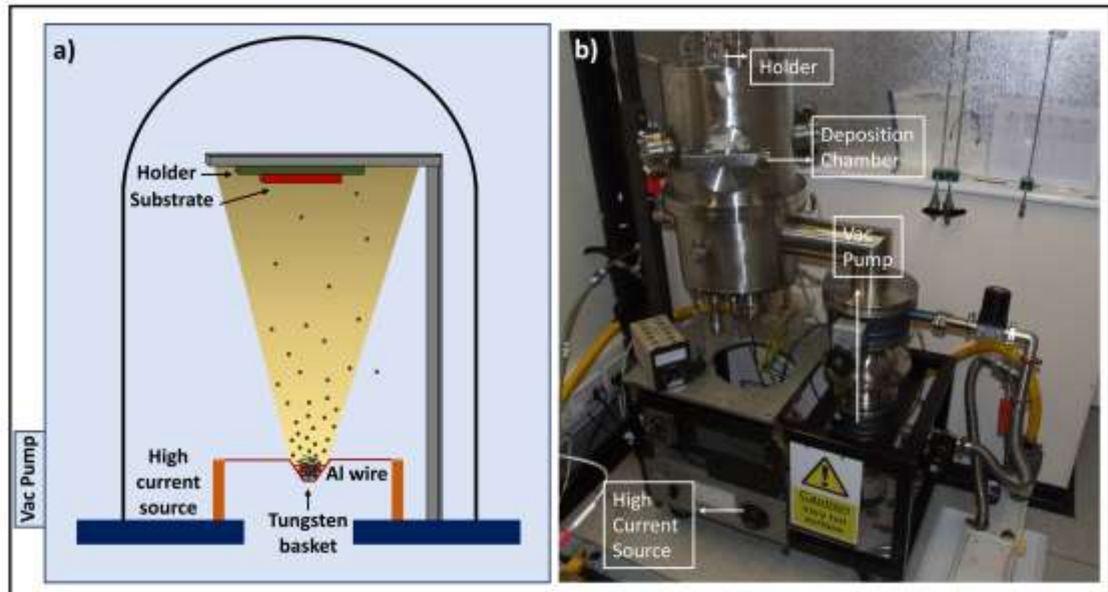

Figure 3-2. a) Illustration of evaporation system employed in Al deposition. The vacuum chamber includes an externally controlled high power supply unit, the feedthroughs which are connected to both ends of a tungsten basket. Al wire is placed inside the basket, the length of which is proportional to thin film thickness. A substrate holder is located above the tungsten basket. The chamber is kept under high vacuum with the assistance of a diffusion pump, **b)** equipment setup used in this work.

Prior to deposition, the evaporation element is placed inside a crucible or, in our case, a tungsten basket. To reach high melting points (especially in metal deposition), the basket is electrically heated by applying large alternating current. The heating is achieved according to the Joule formula, with typical temperatures reaching $2800\ \mathrm{K}$ (for tungsten or molybdenum). To avoid oxidation of the basket as well as harmful reactions between the basket and deposition material, establishing a high vacuum is of upmost importance [193]. In this work, a thermal evaporation system was employed for deposition of Al contacts on the devices of interest. Al wire was used as a deposition material, which after native oxide removal (Acetone cleaning) was placed into Tungsten baskets (Kurt J. Lesker) inside the evaporation chamber. Al evaporation was then conducted at deposition rate of $15\ \mathrm{Å/s}$. The typical contact thickness was chosen at $150\ \mathrm{nm}$.

3.2. Excimer Laser Annealing

3.2.1. The Laser Annealing System

A research grade laser annealing (LA) system can be a complex and expensive experimental apparatus. To identify the most efficient LA recipe for a given material or device, the system should involve several elements and a variety of beam path configurations. This allows for investigations into the multiple experimental parameters involved in the process. Once a robust recipe is identified, a custom-designed system able to deliver a specific LA process in a potential

mass volume production line can be manufactured for a fraction of the cost in comparison to the research tool [55]. A generic LA experimental set-up could be divided into three parts: the laser source, the beam delivery system, and the sample manipulator. The laser source includes the source of the laser light and depending on the type of laser it will offer variability of some of the experimental parameters in question (*e.g.,* repetition rate, pulse intensity, wavelength, *etc.*). The beam delivery system is often the most complex part. It serves three purposes:

i) Receiving the raw beam from the laser and manipulating the beam to provide the required processing characteristics,

ii) Delivering the suitably manipulated beam to the sample,

iii) Offering online diagnostics for the monitoring of the critical process characteristics.

Finally, the sample manipulator houses the sample appropriately and manipulates it as needed for the process. Translation stages (or rollers in the case of R2R systems) are often involved and contribute to the sample environment (temperature *etc.*) to achieve the desired annealing result. An example of such a system that considers most of the LA parameters is shown in **Figure 3-3**.

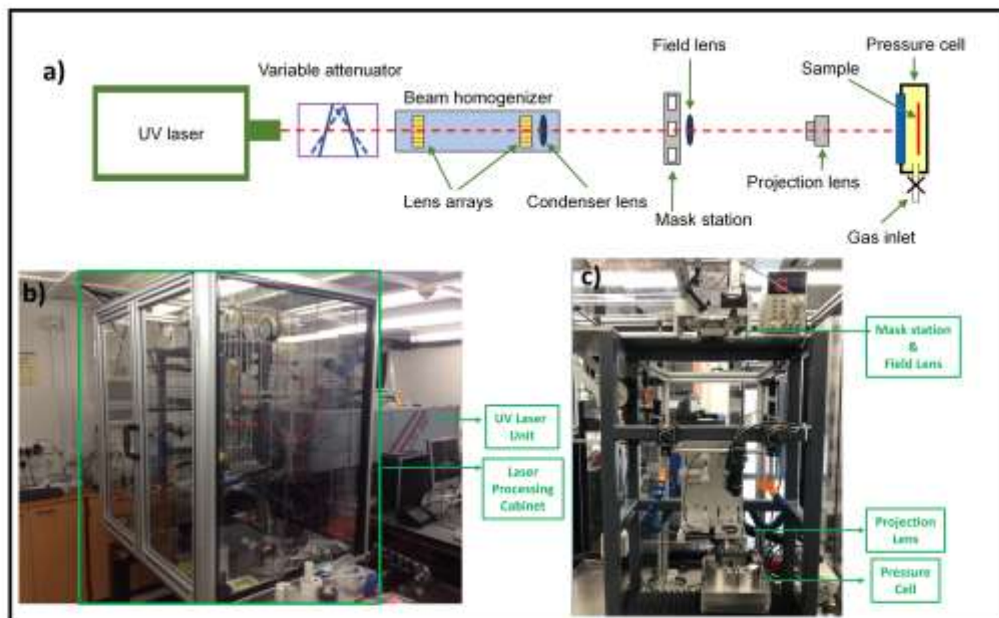

Figure 3-3. a) Illustration of a typical laser annealing system, **b)** experimental setup used in this work, **c)** compartment of the Laser Processing Unit (seen in **b)**), where Mask Station, Field Lens, Projection Lens and Pressure Cell are located.

In this system, the laser is a KrF Excimer Laser (248 nm) and the beam delivery system comprises a variable attenuator (employs a partially reflective first plate and a second plate that compensates for the parallel displacement of the beam caused by the first plate), a beam homogeniser (employs two lens arrays and a condenser lens which provides a top-hat profile on both axes), a stage for interchangeable masks that provide various spot shapes onto the sample and a combination of field and projection lenses that will define the size of the mask shape onto the sample. The sample sits inside a pressure cell on an X-Y-Z translational stage that allows for

the introduction of specific pressures of various gas mixtures during LA. Alternatively, X-Y motion can be achieved by moving the beam with the use of flying or rotating optics (aka 'galvo') while the stage remains stationary. Note that, here, we do not consider an additional set of parameters relating to the materials' optical and thermal properties, geometrical configurations (*e.g.*, design of optical spacers and mirror designs to enhance absorption) or the type and characteristics of its substrate.

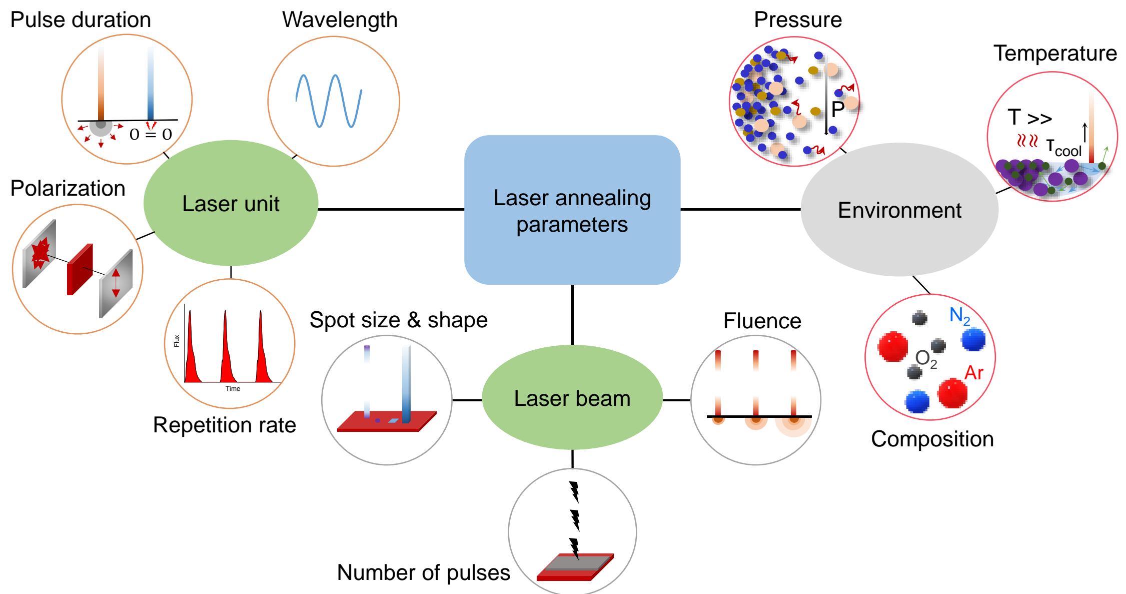

Figure 3-4. Important parameters associated with the laser annealing process.

The laser annealing system parameters can be divided into three categories (reflecting the three parts of a generic laser annealing system):

(i) laser unit parameters (wavelength, polarization, pulse duration and repetition rate),

(ii) laser beam parameters (fluence, number of pulses, spot size, and spot shape)

(iii) environmental parameters (atmosphere, pressure, and temperature).

Detailed descriptions of each of these parameters are provided in the following section.

3.2.2. Laser Annealing Parameters

The abovementioned laser system offers the flexibility of tuning its operating parameters, thus offering the opportunity of completely controlling the laser annealing procedure. These operational parameters play a crucial role as they define the upcoming experimental results.

1. **Laser fluence ($\mathrm{mJ/cm^2}$):** The energy density to be delivered to the processing sample, defined by the variable attenuator. The mask along with the objective lens used to project the laser spot onto the sample's surface define the maximum fluence. The laser spot sized is defined by the combination of field and projection lens along with the masks chosen on the mask station.

2. **Laser wavelength (nm):** In most cases, the wavelength of the laser annealing system is in the UV region. This lies upon the highest energy absorption of the MOs in this region along with the smallest penetration depth, which is highly desirable considering the lowest possible destruction of the substrate. Due to the high UV absorption by O_2 molecules in the air near the sample's surface (and their transition onto ozone), the beam delivery system is ideally enclosed in sealed tubes, allowing simultaneous N_2 flow during the laser process.
3. **Pulse duration (ns):** Most pulsed laser annealing systems produce pulses of a few ns.
4. **Number of pulses:** Alongside the laser fluence, the number of pulses to be delivered onto the sample's surface defines the amount of heat generation, thus controlling the response of the film and its percentage of transition into the desirable MO film.
5. **Repetition rate (Hz):** The repetition rate is externally controlled and may vary from a few Hz up to hundreds of Hz.
6. **Environment composition:** Depending on the desired film properties after laser annealing, the pressure cell (which contains the sample) can be supplied with different gases (through pipelines connected to the cell). LA under different environmental compositions can be used for surface doping purposes (*e.g.,* annealing in N_2 environment) or thin film conductivity control [194].
7. **Environmental temperature ($^\circ\mathrm{C}$):** The temperature at which the sample is kept during laser processing is of importance, as it will determine the cooling rate of the sample following the immense heat rise from the laser pulse. The effect of LA will vary in case of the sample being at an elevated temperature (heated), at room temperature, or at lower temperature (cooled).
8. **Pressure:** In certain cases, applying a vacuum or high-pressure of any gaseous environment during LA is considered advantageous to avoid detrimental effects of ablation.
9. **Polarisation:** While an excimer laser is usually producing completely randomly polarised light, an optical filter that passes light of a specific polarisation (polariser) may be used to block waves of other polarisations and convert a beam of light of undefined or mixed polarisation into a beam with a well-defined polarisation state.

3.2.3. Laser Annealing Mechanism

If considering LA to be the most prominent annealing technique due to its advantageous characteristics (compatibility with flexible substrates and Roll-to-Roll manufacturing systems, complete control of the energy transfer parameters), a thorough understanding of the metal oxide formation during energy transfer is essential. The predefined laser annealing parameters (laser fluence, number of pulses, pulse duration) play a crucial role into achieving the optimal result amongst various physical phenomena such as heating, melting, or ablation of the treated film. Alongside these parameters, the properties of the material to be treated such as the

thermal conductivity, energy band gap, and absorption coefficient (defining the light absorption as a function of depth) also determine the energy transfer phenomena [195–197]. The correlation between photon energy of the laser beam and energy band gap of the material to be irradiated discrete the light-material interactions into 2 particular cases; In the first case, where the photon beam energy $\hbar\omega$ is lower than the material's energy band gap E_g, the absorption is restricted into weak interband electronic excitations (excluding the case of multiphoton absorption due to the presence of defects or a coherent multiphoton absorption) [198]. In the second case, when $\hbar\omega$ exceeds the band gap energy E_g, strong interband excitations are conducted, leading to the energy transfer into phonons, inducing strong lattice vibrations. Apart from interband, intraband excitations may also occur, especially in the case of high temperatures, due to the presence of an increased number of free carriers [199].

This electron-photon interaction, along with the energy transfer on the lattice *via* phonon transport, is restricted into a time scale defined by the material's properties and the laser pulse duration. Therefore, the correlation between these parameters will define the material's response to the amount of energy transferred from the laser pulses. The overall time of the overlapping procedures (excitation- energy transfer on phonons- photothermal response) ranges from fs to ms, thus determining the phenomena occurring to the processing material. Due to their remarkable opto-electronic characteristics, the urgent need of MO insertion into the large-scale manufacturing scheme has led to their extensive processing with solution-based techniques, with sol-gel procedure comprising their common background. Regarding the sol-gel process, metalorganic precursor solutions are deposited onto a selected substrate, forming an intermediate phase, which subsequently demands a high energy amount to transform into MO films *via* a photochemical reaction. Therefore, considering the increased energy demand during the transition of precursors into MO films, the high energy and swallow penetration depth (short wavelength) of UV lasers establish them as the ideal candidate among various LA systems [200,201].

It is noteworthy that, although the term "photochemical" has been widely used in both fs and ns laser annealing processes, the origin of these phenomena lies on different heat absorption mechanisms. In detail, during fs irradiation, the direct energy transfer provokes the ablation of the material, inducing instant photochemical processes, such as direct bond breaking. In the case, though, of ns laser pulses, the photon absorption is associated with intense lattice vibration which determines the origin of the material response as photothermal. Therefore, since the origin of sol-gel photochemical transition (which comprises of removal of organic molecules and generation of M-O-M bonds) is thermal, a ns pulsed laser annealing is the ideal way of inducing this photothermally induced chemical reaction [58,202].

3.2.4. Heat propagation Model

To unveil the heat transport mechanism conducted during pulsed laser annealing, we utilize the 1D heat conduction equation:

$$c(z)\rho_m(z)\,\partial_t T(z,t) = \partial_z[k_{th}(z)\,\partial_z T(z,t)] + Q(z,t) \qquad 3.8$$

where $\partial t, \partial z$ denote partial derivatives with respect to t and z respectively(where t, z are the time and distance from the top surface respectively).The laser heating source term $Q(z,t)$ is defined by the product of the absorption spatial profile $\alpha(z)$ and the laser pulse temporal profile $\phi(t)$, i.e. $Q(z,t) = a(z) \cdot \phi(t)$, with the total laser fluence f given by:

$$f = \int_{-\infty}^{+\infty} \varphi(t)dt \qquad 3.9$$

The rest of the terms in **Eq.3.8** are the specific heat capacity c, the mass density ρ_m and the thermal conductivity k_{th}, all three having a spatial dependence due to the interchange of different materials. **Eq.3.8** is time-integrated numerically in order to obtain the explicit temperature transient. In doing so, we assume that (i) electronic and lattice temperatures are in equilibrium (valid for slow heating times in the ns regime), (ii) radiation and convection losses are insignificant, (iii) material properties (absorption, heat capacity, mass density and thermal conductivity) remain constant during heating [203].

3.2.5. Optical model

In the material of interest, several effects such as absorption, plasmon resonances and interference contribute to how the absorption is distributed, while the material thermal properties and the laser pulse profile determine the temperature transients developed. To investigate the light propagation and obtain a detailed spatial absorption distribution in the material of interest as well as the substrate, a semi-analytical opto-thermal model is developed [204]. Firstly, the UV optical constants of the materials of interest and develop an analytical model which provides the absorption spatial distribution in the multilayer. The complex refractive index of a material indicated with subscript i, $\tilde{n}_i$, is:

$$\tilde{n}_i = \sqrt{\tilde{\varepsilon}_i} = n_i + i\kappa_i \qquad 3.10$$

where $\tilde{\varepsilon}_i$, is the complex dielectric function. n_i and κ_i are the real and the imaginary part of the materials' complex refractive index, respectively. Under laser irradiation, a portion of light is reflected (reflection amplitude r) and the rest undergoes multiple reflections from the air/film and film/substrate interfaces and gets absorbed along the way. The resulting coherent downward and upward waves are denoted by $A(x)$ and $B(x)$ respectively. The transmitted wave is denoted by C, with $C(x_s)$ representing the wave at a specific distance x_s from the Si-film interface. The transfer matrices are used to calculate the incident and transmitted waves from the effective film:

$$\begin{pmatrix} C_0 \\ C \end{pmatrix} = I_{\tilde{n}_{Sub}\tilde{n}_f} P_{\tilde{n}_f l_{tot}} I_{\tilde{n}_f n_a} \begin{pmatrix} 1 \\ r \end{pmatrix} = \begin{pmatrix} M_{11} & M_{12} \\ M_{21} & M_{22} \end{pmatrix} \begin{pmatrix} 1 \\ r \end{pmatrix} \tag{3.11}$$

where $I_{\tilde{n}_f n_a}$ is the interface matrix from air to the film, $P_{\tilde{n}_f l_{tot}}$ is the propagation matrix in the film and $I_{\tilde{n}_{Sub}\tilde{n}_f}$ is the interface matrix from film to substrate:

$$I_{\tilde{n}_f n_a} = \frac{1}{2\tilde{n}_f} \begin{pmatrix} \tilde{n}_f + n_a & \tilde{n}_f - n_a \\ \tilde{n}_f - n_a & \tilde{n}_f + n_a \end{pmatrix} \tag{3.12}$$

$$P_{\tilde{n}_f l_{tot}} = \begin{pmatrix} e^{ik_f l_{tot}} & 0 \\ 0 & e^{-ik_f l_{tot}} \end{pmatrix} \tag{3.13}$$

$$I_{\tilde{n}_{Sub}\tilde{n}_f} = \frac{1}{2\tilde{n}_{Sub}} \begin{pmatrix} \tilde{n}_{Sub} + \tilde{n}_f & \tilde{n}_{Sub} - \tilde{n}_f \\ \tilde{n}_{Sub} - \tilde{n}_f & \tilde{n}_{Sub} + \tilde{n}_f \end{pmatrix} \tag{3.14}$$

where n_a, $\tilde{n}_f \equiv \tilde{n}_i$, $\tilde{n}_{sub}$ are the refractive indexes of the air, the effective index of the film and the refractive index of the substrate respectively. From **Eq. 3.11** and **Eq. 3.12**, one derives the complex components of the transfer matrix, M:

$$M_{11} = \frac{1}{2}\left(1 + \frac{n_a}{\tilde{n}_{Sub}}\right)\cos(k_f l) + \frac{i}{2}\left(\frac{n_a}{\tilde{n}_f} + \frac{\tilde{n}_f}{\tilde{n}_{Sub}}\right)\sin(k_f l) \tag{3.15}$$

$$M_{21} = \frac{1}{2}\left(1 - \frac{n_a}{\tilde{n}_{Sub}}\right)\cos(k_f l) + \frac{i}{2}\left(\frac{n_a}{\tilde{n}_f} - \frac{\tilde{n}_f}{\tilde{n}_{Sub}}\right)\sin(k_f l) \tag{3.16}$$

where $k_f = 2\pi\tilde{n}_f/\lambda$ is the wave vector inside the film and l is the film thickness. The other two components are the respective complex conjugates, *i.e.,* $M_{12} = M_{21}^*$ and $M_{22} = M_{11}^*$. Combining **Eqs. 3.11 - 3.16** we get the reflected, $r = -M_{21}/M_{22}$, and transmitted, $C_0 = \det(M)/M_{22}$, waves. Focusing next on the air-film interface, one can associate the waves before the interface with the waves after the interface:

$$\begin{pmatrix} A_0 \\ B_0 \end{pmatrix} = I_{\tilde{n}_f n_a} \begin{pmatrix} 1 \\ r \end{pmatrix} = \begin{pmatrix} N_{11} & N_{12} \\ N_{21} & N_{22} \end{pmatrix} \begin{pmatrix} 1 \\ r \end{pmatrix} \tag{3.17}$$

The fields after the air-film interface thus are:

$$A_0 = \frac{N_{11}M_{22} - N_{12}M_{21}}{M_{22}} \tag{3.18}$$

$$B_0 = \frac{N_{21}M_{22} - N_{22}M_{21}}{M_{22}} \tag{3.19}$$

These waves are counter propagating in the film and at a distance x from the interface they are described by the wave equations $A(x) = A_0 e^{ik_f x}$ and $B(x) = B_0 e^{-ik_f x}$, both waves decreasing exponentially with distance along the propagation direction ($+x$ for the forward wave, $-x$ for the backward wave). Also, the wave propagating in the semi-infinite substrate is described as

$$C(x_s) = C_0 e^{ik_s x_s} \tag{3.20}$$

where x_s is the distance from the film-substrate interface and

$$k_s = 2\pi\tilde{n}_s/\lambda \tag{3.21}$$

is the wave vector in the substrate. We can calculate the Poynting vector, S, at each point in the film and in the substrate:

$$S(x) = \mathrm{Re}\{\tilde{n}_f\}(|A(x)|^2 - |B(x)|^2) - 2\mathrm{Im}\{\tilde{n}_f\}\mathrm{Im}\{A(x)B^*(x)\} \tag{3.22}$$

$$S(x_s) = \mathrm{R\,e}\{\tilde{n}_f\}(|C(x_s)|^2) \tag{3.23}$$

The first term in **Eq. 3.22** is associated with the forward $A(x)$ and backward $B(x)$ waves, as if each of them was propagating independent of each other. The second term, which is absent in the case of non-absorbing media, appears here because of the interference between the counter-propagating waves in the absorbing film. To get the detailed absorption profile, we calculate the absorption per nm from the top of the film down to the Si substrate:

$$a(x) = S(x) - S(x-1) \qquad 3.24$$

where x is measured in nm. The obtained absorption spatial distribution $\alpha(x)$ combined with the experimental laser pulse profile $\phi(t)$ are used as the laser induced heating source:

$$Q(x,t) = \alpha(x)\varphi(t) \qquad 3.25$$

and solved numerically in the 1D heat diffusion equation:

$$(c\rho_m)_{eff}(x)\frac{\partial T(xt)}{\partial t} = \frac{\partial}{\partial x}\left[k_{eff}\big(T(xt)\big)\frac{\partial T(xt)}{\partial t}\right] + Q(xt) \qquad 3.26$$

where T is the local temperature transient and the material parameters mass density ρ_m, heat capacity c, thermal conductivity k are in general both space and temperature dependent. By time integrating **Eq.3.26**, one gets the transient temperature at each point in the multilayer.

3.2.6. Laser Annealing of Metal Oxide Thin Films

Since MOs constitute an extraordinary group of materials due to their remarkable optical, electrical and mechanical properties (tuneable resistance, transparency), controlling these properties enables their utilization in multiple applications [185]. Therefore, tuning their optoelectronic behaviour *via* using the extraordinary properties of laser annealing constitutes a challenge. MO nanoparticles (NPs), electrodes, semiconductor and dielectric layers have been reportedly treated *via* laser annealing [183,205–207]. By utilising a series of deposition techniques (sputtering, spin-coating, printing techniques) for MO film fabrication, the effect of LA in film crystallinity has been extensively studied, as it is strongly connected to significant film properties such as the optical transparency, electrical conductivity, and carrier mobility.

3.3. Characterisation

3.3.1. Atomic Force Microscopy (AFM)

Atomic Force Microscopy (AFM) constitutes the most widely used scanning probe microscopy characterisation technique, which provides vital information on the topological features of a surface of interest. The standard operation procedure of AFM involves a 3D high-resolution (up to pm scale) surface profiling, which can be used in studies of surface roughness, particle size and crystal topologies, whereas advanced AFM operation forms can also display localised conductivity profiles of thin films on a nanoscale level. Another advantage of AFM (in comparison to conventional microscopy techniques such as SEM and TEM) is the operation under various controlled atmospheres and environments, such as pure N_2 and water.

In AFM imaging, surface data is captured by scanning a sharp tip, typically featuring a $10\ \mathrm{nm}$ radius of curvature, across the sample's surface in a raster pattern. This tip, usually made from Si or SiN, is affixed to a pliable, reflective cantilever. AFM offers three imaging modes: contact, non-contact, and tapping. Each mode utilises distinct scanning techniques based on the interaction between the AFM tip and the sample's surface. Contact and tapping modes are most frequently employed. This work employs tapping mode due to its straightforwardness, superior lateral resolution, reduced damage to the sample, and less time-consuming setup. In tapping mode, lateral dragging forces are minimised, preventing sample damage. The tip/cantilever assembly oscillates vertically at or near its resonant frequency ($200 - 300\ \mathrm{kHz}$) with an amplitude ranging from $20 - 100\ \mathrm{nm}$, driven by a piezo actuator. The tip gently contacts the sample surface for a moment during its downward motion, producing a repulsive force between the tip and sample atoms as their electronic shells interpenetrate. This results in Z-axis cantilever deflection as surface morphology varies in the X and Y axes (**Figure 3-5**). During scanning, the oscillation is regulated using a feedback loop to ensure a constant amplitude, as well as uninterrupted interaction between sample and tip.

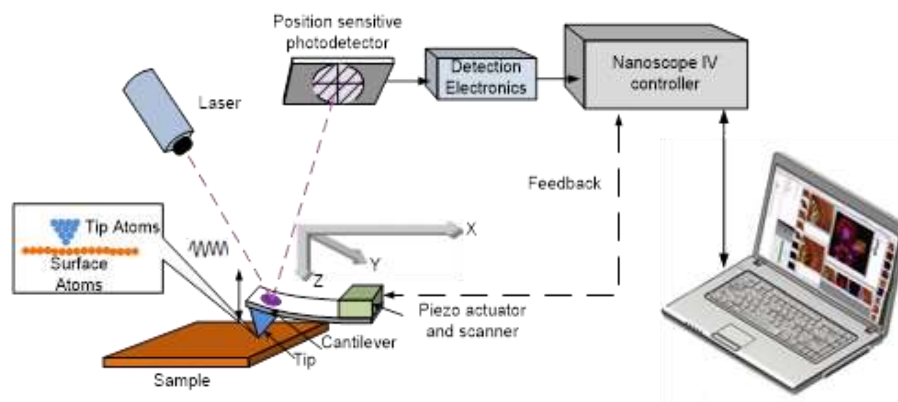

Figure 3-5. Principles and operation of AFM. Re-used, with permission, from Ref [208].

Cantilever deflection is typically monitored by a laser beam reflecting off the cantilever's back and onto a position-sensitive photodiode. Subsequently, Z-position changes in the tip/cantilever assembly reveal local height variations for each X and Y data point on the sample surface, which are then used to generate an image. The colour contrast in this image is associated to the sample's surface profile. By utilising tapping mode, AFM imaging provides valuable insights into the intricate details of a sample's surface while minimising damage [208]. To obtain surface roughness information, one must account for the following roughness-associated AFM parameters:

1. The root-mean-square roughness, $\mathrm{R_{RMS}}$ or $\mathrm{R_q}$, is the standard deviation of the surface height values, Z, from their arithmetic mean height:

$$R_{RMS} = \left[1/n \sum_{i=1}^{n} (Z_i - \overline{Z})^2\right]^{1/2} \qquad 3.27$$

2. The arithmetic roughness, R_a, is the arithmetic mean value of the surface data points deviations from the arithmetic mean height.

$$R_a = 1/n \sum_{i=1}^{n} (|Z_i - \overline{Z}|) \qquad 3.28$$

where n is the total number of data points in each image, Z_i is the surface height at a given point, and $\overline{Z}$ is the arithmetic mean of the surface height.

3. The Z range is defined as the difference in the vertical distance between the highest and lowest points in the scanned area.

$$Z_{range} = Z_{max} - Z_{min} \qquad 3.29$$

where Z_{max} and Z_{min} are the highest and lowest points of the scanned area respectively.

In this work, tapping mode AFM was used to extract information on the surface profile of In_2O_3, ZnO, ZrO_2, and Al_2O_3 films with a Brucker Dimension Icon Scanning Probe Microscope. Gwyddion software was used for real time operation and post-capture image analysis. An area of $1\ \mu m$ x $1\ \mu m$ was scanned, forming a 256×256 array of pixels.

3.3.2. Optical reflection spectroscopy (ORS)

In order to derive the Fresnel reflection and transmission coefficients at photon energy, E, ($r_F(E)$ and $t_F(E)$ respectively), one needs to define the boundary conditions for plane waves at a planar interface between two materials characterised by their complex dielectric functions $\tilde{\varepsilon}_i(E)$ and $\tilde{\varepsilon}_t(E)$ (see **Figure 3-6**) [209]. The Fresnel coefficients are defined separately for transverse electric (TE) and transverse magnetic (TM) waves. Two cases are thus described: a linearly polarised wave perpendicular (for TE) or parallel (for TM) to the plane of incidence. TE and TM waves are denoted as s- or p-polarised, respectively, and are indicated within the superscript.

$$r_F^p(E) = \frac{\tilde{\varepsilon}_t(E)k_i(E) - \tilde{\varepsilon}_i(E)k_t(E)}{\tilde{\varepsilon}_t(E)k_i(E) + \tilde{\varepsilon}_i(E)k_t(E)} \qquad 3.30$$

$$r_F^s(E) = \frac{k_i(E) - k_t(E)}{k_i(E) + k_t(E)} \qquad 3.31$$

$$t_F^p(E) = \frac{2k_i(E)}{\tilde{\varepsilon}_t(E)k_i(E) + \tilde{\varepsilon}_i(E)k_t(E)} \qquad 3.32$$

$$t_F^s(E) = \frac{2\tilde{\varepsilon}_t(E)k_i(E)}{k_i(E) + k_t(E)} \qquad 3.33$$

where $k_i(E)$ and $k_t(E)$ are the wavevectors of the incident and transmitted wave perpendicular to the interface. The polarisation dependence of the Fresnel coefficients is an essential part of ellipsometric measurements [210].

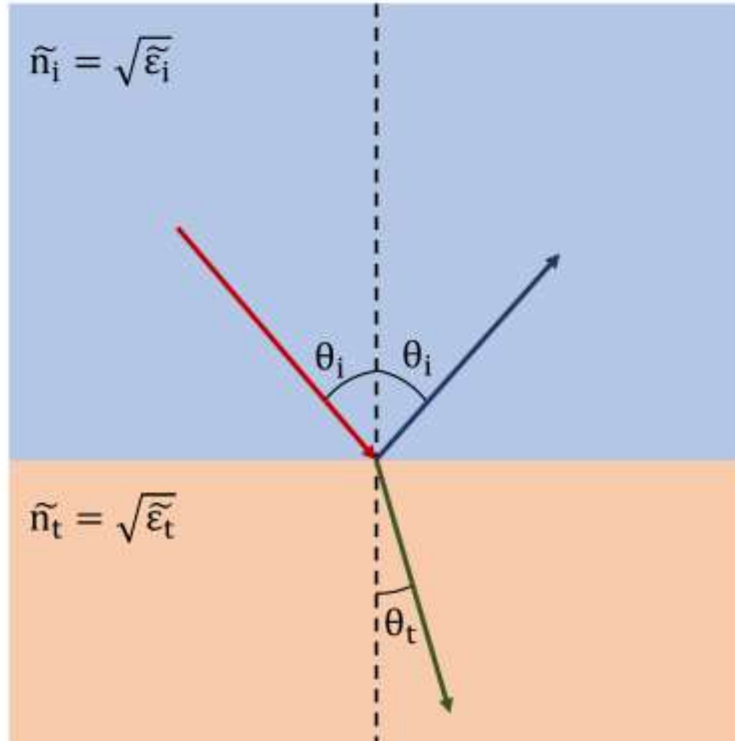

Figure 3-6. Schematic of light refraction and reflection at a boundary between two materials with different refractive indexes, $\tilde{n}_i$ and $\tilde{n}_t$. The incoming light (red arrow) with an angle of incidence θ_i is either transmitted (green arrow) at a refracted angle, θ_t, or reflected at a reflected angle $\theta_r = \theta_i$. Adapted from [209].

In a non-absorbing incident medium (ε_i is real and positive), the Fresnel coefficients can be used to determine the frequency-dependent reflectance, $R(E)$, and transmittance, $T(E)$, for p- and s-polarised electromagnetic waves [209]:

$$R^P(E) = \frac{|\xi_r(E)|}{|\xi_i(E)|} = \left|r_F^p(E)\right|^2 = \left|\frac{1 - \frac{\varepsilon_i(E)k_t(E)}{\tilde{\varepsilon}_t(E)k_i(E)}}{1 + \frac{\varepsilon_i(E)k_t(E)}{\tilde{\varepsilon}_t k_i}}\right| \quad 3.34$$

$$R^S(E) = \frac{|\xi_r(E)|}{|\xi_i(E)|} = \left|r_F^p(E)\right|^2 = \left|\frac{1 - \frac{k_t(E)}{k_i(E)}}{1 + \frac{k_t(E)}{k_i(E)}}\right| \quad 3.35$$

$$T^P(E) = \frac{|\xi_t(E)|}{|\xi_i(E)|} = 1 - R^P(E) = \frac{4\left(\frac{\varepsilon_i(E)k_t(E)}{\tilde{\varepsilon}_t(E)k_i(E)}\right)}{\left|1 + \frac{\varepsilon_i(E)k_t(E)}{\tilde{\varepsilon}_t(E)k_i(E)}\right|} \quad 3.36$$

$$T^S(E) = \frac{|\xi_t(E)|}{|\xi_i(E)|} = 1 - R^S(E) = \frac{4\frac{k_t(E)}{k_i(E)}}{\left|1 + \frac{k_t(E)}{k_i(E)}\right|} \quad 3.37$$

At normal incidence, $R(E)$ is identical for p- and s-polarised light and $\theta_i = 0°$ so that:

$$R(E) = \left|\frac{n_i - \tilde{n}_t(E)}{n_i + \tilde{n}_t(E)}\right| \quad 3.38$$

where n_i is the refractive index of the non-absorbing incident medium (Air) and $\tilde{n}_t = \sqrt{\tilde{\varepsilon}_t} = n_i + i\kappa_i$ is the complex refractive index of the potentially absorbing material with real refractive index, n_t, and extinction coefficient, κ_t. When studying multilayer structures, one must account for the contribution of back-reflections at the material interfaces, which may lead to interference effects in the collected light (see Figure 3-7). To analyse such structures, the "Matrix Method" is implemented [209]. In this method, 2×2, or 4×4 [211], matrices are used to describe both the reflection and transmission Fresnel coefficients of each individual layer. The final optical response (*i.e.,* the reflectance) is then determined from the multiplication of all the individual matrices. A short description of the method has been described by Heavens, by examining the electric vector of a wave travelling in the direction of incidence, ξ_n^+, and in the opposite direction, ξ_n^-, within the nth layer [212]. These waves are described by:

$$\xi_n^+ = \frac{1}{t_n}(\xi_{n-1}^+ \exp(i\theta_{n-1}) + r_n(\xi_{n-1}^- \exp(-i\theta_{n-1}))) \qquad 3.39$$

$$\xi_n^- = \frac{1}{t_n}(r_n\xi_{n-1}^+ \exp(i\theta_{n-1} -) + (\xi_{n-1}^- \exp(-i\theta_{n-1}))) \qquad 3.40$$

where t_n and r_n are the transmission and reflection Fresnel coefficients, respectively.

Eq. 3.39 and Eq. 3.40 can be written in matrix form:

$$\begin{pmatrix} \xi_n^+ \\ \xi_n^- \end{pmatrix} = \frac{1}{t_n}\begin{pmatrix} \exp(i\theta_{n-1}) & r_n\exp(-i\theta_{n-1}) \\ r_n\exp(i\theta_{n-1}) & \exp(-i\theta_{n-1}) \end{pmatrix}\begin{pmatrix} \xi_{n-1}^+ \\ \xi_{n-1}^- \end{pmatrix} = \frac{1}{t_n}M_{n-1}\begin{pmatrix} \xi_{n-1}^+ \\ \xi_{n-1}^- \end{pmatrix} \qquad 3.41$$

and for a stack of N layers, it can be derived that:

$$\begin{pmatrix} \xi_{N+1}^+ \\ \xi_{N+1}^- \end{pmatrix} = \frac{M_N M_{N-1} \cdots M_2 M_1}{t_N t_{N-1} \cdots t_2 t_1}\begin{pmatrix} \xi_0^+ \\ \xi_0^- \end{pmatrix} \qquad 3.42$$

Finally, the reflectance, $R(E)$, can be calculated from:

$$R(E) = \frac{|\xi_{N+1}^-|^2}{|\xi_{N+1}^+|^2} \qquad 3.43$$

In this study, optical reflectance measurements were primarily conducted to determine film thicknesses. The VIS-UV optical properties of normal-incidence optical reflectance spectra were measured in the $250 - 900$ nm $(1.4 - 5.0$ eV$)$ range using the Ocean Optics SpectraSuite Software, VIS-UV (Ocean Optics USB4000) spectrometer, a balanced deuterium-halogen light source (Ocean Optics DH2000BAL), and VIS-UV transparent optical fibres.

The experimental setup is illustrated schematically in Figure 3-7. The lamp's spectral light intensity, $I_L(E)$, was recorded using a ~300 nm Al thin film deposited onto Si as a reference mirror. The spacing between the optical fiber head and the sample surface was adjusted to ensure maximum reflected intensity, and the number of counts was adjusted to keep the peak intensity below the detector's saturation limit. The light source was then closed to record the dark intensity, $I_D(E)$. Subsequently, the source was reopened, the sample was placed under the

probe, and the reflective light intensity of the measured sample, I_S, was recorded. Reflectance, $R(E)$, was calculated using the following formula:

$$R(E) = \frac{I_S(E) - I_D(E)}{\left(I_L(E) - I_D(E)\right)} R_{Al}(E) \quad 3.44$$

Here, $R_{Al}(E)$ represents the theoretical reflectivity of the Al mirror, as determined through ellipsometry [213]. The J. A. Woollam propriety software of CompleteEase™ was employed to solve the matrix method for multiple potentially semi-absorbing layers and a general incident angle. A geometric model is built layer by layer with the optical constants ($\tilde{n}$ or $\tilde{\varepsilon}$) of each layer. The region below the estimated band gap ~ 3 eV is used to fit a constant n and d to the data with a Levenberg-Marquardt nonlinear regression algorithm [214].

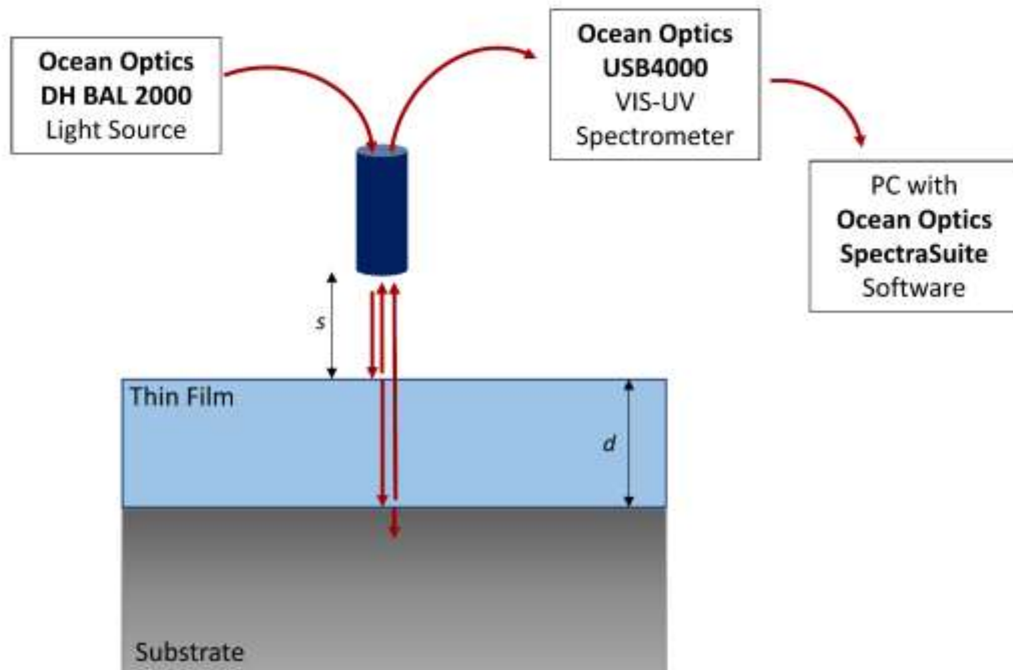

Figure 3-7. Schematic of the set-up employed during an ORS measurement. The setup involves the sample (thin film (blue) on top of substrate (grey)), a light source, and a set of optical fibres. Light (dark red arrows) is directed from the source to a distance, s, above the surface of a thin film material, with thickness d. The light reflects from the surface of the thin film, the film/substrate interface or is reflected after one or more internal reflections between the surface and interface. Then, the spectrometer detects the light reflection as a function of photon energy. The presence of one or more internal reflections allows for the determination of the film thickness from the spacing on the interference fringes.

3.3.3. Infrared Spectroscopic Ellipsometry (IRSE)

Infrared Spectroscopic Ellipsometry (IRSE) measurements were performed to determine the optical constants of the films after each thermal processing step. The ellipsometric parameters

Ψ and Δ were recorded at 3 angles of incidence (55°, 65° and 75°), in order to increase the reliability of the obtained relative complex permittivity, $\tilde{\varepsilon}(\omega)$.

Optical model and fitting

Spectroscopic ellipsometry (SE) is a non-destructive and non-invasive optical characterisation technique, primarily used to determine the optical properties, composition as well as thickness of thin films. It is based on the frequency, ω, dependent change in polarization ($\rho(\omega)$) of a reflected light beam from the surface of interest. This change is described by [215]:

$$\rho(\omega) = \tan\,(\Psi(\omega)^{i\Delta(\omega)} = \frac{r_{p(\omega)}}{r_{s(\omega)}} \quad 3.45$$

where $r_{p(\omega)}$ and $r_{s(\omega)}$ are the Fresnel reflection coefficients for the parallel (p) and perpendicular (s) polarized light to the plane of incidence.

The phase difference between the p-polarized and s-polarized light upon reflection can be defined as “delta”, Δ. In addition to a phase shift, the reflection will also induce an amplitude reduction for both the p- and s- polarized light, and it will differ between the two. The ratio of the outgoing light amplitude to the incoming amplitude defines the quantity “psi”, Ψ, and is a real number.

Δ and Ψ constitute the parameters defined upon measurement (raw data), that are afterwards utilized into an appropriate model in order to extract $\tilde{\varepsilon}(\omega)$. The real and imaginary parts of the permittivity of the entire sample, the ‘pseudo permittivity’, $<\tilde{\varepsilon}(\omega,\theta)>$, is extracted during measurement, by $\rho(\omega)$ at each angle of incidence θ [215]:

$$<\tilde{\varepsilon}(\omega,\theta)> = <\varepsilon_1(\omega,\theta)> + i <\varepsilon_2(\omega,\theta)> = \sin^2(\theta)\left(1+\tan^2(\theta)\left[\frac{1-\rho(\omega)}{1+\rho(\omega)}\right]^2\right) \quad 3.46$$

However, $<\tilde{\varepsilon}(\omega,\theta)>$ represents an extrinsic property of the entire sample and depends on the geometry and properties of each individual layer. To extract the permittivity of the layer of interest, a model is developed that comprises both a geometric and optical part. The geometric part describes the stack of layers forming the sample. The optical part introduces the individual layer thickness and permittivity. The combination of these parts transforms $<\tilde{\varepsilon}(\omega,\theta)>$ into the individual $\tilde{\varepsilon}(\omega)$ for each layer.

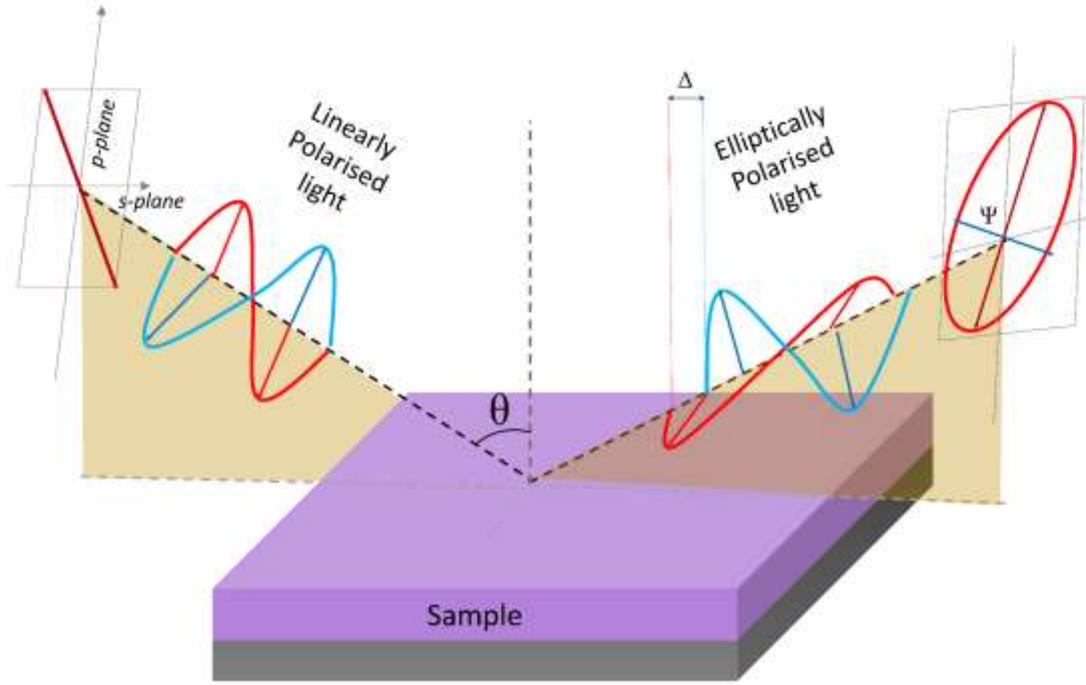

Figure 3-8. Illustration of the Ellipsometry main principle. Linearly polarised light (red represents the electric and blue the magnetic wave) hits the surface of interest (purple sample) at an angle θ. Upon reflection from the sample, the light becomes elliptically polarised and is thus represented by a phase, $\Delta(\mathrm{E})$ and an amplitude, $\tan(\Psi(\mathrm{E}))$.

Gaussian Oscillator

To extract the permittivity of an unknown layer, we introduce a summation of individual oscillators in our fitting model. These oscillators can represent contributions of interband, intraband and optical phonon absorptions. The optical phonon absorptions corresponding to the films of our study are described by Gaussian oscillators:

$$\tilde{\varepsilon}_{\mathrm{Guassian}}(\mathrm{E}) = \mathrm{A_n}\left\{\left[\Gamma\left(\frac{\mathrm{E}-\mathrm{En}}{\sigma_\mathrm{n}}\right)+\Gamma\left(\frac{\mathrm{E}+\mathrm{En}}{\sigma_\mathrm{n}}\right)\right]+\mathrm{i} \cdot\left(\exp\left[-\left(\frac{\mathrm{E}-\mathrm{En}}{\sigma_\mathrm{n}}\right)^2\right]-\exp\left[-\left(\frac{\mathrm{E}+\mathrm{En}}{\sigma_\mathrm{n}}\right)^2\right]\right)\right\} \quad 3.47$$

where E is the photon energy ($\mathrm{E} = \hbar\omega$), $\hbar$ is the reduced Planck constant, A is the amplitude, $\mathrm{E_n}$ is the peak central energy, $\sigma_\mathrm{n} = \gamma_\mathrm{n}/2\sqrt{\mathrm{In}(2)}$, γ_n is the broadening of the oscillator and Γ is a convergence series.

Drude-Smith oscillator

The Drude model is the most used optical model that describes the presence of free carriers in metals and semiconductors. This model considers a free electron gas with complete momentum randomisation following elastic scattering events and is described as:

$$\tilde{\varepsilon}(\omega) = \varepsilon_1(\omega) + \mathrm{i}\varepsilon_2(\omega) = 1 - \frac{\omega_\mathrm{p}^2}{-\omega^2 + \frac{\mathrm{i}\omega}{\tau}} \quad 3.48$$

where $\tilde{\varepsilon}(\omega)$ is the complex dielectric permittivity, ω_p is the plasmon frequency and τ is the collision-modified carrier lifetime. However, various materials and structures such as VO_2,[216] ZnO,[217] Ag nanowires [218], and TiO_2 nanoparticles [219] are often described by a modified Drude model produced by Smith,[220] where collision-related backward scattering of electrons is also included. The complex dielectric permittivity as extracted from Drude-Smith model is given by $\tilde{\varepsilon}(\omega) = \varepsilon_1(\omega) + i\varepsilon_2(\omega)$ with:

$$\varepsilon_1(\omega) = -\omega_p^2 \left[\frac{\frac{1+2c}{\tau^2+\omega^2}}{\left(\frac{1}{\tau^2}+\omega^2\right)^2} \right] \qquad 3.49$$

$$\varepsilon_2(\omega) = \frac{\omega_p^2}{\omega\tau} \left[\frac{\frac{1+2c}{\tau^2}+(1-c)\omega^2}{\left(\frac{1}{\tau^2}+\omega^2\right)} \right] \qquad 3.50$$

where $\omega_p^2 = Ne^2/\epsilon_0 m^*$ and c is the coefficient representing the expectation value of cos (θ), where θ is the scattering angle. The Drude-Smith model accounts for electron collisions that are randomly distributed in time, but with an average time interval between them. The electron collisions may originate from scattering events due to lattice defects, as well as grain boundaries.[219] The negative values of c indicate a larger carrier backscattering and a divergence to Drude model. For $c = 0$, the Drude model is restored [217]. In this study, Drude-Smith model was included in the fitting of thermally annealed $Zn(CH_3COO)_2$ thin films. The fitted values were c, plasma frequency ω_p, and $\gamma = 1/\tau$. The reported carrier concentration, N, for the $Zn(CH_3COO)_2$ films is extracted from ω_p using an effective mass, m^*, of $0.24\ m_e$ [217,221].

Acquisition parameters in IRSE measurements

IRSE and IRT measurements were performed with a J.A. Woollam Mark II IR Variable Angle Spectroscopic Ellipsometer (VASE) $(1.6 - 40\ \mu m)$. For IRSE measurements, the ellipsometric parameters Ψ and Δ were recorded at multiple angles of incidences ($55° - 75°$, by $10°$). The experimental parameters of the IRSE and IRT measurements are given in **Table 3-1**:

Table 3-1. experimental parameters of the IRSE and IRT measurements.

Parameter	Definition	Value
Resolution	Intended Spectral Resolution	$4\ cm^{-1}$
Spectra/Rev	Number of measurement positions per revolution of the rotating element	15
Scans/Spectrum	Number of FTIR spectrometer mirror scans that will be performed at each measurement point during the revolution	20
Cycles/Angle	Number of complete measurements at each angle that will be averaged over	3

Experimental Setup

A schematic diagram of the IR-VASE used in this work is presented in **Figure 3-9**:

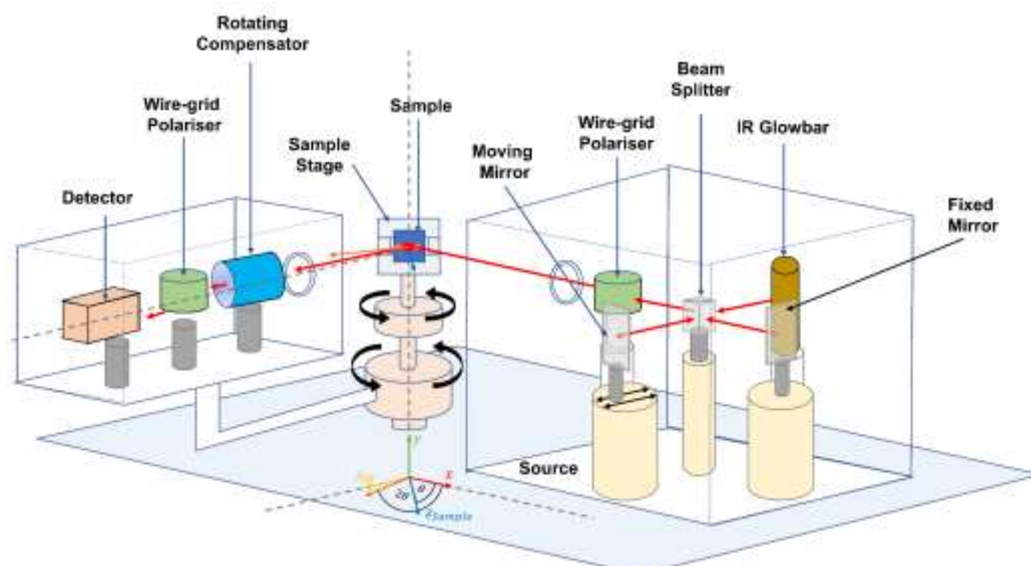

Figure 3-9. Illustration of the Mark II IR-VASE. The system consists of three main parts: an IR source, the sample manipulator, and the detector. The source comprises an IR glow bar, a beam splitter, a fixed mirror, a moving mirror, a wire-grid polariser, and an iris. This delivers linearly polarised light to the sample surface, which is rotated with by the sample stage to ensure the light is incident at an angle, θ, normal to the sample surface. The sample is vertically mounted on a semi-hollow stage and held in place with a vacuum pump to allow measurement of the IR transmission. The detector unit is rotated at an angle of 2θ and houses a rotating compensator, a wire-grid polariser, and a detector. The rotating compensator allows for simultaneous measures of $\Psi(E, \theta)$ and $\Delta(E, \theta)$.

3.3.4. Infrared Transmission (IRT)

Prior to thin film fabrication, Infra-Red Transmission (IRT) measurements of Indium nitrate hydrate ($In(NO_3)_3 \cdot xH_2O$, Fisher Scientific) and Zinc Acetate Dihydrate ($Zn(CH_3COO)_2 \cdot 2H_2O$, Merck) in 2-Methoxy-Ethanol (2-ME) (Acros), 30 mg/mL were employed, using a J. A. Woollam Mark II IR Variable Angle Spectroscopic Ellipsometer (VASE) ($250 - 8000\ cm^{-1}$). Monoethanolamine (MEA, Acros) was added to $Zn(CH_3COO)_2$ solution, in $1:1$ molar ratio, aiming to enable the dissolution of $Zn(CH_3COO)_2$ in 2-ME. The solution was drop casted onto silicon substrates, following their UV with ozone treatment for wettability enhancement. Transmission measurements of the precursor solution were conducted immediately after deposition (IRT of solution), as well as a few minutes after the deposition (IRT of dried film).

IRT measurements of 2-Methoxyethanol on intrinsic Si (IRT of solution) were also performed, in order to distinguish the spectral features corresponding to $In(NO_3)_3$ and ($Zn(CH_3COO)_2$). The utilised IR-VASE system enabled measurements of spectral transmission, $T_{IR}(E)$ in the range of $1.55 - 35.5\ \mu m$ ($0.034 - 0.8$ eV) at normal incidence. n-Si substrates and not metal substrates (which were widely used in **Chapter 4**) were used for IRT measurements due to transparency of Si in the spectral range of measurements. $T_{IR}(E)$ can be described as:

$$T(E) = \frac{n_0(E)\cos^2\theta_{N+1})|\xi_0^+|^2}{n_{N+1}(E)\cos^2(\theta_0)|\xi_{N+1}^+|^2} \quad 3.51$$

where N is the total number of layers ($N = 0$ is the layer of the incident light). ξ_0^+ and ξ_{N+1}^+ can be extracted from the Fresnel coefficients. Gaussian functions produced the best fit when used for IR absorption centres. They are described by **Eq. 3.47**.

3.3.5. Electrical characterisation

A large portion of the results based in this work involved the electrical characterisation of TFTs and Thin Film Capacitors. These sets of measurements were performed on a setup including a Keithley 4200 as the principal measurement source, along with a Semiprobe device measuring equipment. **Figure 3-10** presents the equipment setup used in device characterisation. The setup can be divided into 5 principal parts:

1. **Keithley 4200 – SCS Parameter Analyser:** Used for designing and performing custom C-V and I-V measurements. The equipment setup used in this work also includes 4200A-CVIV Multiswitch (four channels) that allowed for an automatic switch between I-V and C-V measurements without the need for re-cabling. All TFT measurements were performed using this feature, to assure accurate extraction of measurements and avoid re-probing.
2. **Semiprobe SMU probing table:** The area where a device is placed prior to measurement, to ensure the sample's accurate probing. The table includes a vacuum chuck to avoid the sample movement during measurement. Probing arms (connected to Keithley 4200 SMUs are located above the sample area, while tungsten probing tips are pinned on the probing arm's edges.
3. **Probing table- position setup:** X and Y position setup of probing table- principally used during sample change.
4. **Microscope:** Used in accurate device probing.
5. **Monitoring Screen:** Used as an alternative to microscope.

Figure 3-10. Equipment setup used for electrical characterisation in this work. The setup includes a Keithley 4200 – SCS Parameter analyser along with 4200A-CVIV Multiswitch, the Semiprobe probing table, probing arms with tips, an X-Y moving stage, a microscope, and a screen monitor.

4. IRSE Investigation on Indium Oxide and Zinc Oxide Ultra-Thin Films

One of the principal objectives of this work, the investigation of temperature effect on In_2O_3 and ZnO thin film formation *via* sol-gel, is presented in this chapter (also note the Appendix, where all IRSE fitting parameters of this chapter are displayed). Complementing the plethora of reported work on metal oxide (MO) formation mechanisms based on sol-gel precursor conversion, this work involves, for the first time, the use of infrared spectroscopic ellipsometry (IRSE) as a single-step characterisation route. The choice of IRSE as a research tool for this work lies on its unique features; non-destructive, self-referencing and highly sensitive. These qualities enable the study of ultra-thin film structures which constitute the core of this work. IRSE has been broadly employed in MO-based studies, providing vital information about the structural (vibrational modes) [222], optoelectronic (carrier transport properties) and geometric (thickness, roughness) features of MO thin films [223]. However, to the best of our knowledge, the complex nature of sol-gel intermediate steps, combined with the demand for ultra-thin (~ 10 nm) MO films has so far hindered the use of IRSE in ultra-thin sol-gel MO films. The following study introduces IRSE as a non-destructive and single characterisation technique to elucidate the underlying chemistry of the sol-gel process of ultra-thin films. Furthermore, to reach the potential of implementation in device manufacturing, an additional challenge is introduced. This challenge is grounded in the fact that IRSE sensitivity heavily depends on the substrate of choice. Unfortunately, Si substrates which has a critical role in CMOS technology, do not meet the requirement limits of IRSE sensitivity (*i.e.,* difficulty in detection of spectral features with low signal-to-noise ratio). To tackle this, IR reflective substrates (TiN, Al, and Au) are employed aiming to enhance IRSE sensitivity. This work introduces a quality factor that correlates the substrate's electronic properties (resistivity and scattering time) with the spectral features of In_2O_3 and ZnO precursor films. Experimental results are also accompanied by ellipsometric simulations in support of the experimental findings. This Chapter is based on the publication "Physicochemical Analysis of Nanoscale Metal Oxide Thin Film Precursors via Infrared Spectroscopic Ellipsometry" (C. Koutsiaki *et al*., *J. Phys. Chem. C* (2023)).

4.1. Infrared Transmission of $In(NO_3)_3$ and $Zn(CH_3COO)_2$

Prior to IRSE analysis of thermally treated $\mathrm{In(NO_3)_3}$ and $\mathrm{Zn(CH_3COO)_2}$ thin films, a study of the corresponding precursor solutions was conducted using infrared transmission (IRT) measurements. The principal aim of this process step involves a mapping of the precursor-related absorption peaks as well as a comparison amongst two precursors (nitrate-acetate). To achieve that, an additional IRT measurement (and analysis) of the solvent (2-Methoxyethanol, simply referred to $\mathrm{2\text{-}ME}$) was performed, to avoid misintepreting absorption peaks that correspond to $\mathrm{2\text{-}ME}$. Water absorption also constitutes a point of interest, as $\mathrm{In(NO_3)_3}$ salt contains an undefined amount of water molecules ($\mathrm{In(NO_3)_3 \cdot xH_2O}$) that may affect film formation when deposited under ambient conditions.

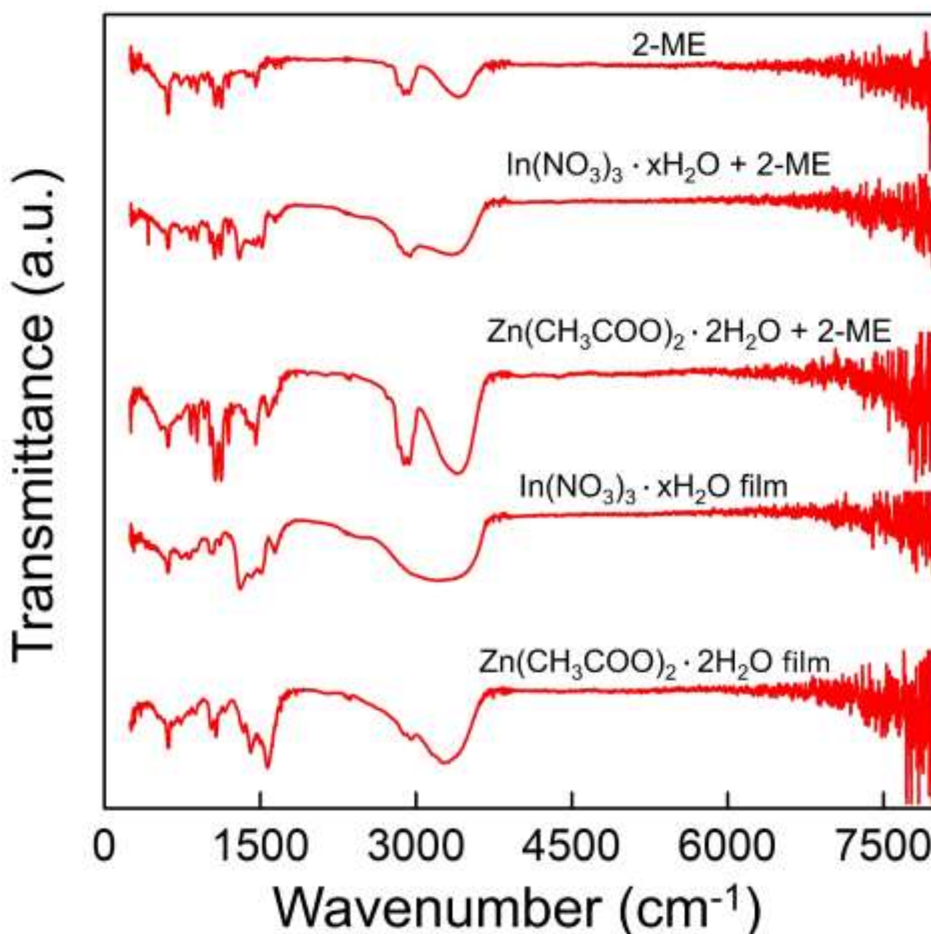

Figure 4-1. IR transmittance intensity measurements (red lines) of (top to bottom) 2-Methoxyethanol (2-ME), $\mathrm{In(NO_3)_3 \cdot xH_2O}$ solution, $\mathrm{Zn(CH_3COO)_2 \cdot 2H_2O}$ solution, $\mathrm{In(NO_3)_3 \cdot xH_2O}$ dried film and $\mathrm{Zn(CH_3COO)_2 \cdot 2H_2O}$ dried film.

Alongside the 'wet' solutions, IRT analysis of the associated dried films (under atmospheric conditions, no thermal treatment) was also performed, in order to examine the induced water adsorption on the film surface. Figure 4-1 and Figure 4-2 present the measured IR transmittance, $\mathrm{T_{IR}(k)}$, and the extracted (fit) imaginary permittivity, $\varepsilon_2(\mathrm{k})$, of $\mathrm{2\text{-}ME}$ (red line), $\mathrm{Zn(CH_3COO)_2}$ in $\mathrm{2\text{-}ME}$ solution (blue line), $\mathrm{In(NO_3)_3}$ in $\mathrm{2\text{-}ME}$ solution (green line), and their corresponding

dried films (magenta and orange lines, respectively). The optical models used for the extraction of $\varepsilon_2(\mathrm{k})$ included Gaussian oscillators, with fitting parameters presented in **Table 9-1**. A comparison between each plot in **Figure 4-2a-c** reveals various similarities amongst the absorption of 2-ME and precursor solutions. The presence of two sharp peaks at ~ 834 and $\sim 895\ \mathrm{cm}^{-1}$ represent C-H bending, originating from the methyl group found in 2-ME. C-H bending is also detected at $1320 - 1457\ \mathrm{cm}^{-1}$(**Figure 4-2**, light pink shaded area), with 2-ME and $Zn(CH_3COO)_2$ solution showing an identical absorption profile in this spectral range. For the $In(NO_3)_3$ solution (**Figure 4-2b**) a transformation in absorption is seen at $1320 - 1457\ \mathrm{cm}^{-1}$, possibly due to the IR absorption of NO_3^- coinciding on this spectral range. Also, three strong peaks at $1014 - 1126\ \mathrm{cm}^{-1}$ are detected in 2-ME, $In(NO_3)_3$ and $Zn(CH_3COO)_2$ solutions, corresponding to C-O stretching (**Figure 4-2**, light pink shaded area). Strong IR absorption due to C-O stretching is also detected at $\sim 1200\ \mathrm{cm}^{-1}$ in **Figure 4-2a-c**. These similarities are well expected.

The spectral features associated to the 2-ME solvent (**Figure 4-2a**) overshadow any distinction of precursor-related peaks. The detection of H_2O is identified in $In(NO_3)_3$ and $Zn(CH_3COO)_2$ solutions (**Figure 4-2b-c**, blue shaded area) from the absorption peak at $\sim 1600\ \mathrm{cm}^{-1}$ (δ(H-O-H) bending of undissociated water molecules). The presence of H_2O can be due to water adsorption during the measurement, as well as the presence of water molecules in the precursor salts. For the $Zn(CH_3COO)_2$ solution (**Figure 4-2c**), a peak at $\sim 600\ \mathrm{cm}^{-1}$ (**Figure 4-2**, lilac shaded area) can be attributed to Zn-O associated vibration modes. The same peak is detected in the corresponding dried film. A set of peaks representing In-O are also apparent at $300 - 500\ \mathrm{cm}^{-1}$ for the $In(NO_3)_3$ solution (**Figure 4-2b**) and the $In(NO_3)_3$ film (**Figure 4-2d**).

A notable change in the absorption spectra of $In(NO_3)_3$ and $Zn(CH_3COO)_2$ dried films is seen in **Figure 4-2d-e**. In the $In(NO_3)_3$ film (**Figure 4-2d**) most of 2-ME associated spectral features are removed. At $1310 - 1500\ \mathrm{cm}^{-1}$, a set of strong absorption peaks remains, which may be attributed to NO_2^-. A H_2O-associated absorption peak at $\sim 1600\ \mathrm{cm}^{-1}$ is also apparent, similarly to $In(NO_3)_3$ solution. For $Zn(CH_3COO)_2$ dried film, the peaks detected at $1028\ \mathrm{cm}^{-1}$ and $1036\ \mathrm{cm}^{-1}$ can be associated to C-N (MEA) and C = O (acetate group) stretching, respectively. Stretching modes of C = O originating from the acetate anion in $Zn(CH_3COO)_2$ are also detected at $1407\ \mathrm{cm}^{-1}$ and $1561\ \mathrm{cm}^{-1}$.

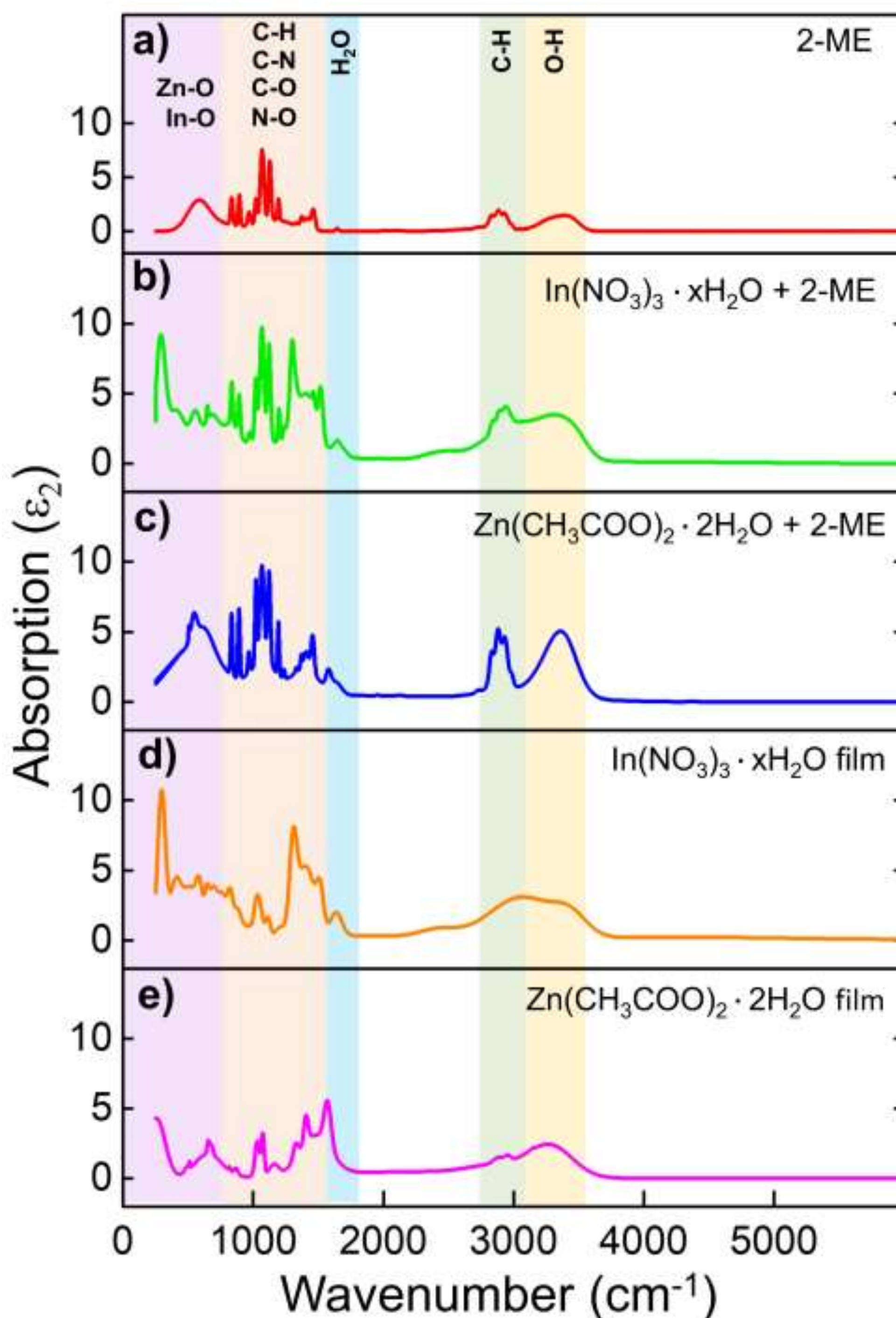

Figure 4-2. Imaginary part of the dielectric permittivity $\varepsilon_2(\mathrm{k})$, of (a) 2-ME (red), (b) $\mathrm{In(NO_3)_3}$ in 2-ME solution (green), (c) $\mathrm{Zn(CH_3COO)_2}$ in 2-ME solution (blue), (d) $\mathrm{In(NO_3)_3}$ dried film (orange) and (e) $\mathrm{Zn(CH_3COO)_2}$ dried film (magenta). The shaded areas represent spectral regions where 2-ME, $\mathrm{In(NO_3)_3}$ and $\mathrm{Zn(CH_3COO)_2}$ absorption peaks are expected. Zn-O and In-O associated peaks are detected in lilac area, C-N, C-H, C-O and N-O in light pink, $\mathrm{H_2O}$ in light blue, C-H in green and -OH in yellow.

In the region between $2730\ \mathrm{cm^{-1}}$ and $3600\ \mathrm{cm^{-1}}$, two distinct absorption features are observed for 2-ME. The first set of absorption peaks at $2800 - 3000\ \mathrm{cm^{-1}}$ (green shaded area in Figure 4-2) is due to C-H stretching, also detected in $\mathrm{In(NO_3)_3}$ and $\mathrm{Zn(CH_3COO)_2}$ solutions.

The second broad absorption peak at $3300 - 3700\ \mathrm{cm}^{-1}$(yellow shaded area in **Figure 4-2**) covers the O-H stretching, representing the -OH groups in H_2O, as well as the 2-ME-related hydroxyl groups. Interestingly, the transition from solutions to $In(NO_3)_3$ and $Zn(CH_3COO)_2$ dried film is accompanied by a transformation of the two peaks into a single, broad peak. Particularly for $Zn(CH_3COO)_2$ dried film, the set of absorption peaks at $2800 - 3000\ \mathrm{cm}^{-1}$ is still apparent, possibly attributed to C-H in acetate anion. The results from IR transmission analysis (**Figure 4-2**) have majorly contributed to our IR ellipsometry analysis, providing vital information regarding the absorption profile of $In(NO_3)_3$ and $Zn(CH_3COO)_2$ films. The well-defined region and shape of NO_2^-, C-H and C=O absorption, the solvent removal as well as the presence of H_2O constituted the cross-examination towards the validity of our IRSE fitting models, later in our analysis.

4.2. Ellipsometric Results and Analysis

IRT analysis provided insightful information on the absorption of precursor solutions and dried films, highlighting their peak discrepancies as well as H_2O adsorption differences. As a next step, IRSE analysis was performed on thermally treated $In(NO_3)_3$ and $Zn(CH_3COO)_2$ films, aiming to investigate the annealing effect on precursor conversion. Thin film fabrication was performed *via* spin coating (see deposition parameters in **Chapter 3**), followed by two thermal treatment steps: Step 1 (stabilisation, $150\ ^\circ\mathrm{C}$, $15\ \mathrm{min.}$) was followed immediately after deposition to obtain a solid film and Step 2 (thermal annealing, $300\ ^\circ\mathrm{C}$, $60\ \mathrm{min.}$) to promote precursor conversion into MO. Starting from IRSE analysis of Step 1, **Figure 4-3** displays the measured Ψ (red lines) and Δ (green lines) values of stabilised ($150\ ^\circ\mathrm{C}$, $15\ \mathrm{min.}$) ultra-thin $In(NO_3)_3$ (**Figure 4-3a-d**) and $Zn(CH_3COO)_2$ (**Figure 4-3e-h**) films on top of various substrates for each angle of incidence, respectively. IRSE spectra of thermally annealed (TA) $In(NO_3)_3$ and $Zn(CH_3COO)_2$ can be found in **Figure 4-4**.

Figure 4-3 also shows the fitted values of Ψ and Δ (black dotted lines). For stabilised $In(NO_3)_3$ on Si (**Figure 4-3a**), a single feature at $469\ \mathrm{cm}^{-1}$ is observed, associated to In-O. For stabilised $Zn(CH_3COO)_2$ on Si (**Figure 4-3e**), a single feature is revealed at $459\ \mathrm{cm}^{-1}$, corresponding to Zn-O vibrational mode. A thourough discussion on the detected vibrational modes of $In(NO_3)_3$ and $Zn(CH_3COO)_2$ is conducted later in the text. The “flat response” seen in **Figure 4-3a** and **Figure 4-3e** manifests that the use of Si as a substrate hinders the detection of $In(NO_3)_3$ and $Zn(CH_3COO)_2$ *via* their associated optical phonons through IRSE. This “substrate unsuitability” is of high importance when considering the potential implementation of IRSE in sol-gel ultra-thin film for research and industry. An improvement in IRSE sensitivity can be achieved by using alternative substrates, as reported by Tompkins *et al.* [224]. Therefore, in order to tackle the poor IRSE response of stabilised films on top of Si (**Figure 4-3a** and **Figure**

4-3e), $In(NO_3)_3$ and $Zn(CH_3COO)_2$ thin films were deposited on top of TiN (**Figure 4-3b** and **Figure 4-3f**), Al (**Figure 4-3c** and **Figure 4-3g**) and Au (**Figure 4-3d** and **Figure 4-3h**). The presence of various spectral features of stabilised $In(NO_3)_3$ and $Zn(CH_3COO)_2$ is revealed, revealing the significant role of the substrate in IRSE sensitivity. The complex permittivity corresponding to stabilised $In(NO_3)_3$ (**Figure 4-5**) and $Zn(CH_3COO)_2$ (**Figure 4-6**) is subsequently extracted, based on the fit of Ψ and Δ (**Figure 4-3**, black dotted line). In the case of Al substrate, an additional peak at $1000\ cm^{-1}$ is detected, representing the native oxide on top of Al.

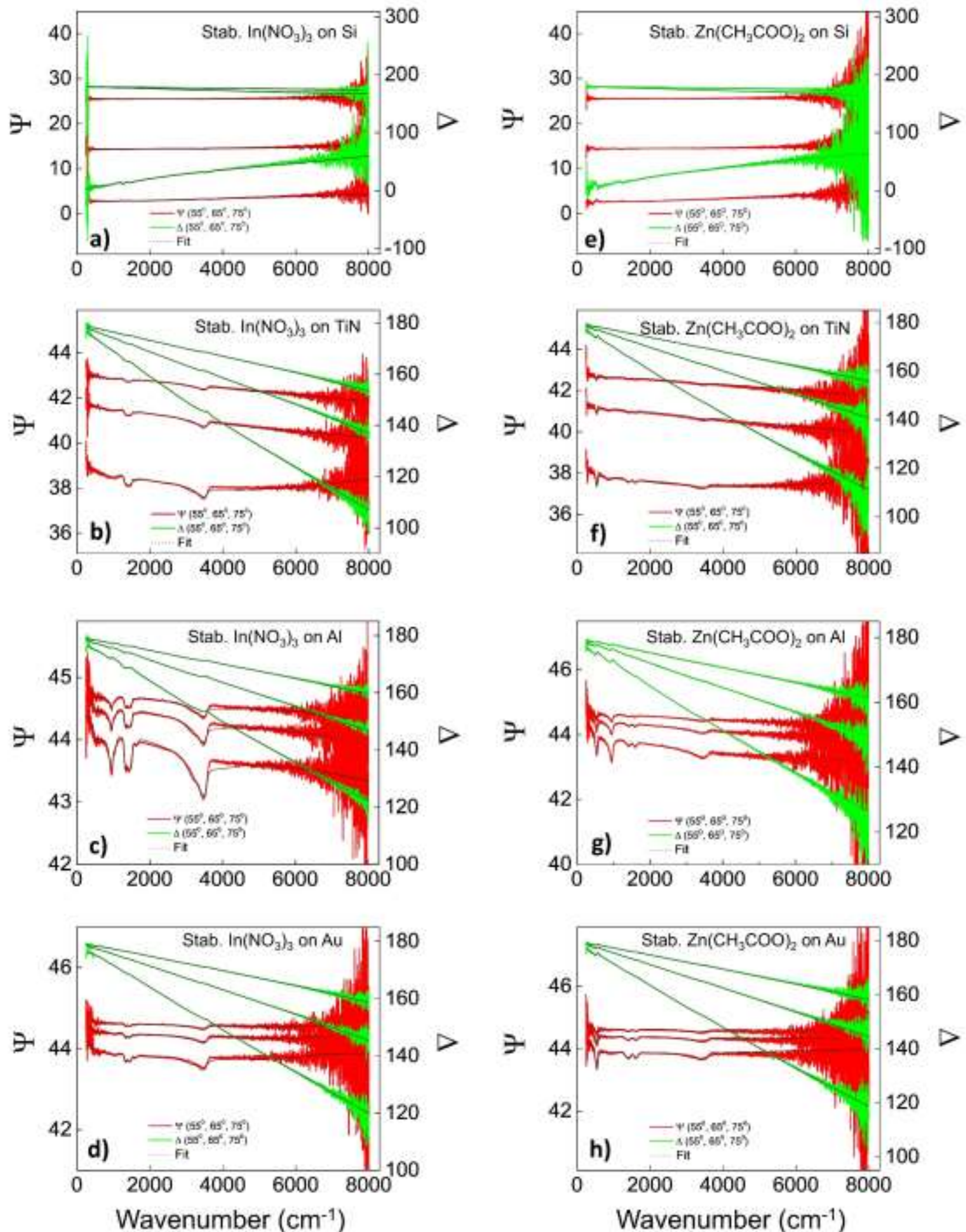

Figure 4-3. Measured Ψ (red lines) and Δ (green lines) for stabilised (step 1) $\mathrm{In(NO_3)_3}$ thin films on top of (a) Si, (b) TiN, (c) Al and (d) Au and $\mathrm{Zn(CH_3COO)_2}$ thin films on top of (e) Si, (f) TiN, (g) Al and (h) Au. Their fitted values (black dotted lines) are also presented, as obtained from the corresponding optical models.

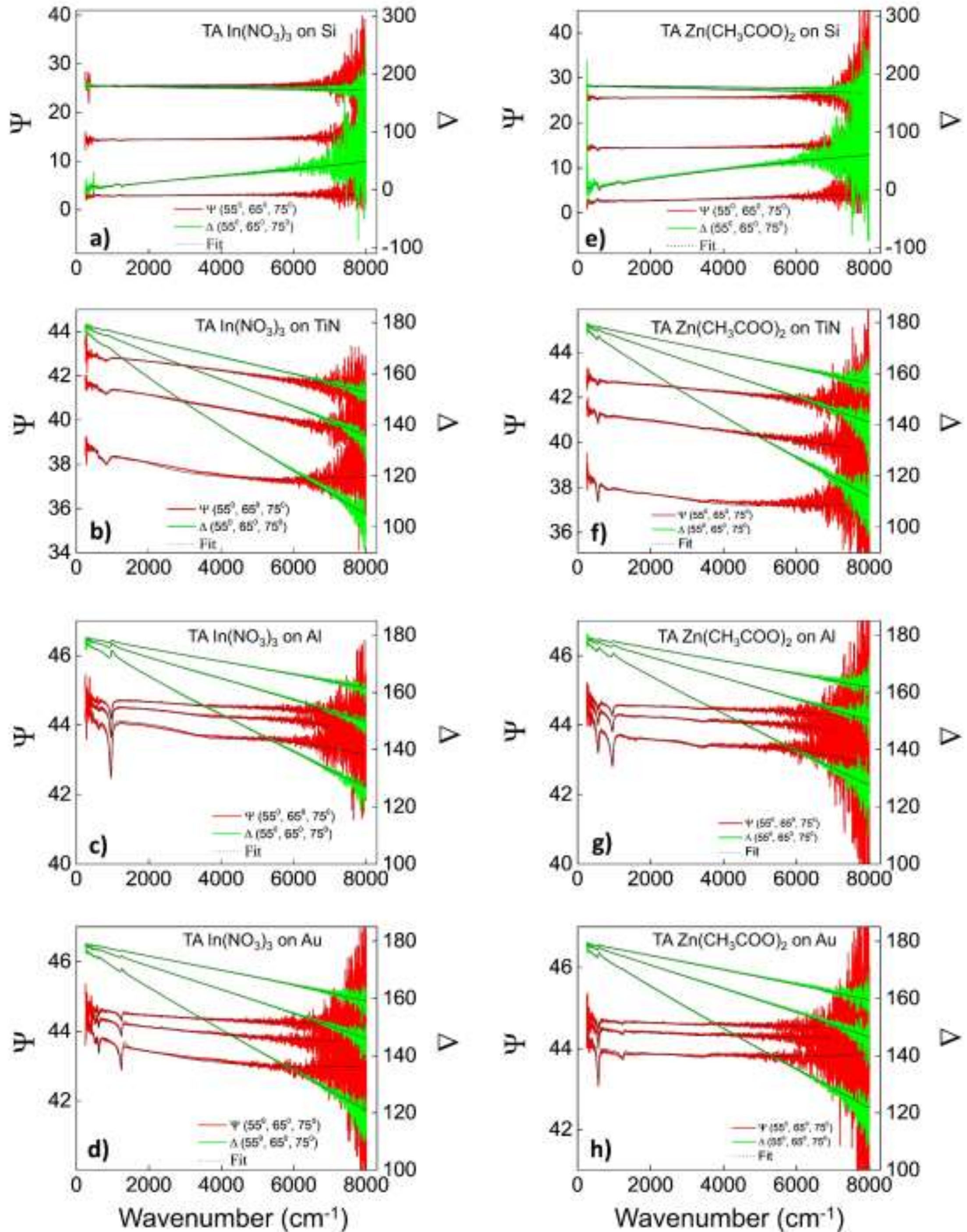

Figure 4-4. Measured Ψ (red lines) and Δ (green lines) for thermally annealed (step 2: $300\,°\mathrm{C}$, 60 min) $\mathrm{In(NO_3)_3}$ thin films on top of (a) Si, (b) TiN, (c) Al and (d) Au and $\mathrm{Zn(CH_3COO)_2}$ thin films on top of (e) Si, (f) TiN, (g) Al and (h) Au. Their fitted values (black solid lines) are also presented, as obtained from the corresponding optical model.

Figure 4-5 shows the imaginary part (ε_2) of complex permittivity for stabilised $In(NO_3)_3$ (see Table 4-1 for the corresponding peaks, interpretations, and References). For $In(NO_3)_3$ on Si, the single feature detected at $469\ cm^{-1}$ in Ψ and Δ (Figure 4-3a) corresponds to a single peak in the absorption spectrum of $In(NO_3)_3$ (Figure 4-5a), assigned to the In-O phonon mode [39,40,225,226].

However, IRSE analysis of stabilised $In(NO_3)_3$ on top of TiN, Al and Au (Figure 4-3b,c and d, respectively) reveals the presence of multiple peaks that are associated to various optical phonon modes found in stabilised $In(NO_3)_3$ (see Figure 4-6b, Figure 4-5c, and Figure 4-5d, respectively). The sharp band at $370 - 550\ cm^{-1}$ is assigned to In-O [39,40,225,226]. followed by the detection of In-OH for $In(NO_3)_3$ at $600 - 100\ cm^{-1}$ (this peak is not apparent for $In(NO_3)_3$ on TiN) [40,225,227].

The presence of NO_3^- is represented by a double peak in the spectral range of $1300 - 1400\ cm^{-1}$ [38–40,147]. which originates from the precursor salt. This peak constitutes a point of debate in literature, with free NO_3^- and $NO_3^- \cdot H_2O$ complexes as their two main interpretations. The double peak at $3100 - 3400\ cm^{-1}$ is assigned to the stretching modes for -OH groups of adsorbed water [39,147,225]. The peak at $\sim 1600\ cm^{-1}$ is attributed to H-O-H bending (H_2O) [39,40]. The presence of H_2O, -OH, as well as NO_3^- ions stand in good agreement with step 1 conditions, since the temperature (150 °C) and atmosphere (ambient conditions) promotes water absorption and limits the NO_3^- ion dissociation.

Table 4-1. ε_2 peaks of stabilised $In(NO_3)_3$ films on top of Au, Al, TiN and Si substrates, along with their corresponding interpretations and references.

No of peak	Stab. $In(NO_3)_3$ on Au (cm^{-1})	Stab. $In(NO_3)_3$ on Al (cm^{-1})	Stab. $In(NO_3)_3$ on TiN (cm^{-1})	Stab. $In(NO_3)_3$ on Si (cm^{-1})	Interpretation	References
1	415	366	371	469	$In-O$	[39,40,225,226]
2	552	423	388	-	$In-O$	[40,225,226]
3	800	685	-	-	$In-OH$	[40,225,227]
4	1008	1032	1024	-	$In-OH$	[40,225,227]
5	1314	1306	1306	-	Free NO_3^-	[38,40,147]
6	1411	1371	1355	-	Free NO_3^-	[38–40,147]
7	1596	1637	1613		$H-O-H$	[39,40]
8	3121	3193	3193		$\nu(O-H)$	[147,225]
9	3419	3452	3443	-	$\nu(O-H)$	[39,147,225]

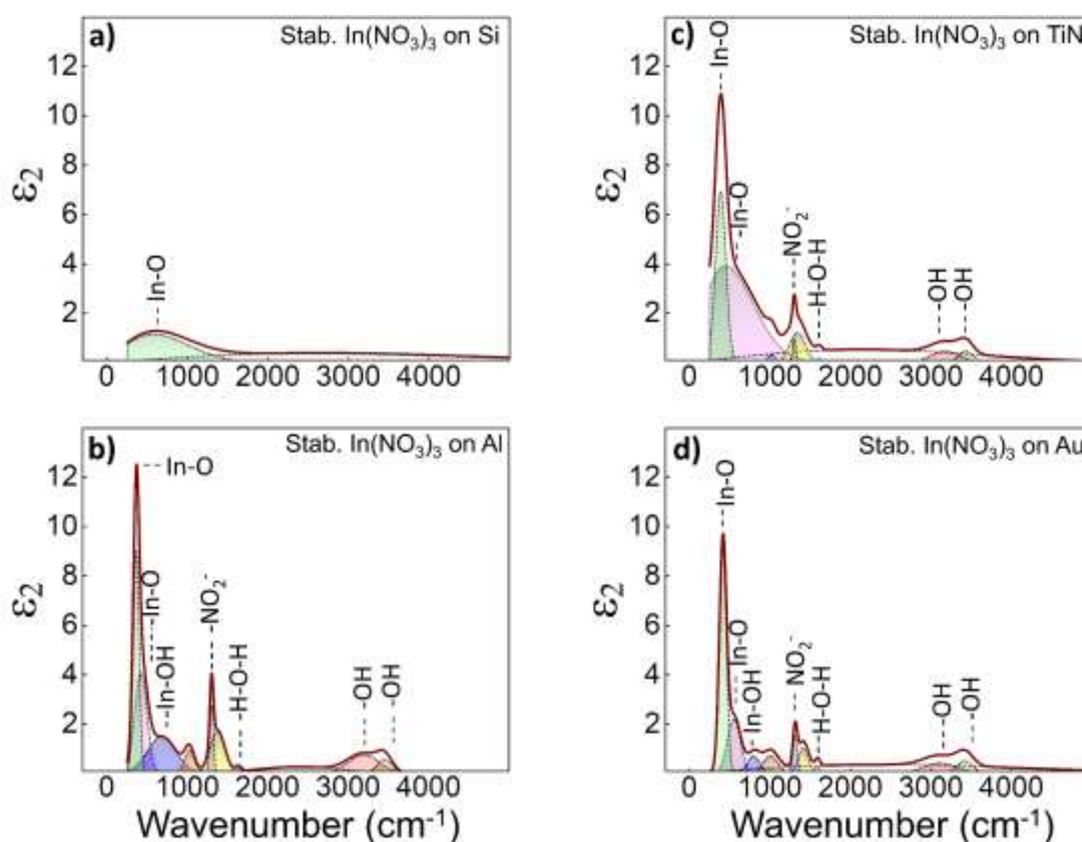

Figure 4-5. Imaginary part of complex permittivity ($\varepsilon_2(\omega)$) for stabilised $In(NO_3)_3$, as extracted from Ψ and Δ fit of $In(NO_3)_3$ films on top of (a) Si, (b) TiN, (c) Al and (d) Au, after step 1 ($150°C, 15\ min$). Each panel presents each peak in colour and is labelled with its interpretation. The peaks corresponding to the same phonon mode in each panel are represented by the same colour. $In-O$ associated peaks are presented in green and magenta, $In-OH$ are shown in blue and orange, NO_3^- in light blue and yellow, $H-O-H$ in cyan and $-OH$ in pink and dark yellow.

Figure 4-6 presents the imaginary part of complex permittivity (ε_2) for stabilised $Zn(CH_3COO)_2$ films, along with their phonon mode interpretations (see Table 4-2 for the corresponding peaks, interpretations, and References) A prominent peak at $\sim 438-483\ cm^{-1}$ (representing $Zn-O$) is apparent in all films [36,228–233]. For $Zn(CH_3COO)_2$ films on Si (Figure 4-6a), no additional absorption peaks are detected. The functional group of $Zn-OH$ ($\sim 760\ cm^{-1}$) also appear for stabilised $Zn(CH_3COO)_2$ films on Al and Au (Figure 4-6c-d) [36,228,230]. This peak is shifted to $838\ cm^{-1}$ for $Zn(CH_3COO)_2$ on TiN. The symmetric stretching vibration of the carboxyl group COO^- (acetate group) is observed at $\sim 1400\ cm^{-1}$(Figure 4-6b-d, inset) [36,228,231–234]. For the stabilised $Zn(CH_3COO)_2$ film on Au, a peak at $1330\ cm^{-1}$ arises due to the deformation of the methyl group (CH_3) Figure 4-6d, inset) [228,232]. However, this phonon mode is not detected within all other stabilised $Zn(CH_3COO)_2$ films. A band at $1596-1613\ cm^{-1}$ resembles the asymmetric vibration of COO^- stretching [36,228,229,234]. Finally, the peak at $\sim 3300\ cm^{-1}$ is assigned to the

stretching modes of $-\mathrm{OH}$ [36,228–230,232,234,235]. This peak was also detected in the stabilised $\mathrm{In(NO_3)_3}$ films.

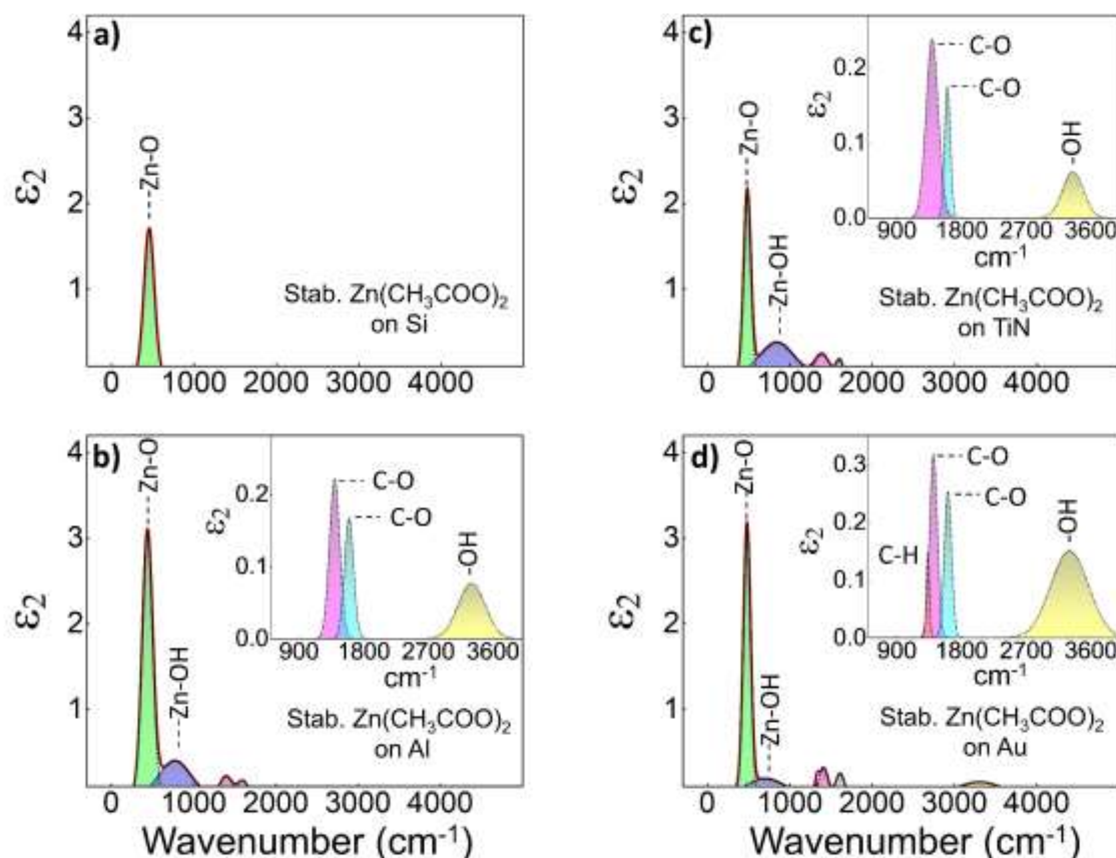

Figure 4-6. Imaginary part of the complex permittivity ($\varepsilon_2(\omega)$) for stabilised $\mathrm{Zn(CH_3COO)_2}$, as extracted from Ψ and Δ fit of of $\mathrm{Zn(CH_3COO)_2}$ films on top of (a) Si, (b) TiN, (c) Al and (d) Au, after step 1 ($150°\mathrm{C}, 15\ \mathrm{min}$). Each panel presents each peak in colour, along with its interpretation. The peaks corresponding to the same phonon mode in each panel are represented by the same colour. The insets show an enhanced view of the absorption peaks in the range of $900 - 4000\ \mathrm{cm^{-1}}$. $\mathrm{Zn-O}$ associated peaks are shown in green, $\mathrm{Zn-OH}$ in blue, $\mathrm{COO^-}$ in magenta and cyan, $-\mathrm{OH}$ in yellow and $\mathrm{C-H}$ in organge (only in $\mathrm{Zn(CH_3COO)_2}$ on Au).

Table 4-2. ε_2 peaks of stabilised $\mathrm{Zn(CH_3COO)_2}$ films on top of Au, Al, TiN and Si substrates, along with their corresponding interpretations and references.

Stab. $\mathrm{Zn(CH_3COO)_2}$ on Au ($\mathrm{cm^{-1}}$)	Stab. $\mathrm{Zn(CH_3COO)_2}$ on Al ($\mathrm{cm^{-1}}$)	Stab. $\mathrm{Zn(CH_3COO)_2}$ on TiN ($\mathrm{cm^{-1}}$)	Stab. $\mathrm{Zn(CH_3COO)_2}$ on Si ($\mathrm{cm^{-1}}$)	Interpretation	References
479	438	483	467	$\nu(\mathrm{Zn-O})$	[36,228–233]
701	772	838	-	$\mathrm{Zn-OH}$	[36,228,230]
1330	-	-	-	$\mathrm{C-H}$	[228,232]
1411	1395	1387	-	$\mathrm{COO^-}$	[36,228,231–234]
1613	1596	1605	-	$\mathrm{COO^-}$	[36,228,229,234]
3298	3298	3347	-	$\nu(\mathrm{O-H})$	[36,228–230,232,234,235]

Figure 4-7 presents the ε_2 values as extracted from the analysis of thermally annealed (300 °C) $In(NO_3)_3$ films (see Table 4-3 for the corresponding peaks, interpretations, and References). The peak corresponding to $In-O$ vibration modes ($315-430\ cm^{-1}$) remains the most dominant, with concurrent presence of $In-OH$ ($550-1000\ cm^{-1}$). Also, no characteristic peaks related to NO_3^-, $-OH$ or H_2O are present, thus addressing the annealing effect on stabilised $In(NO_3)_3$ thin films. These results confirm the dissociation of precursor-related by-products (H_2O, NO_3^-) *via* thermal annealing (300 °C, 60 min), thus enabling us to monitor the conversion of $In(NO_3)_3$ into In_2O_3.

Figure 4-8 displays the ε_2 values as extracted from the analysis of thermally annealed (300 °C) $Zn(CH_3COO)_2$ (see Table 4-4 for the corresponding peaks, interpretations, and References). For $Zn(CH_3COO)_2$ on Si, a single absorption peak corresponding to Zn-O is apparent. In contrast, a plethora of absorption peaks associated to $Zn(CH_3COO)_2$ are shown in Figure 4-8b-d, presenting various similarities to the stabilised $Zn(CH_3COO)_2$ films.

Table 4-3. ε_2 peaks of thermally annealed (300 °C) $In(NO_3)_3$ films on top of Au, Al, TiN and Si substrates, along with their corresponding interpretations and references.

TA $In(NO_3)_3$ on Au (cm^{-1})	TA $In(NO_3)_3$ on Al (cm^{-1})	TA $In(NO_3)_3$ on TiN (cm^{-1})	TA $In(NO_3)_3$ on Si (cm^{-1})	Interpretation	References
301	412	338	461	$In-O$	[39,40,225,226]
338	552	490	-	$In-O$	[40,225,226]
589	823	685	-	$In-OH$	[225,227]
975	911	1040	-	$In-OH$	[225,227]

In detail, the peaks attributed to carboxyl group stretching COO^- (~ $1400-1600\ cm^{-1}$)[36,228,231–234] and -OH stretching (~$3300\ cm^{-1}$) have been detected within the thermally annealed $Zn(CH_3COO)_2$ films (Figure 4-8b-d, inset). For the carboxyl groups in particular, their persistent presence after this thermal step (300°C) has been previously reported [236], where acetate groups bonded to Zn-O were detected after heating at 350 °C. Zn-O and Zn-OH bands have once more been detected at $\sim 410\ cm^{-1}$ and $\sim 780\ cm^{-1}$ [36,228–233], similarly to the stabilised films. The position of the phonon peaks in the thermally annealed $Zn(CH_3COO)_2$ films (step 2) are in excellent agreement with the corresponding peaks in stabilised films (Figure 4-6b-d). In addition, the height of the residual-related absorption peaks (*i.e.,* C-O, H-O-H, -OH) is weakened in step 2, with Zn-O peaks exhibiting an opposite behaviour. This indicates a promoted conversion of $Zn(CH_3COO)_2$ into ZnO during step 2.

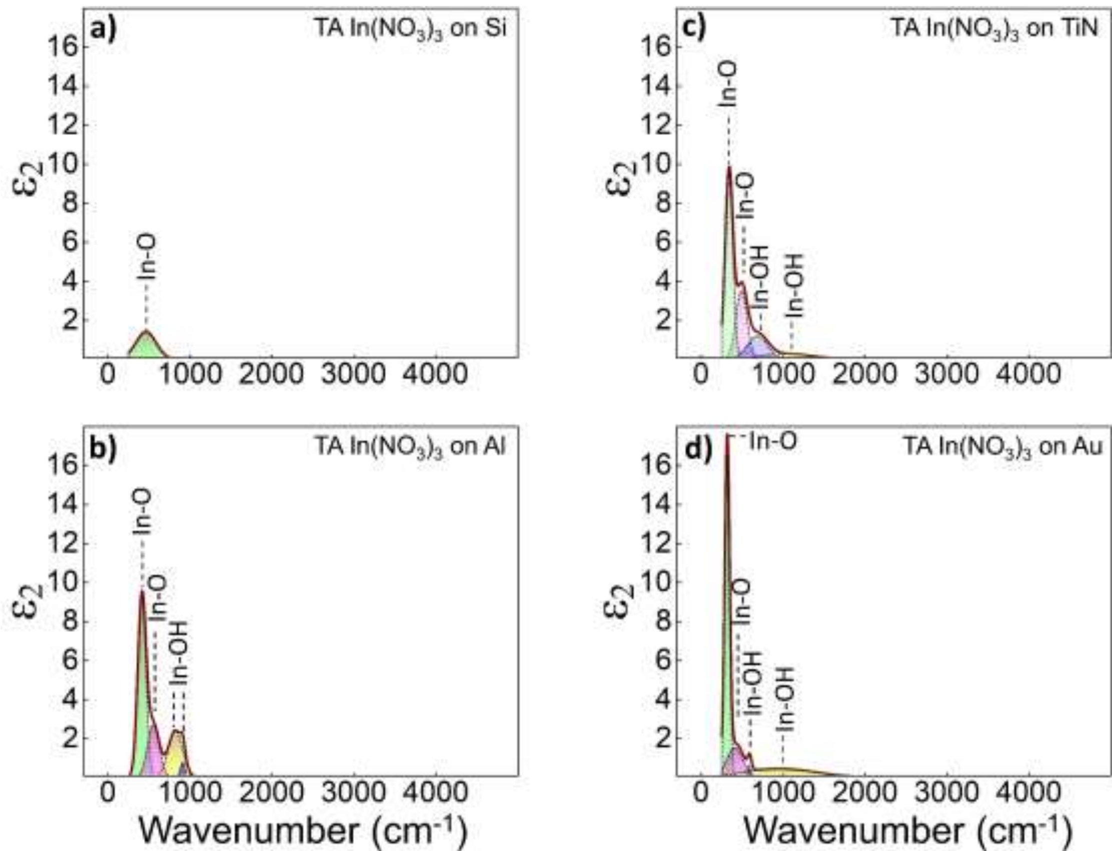

Figure 4-7. Imaginary part of the complex permittivity ($\varepsilon_2(\omega)$) for thermally annealed $\mathrm{In(NO_3)_3}$, as extracted from Ψ and Δ fit of of $\mathrm{In(NO_3)_3}$ films on top of (a) Si, (b) Al, (c) TiN and (d) Au, after step 2 ($300℃, 60\ \mathrm{min}$). Each panel presents each peak in colour, along with its interpretation. The peaks corresponding to the same phonon mode in each panel are represented by the same colour. $\mathrm{In-O}$ associated peaks are presented in green and magenta, while $\mathrm{In-OH}$ is shown in blue and yellow.

In addition to the Gaussian oscillators, a Drude-Smith oscillator was used to model the free-carrier contribution to the complex permittivity of the thermally annealed $\mathrm{Zn(CH_3COO)_2}$ [220]. The Drude-Smith model takes into account carrier localisation through enhanced carrier backscattering and has been reported as an excellent model to describe photoconductivity in ZnO based nanowires/nanoparticles/thin films [217].

The contribution of Drude-Smith oscillator is displayed in Figure 4-8b-d with the light pink colour. Values of the carrier concentration for thermally annealed $\mathrm{Zn(CH_3COO)_2}$ were extracted from the Drude-Smith oscillator. These values ranged between $2.83 - 3.27 \times 10^{18}$ $\mathrm{cm^{-3}}$ and are in agreement with previous reported studies of thermally annealed $\mathrm{Zn(CH_3COO)_2}$ films [217]. A parameter associated with the "strength" of carrier backscattering, namely c, is also determined, with values ranging from -0.8858 to -0.8679. For values of c close to zero, a Drude model is restored, whereas the negative values of c indicate strong carrier

backscattering and clearly non-Drude behaviour [216]. As comparison, Baxter *et al.* have reported that $c = -0.84$ for $Zn(CH_3COO)_2$ films thermally annealed at $360\ °C$ for $30\ min$.

Table 4-4. ε_2 peaks of thermally annealed ($300\ °C$) $Zn(CH_3COO)_2$ films on top of Au, Al, TiN and Si substrates, along with their corresponding interpretations and references.

TA $Zn(CH_3COO)_2$ on Au (cm^{-1})	**TA $Zn(CH_3COO)_2$ on Al (cm^{-1})**	**TA $Zn(CH_3COO)_2$ on TiN (cm^{-1})**	**TA $Zn(CH_3COO)_2$ on Si (cm^{-1})**	**Interpretation**	**References**
412	406	414	492	$\nu(Zn-O)$	[36,228–233]
959	806	762	-	$Zn-OH$	[36,228,230]
1379	1395	1395	-	COO^-	[36,228,231–234]
1548	1572	1572	-	COO^-	[36,228,231–234]
3169	3306	3363	-	$\nu(O-H)$	[36,228–230,232,234,235]

A comparison amongst ε_2 values of thermally annealed $In(NO_3)_3$ and $Zn(CH_3COO)_2$ (step 2, **Figure 4-7** & **Figure 4-8**), reveals a noteworthy differentiation in the temperature effect ($300°C$) between the two precursors. For thermally annealed $In(NO_3)_3$, the removal of all by-products is apparent, as no precursor-associated peaks are detected (**Figure 4-7**). However, for $Zn(CH_3COO)_2$ the thermal treatment at this temperature does not lead to a similar result, since the majority of precursor-related peaks found in the stabilised film (**Figure 4-8**) are also detected after step 2 (**Figure 4-8**). Thus, an additional thermal treatment (step 3) was applied for the $In(NO_3)_3$ and $Zn(CH_3COO)_2$ films (following step 2) annealed at 450°C for 1 hour. However, Al was the only viable substrate to be used in this step, as this temperature led to deformations in Au (melting) and TiN (oxidation). Si was also excluded, as the principal purpose of this final treatment was to focus on the detection of precursor-related by-products.

For the $Zn(CH_3COO)_2$ films on top of Al (**Figure 4-9a**, **Table 4-5**), step 3 (450°C) led to the removal of peaks corresponding to the precursor by-products, such as carboxyl (COO^-) and hydroxyl ($-OH$) groups. A sharp peak, located at $\sim 400\ cm^{-1}$, was detected instead and is associated with the $Zn-O$ mode. Also, a Drude-Smith model represented the screened free electrons, similarly to step 2 of $Zn(CH_3COO)_2$. A carrier concentration of $2.63 \times 10^{18} cm^{-1}$ was extracted, along with a c value of $c = -0.78$. A decrease in c (with respect to step 2) manifests the promoted elimination of organic residuals, which are associated to backscattering mechanisms.

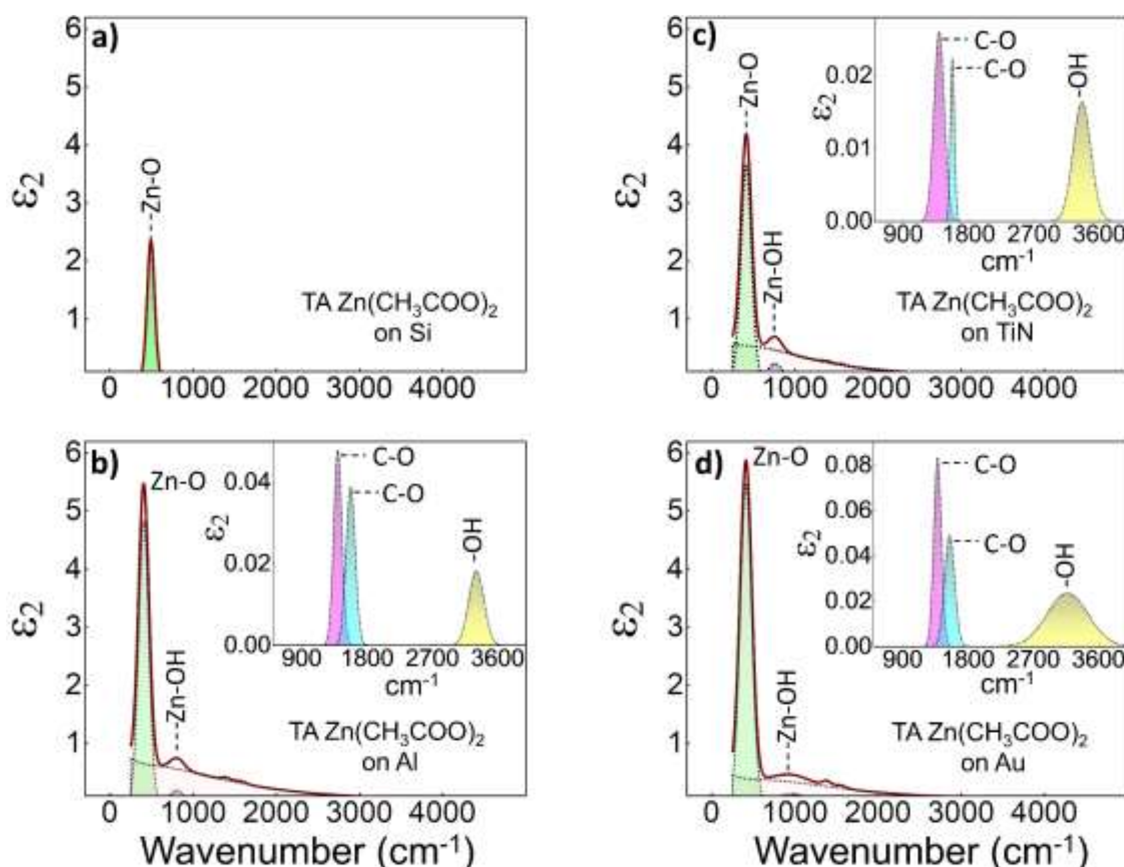

Figure 4-8. Imaginary part of the complex permittivity ($\varepsilon_2(\omega)$) for thermally annealed $\mathrm{Zn(CH_3COO)_2}$, as extracted from Ψ and Δ fit of of $\mathrm{Zn(CH_3COO)_2}$ films on top of (a) Si, (b) Al, (c) TiN and (d) Au, after step 2 ($300°\mathrm{C}, 60\ \mathrm{min}$). Each panel presents each peak in colour, along with its interpretation. The peaks corresponding to the same phonon mode in each panel are represented by the same colour. The insets show an enhanced view of the absorption peaks in the range of $900 - 4000\ \mathrm{cm^{-1}}$. $\mathrm{Zn-O}$ associated peaks are shown in green, $\mathrm{Zn-OH}$ in blue, $\mathrm{COO^-}$ in magenta and cyan and $\mathrm{-OH}$ in yellow. The contribution of Drude-Smith oscillator in ($\varepsilon_2(\omega)$ is presented in light pink.

Table 4-5. ε_2 peaks of thermally annealed ($450\ °\mathrm{C}$) $\mathrm{In(NO_3)_3}$ and $\mathrm{Zn(CH_3COO)_2}$ films on top of Al substrates, along with their corresponding interpretations and references.

TA $\mathrm{In(NO_3)_3}$ on Al (cm^{-1})	Interp.	References	TA $\mathrm{Zn(CH_3COO)_2}$ on Al (cm^{-1})	Interp.	References
392	In-O	[39,40,225,226]	397	Zn-O	[36,228–233]
473					

For step 3 of $\mathrm{In(NO_3)_3}$ films on top of Al (**Figure 4-9b**, **Table 4-5**), the thermal treatment at 450°C led to the elimination of $\mathrm{In-OH}$ related peaks, thus indicating the formation of pure $\mathrm{In_2O_3}$. The absorption peaks of $\mathrm{Zn(CH_3COO)_2}$ per thermal annealing step, manifest the formation of ZnO. In step 1 (stabilisation at $150°\mathrm{C}$,shown in **Figure 4-6**), the initiation of $\mathrm{Zn-O(-H)}$ bonds formation is detected, along with limited dissociation of carbonyl groups. However, above $150\,°\mathrm{C}$ (step 2, thermal annealing at $300\,°\mathrm{C}$), the removal of $\mathrm{-OH}$ groups (dihydroxylation) initiates (decrease in $\mathrm{-OH}$ associated peak intensity, **Figure 4-8**), further

promoting ZnO formation. The remaining acetate anions (CH_3COO^-) are attracted to the basic nature of ZnO (acid-base pair), thus forming $ZnO - CH_3COO^-$ chains, which are further removed *via* ketonization ($250°C - 350°C$) [236,237]. This reaction involves the formation of acetone and CO_2, thus explaining the detected bands at ($\sim 1570\ cm^{-1}$ and ($\sim 1390\ cm^{-1}$). Further treatment above these temperatures (step 3, thermal annealing at $450°C$) removes remnant organic by-products, completing the formation of ZnO.

The absorption profiles of $In(NO_3)_3$ and $Zn(CH_3COO)_2$ shown in **Figure 4-9**) manifest the discrepancy amongst nitrate and acetate-based salts, as acetate precursors demand higher temperature treatments to convert. The analysis above has revealed a "substrate-dependent" detection of $In(NO_3)_3$ and $Zn(CH_3COO)_2$ vibrational modes. This signal-to-noise-ratio variation has been correlated to the substrate's reflectivity by Tompkins *et al.* [224], where the spectral features of organic thin films were studied with IRSE. According to Tompkins *et al.*, an improvement in the detection of spectral features is achieved, when highly conductive substrates (in their case Au) are used.

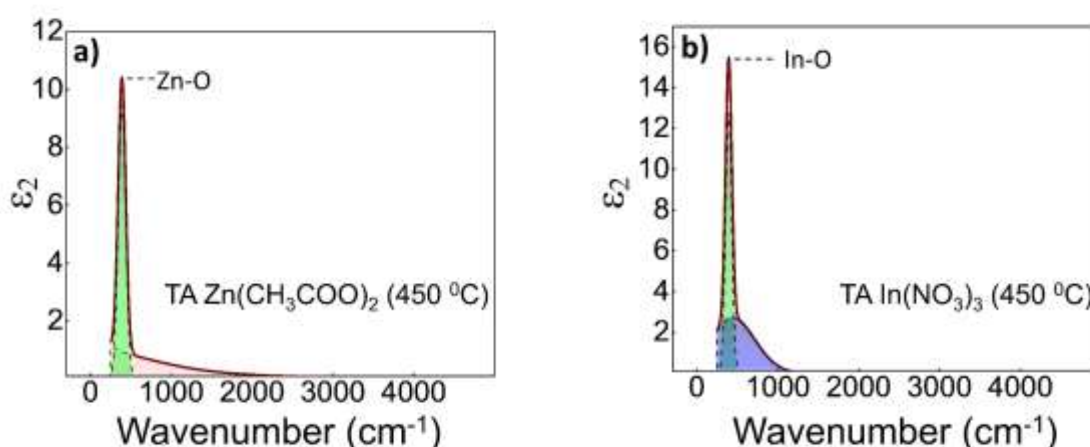

Figure 4-9. Imaginary part of the complex permittivity, $\varepsilon_2(\omega)$, for thermally annealed ($450\ °C$, step 3) (a) $Zn(CH_3COO)_2$ and (b) $In(NO_3)_3$ films on Al. The panels present each peak labelled with its interpretation. For thermally annealed $Zn(CH_3COO)_2$, a $Zn - O$ associated peak is shown in green while the contribution of Drude-Smith oscillator in ($\varepsilon_2(\omega)$ is presented in light pink. For thermally annealed $In(NO_3)_3$, $In - O$ absorption is represented by the superposition of two peaks (green and blue).

This comes because of the substrate's increased reflectivity in IR spectral ranges, due to the presence of free carriers. This effect is also apparent in this work, where an enhancement in the detection of $In(NO_3)_3$ and $Zn(CH_3COO)_2$ films' spectral features is obtained on the highly conductive substrates (in contrast to Si). To further investigate the reflectivity effect, we present the reflectivity values of Si, Al, TiN and Au (**Figure 4-10**) as calculated from their corresponding optical constants (extracted by IRSE). In addition to the substrates used in our experiments, a set of widely used substrates (ITO, highly doped Si ($(p/n)Si^{++}$), as well as moderately p-doped

Si (p-Si)) were included, for comparison. **Figure 4-10** shows the reflectivity for a variety of materials (Al in red, Au in orange, and TiN in yellow), compared to Si (light green) for the spectral range of interest. For p-Si (petrol blue), ITO (magenta) and $(\mathrm{p/n})\mathrm{Si}^{++}$ (blue and purple), the reflectivity values present large frequency-dependent changes. In a narrow "spectral window" of low frequencies (up to $800\ \mathrm{cm}^{-1}$), the reflectivity for all substrates (excluding Si) exceeds 70%. However, above this window, a discrepancy between the various substrates arises. For $(\mathrm{p/n})\mathrm{Si}^{++}$ (blue and purple), a sharp decrease is observed in a low frequency threshold ($800\ \mathrm{cm}^{-1}$ for moderately doped $\mathrm{p-Si}$ (petrol blue) and $1300\ \mathrm{cm}^{-1}$ for $(\mathrm{p/n})\mathrm{Si}^{++}$(blue and purple)), with reflectivity values even lower for Si (green). This behaviour extends to a large spectral window, up to $5000\ \mathrm{cm}^{-1}$.

In our study, $\mathrm{In(NO_3)_3}$ and $\mathrm{Zn(CH_3COO)_2}$ spectral features are detected in the range of $300-3400\ \mathrm{cm}^{-1}$. The spectral range where $\mathrm{In(NO_3)_3}$ and $\mathrm{Zn(CH_3COO)_2}$ associated phonon modes are detected is highlighted in light blue and grey (**Figure 4-10**). Within this range, the choice of highly reflective (*i.e.,* conductive) substrates (like Au, Al, and TiN) eliminates any detection issues associated to the abovementioned "spectral window". However, the rapid change in the reflectivity within a small frequency window requires further attention, since it may affect studies that involve the use of commercially favourable substrates, like highly doped Si, as well as ITO. This complexity encourages the introduction of a universal tool for associating the optoelectronic properties of the substrate to the enhancement of IRSE detectivity.

A conductive substrate is not the only strategy for increased reflectivity in the IR spectral range, however. One could take advantage of the Reststrahlen effect in ionic crystals; *e.g.* $\mathrm{SrTiO_3}$ demonstrates flat reflectivity $>90\%$ in the spectral region $160–403\ \mathrm{cm}^{-1}$ and $580–725\ \mathrm{cm}^{-1}$ [222], so it could be ideal for chemical recognition of substances with vibrational modes in this spectral range. Bragg mirrors [238,239] could be another strategy for increased reflectivity with the caveat that they need to be designed at a specific angle of incidence (thus, while in ellipsometry measurements are taken at different angles of incidence in such case they should be captured at one angle). In this work, we focus our attention to substrates that present high reflectivity due to the presence of free carriers. To create a "global map" per the substrate's effect on IRSE sensitivity we employ the mean squared error (MSE) analysis, typically used as a performance indicator for a regression model, described as [240]:

$$\mathrm{MSE_{NCS}} = \sqrt{\frac{1}{3n-m}\sum_{i=1}^{n}\left[\left(\frac{N_{E_i}-N_{G_i}}{.001}\right)^2+\left(\frac{C_{E_i}-C_{G_i}}{.001}\right)^2+\left(\frac{S_{E_i}-S_{G_i}}{.001}\right)^2\right]} \qquad 4.1$$

where "n" is the number of wavelengths, "m" is the number of fit parameters and $\mathrm{N}=\cos(2\Psi)$, $\mathrm{C}=\sin(2\Psi)$, $\mathrm{S}=\sin(2\Psi)\sin(\Delta)$. The "E" subscript defines the experimental values while "G" subscript is for the generated *via* the optical model values. **Eq. 4.1** describes the main

function of MSE, which sums over all the measurement wavelengths the differences between the measured and model generated data.

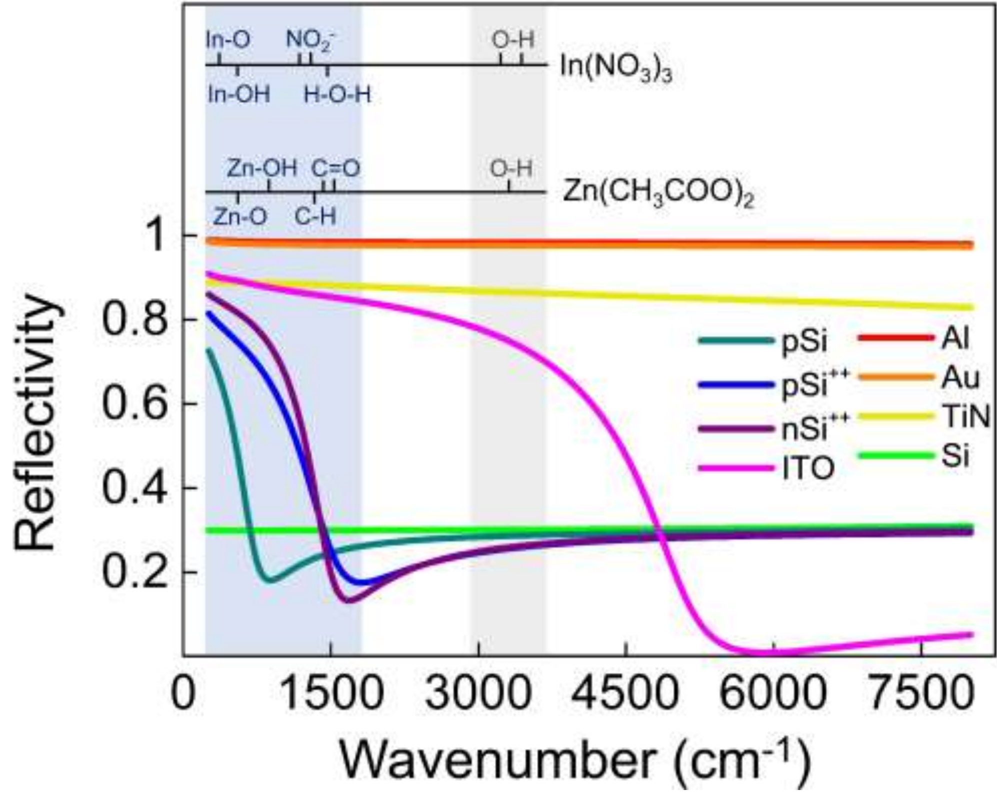

Figure 4-10. IR Reflectivity of Al (red), Au (orange), TiN (yellow), Si (light green), p-Si (petrol blue), (p/n)Si^{++} (blue and purple), as well as ITO (magenta). Light blue and grey shaded regions denote the areas where $In(NO_3)_3$ and $Zn(CH_3COO)_2$ spectral features are detected.

We use this quantification of the effective area between model and measurement to describe the change in Ψ and Δ of substrates, when an ultra-thin ($1\ \mathrm{nm}$) film of $In(NO_3)_3$ is placed on top. Despite the main purpose of fitting, namely the MSE reduction, we are benefiting from **Eq. 4.1** and utilising it in the opposite way: an increased MSE is correlated to higher effective area between the data for the substrate and the data for the thin film on substrate, which implies an enhancement in detection of $In(NO_3)_3$ spectral features. To introduce MSE to our analysis, an optical model describing the substrate's complex permittivity is needed. This model should also allow for the description of substrates that present a wide range of reflectivity values, as presented in **Figure 4-10**. As the reflectivity values in this spectral range are defined by the presence of free carriers, a Drude oscillator was thus chosen, representing free electrons:

$$\varepsilon_{\mathrm{Drude}}(\mathrm{E}) = \frac{-\hbar^2}{\varepsilon_0 \rho_{\mathrm{opt}}(\tau_{\mathrm{opt}} \cdot \mathrm{E}^2 + i\hbar \mathrm{E})} \qquad 4.2$$

where $\hbar$ is Plank's constant, ε_0 is the vacuum permittivity, ρ_{opt} is the optical resistivity, τ_{opt} is the scattering time. In our analysis, the free parameters for this oscillator are ρ_{opt} and τ_{opt}. We then run a set of simulations while variating ρ_{opt} and τ_{opt}, whose "seed" values provide us a

corresponding Ψ and Δ set of values (simulated data). This "scan" of ρ_{opt} and τ_{opt} values enable exploration of a wide spectrum of possible conductive substrates, thus create a phase space where a substrate's optoelectronic properties is correlated to IRSE detection limits.

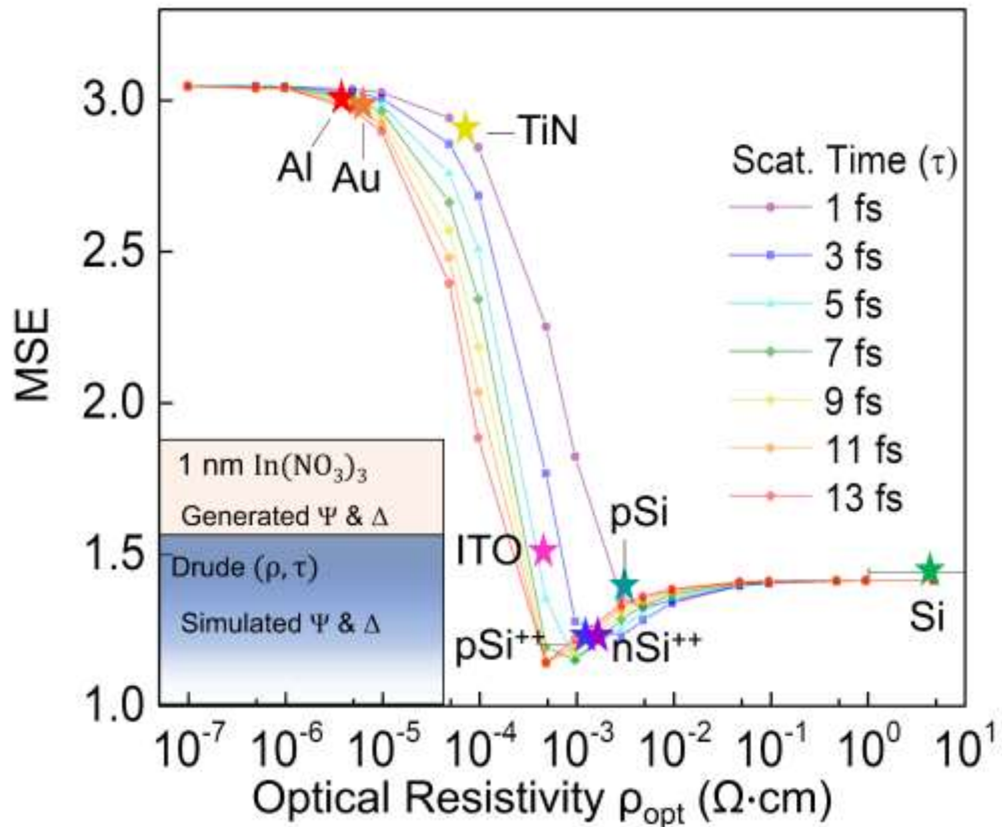

Figure 4-11. MSE of generated optical model of stabilised $\mathrm{In(NO_3)_3}$ on various substrates that are described by a Drude oscillator, with respect to simulated optical resistivity ρ_{opt} and scattering time τ_{opt} (coloured lines) of the substrate. The optical models describing the optical constants of stabilised $\mathrm{In(NO_3)_3}$ is based on our IRSE analysis, presented in **Figure 4-5d**. The stars are representing the ρ_{opt} and τ_{opt} values of various substrates (colours are associated to the corresponding reflectivities of **Figure 4-10**). The opto-geometrical model used for the MSE extraction is also displayed.

For each set of simulated ρ_{opt} and τ_{opt} in our optical model, we then added an ultra-thin layer of $\mathrm{In(NO_3)_3}$ (1 nm), as extracted from the IRSE analysis of our experimental data. Therefore, the generated data represented the Ψ and Δ values of the "sample" ($\mathrm{In(NO_3)_3}$ on top of substrate). The MSE was subsequently extracted, representing the effective area between the simulated data (bare substrate) and generated data ($\mathrm{In(NO_3)_3}$ and $\mathrm{Zn(CH_3COO)_2}$) on top of substrate). **Figure 4-11** presents the MSE versus the substrate's Drude oscillator parameters (optical resistivity and scattering time), with a 1 nm thin film of $\mathrm{In(NO_3)_3}$ on top. The stars represent ρ_{opt} and τ_{opt} for the substrates used in the experimental part of this study (Au, Al, TiN, Si), as well as ITO, moderately ($\mathrm{p-Si}$) and highly doped Si ($\mathrm{(p/n)Si^{++}}$) (see **Table 4-6** for

Drude parameters of each substrate). The metal substrates (Au, Al) chosen for our experimental work are associated to the highest MSE values ($2.973 - 2.987$).

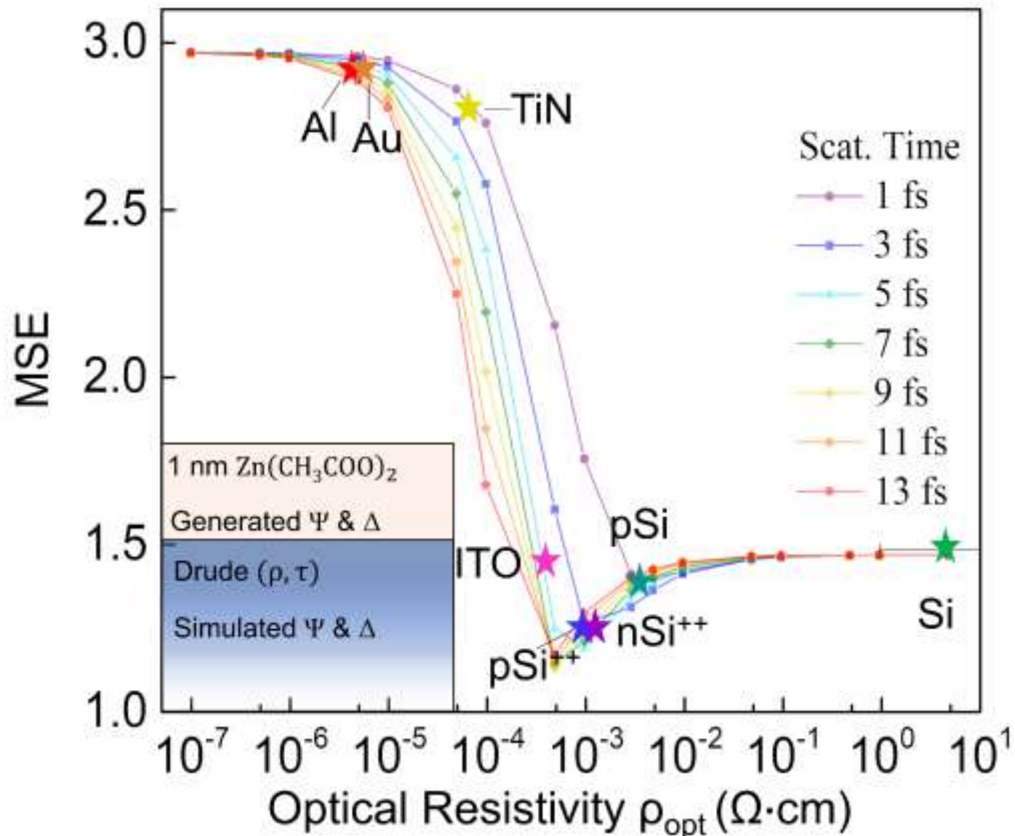

Figure 4-12. MSE of generated optical model of stabilised $Zn(CH_3COO)_2$ on various substrates that are described by a Drude oscillator, with respect to simulated optical resistivity ρ_{opt} and scattering time τ_{opt} (coloured lines) of the substrate. The optical models describing the optical constants of stabilised $Zn(CH_3COO)_2$ is based on our IRSE analysis, presented in Figure 4-8b. The stars are representing the ρ_{opt} and τ_{opt} values of various substrates. The opto-geometrical model used for the MSE extraction is also displayed (bottom left).

This observation agrees with the associated ε_2 results (Figure 4-5), where the detection of the precursor's vibrational modes was most successful. TiN is also associated to increased MSE (2.902). These results confirm the beneficial effect of Al, Au and TiN on phonon mode detection, as compared to Si, where MSE drops significantly (1.404 for $In(NO_3)_3$). However, the increase in resistivity is not monotonically related to MSE. At $\rho_{opt} < 5 \cdot 10^{-6}\ \Omega \cdot cm$, MSE remains constant, regardless of change in τ_{opt}. As resistivity increases, the importance of scattering time is revealed, with a decrease in τ corresponding to increase in the MSE. Interestingly, this trend presents a "dip" region at $\rho_{opt} < 5 \cdot 10^{-3}\ \Omega \cdot cm$ remains constant, regardless of the change in τ_{opt}. As optical resistivity increases, the importance of scattering time is revealed, with a decrease in τ_{opt} corresponding to an increase in MSE. The same concept

was applied to a 1nm $Zn(CH_3COO)_2$ film (Figure 4-12), showing a similar trend in MSE decrease. Highest MSE values are obtained for lowest optical resistivity and scattering times. When $\rho_{opt} > 10^{-6}\ \Omega cm$, the role of τ_{opt} is more visible. At $\rho_{opt} = 5 \cdot 10^{-4}\ \Omega cm$, the lowest MSE values are observed, followed by a slight increase; MSE response remains flat after $\rho_{opt} > 5 \cdot 10^{-2}\ \Omega cm$.

Table 4-6. Resistivity (ρ_{opt}) and scattering time (τ) of substrates used in this work, as extracted from IRSE analysis.

Oscillator Parameters		Al	Au	TiN	ITO	$p-Si$	$p-Si^{++}$	$n-Si^{++}$	Si
Drude	ρ_{opt} (Ωcm)	5.17×10^{-06}	8.85×10^{-06}	7.59×10^{-05}	4.43×10^{-04}	3.64×10^{-03}	1.52×10^{-03}	1.101×10^{-03}	5.00
	τ_{opt} (fs)	5.681	5.893	1.247	9.469	13.829	7.407	11.752	1.00

4.3. IRSE and IRT Simulations

4.3.1. Simulation Process

To investigate the substrate effect on the IRSE and IRT analysis of $In(NO_3)_3$ and $Zn(CH_3COO)_2$ thin films, various sets of simulations were employed. All simulations were based on the setup of an optogeometric model, similarly to the fitting procedure of the IRSE raw datasets. The process flow followed during simulation is shown in Figure 4-13. The simulation process is divided into two parts: the simulated (step 1) and generated (step 2) data.

The optogeometric model in step 1 includes a single layer (Figure 4-13) ,substrate (grey rectangle)) and describes the simulated Ψ and Δ values (or Transmittance for IRT simulations) of a substrate of interest, with the substrate's optical constants comprising the "seed" of the simulation; the optical constants can either be extracted from fitting an IRSE measurement (of the substrate) or described theoretically using oscillators of interest (i.e., a Drude oscillator to describe a conductive substrate). Figure 4-13a displays the simulated Ψ values (red line) representing a conductive substrate (described by a Drude term).

To perform an accurate comparison between simulated and measured Ψ, noise is added as a parameter during simulation. Figure 4-13b shows the change in Ψ where 15% noise is added to the Ψ values shown in Figure 4-13a (a comparison of simulated and measured IRSE data is presented in Figure 4-13b-c). Once the simulated Ψ values (substrate) are obtained, a layer representing the thin film of study is added in the optogeometric model, on top of the substrate (Figure 4-13, yellow rectangle).

To describe the thin film's optical constants, the same protocol as step 1 applies; the optical constants can either be extracted from IRSE analysis or described theoretically (using oscillators of interest). Ψ values representing the optical response of the optogeometric model (thin film on top of substrate) are described as generated data. Figure 4-13c displays the

generated data (black dotted line) of a thin film (described by a Gaussian oscillator) on top of the substrate (Drude, Figure 4-13b). The integrated area between simulated and generated data (blue shaded area in Figure 4-13c) is thus representing the discrepancy in Ψ values between bare substrate and thin film on top of a substrate. This discrepancy is associated to IRSE sensitivity; increased discrepancy leads to a clearer distinction of spectral features corresponding to the thin film.

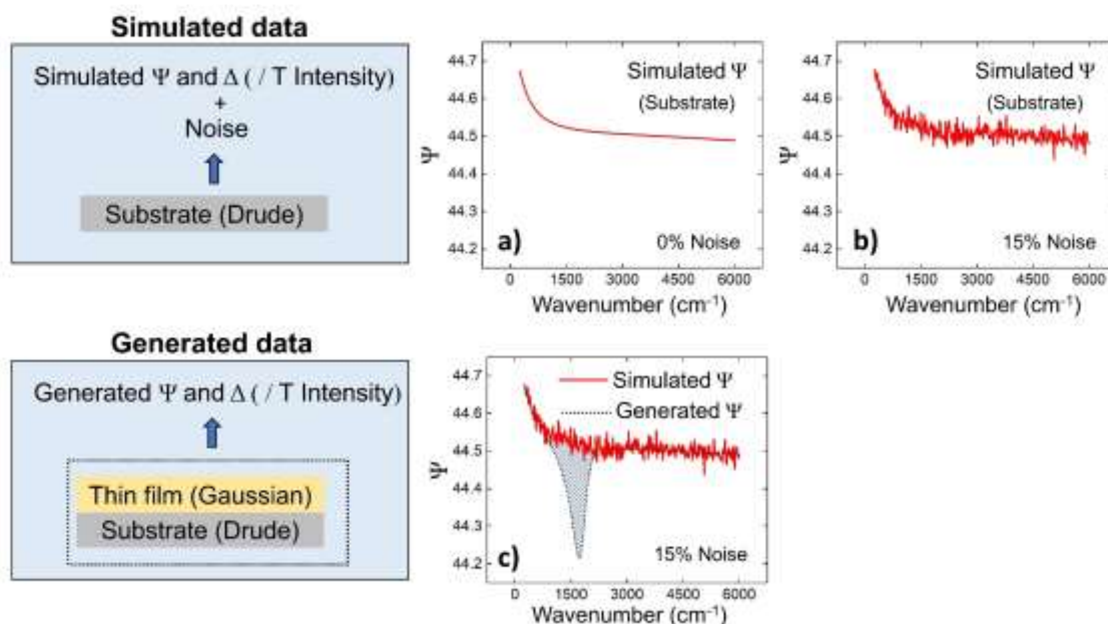

Figure 4-13. Simulation- process flow. The substrate optical constants (extracted experimentally or theoretically) constitute the seed to obtain simulated Ψ values (a), while noise constitutes an additional simulation parameter (b). Generated data (c) include Ψ values describing the optical response of the entire structure of study: thin film (of interest) on top of substrate (simulated data).

4.3.2. IRT Simulations of $Zn(CH_3COO)_2$ and $In(NO_3)_3$ Films

To investigate the thickness effect on the detection of thin film spectral features in Infrared Transmission (IRT) analysis, a set of simulations were performed with $\mathrm{In(NO_3)_3}$ and $\mathrm{Zn(CH_3COO)_2}$ as materials of interest on top of Si. The simulation methodology is analysed in 4.4.1. Noise (15%) was included while simulating Transmittance values of bare Si, aiming to represent the noise levels of a real measurement. The complex permittivity of stabilised $\mathrm{In(NO_3)_3}$ and $\mathrm{Zn(CH_3COO)_2}$ used in this simulation are presented in Figure 4-5a and Figure 4-6a, respectively. Figure 4-14 shows the IRT values of $\mathrm{In(NO_3)_3}$ and $\mathrm{Zn(CH_3COO)_2}$ (various thicknesses, each represented with different colour), on top of Si (black line) at $250 - 8000\ \mathrm{cm^{-1}}$.

Simulated IRT spectra are divided into two spectral regions of interest where absorption peaks are observed (Figure 4-14a and Figure 4-14c for of $\mathrm{In(NO_3)_3}$, Figure 4-14b and Figure

4-14d for $\mathrm{Zn(CH_3COO)_2}$). An increase in thickness of $\mathrm{In(NO_3)_3}$ and $\mathrm{Zn(CH_3COO)_2}$ leads to an improvement in distinction of the associated spectral features. A clear feature corresponding to metal-oxygen bond is apparent in low wavenumbers ($400 - 500\ \mathrm{cm^{-1}}$) for $\mathrm{Zn(CH_3COO)_2}$ (**Figure 4-14a**) and $\mathrm{In(NO_3)_3}$ (**Figure 4-14b**), representing $\mathrm{Zn - O}$ and $\mathrm{In - O}$ bonds, respectively.

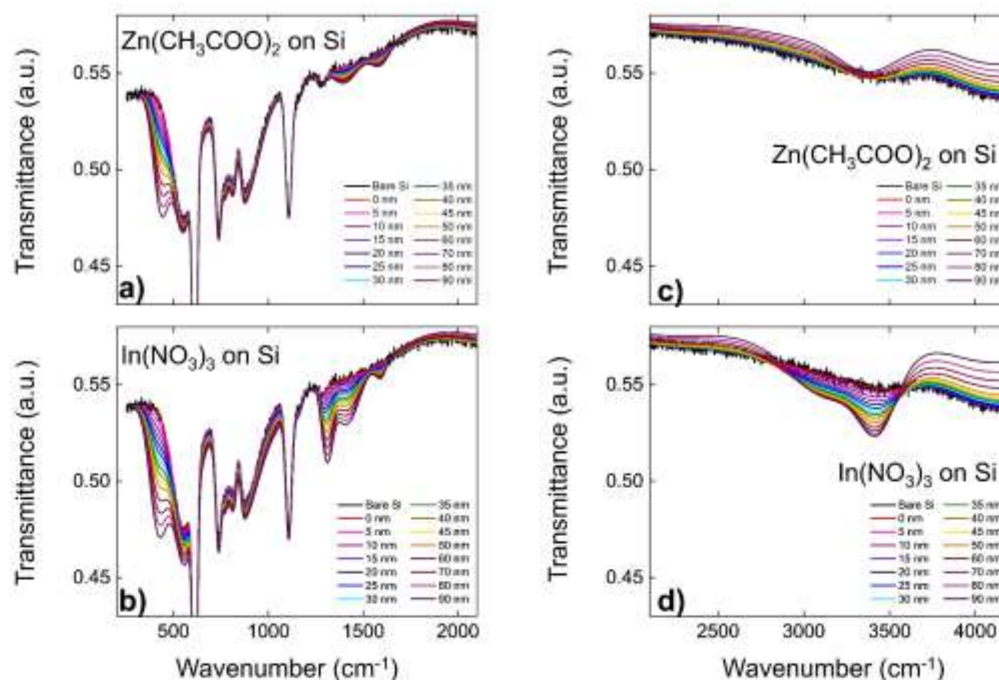

Figure 4-14. Simulated transmittance values of $\mathrm{Zn(CH_3COO)_2}$ (a-c) and $\mathrm{In(NO_3)_3}$ (b-d) on top of Si (substrate). Simulation of Si transmittance includes the addition of 15% noise and is shown in black. Simulated transmitted values of $\mathrm{Zn(CH_3COO)_2}$ and $\mathrm{In(NO_3)_3}$ thin films on top of Si are presented in colour, with thin film thicknesses ranging from 0-90 nm. To perform simulations of $\mathrm{Zn(CH_3COO)_2}$ and $\mathrm{In(NO_3)_3}$ transmittance (on top of Si), optical models of $\mathrm{Zn(CH_3COO)_2}$ on top of Si and $\mathrm{In(NO_3)_3}$ on top of Si were employed. The absorption spectra of $\mathrm{In(NO_3)_3}$ and $\mathrm{Zn(CH_3COO)_2}$used in these models are presented in **Figure 4-5a** and **Figure 4-6a**, respectively.

This result is well expected as the metal-oxygen bonds are represented by the most prominent peaks in the absorption spectra as extracted from IRSE analysis (**Figure 4-5a** and **Figure 4-6a**). For $\mathrm{Zn(CH_3COO)_2}$ (**Figure 4-14a**), the double peak representing C=O ($1400 - 1560\ \mathrm{cm^{-1}}$) is only apparent for thicknesses above $50\ \mathrm{nm}$. For $\mathrm{Zn(CH_3COO)_2}$ thicknesses lower than $50\ \mathrm{nm}$, Si hinders any distinction of spectral features associated to the thin film. For $\mathrm{In(NO_3)_3}$ on Si (**Figure 4-14b**) the double peak representing $\mathrm{NO_2^-}$ absorption ($1300 - 1550\ \mathrm{cm^{-1}}$) is detectable in $\mathrm{In(NO_3)_3}$ thicknesses higher than $30\ \mathrm{nm}$. However, the absorption peak associated to $\mathrm{H_2O}$ (**Figure 4-5b-d**, cyan peak) at $\sim 1600\ \mathrm{cm^{-1}}$ can only be detected for thicknesses above $70\ \mathrm{nm}$ (**Figure 4-14b**). The presence of -OH peaks at ($2800 - 3600\ \mathrm{cm^{-1}}$) is also shown in **Figure 4-14c** and **Figure 4-14d**. In $\mathrm{Zn(CH_3COO)_2}$ (**Figure 4-14c**), the peak is only

detectible in thicknesses over $60\ \mathrm{nm}$, while for $\mathrm{In(NO_3)_3}$ (**Figure 4-14d**) the peak is well distinguished in thicknesses above $15\ \mathrm{nm}$. **Figure 4-14** highlights the challenge in IRT analysis of $\mathrm{In(NO_3)_3}$ and $\mathrm{Zn(CH_3COO)_2}$ ultra-thin films, where a plethora of absorption peaks were not detectable in small thicknesses ($< 30\ \mathrm{nm}$).

4.3.3. Noise in IRSE Measurements

The IRSE measurements presented in **Figure 4-3** and **Figure 4-4** show a disuniformity in noise distribution along the measurement, with signal-to-noise ratio at the edges of the spectrum decreasing significantly. The increased noise originates from the Gaussian-shaped distribution of the IR source presented in **Figure 4-15a**. As the emission intensity of the IR source drops below a certain threshold (blue shaded areas), a sharp noise increase is recorded in the IRSE measurement, as seen in **Figure 4-15b** where measured Ψ and Δ values of stabilised $\mathrm{In(NO_3)_3}$ thin film on top of Au are presented.

Figure 4-15b can be divided into two areas of interest: the blue-shaded regions where the presence of noise maximises and the white region where signal-to-noise ratio is significantly improved. IRSE analysis of $\mathrm{In(NO_3)_3}$ involves the detection of spectral features corresponding to $\mathrm{In-O}$ and $\mathrm{In-OH}$ phonon modes, located in the leftmost blue shaded region. In higher wavenumbers (white area) IR intensity is stronger and the signal-to-noise ratio improves (**Figure 4-15b**), hence the detection of $\mathrm{In(NO_3)_3}$ associated peaks improve significantly.

In wavenumbers above $4000\ \mathrm{cm^{-1}}$ (rightmost, blue-shaded region), the drop in IR emission intensity causes again a signal-to-noise ratio deterioration. For $\mathrm{In(NO_3)_3}$, no spectral features are apparent in this region, therefore the analysis of this work is not affected. However, when IRSE analysis is performed in materials with a different distribution of spectral features across this range, the interference of noise should always be taken into consideration.

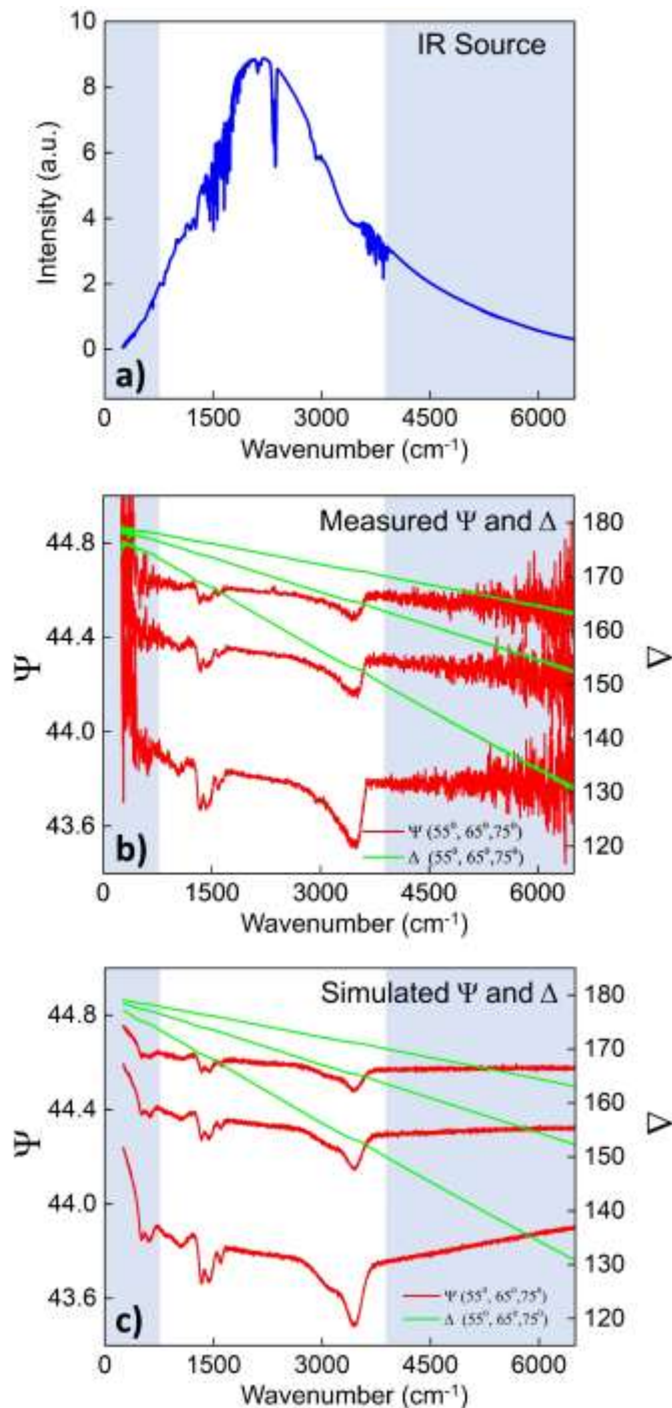

Figure 4-15. (a) Emission intensity of IR source used in IRSE and IRT measurements, (b) measured Ψ and Δ values of stabilised $\mathrm{In(NO_3)_3}$ thin film on top of Au, (c) Simulated Ψ and Δ values of stabilised $\mathrm{In(NO_3)_3}$ thin film on top of Au. Simulations in (c) include the addition of 15% noise. Blue shaded regions in (a), (b) and (c) represent the area where emission intensity drops, thus causing a rapid increase on the noise levels in measured Ψ and Δ.

4.3.4. Noise in Ψ and Δ simulations

A comparison of measured and simulated Ψ and Δ values (**Figure 4-15b** and **Figure 4-16c**) manifests the importance of noise levels in an IRSE measurement. The addition of 15% voice in

simulated Ψ and Δ values of **Figure 4-15c** replicated the noise profile of **Figure 4-15b** to a sufficient extent (in the non-shaded area), however further investigation into the noise effect was deemed necessary. **Figure 4-16** presents the effect noise would have on the detection of spectral features corresponding to 1 nm film of stabilised $\mathrm{In(NO_3)_3}$ on top of Au. Red and green lines represent Ψ and Δ values of simulated bare substrate (Au), while black line shows the generated data of 1 nm film of $\mathrm{In(NO_3)_3}$ on top of Au. The simulation process is analysed in 4.4.1. For 0% and 20% noise (**Figure 4-16a** and **Figure 4-16b**), the spectral features associated to $\mathrm{In(NO_3)_3}$ are distinct. However, for noise above 40%, the signal-to-noise ratio is gradually decreasing, with 120% noise (**Figure 4-16g**) constituting the limit of discrepancy amongst generated ($\mathrm{In(NO_3)_3}$ on Au substrate) and simulated (bare Au) data. This highlights the challenge introduced by increased noise at the edges of the IRSE measurement when the materials of study present features to be fitted in areas with increased noise.

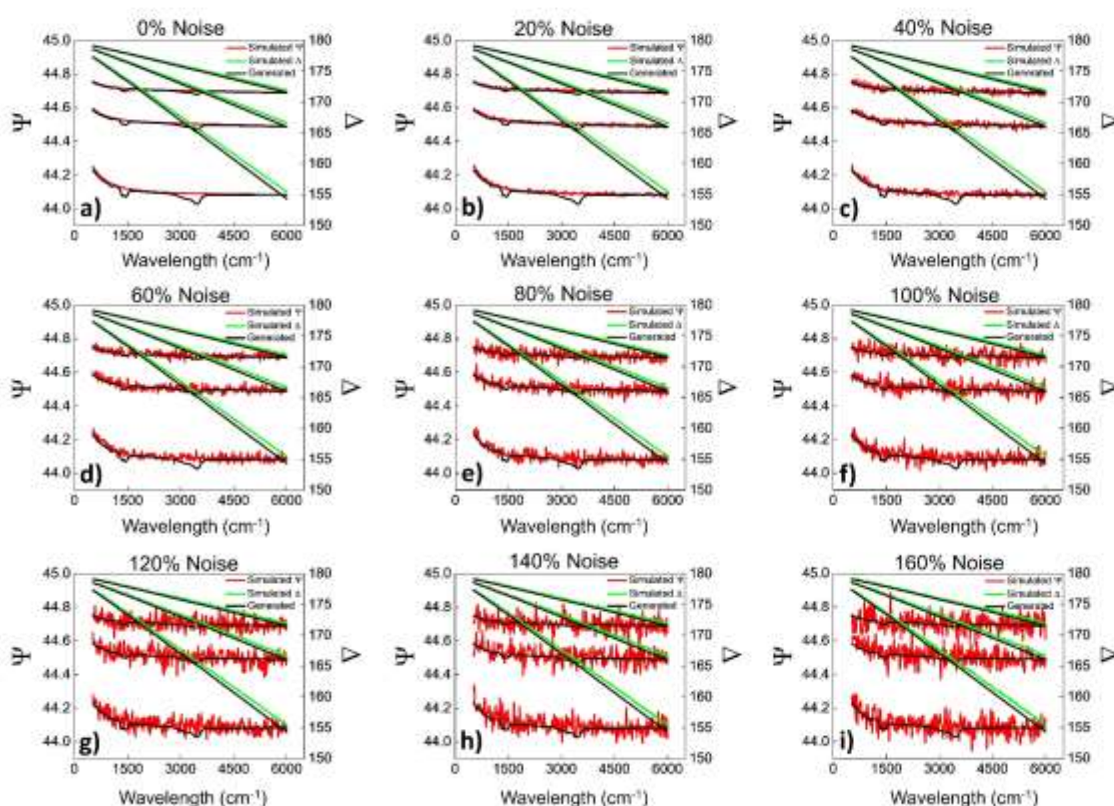

Figure 4-16. Simulated Ψ (red) and Δ (green) values of Au substrate, with noise levels ranging from 0 to 160%. Ψ and Δ values of 1 nm film of stabilised $\mathrm{In(NO_3)_3}$ on top of Au (generated data) are also presented in each panel, for comparison to bare Au. At low noise levels, the generated (black) data present a clear distinction from simulated values of Au, while at increased noise levels the distinction between generated data ($\mathrm{In(NO_3)_3}$ on Au) and simulated (bare Au) is increasingly difficult or even unattainable.

4.4. Concluding Remarks

IRSE analysis of $In(NO_3)_3$ and $Zn(CH_3COO)_2$ films on top of Au, Al and TiN substrates demonstrated a successful monitoring of the corresponding metal oxide formation, *via* various thermal annealing steps. For $In(NO_3)_3$, thermal treatment at 3 annealing steps revealed the precursor conversion into In_2O_3, *via* the gradual removal of temperature related by-products (NO_3^-, $-OH$, H_2O). Decomposition of any nitrate-related optical phonon modes was detected *via* IRSE after step 2 (300°C), with the precursor's complete conversion observed following thermal treatment at $450°C$. For the $Zn(CH_3COO)_2$ films, IRSE revealed the demand of higher temperatures into achieving conversion into ZnO, as acetate-related products were detected after step 2. This result stands in excellent agreement with acetate dissociation temperature ($250 - 350°C$), thus supporting our analysis. Finally, thermal treatment at $450°C$ led to detection of exclusively $Zn - O$ optical phonon modes. To the best of our knowledge, this is the first attempt of an implementation of IRSE into the analysis of ultra-thin sol gel precursor films.

Despite the existing knowledge in precursor dissociation process (based on the type of salt used *e.g.* nitrates, acetates, perchlorates, *etc.* [38,147]) the corresponding findings from the perspective of IR Ellipsometry constitute a significant addition in the field of sol-gel technologies, as a novel, non-invasive and highly sensitive technique as IRSE can deconvolute the metal oxide formation mechanism.

A key aspect to such extended analysis of the precursor conversion delivered, was the choice of substrate. In this study, Au, Al, TiN and Si substrates were employed, with the latter having a poor effect into the collection of precursor information *via* IRSE. On the contrary, Au, Al and TiN delivered excellent results, by enabling a detection enhancement of the spectral features corresponding to the precursor films on top. This effect on IRSE "sensitivity" improvement was attributed to high reflectivity of Au, Al and TiN ($> 85\%$) in the IR spectral range, due to free electron contribution in the IR absorption. Mean squared error (MSE) analysis was then employed into creating a versatile tool of linking this effect to a substrate's conductivity. Interestingly, MSE – thus IRSE sensitivity- drops monotonically with a substrate's resistivity, however this pattern is inverted in higher resistivities, finally reaching a plateau at $\rho_{opt} > 0.05\,\Omega \cdot cm$.

A successful mapping of precursor conversion *via* IRSE combined with a tool to optimise IRSE sensitivity constitute the key points of this study. Implementation of IRSE in sol-gel technologies can directly contribute to the optimisation of thermally assisted processes, such as fabrication of electronics based on ultra-thin sol-gel films. The detection of optimum temperature processing windows for precursor conversion can be achieved by IRSE analysis (as

conducted in this study for $In(NO_3)_3$ and $Zn(CH_3COO)_2$), thus overpassing the destructive and expensive characterisation techniques used so far (*e.g.,* XPS). In addition, the versatility of Ellipsometry as an optical characterisation tool elevates the importance of this study, considering the potential of employing ellipsometry tools in production lines of electronics. Moreover, as the new generation of nanoelectronics deviates from the use of Si substrate and leans towards alternative electrode materials (ITO, Ag, Al) [241,242], the use of such conductive substrates will ease the implementation of IRSE into the field of electronics fabrication. Importantly, the introduction of MSE use as an indication tool of Ellipsometric "sensitivity" can directly improve the efficiency of this characterisation tool *via* indicating its optimum use (pairing of material-substrate).

5. Laser Annealed Sol-Gel Thin Film Transistors

This chapter focuses on one of the principal research objectives of this dissertation, presenting the analysis in electrical performance of Thin Film Transistors (TFTs), based on Laser Annealed sol-gel metal oxide thin films. TFT devices are fabricated in BGTC structure [243], with thermally grown $\mathrm{SiO_2}$ in the role of gate dielectric on top of $\mathrm{n-Si}$ $(1-20\ \Omega\cdot\mathrm{cm})$. For the semiconductor, metal oxide precursor solutions are deposited on top of $\mathrm{SiO_2}$ *via* spin coating. A summary of solution fabrication as well as spin coating deposition conditions can be found in Chapter 3. The precursor conversion is realised *via* Laser Annealing, thus forming the semiconducting layer. Indium oxide ($\mathrm{In_2O_3}$) constitutes the principal material of study in this chapter, followed by IGZO and ZnO as alternative semiconductor materials of interest. To complete device fabrication, thermally evaporated Al was employed as an electrode material (Gate (G) and Source-Drain (S-D)). For top electrodes (S-D), a patterning contact mask was employed (TFT channel width W=1500 μm and length L=250 μm), aiming to form the TFT channel. Further detail on the electrode deposition and TFT geometrical features can be found in Chapters 2 and 3. Figure 5-1 displays a schematic view of a sol-gel LA $\mathrm{In_2O_3}$ TFT device (along with the corresponding microscope image), showing the source-drain pattern obtained from the contact mask used in this work.

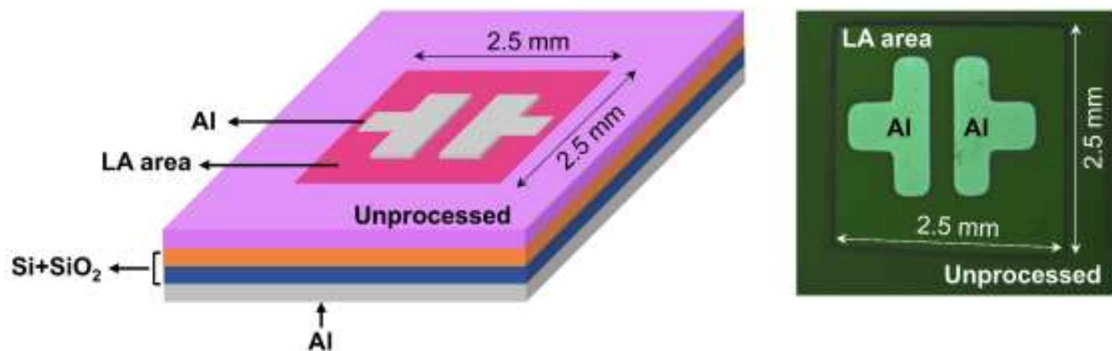

Figure 5-1. 3D structure and optical microscopy image of TFT device geometry.

The electrical characteristics of devices is analysed to great extent, aiming to correlate the Laser Annealing effect to device performance. Focus is paid on a set of TFT performance parameters, in correlation to Laser Annealing conditions, thin film thicknesses and performance degradation. A detailed description of the TFT electrical characterisation process followed in this work is discussed in Chapter 2. Transfer characteristics obtained at low $\mathrm{V_{DS}}$ are performed (linear region), where field effect mobility μ_{FE}, $\mathrm{V_{ON}}$ and $\mathrm{I_{ON/OFF}}$ are derived. An investigation on μ_{FE} dependence of $\mathrm{V_{GS}}$ is also performed, aiming to highlight the discrepancies in TFT channel formation mechanisms amongst various materials and conditions. Output

characteristics are also presented in order to conduct a qualitative evaluation of the device performance, as well as propose potential applications. All devices were characterised under the same protocol (voltage range, number of measurements *etc.*), unless stated otherwise. A comparison amongst the electrical performance of TFTs based on In_2O_3, IGZO and ZnO semiconductor films is also performed (accompanied by surface morphology analysis (AFM)), aiming to identify the structural and compositional difference amongst semiconductor materials through the scope of a TFT device. A conclusion highlighting the principal findings of this work is displayed at the end of the chapter.

5.1. Materials of Interest and Reference Devices

To verify the integrity of the process flow used for TFT fabrication, reference devices based on thermally annealed sol-gel semiconductors were initially fabricated, with In_2O_3, IGZO and ZnO as materials of interest. $n-Si$ with thermally grown $200\ nm\ SiO_2$ were employed as a substrate and device dielectric respectively, while deposition parameters were kept similar to the rest of this work. After deposition of precursor solution (spin coating), films were thermally annealed ($300\ ^\circ C, 60$ min) to promote precursor conversion into metal oxide. Following the completion of TFT fabrication, devices based on sol-gel In_2O_3, IGZO and ZnO were electrically characterised, with transfer and output plots presented in **Figure 5-2**:

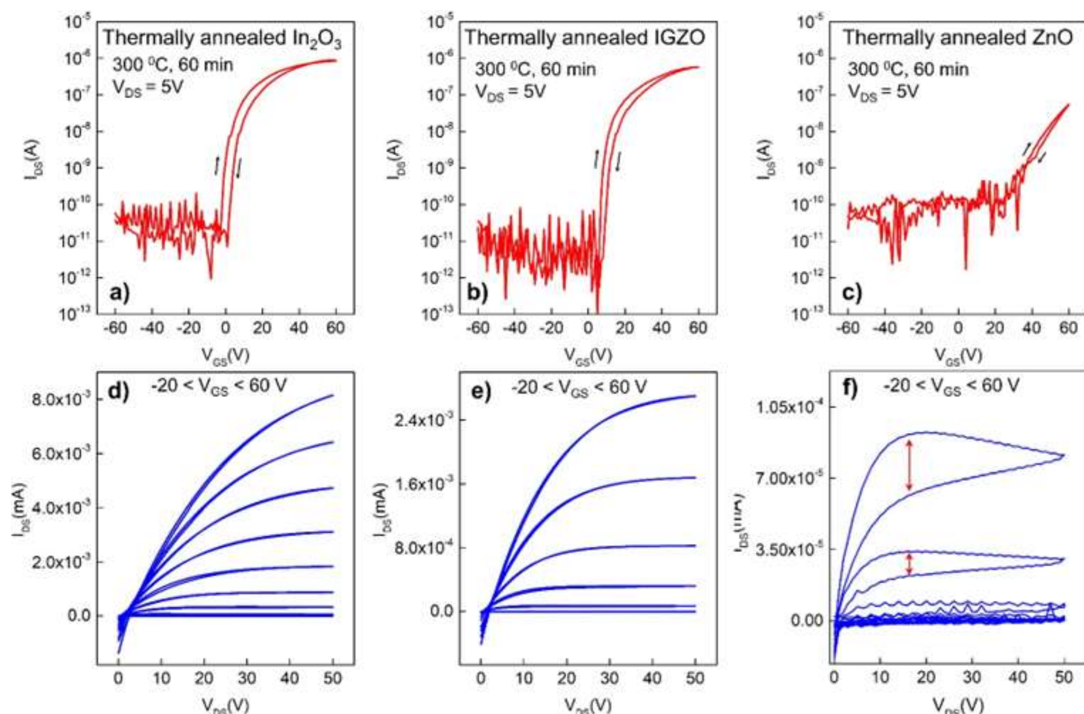

Figure 5-2. Transfer (red) and output (blue) characteristics of BGTC TFT devices based on thermally annealed ($300\ ^\circ C, 60$ min) sol-gel In_2O_3 (a,d), IGZO (b,e) and ZnO (c,f) thin films. Thermally grown SiO_2 ($200\ nm$) and $n-Si$ were employed as a device dielectric and substrate respectively. Drain voltage (V_{DS}) was maintained at 5V during transfer measurements (a-c), to account for linear region operation. Gate voltage (V_{GS}) ranged at $-20\ \leq V_{GS} \leq 60\ V$ over output measurements (d-f), with a step of $10\ V$. Black

arrows (a,c) denote I_{DS} orientation during forward and reverse voltage sweep, while red arrows (f) highlight hysteresis area detected in output plot of ZnO TFTs.

Transfer curves of devices based on thermally annealed In_2O_3 and IGZO

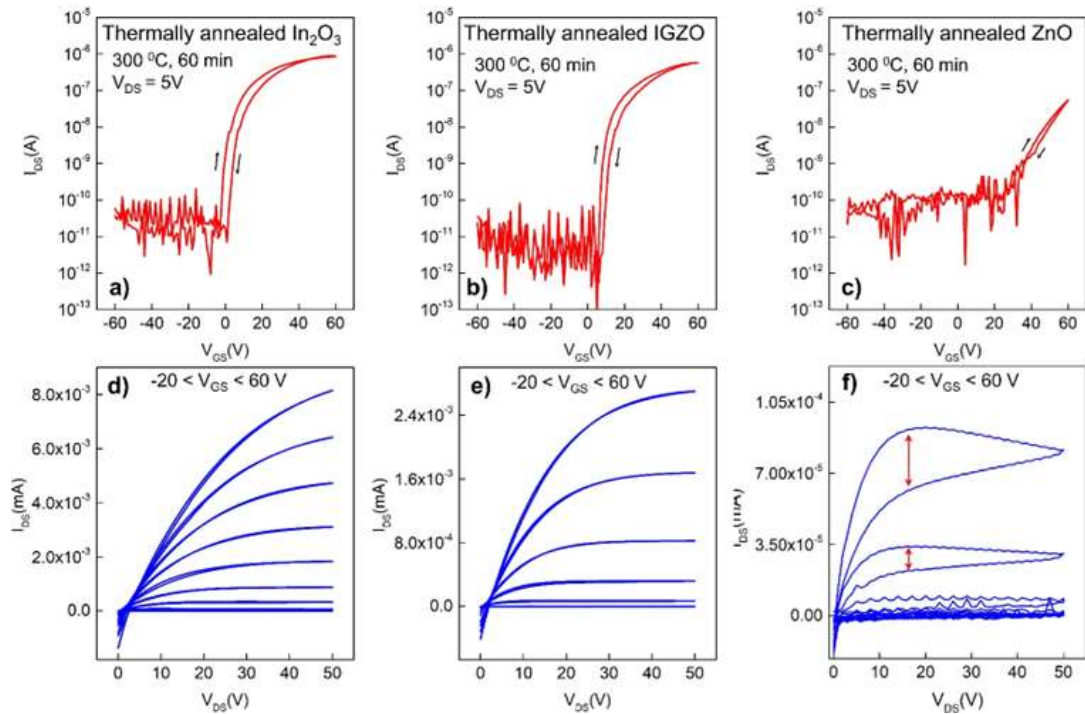

Figure 5-2, red line) manifest a characteristic TFT behaviour, presenting well-defined ON and OFF states, V_{ON} values close to zero, as well as high $I_{ON/OFF}$ ratio ($\sim 10^5$) and $I_{ON} \sim 10^{-6}A$. Clockwise hysteresis is also observed, possibly due to carrier trap sites originating from incomplete conversion of precursor into pure metal-oxide. Especially for In_2O_3, a cross-reference to our IRSE findings (Chapter 4) can be extracted. IRSE analysis of thermally annealed $In(NO_3)_3$ films (similar deposition and annealing conditions) showed the removal of precursor-related by-products along with $In-OH$ associated peak. The presence of $-OH$ bonded to In^+ can act as a carrier trap thus explaining the observed hysteresis in the transfer curve.

In contrast to well-expected device performance of In_2O_3 and IGZO devices, transfer curves of TFTs based on thermally annealed ZnO (Figure 5-2c) display a poor electrical performance involving decreased $I_{ON/OFF}$ ($\sim 10^3$) and $I_{ON} < 10^{-7}A$. Gate voltage sweep at $-60\ V < V_{GS} < 60\ V$ is not sufficient to induce current increase, as the device remains mostly in OFF state, with $V_{ON} > 20\ V$. Such behaviour could be attributed to the presence of carrier traps amongst the channel which capture electrons over voltage sweep thus preventing carrier collection on drain electrode. As V_{GS} shifts towards higher positive values, filled traps along with increased electric field across the channel provoke the activation of I_{DS} increase. The origin of carrier traps on thermally annealed ZnO film can be attributed in two factors: Incomplete precursor ($Zn(CH_3COO)_2$) conversion and grain boundary scattering (nanocrystal formation). The first case (incomplete $Zn(CH_3COO)_2$ conversion) is investigated in detail in Chapter 4.

Indeed, IRSE analysis of thermally treated (300 °C, 60 mins) $Zn(CH_3COO)_2$ films reveals the presence of acetate-associated by-products which confirm the incomplete conversion of $Zn(CH_3COO)_2$ into ZnO. As a result, the presence of associated carrier traps can explain the poor electrical performance seen in **Figure 5-2c**.

A comparison amongst output curves of TFTs based on thermally annealed In_2O_3, $IGZO$ and ZnO films comes in excellent agreement with the associated precursor conversion scenario: In_2O_3 and $IGZO$ precursors sufficiently convert into the corresponding metal oxides, thus displaying output curves with no present hysteresis while V_{GS} is directly defining the channel formation (well-separated output curves). Especially for $IGZO$, a current increase is achieved at $V_{GS} > 10$ V (for lower V_{GS}, output curves remain at similarly low values and cannot be distinguished in output plot), in agreement to V_{ON} values shown in **Figure 5-2b**. For ZnO TFTs, high hysteresis is detected along forward and reverse V_{DS} sweep while I_{DS} is presented in sawtooth form, indicating channel formation instability during measurement.

To examine the assumption on poor electrical performance of ZnO TFTs due to grain boundary scattering, AFM analysis was employed alongside electrical characterisation, in order to correlate the carrier transport mechanism across the channel to thin film topology. AFM analysis on $IGZO$ and In_2O_3 films was also performed, for comparison, along with the associated stabilised films (stabilisation was performed immediately after deposition, at 150^0C, for 15 min) **Figure 5-3** presents the surface morphologies of stabilised **Figure 5-3a-c**) and thermally annealed (**Figure 5-3d-f**) In_2O_3, $IGZO$ and ZnO (precursor) thin films. An evident similarity amongst stabilised In_2O_3 and $IGZO$ precursor films is shown in **Figure 5-3a-b**), where films present an amorphous nature. Following thermal treatment (**Figure 5-3d-e**), the films maintain an amorphous structure. In contrast, as-deposited ZnO precursor (**Figure 5-3c**) is formed into spherical nanocrystals, which transform into ZnO nanorods (**Figure 5-3e**) after thermal annealing. The transition of spherical $Zn(CH_3COO)_2$ nanocrystals [244] into nanorods [245] is accompanied by increase in nanorod length. It is also possible to observe the alignment of ZnO nanorods across the substrate. According to Pimentel *et al.* [246], the nanorod formation can be attributed to interaction of $Zn(CH_3COO)_2$ grains during thermal annealing, leading to the grains merging together. The formation of nanorods introduces a potential barrier during electron transport across the channel, which combined with remaining organic residuals (associated to $Zn(CH_3COO)_2$ incomplete conversion) lead to poor device performance.

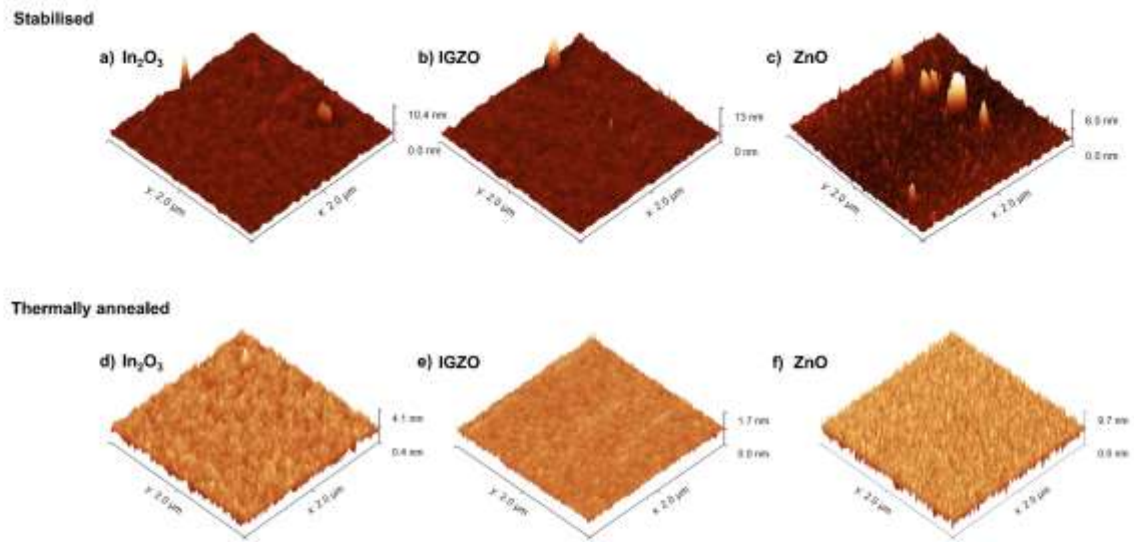

Figure 5-3. AFM images of stabilised (a-c) and thermally annealed (d-f) In_2O_3, IGZO and ZnO thin films. Stabilisation and thermal annealing conditions involved hot plate treatment at 150 ℃ (15 min) and 300 ℃ (60 mins), respectively. AFM images were taken in the channel regions of the corresponding TFT devices, the electrical characterisation of which is presented in Figure 5-2.

5.2. Sol-gel Laser Annealed of In_2O_3 TFTs

5.2.1. SiO_2 Dielectric Thickness Investigation

An initial step, prior to the In_2O_3 film fabrication, was the investigation of the SiO_2 dielectric thickness to be used, including its effect on the energy absorption, during Laser Annealing, of the film to be deposited. In detail, since the principal aim of Laser Annealing includes the high temperature induction into the as-spun metalorganic layer [55,247,248], an examination of Laser Annealing thermal effect on the composite structure - comprising of a SiO_2 dielectric layer atop of Si substrate (Figure 5-4) is demanded. This irradiation-induced temperature increase strongly governs the photochemical precursor conversion process *via* activation of a chemical reaction cascade including hydrolysis, condensation, and solvent removal. Therefore, in order to examine the effect of the SiO_2 layer onto the overall In_2O_3 absorption, a set of simulations based on the numerical solutions of Fresnel equations, as well as the optical constants of each layer was completed [204].

The principal concept of this numerical simulation lies on the representation of laser irradiation as an electromagnetic wave of a precise wavelength - in our case 248 nm (KrF laser system) interacting with each layer *via* absorption, transmission, and reflection. During Laser Annealing, an initial energy absorption is occurring in the film. However, the reduced layer thickness (~10 nm) leads to low absorption, while the remaining energy penetrates the layer, transmits through the SiO_2, and eventually gets absorbed by the Si substrate.

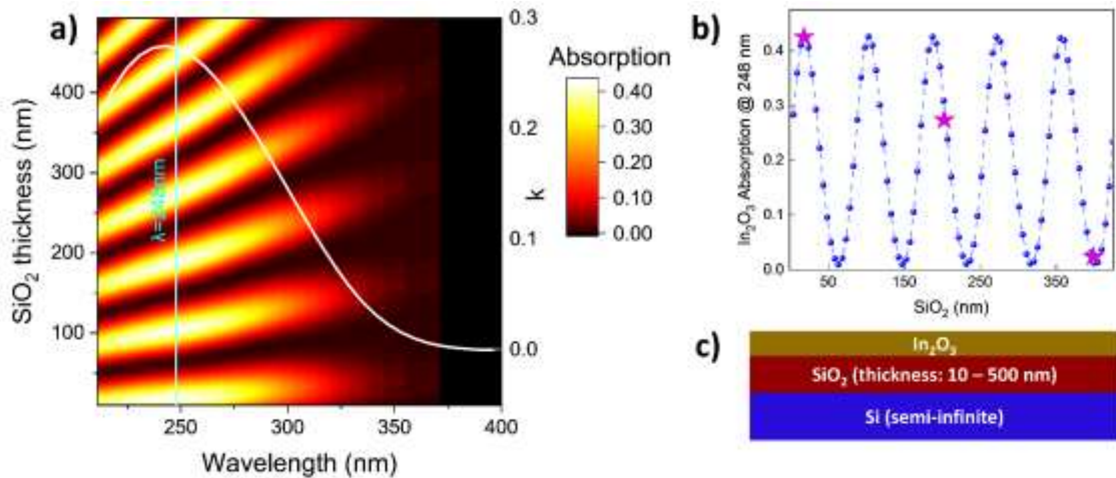

Figure 5-4. a) Numerical simulation of $\mathrm{In_2O_3}$ absorption coefficient in various $\mathrm{SiO_2}$ thicknesses and irradiation wavelengths. White line shows the extinction coefficient of $\mathrm{In_2O_3}$, k. b) absorption of $\mathrm{In_2O_3}$ at irradiation wavelength of 248 nm, for various $\mathrm{SiO_2}$ thicknesses. Magenta stars denote the absorption for 100, 200 and 400 nm of $\mathrm{SiO_2}$, which are thicknesses that were used in this work. c) schematic illustration of the structure used during the numerical modelling.

Since the intermediate $\mathrm{SiO_2}$ layer is transparent at $248\ \mathrm{nm}$, it is thus considered as a "optical spacer" (no absorption) between the metalorganic layer and the Si substrate. Therefore, the spacer thickness plays a crucial role in the induced temperature rise of the film, defined by both interference phenomena (optical effects) – and the thermal properties of $\mathrm{SiO_2}$ (thermal barrier effects). Consequently, the $\mathrm{SiO_2}$ layer thickness (which defines the optical path of the traveling electromagnetic wave thus the interference phenomena) plays an essential role in the outcome. This is evident from the results presented in Figure 5-4, which demonstrates a color-coded map of the absorption taking place in a $10\ \mathrm{nm}\ \mathrm{In_2O_3}$ layer – while varying the $\mathrm{SiO_2}$ thickness at various wavelengths. As previously reported in a relevant research study[24] the fabrication of sol-gel laser annealed BGTC $\mathrm{In_2O_3}$ TFTs devices, while employing $400\ \mathrm{nm}$ of $\mathrm{SiO_2}$ as a dielectric layer, led to the requirement of a laser fluence ranging from $300 - 450\ \mathrm{mJ/cm^2}$ in order to achieve an optimized photochemical conversion. According to Figure 5-4, the absorption of $\mathrm{In_2O_3}$ atop $400\ \mathrm{nm}$ of $\mathrm{SiO_2}$ is minimum at $248\ \mathrm{nm}$ (KrF laser), thus explaining the demand for high laser fluences. Therefore, in order to investigate the Laser Annealing efficiency upon $\mathrm{In(NO_3)_3}$ conversion into $\mathrm{In_2O_3}$, three thicknesses of $\mathrm{SiO_2}$ were chosen, namely $100, 200$ and $400\ \mathrm{nm}\ \mathrm{SiO_2}$, representing a highly absorbing ($100\ \mathrm{nm}$), a semi-absorbing ($200\ \mathrm{nm}$), as well as a non-absorbing ($400\ \mathrm{nm}$) region, according to Figure 5-4.

5.2.2. Electrical Characterisation- Transfer and Output Characteristics

To verify the $\mathrm{SiO_2}$ thickness correlation to $\mathrm{In_2O_3}$ formation during laser annealing, sol gel $\mathrm{In_2O_3}$ TFT devices with dielectric thickness of thermally grown $100, 200$ and $400\ \mathrm{nm}\ \mathrm{SiO_2}$ were

fabricated. **Figure 5-5** presents the transfer characteristics of TFT devices with sol-gel LA In_2O_3 semiconducting layer on top of $100\ nm\ SiO_2$. The gate voltage range was restricted to $-50 < V_{GS} < 50\ V$ (lower than $-60 < V_{GS} < 60\ V$ chosen for the rest of TFT analysis presented in this chapter), due to dielectric breakdown in higher gate voltages. As seen in **Figure 5-5**, Laser Annealed TFTs based on $100\ nm\ SiO_2$ dielectric exhibit poor device performance when fabricated under these Laser Annealing conditions. The channel conductivity modulation is rather poor, with most of the employed Laser Annealing conditions leading to an overly conductive semiconducting film, hence causing the device to remain in ON state. Despite the highly negative V_{GS} values (up to $-50\ V$), TFTs cannot transit to off-state, with I_{OFF} values remaining comparable to I_{ON}. For Laser Annealed devices at $100\ mJ/cm^2$ (**Figure 5-5a**), a variation amongst 1,5 and 10 pulses is recorded. The transition from 1 to 5 pulses leads to increase in I_{ON}, while maintaining the I_{OFF} at $\sim 10^{-6}\ A$. However, the effect of 10 pulses is notable (blue line), as I_{OFF} exhibits an abrupt increase to $10^{-4}\ A$. The pulse effect is less notable at $150\ mJ/cm^2$ (**Figure 5-5b**), where the device is independent on V_{GS} while remaining in ON state regardless of pulse increase.

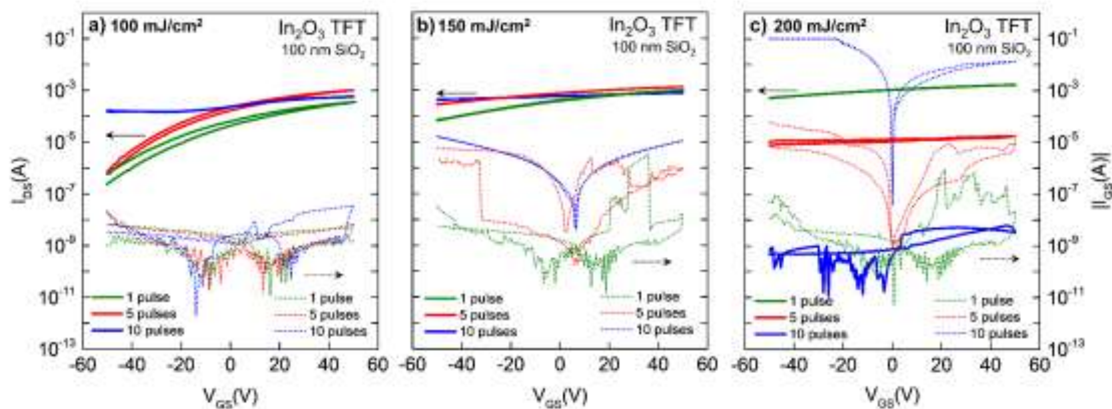

Figure 5-5. Transfer characteristics of sol-gel Laser Annealed In_2O_3 TFT devices, treated with 100 (a), 150 (b) and (c) 200 mJ/cm^2. V_{GS} is limited to $-50 < V_{GS} < 50\ V$ to avoid dielectric breakdown caused at higher gate voltages. Green, red, and blue lines represent devices treated with 1, 5 and 10 laser pulses, respectively. Dotted lines show the corresponding I_{GS} current - same colour code applied as in I_{DS}. V_{DS} is set at 5V to obtain a linear region operation.

Figure 5-5a-b manifest an improvement in I_{ON} with respect to pulse number increase, however this pattern is altered under treatment at $200\ mJ/cm^2$ (**Figure 5-5c**). A highly conductive In_2O_3 film is obtained following treatment at 1 pulse of $200\ mJ/cm^2$, leading to device performance similar to TFTs treated at 5 pulses of $150\ mJ/cm^2$. However, further increase in number of pulses is associated to abrupt deterioration in transfer plot (**Figure 5-5c**, red line), where I_{DS} current values drop significantly regardless of V_{GS} sweep. As number of

pulses is increased to 10, the device performance is significantly deteriorated. Nonetheless, all devices shown in **Figure 5-5** display V_{ON} values exceeding the lowest gate voltage ($V_{GS} < -50\ V$), therefore V_{ON} is not recorded as a parameter of the study presented here. **Figure 5-5** also displays I_{GS} values as per LA condition (in dotted lines). At $100\ mJ/cm^2$, I_{GS} is maintained at low current values ($10^{-9} - 10^{-7}\ A$). However, as fluence increases, a significant increase in I_{GS} is recorded, indicating dielectric damage that leads to leakage current increase. For devices treated under $200\ mJ/cm^2$, a significant pulse effect is obtained, as I_{GS} increases dramatically. At 10 pulses the highest I_{GS} values are recorded, which combined with I_{DS} strongly indicate a failure in device operation due to dielectric damage. A clear view of LA fluence and pulse effect on device performance can be seen through $I_{ON/OFF}$ (solid lines) and Field Effect mobility μ_{FE} (dotted lines) values, presented in

Figure 5-6. At $100\ mJ/cm^2$ (**Figure 5-6a**), Laser Annealing is causing a notable drop in $I_{ON/OFF}$ with respect to number of pulses. However, at higher fluences $I_{ON/OFF}$ remains low while no variations are recorded with pulse increase. The high I_{ON} values reported in transfer curves (**Figure 5-5a-c**) are corresponding to high mobility values, shown in **Figure 5-6b**. As the number of pulses increase, the decrease in mobility has a negative effect on I_{DS}.

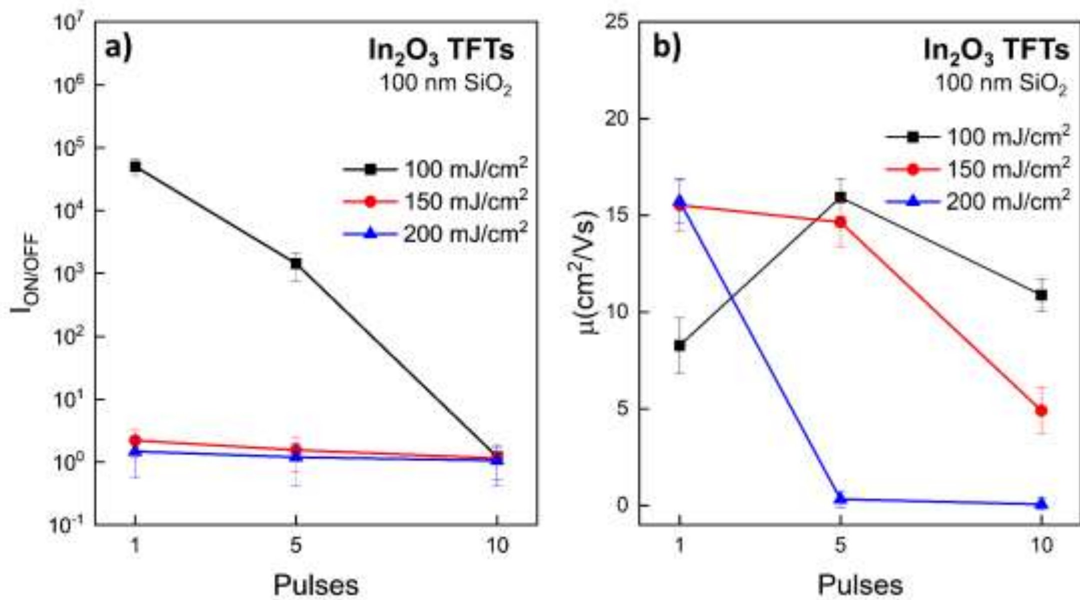

Figure 5-6. Field Effect mobility μ_{FE} and $I_{ON/OFF}$ values for LA sol-gel In_2O_3 TFTs with $100\ nm\ SiO_2$ as dielectric. Black lines display μ_{FE} and $I_{ON/OFF}$ values of devices treated at $100\ mJ/cm^2$, while red and blue lines correspond to 150 and 200 mJ/cm^2, respectively. Solid lines represent $I_{ON/OFF}$ values, while dotted lines show μ_{FE}.

In general, the increased I_{OFF} along with largely negative V_{ON} values can be associated to high carrier concentration of In_2O_3, which renders Fermi level E_F to be very close to CBM, making it impossible to deplete the semiconductor with reasonable V_{GS} values. Therefore, even

if a large value of mobility is achieved, due to the E_F pinning above CBM as V_{GS} is increased, the devices are not usable as operating TFTs, as they always operate in ON mode. The fabrication of a very conductive In_2O_3 under this LA processing conditions (using 100 nm SiO_2 as a dielectric) manifests a poor modulation of the channel conductivity. This clearly shows that, to tailor the oxide semiconductor properties towards a specific application, one needs to have in mind that these properties are affected by laser annealing parameters. A more qualitative analysis of the Laser Annealing effect on the device performance can be obtained from output characteristics in **Figure 5-7**, where output curves of Laser Annealed sol-gel In_2O_3 TFTs with 100 nm SiO_2 dielectric are displayed, after 1 pulse of $100, 150$ and 200 mJ/cm^2. An increase in I_{DS} is achieved with respect to fluence, in agreement with the reported increase in mobility values. Also, no current crowding is presented in low drain voltages, thus indicating low series resistance at the source-drain $Al - In_2O_3$ interface. For 1 pulse of 100 mJ/cm^2, the device approaches saturation in high drain voltages, although a slightly positive slope is detected, indicating high semiconductor conductance. As fluence increases, no flat regions are observed in high drain voltages; the channel cannot achieve saturation. The continuous current increase reported even in negative biasing voltages is a strong indicative of a highly conductive In_2O_3 film.

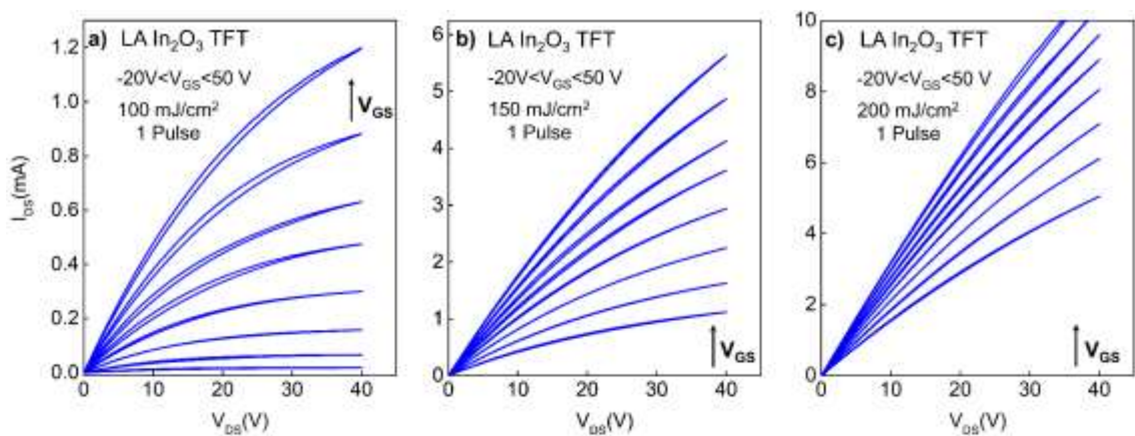

Figure 5-7. Output characteristics of LA sol-gel In_2O_3 TFTs with 100 nm SiO_2 as dielectric, annealed at 1 pulse at (a) 100 mJ/cm^2, (b) 150 mJ/cm^2 and (c) 200 mJ/cm^2. Gate voltage V_{GS} ranged from -20 to 50 V, with a step of 10 V. V_{DS} is dually swept at $0 < V_{DS} < 40$ V. A clear transition from linear to saturation region is shown in (a), while saturation is not obtained at (b) and (c). For devices treated at 200 mJ/cm^2, current values exceeded 10 mA – the top current limit of the measurement setup.

The absence of saturation manifests the channel inability to deplete close to the drain electrode, thus failing to create a pinch-off region. These results highlight the strongly conductive behaviour of In_2O_3, while in excellent agreement with transfer curve outcome where devices are continuously operating in ON state. The use of 100 nm SiO_2 resulted in undesirably conductive In_2O_3 films due to the enhanced absorption, as predicted in **Figure 5-4**.

Within the chosen fluence ($100 - 200\ \mathrm{mJ/cm^2}$) and pulse ranges (1,5,10 pulses) only very conductive $\mathrm{In_2O_3}$ formation is observed, up to the point of film destruction (at highest fluence and pulse number of $10\mathrm{x}200\mathrm{mJ/cm^2}$), meaning that laser annealing cannot lead to appropriate device performance. In an effort to gain further control into the laser annealing effect on the formation of semiconducting $\mathrm{In_2O_3}$, a $200\ \mathrm{nm}$ $\mathrm{SiO_2}$ film was chosen as a dielectric layer. According to **Figure 5-4**, this oxide thickness is expected to be semi-absorbing. Thin film deposition parameters remained the same while laser fluence window was expanded to $100 - 250\ \mathrm{mJ/cm^2}$ (with a step of $50\ \mathrm{mJ/cm^2}$). This oxide thickness allowed for a higher gate voltage sweep without leading to device breakdown, therefore the voltage range was extended to $-60 < \mathrm{V_{GS}} < 60\ \mathrm{V}$.

Figure 5-8 displays the transfer curves of $\mathrm{In_2O_3}$ TFTs where $200\ \mathrm{nm}$ $\mathrm{SiO_2}$ was employed as a dielectric layer. Increase in fluence and number of pulses is transforming the transfer curve evolution, impacting drain current along with directly ($\mathrm{V_{ON}}$, $\mathrm{I_{ON/OFF}}$) and indirectly (μ_{FE}) measured TFT performance parameters. As the number of pulses increases, a shift of $\mathrm{V_{ON}}$ onto negative values is reported. Starting from $100\ \mathrm{mJ/cm^2}$, $\mathrm{V_{ON}}$ decreases to highly negative values, reaching the measured voltage limit ($-60\ \mathrm{V}$). A similar pulse effect is detected at $150\ \mathrm{mJ/cm^2}$, where 1 pulse creates a well-defined off-state for $\mathrm{V_{GS}} < -30\ \mathrm{V}$, while higher pulses lead to $\mathrm{V_{ON}}$ shift towards more negative values. At 10 pulses, the device reaches a constant on-state, possibly due to a highly conductive $\mathrm{In_2O_3}$ film. This transition is more evident in higher fluences ($200 - 250\ \mathrm{mJ/cm^2}$) where 1 pulse creates a well-defined device operation area, however an increase in pulses is correlated to constantly ON operation mode of the devices. Overall, drain current $\mathrm{I_{DS}}$ increases with respect to fluence and pulse increase, until 10 pulses of $250\ \mathrm{mJ/cm^2}$ where a slight decrease is observed. This effect has also been detected in devices with $100\ \mathrm{nm}$ $\mathrm{SiO_2}$ as a dielectric (**Figure 5-5**), where an increase in pulses led to performance deterioration. Also, a clear effect of fluence and pulse increase on the reduction of hysteresis is displayed in **Figure 5-8** (black arrows).

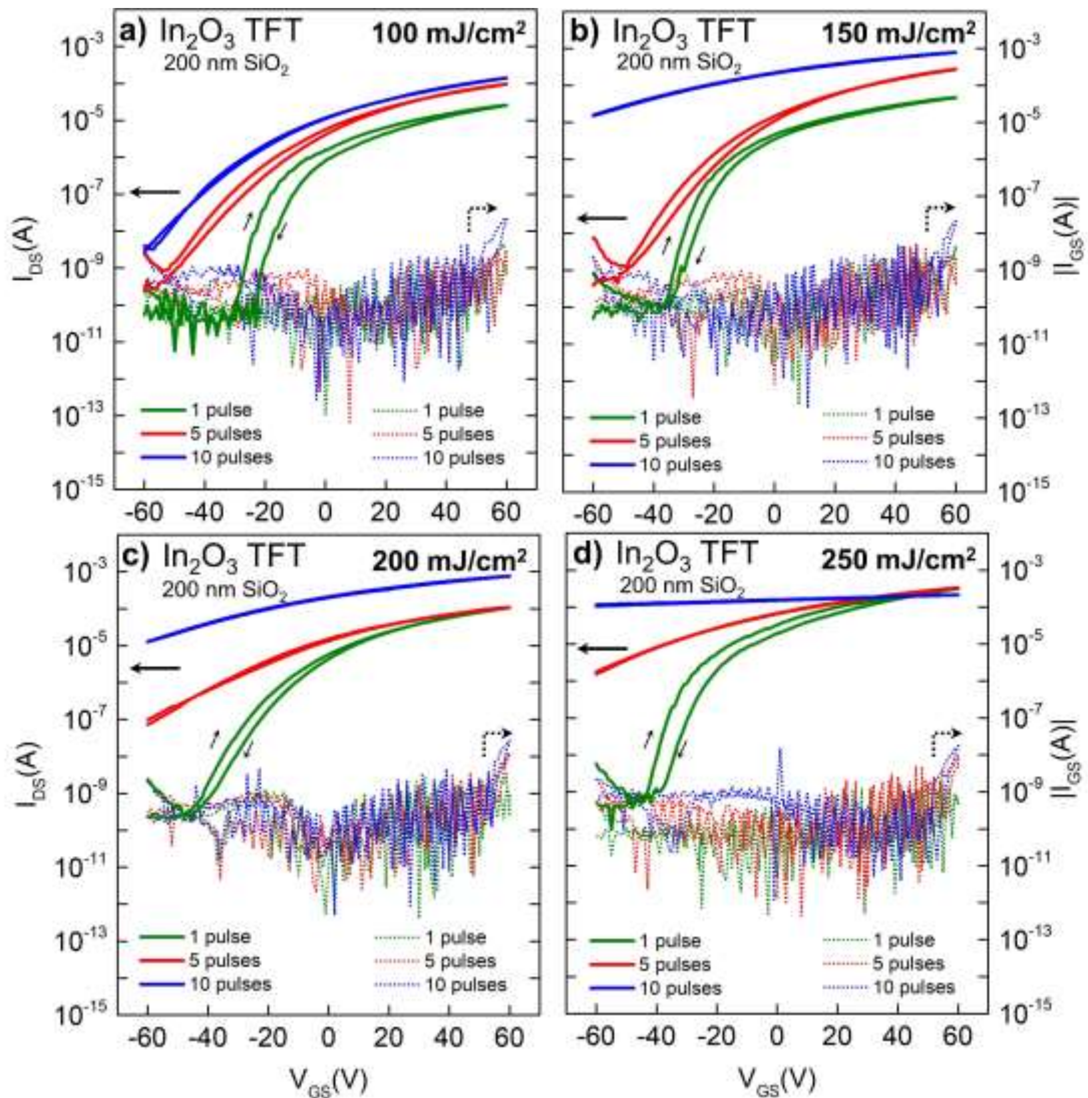

Figure 5-8. Transfer characteristics of sol-gel Laser annealed $\mathrm{In_2O_3}$ TFT devices with 200 nm $\mathrm{SiO_2}$ as a dielectric, treated at (a) 100, (b) 150, (c) 200 and (d) 250 $\mathrm{mJ/cm^2}$. Green, red, and blue lines represent devices treated with 1, 5 and 10 pulses, respectively. Dotted lines show the corresponding $\mathrm{I_{GS}}$ current- same colour code applied as $\mathrm{I_{DS}}$. Arrows display the current direction during $\mathrm{V_{GS}}$ dual sweep at $-60 < \mathrm{V_{GS}} < 60$ V. $\mathrm{V_{DS}}$ is set at 5V to obtain a linear region operation.

In all cases, 1 pulse is correlated to hysteresis in transfer curves, however an increase in number of pulses improves hysteresis dramatically, with fluences over 200 $\mathrm{mJ/cm^2}$ completely vanishing hysteresis at 5 pulses. The presence of hysteresis is also found in low fluences, and although the verified hysteresis is always clockwise, consistent with trap filling by accumulated electrons (rather than counter-clockwise, which might mitigate ionic drift [249]), this hysteresis is almost negligible for higher fluences. A more thorough representation of transfer plot-extracted parameters is shown in Figure 5-9. A significant improvement in field effect mobility values is reported with respect to pulse and fluence increase, with 10 pulses of 150 $\mathrm{mJ/cm^2}$ producing the highest mobility value. However, the transfer characteristics should also be taken

into consideration, as these conditions led to a device that does not switch off. Regarding 1 pulse, a monotonic relation between mobility and fluence is recorded, with $250\ \mathrm{mJ/cm^2}$ reaching mobility values of $\mu_{FE} = 18\ \mathrm{cm^2/Vs}$. This monotonic relation is maintained for higher number of pulses and fluence values, with an exemption of $250\ \mathrm{mJ/cm^2}$. At this fluence, a gradual drop in mobility is manifested, possibly related to thin film damage due to high irradiation.

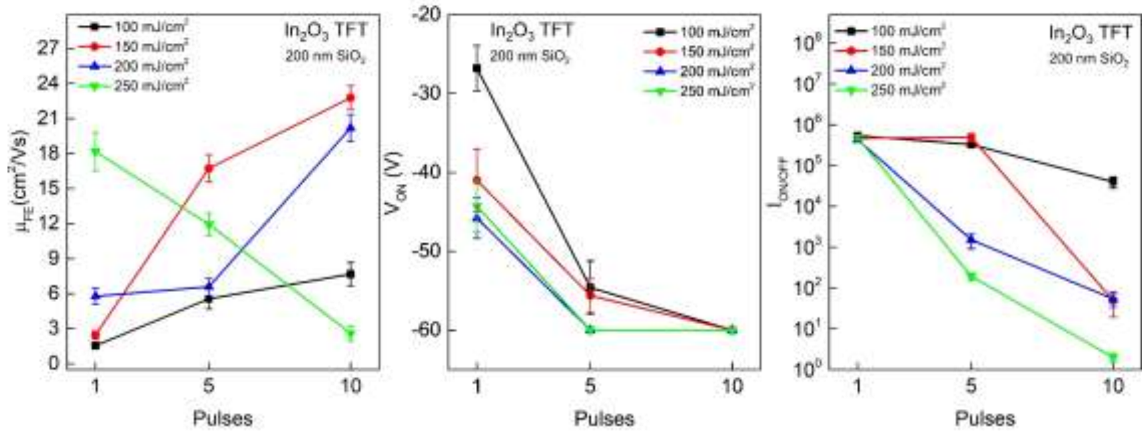

Figure 5-9. (a) Field Effect mobility μ_{FE}, (b) V_{ON} and (c) $I_{ON/OFF}$ values of LA sol-gel In_2O_3 TFTs with 200 nm SiO_2 as a dielectric. Black, red, blue, and green lines represent values extracted from devices treated at 100, 150, 200 and $250\ \mathrm{mJ/cm^2}$ respectively.

Figure 5-9b displays the change in V_{ON}. A clear pattern is observed in all laser annealing fluences, where an increase in pulses leads to V_{ON} shift towards more negative values. A discrepancy amongst V_{ON} at laser annealing of 1 pulse is observed, where lower fluences lead to V_{ON} closer to zero. However, as pulses increase, V_{ON} values approach -60 V – the lowest limit of V_{GS}. In order to shed light into the change in V_{ON}, one needs to comprehend the origin of V_{ON} shift. In devices treated under higher laser fluences and number of pulses, the carrier concentration is expected to be higher. As fluence decreases, the lower N is correlated to a larger number of unfilled traps, which are present in the unbiased device. These traps could originate from discontinuities or incomplete conversion of In_2O_3 precursor, as well as defects on semiconductor-dielectric interface. An increase in gate voltage promotes the trap filling by the first voltage-induced charges. Lower laser annealing fluence is correlated to lower N, as oxygen vacancies promoted by laser annealing are the principal source of free carriers in amorphous semiconductors like In_2O_3 [250]. For semiconducting materials with a decreased number of free carriers under a non-biased mode, Fermi levels are located away from CBM, deeper inside the bandgap. Hence, for lower N a larger number of traps have to be filled by the induced charges supplied by V_{GS} before E_F reaches tail and extended states, where the induced carriers start to be free to increase I_{DS}. Also, the lower fluence can yield a less compact film and generate more defects, both at the semiconductor's bulk and at its interface with SiO_2,

contributing also to the increase of V_{ON}. The fact that the pattern of V_{ON} decrease remains the same in all laser fluences verifies the similarity of LA effect upon $In(NO_3)_3$ conversion [251].

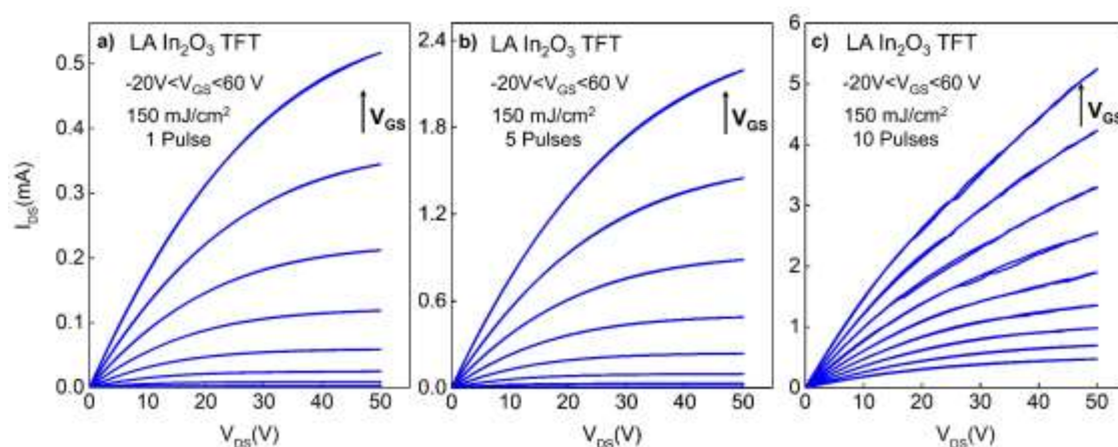

Figure 5-10. Output characteristics of LA sol-gel In_2O_3 TFTs with 200 nm SiO_2 as dielectric, annealed at $150\ mJ/cm^2$ with (a) 1 pulse, (b) 5 pulses and (c) 10 pulses. Gate voltage V_{GS} ranged from -20 to 60 V, with a step of 10 V. V_{DS} is dually swept at $0 < V_{DS} < 50$ V. A clear transition from linear to saturation region is shown in (a) and (b), while saturation is not obtained at (c), with this corresponding device remaining in ON mode. Note the I_{DS} scales are different.

Figure 5-10 displays the output curves of laser annealed In_2O_3 TFTs with 200 nm SiO_2 as a dielectric, processed at $150\ mJ/cm^2$. A considerable increase in I_{DS} is obtained with respect to pulse number, in agreement with the increase in mobility (Figure 5-9). For 10 pulses, I_{DS} values are increased by an order of magnitude, compared to 1 pulse. Also, after 1 and 5 pulses saturation is achieved in low gate voltages, however a positive slope is obtained as gate voltage increases. At 10 pulses, the slope effect is more apparent, with I_{DS} not reaching saturation for $V_{GS} > 20$ V. No evidence of current crowding is observed, thus indicating low series resistance at the source-drain Al- semiconducting contact. The shift into non-saturated output curves after 10 pulses is an additional verification of the highly conductive In_2O_3 formed after processing under these conditions. The channel cannot be depleted in high drain voltages (pinch-off effect), an effect rather possible for In_2O_3 treated with 1 and 5 pulses.

The investigation of SiO_2 thickness effect on laser annealing of In_2O_3 was completed with the use of 400 nm SiO_2 as a dielectric. According to Figure 5-4, this thickness induces minimal absorption of the laser irradiation ($\lambda = 248$ nm) for In_2O_3 deposited on top. The Laser Annealing parameters used in this experimental set were identical to the ones used for 200 nm SiO_2. i.e. fluence of $100 - 250\ mJ/cm^2$ (with a step of $50\ mJ/cm^2$) and 1,5 and 10 pulses. Figure 5-11 displays the transfer characteristics of Laser Annealed In_2O_3 TFT devices, with 400 nm SiO_2 as a dielectric layer. A discrete difference amongst 1, 5 and 10 pulses is observed at fluences of 100 and $150\ mJ/cm^2$.

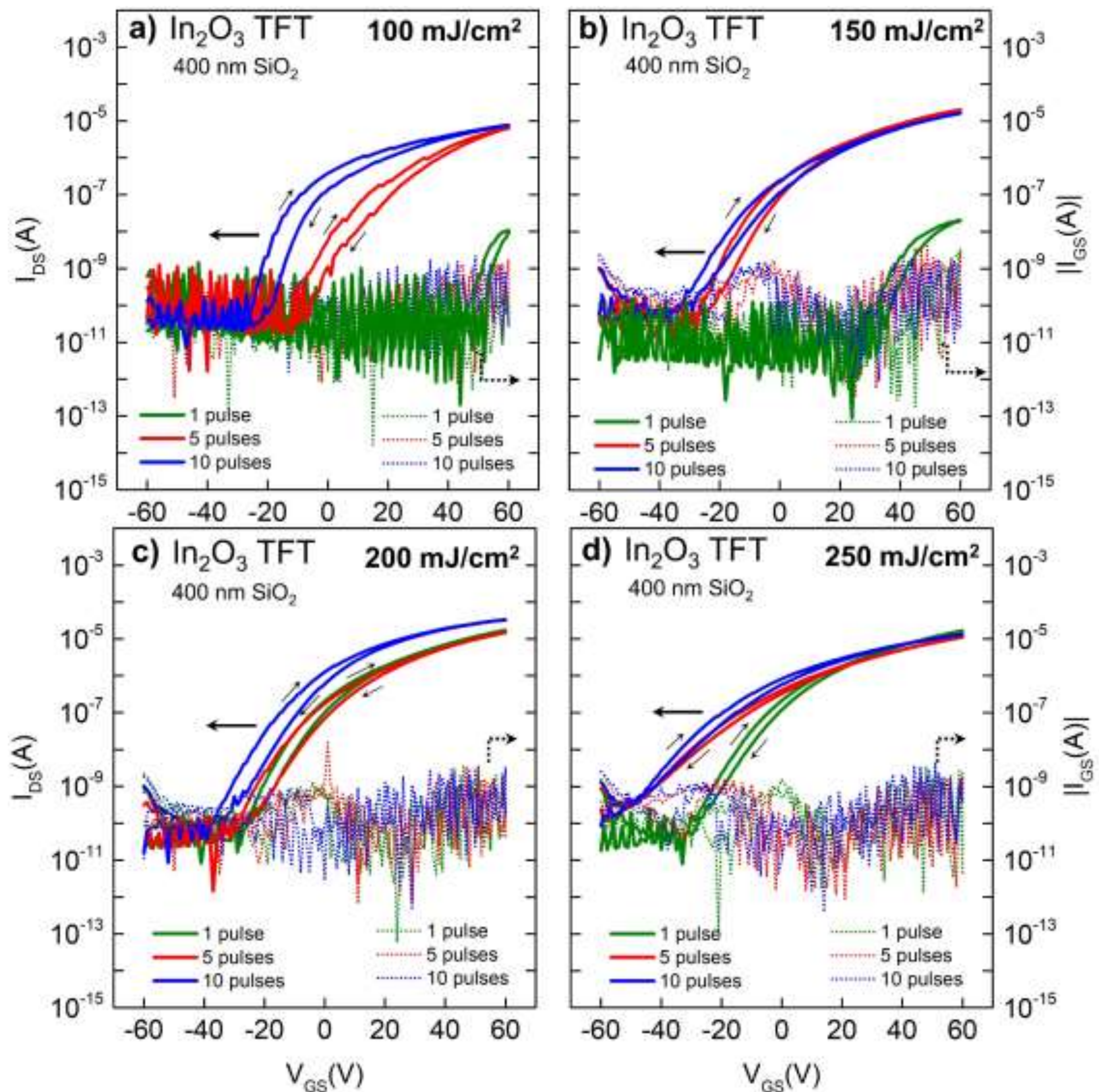

Figure 5-11. Transfer characteristics of sol-gel Laser annealed In_2O_3 TFT devices with 400 nm SiO_2 as a dielectric, treated at (a) 100, (b) 150, (c) 200 and (d) 250 mJ/cm^2. Green, red, and blue lines represent devices treated with $1, 5$ and 10 pulses, respectively. Dotted lines show the corresponding I_{GS} current- same colour code applied as I_{DS}. Arrows display the current direction during V_{GS} dual sweep at $-60 < V_{GS} < 60$ V. V_{DS} is set at 5V to obtain a linear region operation.

In the lowest fluence (100 mJ/cm^2), the treatment at 1 pulse leads to a poor device performance, with low I_{DS} and a difficulty of the device to turn on. As pulses increase, the performance is improved with increase in I_{DS}, however large hysteresis is reported. At 150 mJ/cm^2 a similar effect is reported at 1 pulse; however, the performance is significantly improved at higher pulses. This poor performance is indicative of low carrier concentration and large number of unfilled traps, possibly originating from incomplete precursor conversion due to insufficient irradiation. The effect of 1 pulse is significantly more impactful in fluences above 200 mJ/cm^2, where I_{DS} is increased, hysteresis is diminished, and the device reaches ON state at lower V_{ON} values. At 200 mJ/cm^2, no variations in device performance are found after 1 and

5 pulses. Interestingly, at 250 mJ/cm^2, I_{DS} is not increasing with respect to pulse number, however a shift of V_{ON} into higher negative values is reported. A clear view of the extracted parameters is seen in **Figure 5-12**. The lower I_{DS} reported in **Figure 5-11** (in comparison to devices on 200nm SiO_2) is correlated to low mobility values (**Figure 5-12**). An enhancement in mobility values is achieved with pulse increase, with 250 mJ/cm^2 as an exception where mobility presents a slight decrease. V_{ON} is significantly improved by increase of fluence and pulses. For devices laser annealed at 250 mJ/cm^2(5 and 10 pulses), V_{ON} approaches the V_{GS} negative measurement threshold (-60 V), highlighting the difficulty to control the ON-OFF operation state of these devices. $I_{ON/OFF}$ is reportedly high in most devices, excluding the ones treated with 1 pulse at low fluences, where I_{DS} is significantly low. Output characteristics of devices treated at 150 mJ/cm^2 (1, 5 and 10 pulses) display the dramatic effect of pulses on the enhancement of device performance. At 1 pulse, the output curve is dominated by hysteresis (see blue arrows), accompanied by noise at high V_{DS}. The presence of noise can be attributed to instability in channel formation during measurement.

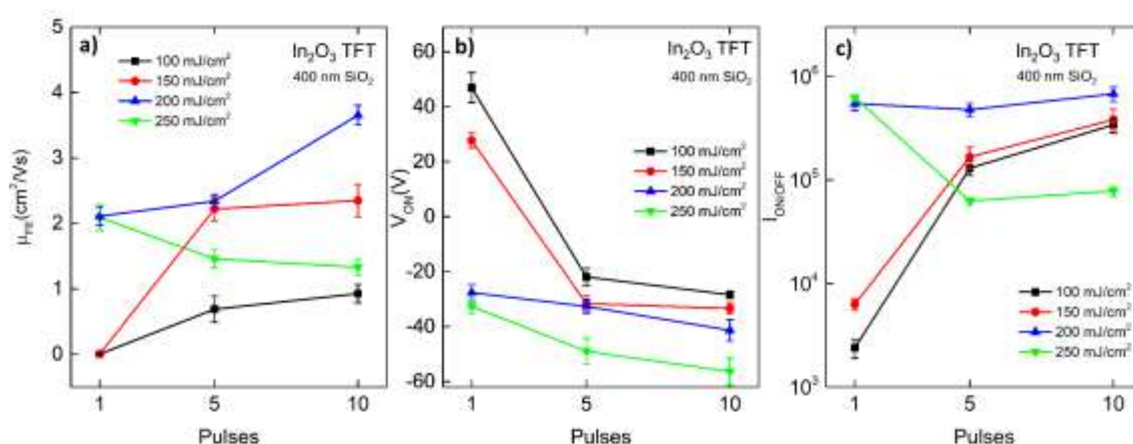

Figure 5-12. (a) Field Effect mobility μ_{FE}, (b) V_{ON} and (c) $I_{ON/OFF}$ values of LA sol-gel In_2O_3 TFTs with 400 nm SiO_2 as a dielectric. Black, red, blue, and green lines represent values extracted from devices treated at $100, 150, 200$ and 250 mJ/cm^2 respectively.

Additionally, the red area highlights the carrier crowding effect during reverse bias: when V_{DS} changes sign (change in acceleration direction) urges carriers to cross the channel similarly to the movement during forward bias. However, a difficulty in direction change is shown– possibly attributed to the presence of carrier traps in the channel area close to the Al electrodes. Carrier trapping hinders the movement of electrons within the channel, keeping them close to their position after forward bias. The collection of these carriers is (from the “wrong” electrode) is presented as negative current at $V_{DS} = 0$. As pulses increase and mobility increases, such undesirable effects are diminished. A comparison amongst transfer curves (**Figure 5-5**, **Figure 5-8**, **Figure 5-11**) provides insightful information regarding the In_2O_3

properties formed during Laser Annealing. In_2O_3 constitutes a highly popular semiconductor material with tunability in optoelectronic properties, which has played a key role on the material's choice as a semiconductor layer in this work.

As Laser Annealing offers a set of parameters (fluence, number of pulses), the formation of a phase space where fluence and pulses can control In_2O_3 properties is of high importance. Sol-gel precursor's incomplete conversion and film destruction can constitute side effects of lack in control of LA parameters, with a significant effect on device performance. Such cases were reported in **Figure 5-5** (100 nm SiO_2) and **Figure 5-11** (400 nm SiO_2) where over/under annealing led to poor device performance. The use of oxide thickness that promotes high absorption in the top (In_2O_3) layer (100 nm SiO_2) led to lack of control in In_2O_3 formation. Highly conductive films were produced, even after treatment of 1 pulse- a condition that leads to undesirable TFT performance as the devices operate constantly in ON- state. Despite the high mobility values (originating from high I_{DS}), the use of 100 nm SiO_2 is not recommended for Laser annealing assisted In_2O_3 formation.

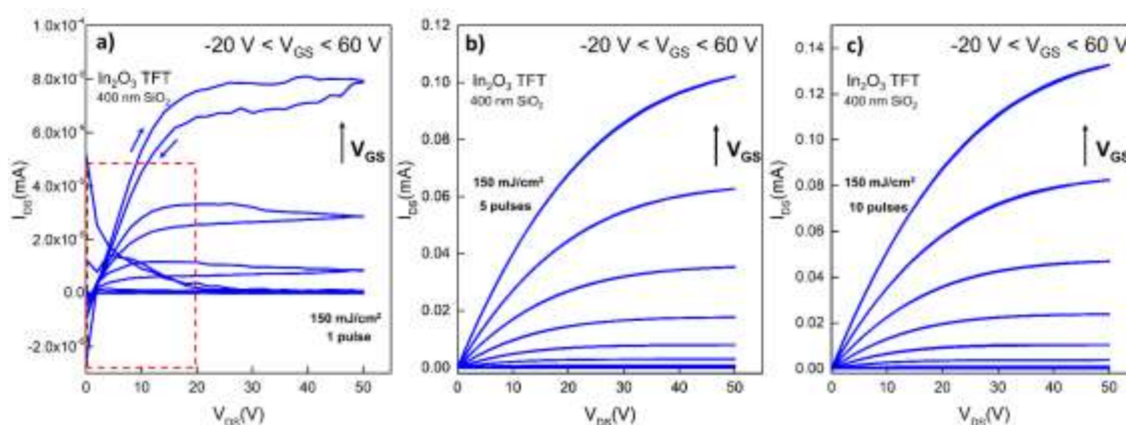

Figure 5-13. Output characteristics of LA sol-gel In_2O_3 TFTs with 400 nm SiO_2 as dielectric, annealed at $150\ mJ/cm^2$ with (a) 1 pulse, (b) 5 pulses and (c) 10 pulses. Gate voltage V_{GS} ranged from -20 to 60 V, with a step of 10 V. V_{DS} is dually swept at $0 < V_{DS} < 50$ V. For devices treated at 1 pulse (a), red area denotes the presence of hysteresis along with abnormal current collection during the return sweep (see blue arrows for forward and reverse bias).

On the other hand, the use of 400 nm SiO_2 as a dielectric seemed indicative of enhanced control over In_2O_3 formation. A wider "spectrum" of TFT device performance is reported, ranging from poor performance in low fluences and number of pulses to significantly improved performance. More accurate control over N is achieved while carrier traps are gradually compensated by increase in N (thus leading to E_F reaching tail and extended states, where the induced carriers start to be free to increase I_{DS}. Nevertheless, TFTs exhibit worse performance in comparison to In_2O_3 devices based on 200 nm SiO_2. Two reasons may justify the moderate performance of In_2O_3 on top of 400 nm SiO_2: first the formation of fewer oxygen

vacancies due to lower energy absorption in In_2O_3; second the presence of many trap densities associated to organic residuals due to incomplete precursor conversion.

5.2.3. Aging Effect

To explore the air exposure effect in TFT electrical performance, In_2O_3 devices (200 nm SiO_2 dielectric) were kept under ambient conditions for 2 years, while I-V measurements were performed every 7 months. **Figure 5-14** displays the evolution of transfer characteristics for a sol-gel Laser Annealed In_2O_3 TFT device over 2 years. At the fabrication time, Laser Annealing parameters ($5x250$ mJ/cm^2) were purposely chosen to produce a highly conductive In_2O_3 film, with the corresponding device always remaining in ON state (blue line). Over time, a shift in V_{ON} towards lower negative values is manifested, with subsequent decrease in I_{DS}. After air exposure for 20 months, the device exhibits a clear OFF-region (magenta), thus implying the free carrier transport control *via* V_{GS}. To explain the air exposure effect in device performance change, a deep insight into the air-semiconductor interaction needs to be conducted. In this work, a Bottom Gate-Top Contact (BGTC) architecture is followed, so the surface of semiconductor film is exposed to environmental conditions. For thin semiconductor films (thickness effect is explored later), alterations in semiconductor surface can significantly interfere with charge transport mechanisms. As In_2O_3 surface is exposed to air, a strong interaction with O_2 and H_2O occurs [252]. The presence of surface defects (such as oxygen vacancies, surface inhomogeneities) constitutes them as sites where oxygen can be adsorbed [253]. The mechanism of oxygen adsorption can be realised *via* 2 chemical pathways: initially water is physisorbed, leading to the formation of weakly bounded molecules; then these physisorbed molecules capture free semiconductor carriers and are converted into chemisorbed and strongly bonded species [254]. Hence, a depletion region is formed in the semiconductor/air interface. As this depletion region is approaching semiconductor/dielectric interface over time, an increase in free carrier trapping by physisorbed molecules occurs. Therefore, an increased gate voltage V_{GS} is demanded to form an accumulation layer where the remaining free carriers are collected (increase in V_{ON}, **Figure 5-14**).

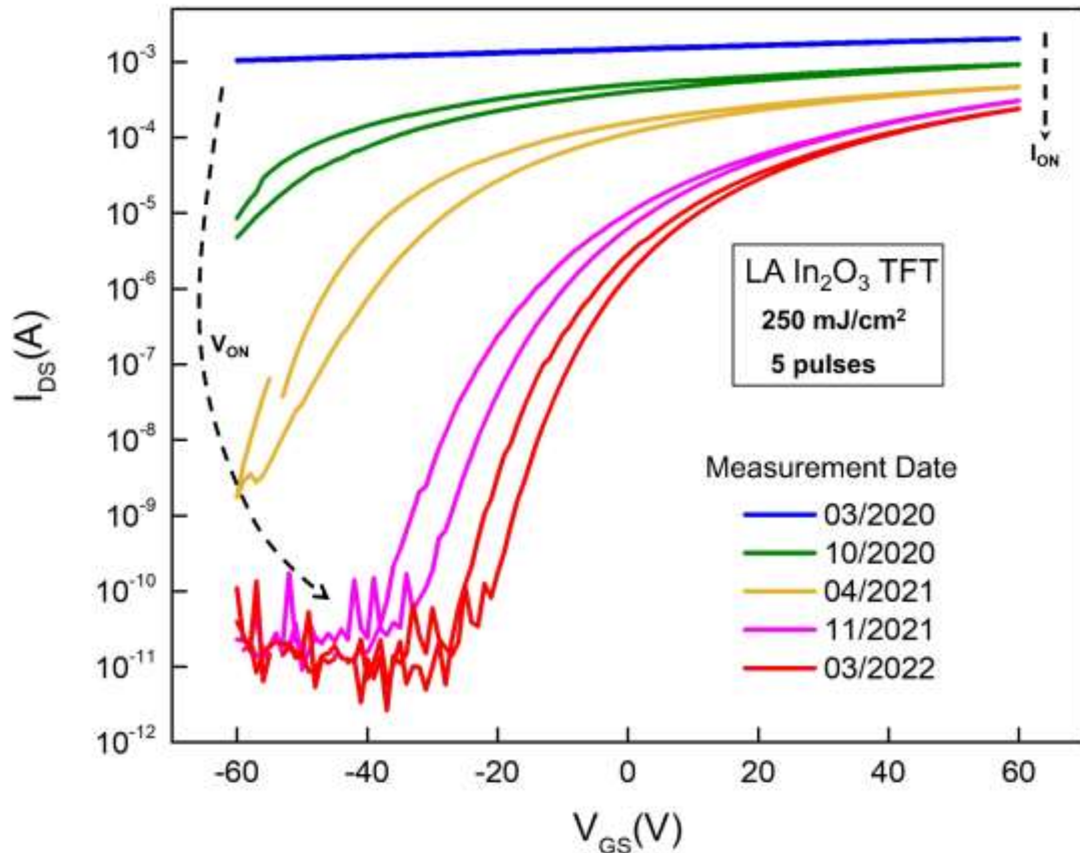

Figure 5-14. Transfer characteristics of sol gel LA In_2O_3 TFT (200 nm SiO_2 dielectric) exposed in ambient conditions. I-V measurements were conducted every 7 months to explore the air - In_2O_3 interaction. Dotted arrows highlight the transfer evolution over time. Laser Annealing conditions ($250\ mJ/cm^2, 5$ pulses) were purposely chosen to obtain a highly conductive semiconductor layer. Measurement dates are shown in figure legend, along with their corresponding colours.

Although the oxygen adsorption rate is not a parameter to be examined in the present work, it appears to be a rather slow process, in agreement with the results of Lagowski, Kang and Bariquinha, for ZnO and IGZO films [252,254,255]. The abovementioned mechanism (adsorbed O_2) can also be vastly accelerated *via* post-annealing thermal treatment. Dellis *et al.* [24] demonstrated a mild thermal treatment on highly conductive In_2O_3 TFT devices, achieving a dramatic shift of threshold voltage into more positive values, thus enabling device switch-off.

5.2.4. In_2O_3 Thickness Dependency

The electrical characterisation of In_2O_3 based TFT devices has revealed an undesirable effect of laser annealing, where high fluences and number of pulses can lead to the production of highly conductive In_2O_3. As a result, always-on TFT devices that cannot be switched off even at largely negative gate voltage (V_{GS} up to -60 V) were obtained. This originates from the high carrier concentration N of those layers, which dominates the switching behaviour in the device. High N results in poor channel conductivity modulation *via* V_{GS}, where voltage cannot effectively

deplete the free carriers to reach Off-state. To tackle this, compositional [256,257], post-annealing [24,258], and deposition [112,259] changes have been proposed in literature- besides our this work's approach (Laser Annealing). Another parameter to be considered as a dominant factor to ON-OFF state in a TFT device is the semiconductor thickness. In this work, the staggered bottom-gate structure has been chosen, an architecture that dictates the depletion mechanism of the semiconductor layer as a high-complexity process. As seen in **Figure 5-14**, the performance of BGTC devices exposed to air is affected by environmental conditions (and exposed time), as the interaction with environmental species such as O_2 and H_2O results in the creation of a depletion region close to the air-exposed semiconductor area. The extend of depletion region, as well as the interaction with the dielectric-semiconductor interface are effects which render oxide semiconductor thickness as an influential parameter.

Figure 5-15 presents the transfer characteristics of In_2O_3 TFTs (solid lines) based on semiconductor films produced with solution of $60\ mg/ml\ In(NO_3)_3$. So far in this work, the solution concentration was set at $30\ mg/ml$, therefore an increase to $60\ mg/ml$ is expected to increase In_2O_3 film thickness. To compare the two cases with regular (30 mg/ml $In(NO_3)_3$) and high ($60\ mg/ml\ In(NO_3)_3$) solution concentration, transfer characteristics based on the regular $In(NO_3)_3$ concentration are shown in comparison (**Figure 5-15**, dotted lines). As for Laser Annealing parameters, similar pulses (1, 5 and 10) and fluence ($100-250\ mJ/cm^2$) values are employed for accurate comparison.

A clear discrepancy amongst the transfer characteristics of devices with high and low solution concentration is detected, regardless of Laser Annealing parameters; devices with lower I_{OFF} and switch-off regions can only be realised for thinner In_2O_3 films, while I_{DS} values are increasing with respect to In_2O_3 thickness. This can be elucidated *via* examination of band and carrier density diagrams for different values of thickness, considering a semiconductor with high carrier concentration, like In_2O_3. To perform this analysis, we introduce a set of modulations to the ideal band diagrams presented in **Figure 5-16**, where differences amongst the work functions of gate electrode and semiconductor ($\Phi_G - \Phi_S$) are neglected, along with interface states. In **Figure 5-16** a representation of the depletion mechanism in the semiconductor film is displayed. To describe the depletion occurring in the semiconductor film, an accumulation layer at the dielectric/semiconductor interface is considered, created by negative $\Phi_G - \Phi_S$, donor-like interface states and positive charges contained in the dielectric [260]. The area close to the semiconductor top surface is depleted of electrons due to the oxygen-semiconductor interaction.

The difference in potential across the depletion region can be described as

$$V_{dep} = \frac{qNy_d^2}{2\varepsilon_0\varepsilon_s} \quad 5.1$$

where q is the elementary charge, N is the carrier concentration, ε_0 is the vacuum permittivity, ε_S is the semiconductor permittivity and y_d is the width of the depletion layer. In the case of semiconductor layer with high thickness d_s, there is always an area within the semiconductor that presents large carrier concentration N (equal to the background N) which cannot be depleted. Therefore, the device is impossible be switched off.

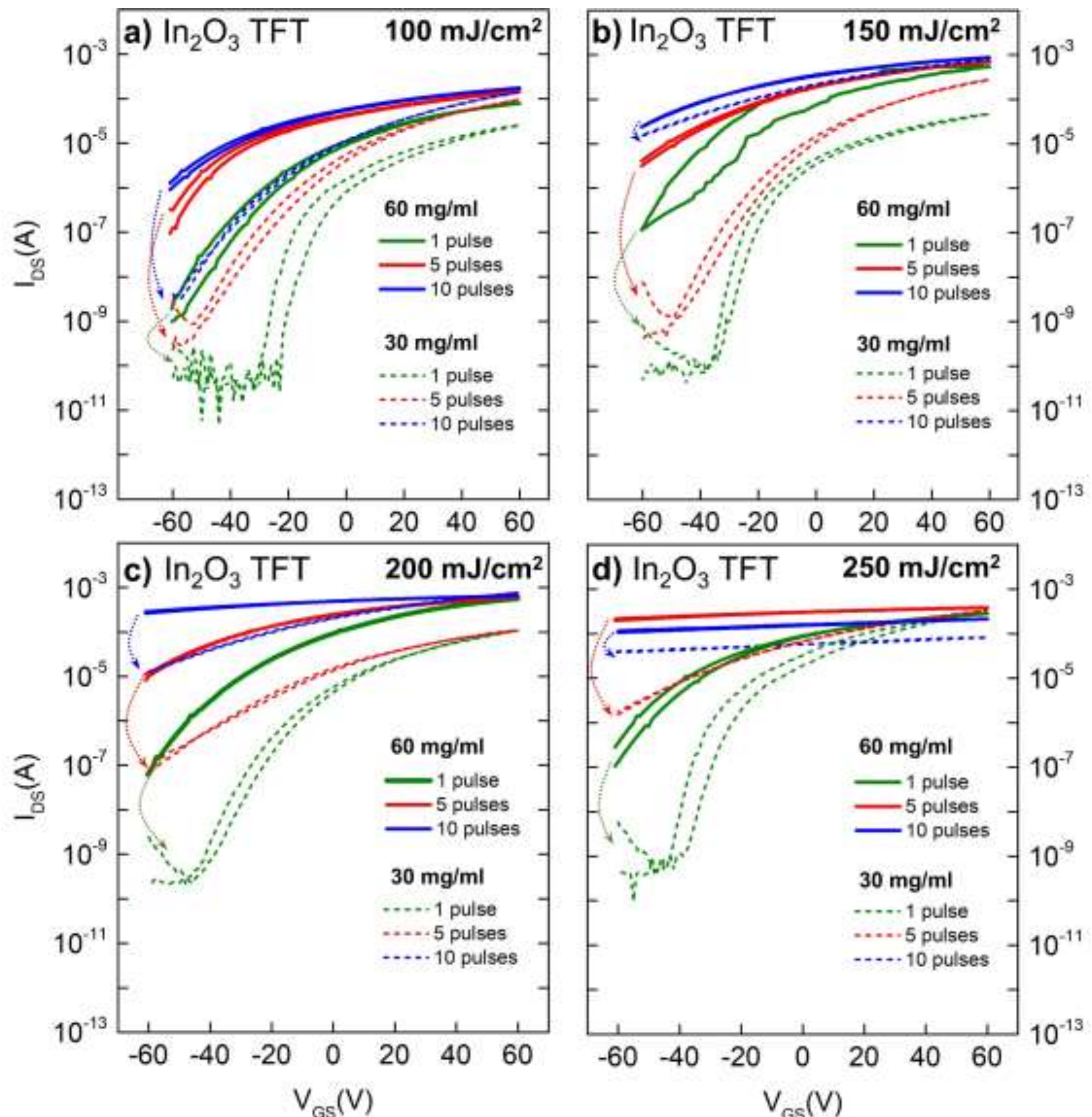

Figure 5-15. Transfer characteristics of sol-gel Laser annealed In_2O_3 TFT devices with 200 nm SiO_2 as a dielectric, treated at (a) 100, (b) 150, (c) 200 and (d) 250 mJ/cm^2. Solid lines represent devices where 60 mg/ml of $In(NO_3)_3$ solution was deposited, and laser processed while dotted lines represent corresponding devices where 30 mg/ml $In(NO_3)_3$ solution was employed. Green, red, and blue lines represent devices treated with 1, 5 and 10 pulses, respectively. Arrows display the change in I_{OFF} during V_{GS} dual sweep at $-60 < V_{GS} < 60$ V. V_{DS} is set at 5V to obtain linear region operation.

To deplete this region, it would be necessary that the dielectric field could penetrate the accumulation layer at the semiconductor/dielectric interface, which involves removing first all the free and trapped electrons from that interface. This could be achieved using a large negative V_{GS}. However, the implementation of highly negative gate voltage would lead to dielectric breakdown thus destroying the device. One possible solution to avoid the dielectric breakdown would be the increase in dielectric thickness (which increases the breakdown voltage). However, an increase in dielectric thickness would simultaneously reduce the capacitance hence the maximum charge density to be induced / withdrawn.

When semiconductor thickness is reduced, the area remaining unaffected by the accumulation (dielectric/semiconductor interface) and depletion (semiconductor/air interface) also reduces. Therefore, at a specific thickness threshold, the accumulation and depletion regions come in contact. Past this threshold, when d_s is lower than y_d, the unperturbed region where N remains unaffected is supressed. When $d_s << y_d$, depletion potential (V_{dep}) will be significantly reduced (**Eq.5.1**) since it is proportional to y_d^2. As depletion and accumulation regions overlap, unfilled traps and physisorbed oxygen in the depletion region (semiconductor/air interface) can capture electrons located in the accumulation layer, thus enabling the full depletion of the entire semiconductor film. As a full depletion is achieved, the device can be effectively switched off. Given a semiconductor with high N, parameters as film thickness d_s, depletion area thickness y_d and the state of semiconductor/dielectric interface would naturally define how effectively off-state would be achieved, which is correlated to the obtained V_{ON} values. Also, as current is not effectively controlled by V_{GS} (rather than N), an increase in I_{OFF} values is observed leading to a decrease in $I_{ON/OFF}$ with respect to thickness increase.

The above discussion assumes a semiconductor with high carrier concentration N, where the trap levels are filled under zero gate bias as E_F is close to CBM in the unbiased state. However, in the case of lower N, E_F is further below CBM and the band diagram presented in **Figure 5-16** would be altered. When d_s decreases, the depletion layer located in the semiconductor surface reaches the semiconductor/dielectric interface. Under zero gate bias (zero free carriers induced by V_{GS}) the depletion layer must be replaced by an accumulation layer first in the semiconductor/dielectric interface. This increases the demanded V_{GS} towards channel formation therefore shifts V_{ON} towards more positive values. In the case of even lower d_s, the depletion layer diffuses even deeper into the semiconductor/dielectric interface, thus requiring a higher V_{GS} (followed by a shift in V_{ON}) to form the accumulation layer. When d_s is further decreased, the semiconductor under zero gate bias is equally dependent on the film's surface state (depletion region) as well as the semiconductor/dielectric interface. At this state

(zero gate bias) the traps found in the depletion region are empty, as there are not enough electrons to fill them. A decrease in y_d is associated to decrease in V_{dep}. This leads to a considerable density of the charges induced by V_{GS} to be captured in the depletion region, associated to an increase in V_{ON}. The decrease in I_{DS} (**Figure 5-15**) in devices with thinner semiconductor can also be associated to decrease in mobility for the thinner semiconductor films. This occurs as a decreased d_s starts being comparable to the electron mean free path within the formed channel. The carrier movement thus is confined within a very narrow region close to the semiconductor/dielectric interface where electrons are prone to discontinuities or interface defects. Also, a decrease in d_s can introduce film discontinuities or inhomogeneous regions which act as carrier traps, thus affecting the device performance.

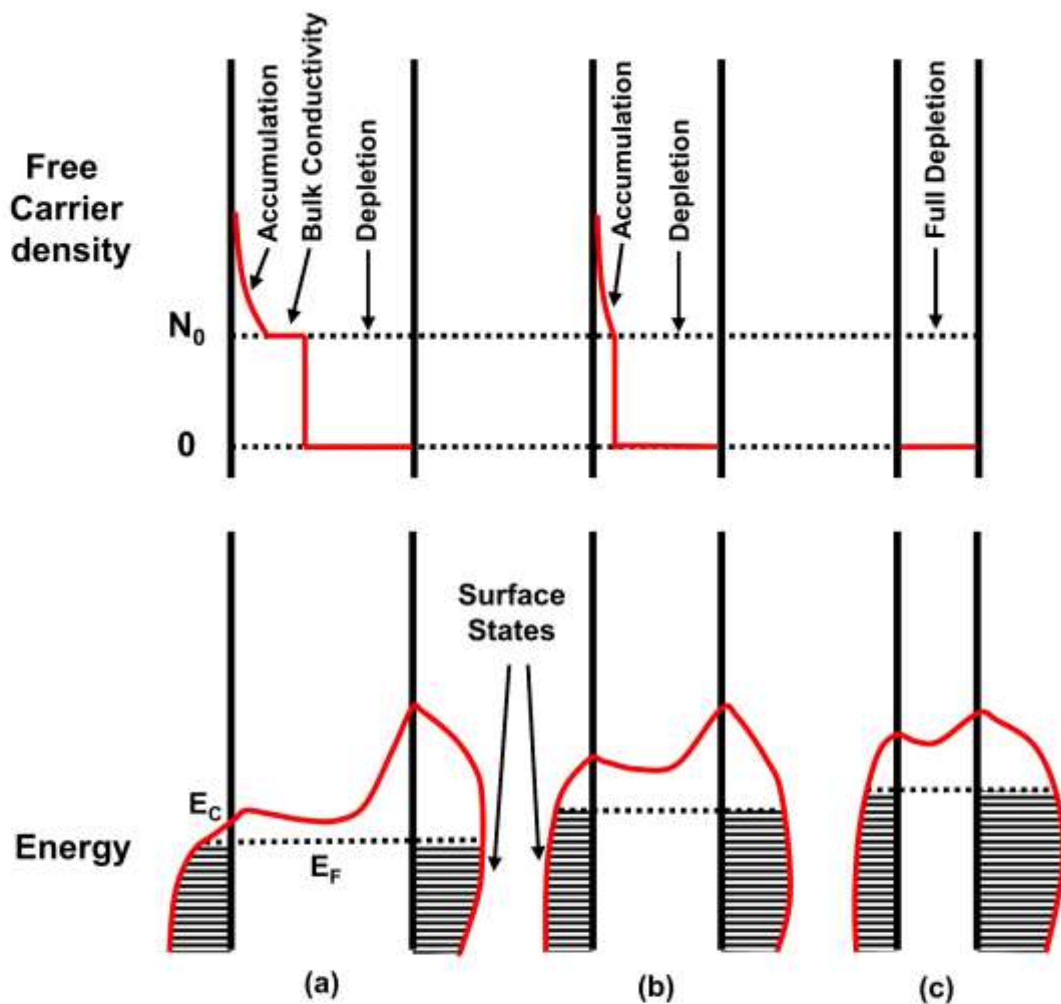

Figure 5-16. N and band diagrams at $V_{GS} = 0\,V$ (unbiased gate) for different semiconductor thicknesses d_s; (a) high; (b) medium; (c) small.

5.3. Sol-gel Laser Annealed IGZO TFTs

A detailed analysis of Laser Annealed In_2O_3 based TFT devices has revealed a significant dependence upon the dielectric thickness- in our case SiO_2. A complex relation amongst laser fluence, number of pulses and dielectric thickness can provide a full spectrum of device performances, based on the fine tuning of In_2O_3 carrier concentration. In_2O_3 has been a widely used material, known for its role as a transparent conducting host, with carrier concentration values comparative with highly conductive TCOs [261–263]. However, when implemented as an active layer in a TFT device, high concentrations may lead to undesirable results, as the device remains in constant ON mode due to exceeded concentration of carriers in the device channel. Such a phenomenon has been reported in our work, where devices treated under high fluences/number of pulses (or in the case of $100\ nm\ SiO_2$) could not provide desirable TFT characteristics. Therefore, IGZO constituted the following step into the exploration of Laser Annealed TFTs based on sol-gel semiconductor films. The use of multicomponent oxides has been well established in the field of electronics, as they often present a superiority compared to binary oxides, in terms of device performance. Their purely amorphous nature minimises the role of grain boundaries (found in ZnO for example), thus narrowing the carrier concentration barriers. In this work, Indium nitrate hydrate, Zinc nitrate hexahydrate and Gallium nitrate hydrate were used as precursor materials in a molar ratio of Indium: Zinc: Gallium of $5:3:1$, while solution concentration remained similar to In_2O_3 work presented earlier in this chapter.

As the previous work on In_2O_3 has revealed the optimum SiO_2 thickness for enhanced device performance tuning to be $200\ nm$, this thickness was therefore employed for the fabrication of Laser annealed TFTs based on sol-gel IGZO. Also, the laser annealing parameters (fluence, number of pulses) remained identical to In_2O_3 study, in order to detect the contribution of compositional effects in the device performance. **Figure 5-17** presents the transfer characteristics of Laser Annealed sol-gel IGZO TFTs. In general, the Laser Annealing effect presents several similarities to In_2O_3; an increase in fluence and number of pulses leads to an enhancement in device performance. This could be attributed to induced changes in IGZO films upon laser annealing, such as complete precursor conversion, reduction of trapping or scattering defects density and enhanced atomic bonding [264,265]. However, after a fluence/pulse threshold, the devices cannot switch off. A deeper comparison amongst **Figure 5-8** and **Figure 5-17**, reveals various differences amongst In_2O_3 and IGZO based TFTs, which can also be spotted in **Figure 5-20** (later in this chapter), where a comparison of mobility and V_{ON} values is presented.

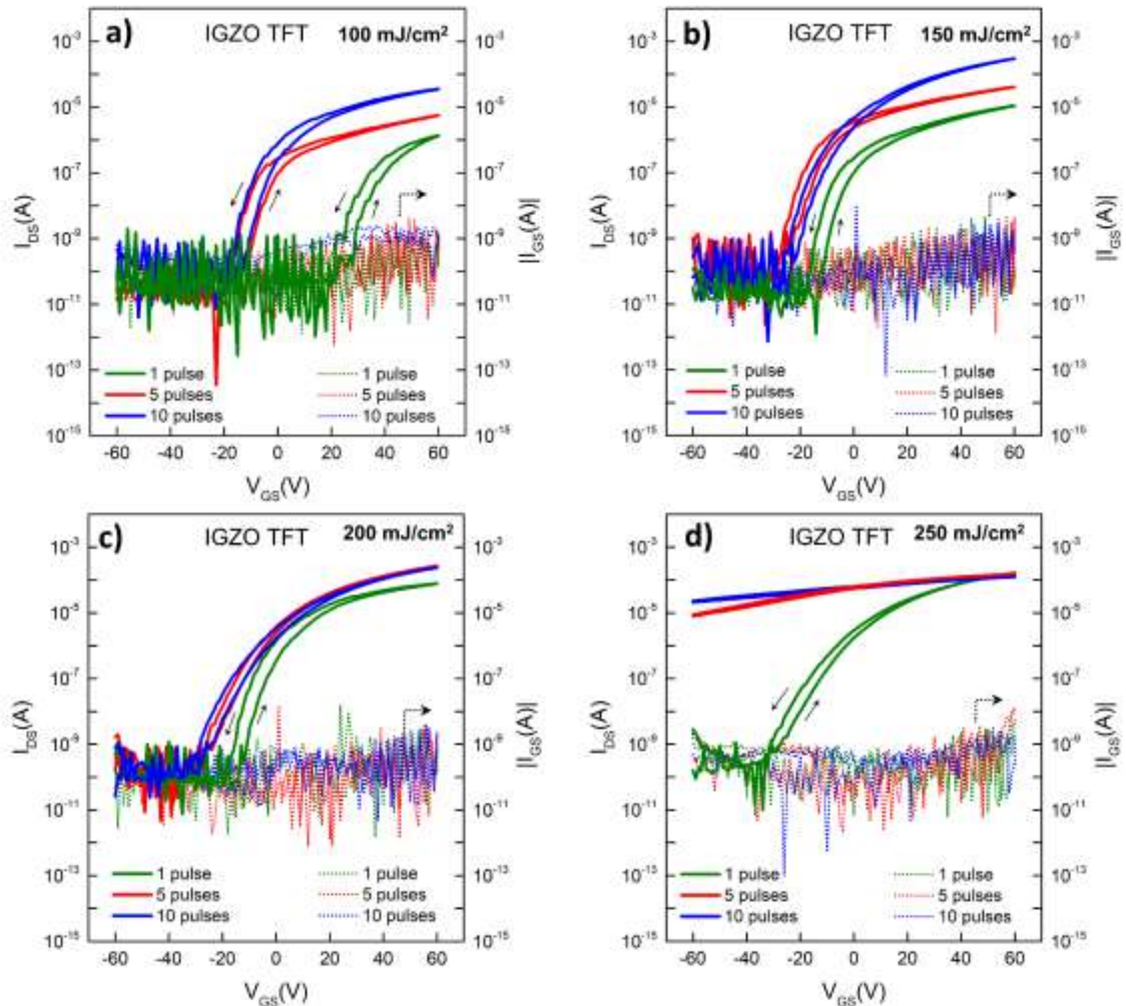

Figure 5-17. (a-d) Transfer characteristics of sol-gel Laser annealed IGZO TFT devices with 200 nm SiO_2 as a dielectric, treated at (a) 100, (b) 150, (c) 200 and (d) 250 mJ/cm^2. Green, red, and blue lines represent devices treated with 1, 5 and 10 pulses, respectively. Dotted lines show the corresponding I_{GS} current- same colour code applied as I_{DS}. Arrows display the current direction during V_{GS} dual sweep at $-60 < V_{GS} < 60$ V. V_{DS} is set at 5V to obtain a linear region operation.

In general, lower I_{DS} values are reported in comparison to In_2O_3 TFT devices, possibly due to a decrease in carrier concentration. This is translated into lower mobility values (Figure 5-20), while the trend followed remains the same. In detail, an increase in mobility values is observed with respect to fluence and pulses up until 250 mJ/cm^2, where a drop in mobility is reported. After Laser Annealing at 1 pulse, the device presents a characteristic TFT behaviour. Hysteresis is apparent in all devices annealed at 1 pulse; however, it is diminished with respect to fluence increase. Hysteresis is also reported in TFTs after treatment of 5 and 10 pulses at 100 mJ/cm^2. This constitutes an indication of the presence of carrier traps, possibly due to structural defects. At 100 mJ/cm^2, an instability (noise) in the measurement is reported, however this is diminished in higher fluences. This phenomenon has also been reported by Lee *et al.* [266], where sol gel a – IGZO- based TFTs were fabricated, incorporating femtosecond

laser irradiation as the precursor conversion medium. According to Lee *et al.*, a possible explanation to the instability during measurement may originate from the ineffective removal of defects and traps in the surface during Laser Annealing. When higher fluence was applied, microparticles and low molecular-weight substances that remained on IGZO surface had reportedly evaporated. This resulted in an enhancement to the overall device performance. However, according to their SEM analysis, overexposure in laser irradiation led to deep-caved cracks occurring throughout the surface, creating an uneven surface shape. A similar behaviour is reported in this work, where a clear improvement in device performance is reported, however at $250\ \mathrm{mJ/cm^2}$, mobility values are decreasing and $\mathrm{I_{ON/OFF}}$ is deteriorating, which leads to deterioration in the device performance. The same effect is also observed in the output characteristics (**Figure 5-18**), where 1 pulse at $150\ \mathrm{mJ/cm^2}$ presents instability during measurement (**Figure 5-18a**), whereas increased pulses diminish this effect (**Figure 5-18b-c**).

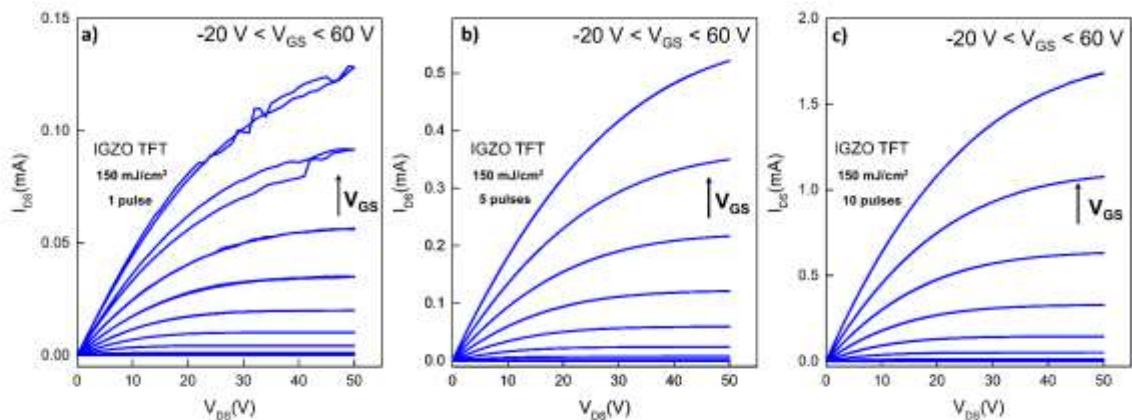

Figure 5-18. Output characteristics of LA sol-gel IGZO TFTs with $200\ \mathrm{nm}\ \mathrm{SiO_2}$ as dielectric, annealed at $150\ \mathrm{mJ/cm^2}$ with a) 1 pulse, b) 5 pulses and c) 10 pulses. Gate voltage $\mathrm{V_{GS}}$ ranged from -20 to $60\ \mathrm{V}$, with a step of $10\ \mathrm{V}$. $\mathrm{V_{DS}}$ is dually swept at $0 < \mathrm{V_{DS}} < 50\ \mathrm{V}$.

5.4. Comparison Between In_2O_3 and IGZO

5.4.1. Structural Characteristics

To investigate the correlation of surface morphology to electrical performance, a comparative morphological study on Laser Annealed sol-gel $\mathrm{In_2O_3}$ and IGZO films was performed *via* AFM analysis. For this, $\mathrm{In_2O_3}$ and IGZO films (on top of 200 nm $\mathrm{SiO_2}$) treated at $150\ \mathrm{mJ/cm^2}$ with 1, 5 and 10 pulses were employed. In fact, AFM analysis was performed on the TFT channel of devices whose transfer curves are presented in **Figure 5-8** and **Figure 5-17**, to directly link AFM and electrical characterisation results. **Figure 5-19** displays the surface morphology of Laser Annealed sol-gel $\mathrm{In_2O_3}$ and IGZO thin films, along with their corresponding stabilised films. Starting from $\mathrm{In_2O_3}$, a significant difference in thin film structure is manifested prior and after

LA at 1 pulse. The amorphous nature of as deposited In_2O_3 precursor is substituted by a porous film where grains of average size ~ 20 nm dominate, forming a crystalline network.

Such a significant change in surface structure can be attributed to the abrupt temperature increase during Laser Annealing. Indeed, various studies have associated the increase in In_2O_3 grain size as a consequence of intense thermal treatment in high temperatures (500 °C) [267–269]. The temperature effect on crystal structure of In_2O_3 involves a range of temperature dependent sequential regimes such as surface diffusion, coarsening, grain boundary diffusion, densification and grain growth [270]. However, the sub-second nature of LA technique hinders the monitoring of temperature-dependent mass transport mechanisms, as the obtained film following a 1 pulse treatment appears to form a dense crystalline network. Sunde *et al*. [271] have proposed grain boundary diffusion as the initial mass transport mechanism towards crystallisation of In_2O_3, due to the high melting point of In_2O_3 (1910 °C). As temperature further increases, grain boundary diffusion is substituted by evaporation-condensation, which is a mass transport mechanism leading to coarsening. According to Sunde *et al.*, at temperatures above 1400 °C, significant grain growth accompanied by pore growth is observed, in agreement to our work. Also, the formation of pores is directly associated to the annealing environment. During evaporation-condensation, the partial pressure of oxygen may affect this mass-transport mechanism by introducing and removing oxygen vacancies and interstitials. Kim *et al.* [272] reported an increase in film densification (and pore removal) during thermal annealing under oxygen environment – in comparison to annealing in atmospheric conditions (where nitrogen is dominant). They suggest that a higher gas solubility prevails the elimination of the remain pores, therefore annealing in oxygen environment (oxygen has a higher solubility than nitrogen), the pore removal was more effectively achieved.

As the number of pulses increases, a qualitative change of grain size distribution takes place. The average grain size increases, with crystallites of ~ 30 nm beginning to prevail in the film. Interestingly, a comparison amongst LA In_2O_3 films treated under 5 and 10 pulses do not reveal any qualitative changes either in surface morphology or in the crystal formation mechanism of the studied films. This result indicates that during Laser Annealing, a rapid transformation occurs during treatment at 1 pulse, leading to a significant change in the film's crystal structure. However, at 5 and 10 pulses the film structure stabilises, while the increase in number of pulses does not provoke further changes in morphology. This conclusion has been confirmed in studies involving thermal annealing of metal oxides. Abello *et al.* [273] studied the thermal annealing (600°C) effect on SnO_2 and reported main changes in grain size during the first 4 hours, while after the following 60 hours the grain size was semipermanent. Also, Korotcenkov et. al [274] have addressed similar results for In_2O_3 thin films.

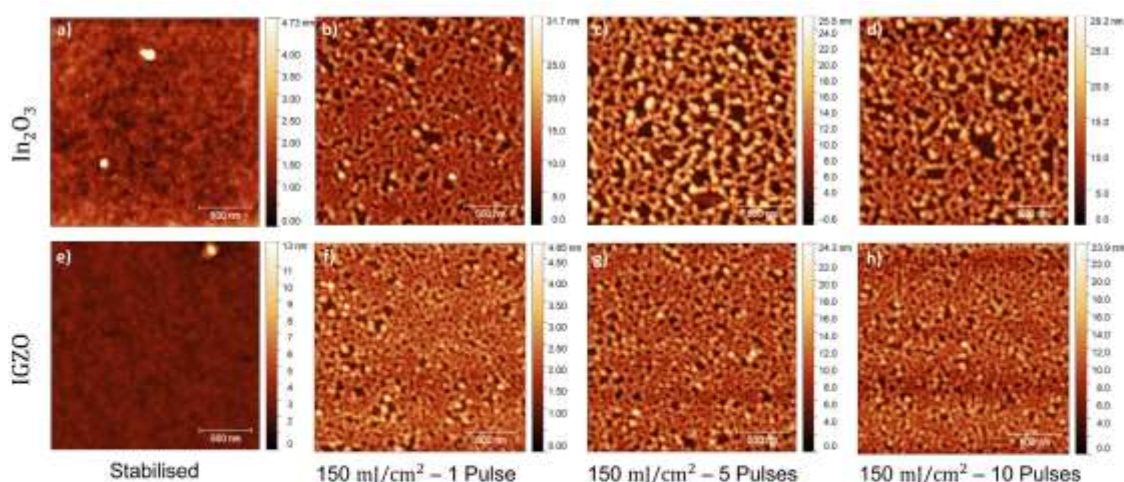

Figure 5-19. AFM images of sol-gel Laser Annealed (b-d) $\mathrm{In_2O_3}$ and (f-h) IGZO thin films, treated at $150\ \mathrm{mJ/cm^2}$ with 1 (b and f), 5 (c and g) and 10 (d and h) pulses. AFM images of stabilised $\mathrm{In_2O_3}$ (a) and IGZO (e) precursor films are displayed for comparison.

After annealing at 800 °C, the film structure was not influenced when the duration of annealing increased from 1 to 4 hrs. According to the results, after a rapid change in film structure, the film stabilises and becomes less dependent on further treatment. This agreement with our results is a good basis for assuming that, even after recrystallization, $\mathrm{In_2O_3}$ crystallites retain their initial orientation. AFM analysis of Laser Annealed IGZO films reveals a similarity in surface morphology to $\mathrm{In_2O_3}$. A single pulse at $150\ \mathrm{mJ/cm^2}$ (**Figure 5-19b-f**) prevails the formation of a dense crystallite network, similarly to $\mathrm{In_2O_3}$. As the number of pulses increases to 5 (**Figure 5-19c-g**) and 10 (**Figure 5-19d-h**), similar structure is obtained, with no apparent change in the grain size. We contribute this morphology to the content ratio of In: Zn: Ga (5: 3: 1). High content of In dominates the crystal formation under Laser Annealing, hence the similarities seen in **Figure 5-19**. The decreased grain size can be correlated to Zn content that has been reported to produce nanocrystalline IGZO films [275]. In fact, the role of Zn in IGZO crystal structure has been emphasized in literature [275–277] as increase in Zn content promotes the transformation of IGZO from amorphous to nanocrystalline structure. Also, the addition of Ga (responsible for imparting amorphous character to IGZO) is maintained at low levels [275], to restrict the role of Ga in controlling the carrier concentration. In general, the similarities amongst IGZO and $\mathrm{In_2O_3}$ crystal structure highlight the importance of In: Zn: Ga, as IGZO morphology is predominantly defined by this ratio. In this work, In: Zn: Ga was maintained constant as the principal objective involved the laser annealing effect, however an investigation in ratio effect of sol-gel Laser Annealed IGZO films constitute a future plan.

5.4.2. Electrical performance

Alongside the investigation on surface structure morphology of Laser Annealed In_2O_3 and IGZO, a comparison on device performance parameters was employed aiming to reveal the LA effect towards the formation of In_2O_3 and IGZO. **Figure 5-20** presents a comparison of μ_{FE}, V_{ON} and $I_{ON/OFF}$ values of sol-gel Laser Annealed In_2O_3 and IGZO TFTs, with 200 nm SiO_2 as a dielectric. A similar trend in mobilities of In_2O_3 and IGZO TFTs is manifested in **Figure 5-20a** where an increase in μ_{FE} is observed with respect to fluence and pulse increase at 100, 150 and 200 mJ/cm^2. As fluence increases to $250\ mJ/cm^2$, a drop in IGZO mobility is reported at 10 pulses. The decreased I_{ON} values reported in IGZO devices (in comparison to In_2O_3) are associated to a drop in mobility. This trend is maintained at most LA conditions (except 10 pulses at $250\ mJ/cm^2$ where similar μ_{FE} values are reported for In_2O_3 and IGZO TFTs). The drop in μ_{FE} constitutes an indication on change in carrier concentration N (hence a decrease in I_{DS}), however this assumption demands further verification which can be provided by an investigation in V_{ON} (directly associated to N). Indeed, **Figure 5-20b** highlights a clear discrepancy amongst V_{ON} values of In_2O_3 and IGZO. As fluence increases, a shift towards further negative values is manifested in both materials.

The same trend is also realised with increasing pulse number, where a clear difference is detected between Laser Annealing at 1 and 5 pulses. For IGZO, the highest variation is reported at $100\ mJ/cm^2$, where V_{ON} values shift from positive to negative values with pulse increase. At slightly higher fluences ($150 - 200\ mJ/cm^2$), V_{ON} remains negative, showing a slight decrease (reaching -30 V) with pulse increase. However, at $250 mJ/cm^2$, a wide shift in V_{ON} is reported, while devices annealed at 5 and 10 pulses remain in ON state (the value at **Figure 5-20b** is at -60V as this is the lowest measured V_{GS} value). This negative shift of V_{ON} could be attributed to an increase in carrier concentration, which fill the carrier traps therefore the remaining carriers can accelerate within the channel while applying V_{GS}. To deconvolute the generation mechanism of carriers in IGZO under Laser Annealing, various studies have been demonstrated *via* XPS analysis. D.H. Yoon *et al.* [278] demonstrated that the conductivity of sputtered IGZO thin films is improved by a quenching effect, because a greater number of excessive oxygen vacancies are generated due to the formation of peroxide anions during a rapid quenching process. According to Yoon, Laser Annealing induces a rapid local increase in temperature in thin films, creating an effect similar to the quenching effect and causing excessive generation of oxygen vacancies. In agreement with Yoon, Tsay *et al.* [279] have suggested that laser annealing process creates oxygen vacancies, resulting in an abrupt increase in carrier concentration N. Also, according to Huang *et al.* [280], additional oxygen vacancies are created within the IGZO film after the laser treatment, which supports the suggested increase

of carrier concentration in the device channel. It is commonly accepted that weak metastable chemical bonds such as zinc oxide, hydrogen, and hydroxide-related species exist within IGZO films [281]. Thus, the increase of oxygen vacancies is likely caused by breaking the weak chemical bonds upon laser irradiation, which indicates the formation of oxygen-deficiency related states [282]. That is, the higher the laser radiation dose, the higher the density of oxygen vacancies. XPS has also been employed to provide results which also verify that LA can realize photo-assisted condensation and densification reaction, leading to the formation of M-O lattices along with the effective dihydroxylation behaviour for OH-related species and the formation of a dense film [283–286]. For IGZO TFTs V_{ON} does not exhibit a dramatic change amongst treatment at 5 and 10 pulses, however an abrupt decrease in V_{ON} is reported amongst 200 and $250\ mJ/cm^2$. This significant drop is not seen with In_2O_3 where the V_{ON} window range is narrowly located at highly negative values ($V_{ON} < -25$ V). As the last parameter of comparison, $I_{ON/OFF}$ values of In_2O_3 and IGZO TFTs are presented in **Figure 5-20**. In contrast to In_2O_3 where fluence and number of pulses deteriorate $I_{ON/OFF}$, this behaviour is not directly reported in IGZO TFTs. In fact, $I_{ON/OFF}$ is enhanced at 100 and $150\ mJ/cm^2$, where the highest $I_{ON/OFF}$ value is reported after treatment at 10 pulses. However, further increase in laser fluence to $250\ mJ/cm^2$ leads to $I_{ON/OFF}$ deterioration, similarly to In_2O_3. The superior V_{ON} (closer to zero) and $I_{ON/OFF}$ values reported in IGZO denote an enhancement in switching performance of IGZO TFTs – in comparison to In_2O_3. This enhancement can be attributed to the role of Ga in IGZO. The strong bonds that gallium forms with oxygen supress the excessive generation of free carriers, thus shifting V_{ON} to more positive values when applying V_{GS} and therefore controlling N [275]. Various studies have focused on tuning of carrier concentration through compositional changes (i.e. changing the molar ratio of In: Zn: Ga, while trying to control the excessive increase in N due to high Indium content [287–290].

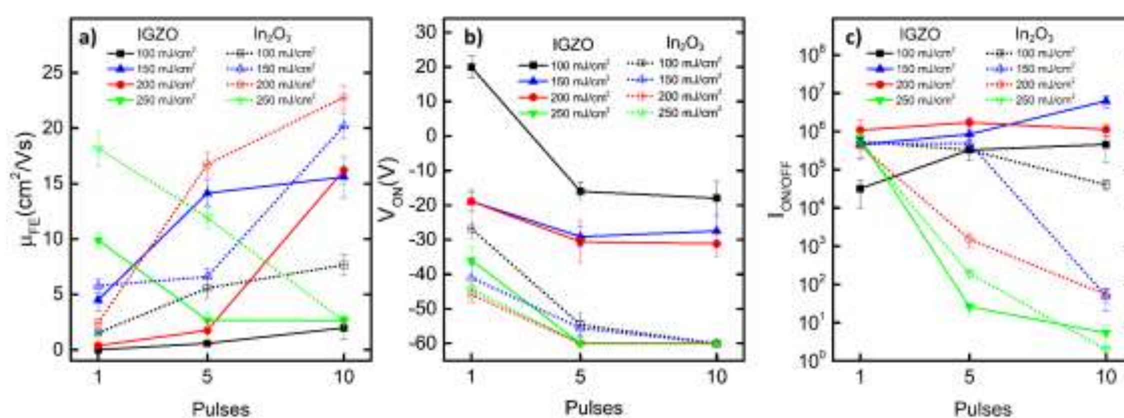

Figure 5-20. Field Effect mobility μ_{FE} (a), V_{ON} (b) and $I_{ON/OFF}$ (c) values of sol-gel Laser Annealed In_2O_3 and IGZO TFTs, treated at 100 (black line), 150 (blue line), 200 (red line) and $250\ mJ/cm^2$ (green line). IGZO and In_2O_3 parameters are displayed in solid and dotted lines, respectively.

Mobility versus Source-Gate Voltage

To further investigate the channel formation mechanism found in In_2O_3 and IGZO TFTs, Field Effect mobility μ_{FE} *vs* V_{GS} plots of devices treated at $150\ mJ/cm^2$ are plotted and displayed in **Figure 5-21**. Devices treated with 1 pulse are presented in green, while 5 and 10 pulses are shown in red and blue, respectively. In all cases, a mobility increase is recorded in accord to V_{GS}, representing the gradual channel formation. Particularly in devices treated with 10 pulses, a remarkable enhancement of mobility is verified as V_{GS} increases. For both materials, devices treated at 1 pulse present a gradual mobility increase while displaying the shallowest slope. As pulses increase (and V_{ON} shifts into more negative values), an increase in mobility is detected at earlier stages of V_{GS} sweep. For In_2O_3, $\mu_{FE,max}$ differs significantly amongst 1 and 5 pulses, while an abrupt increase is manifested at 10 pulses during V_{GS} sweep. Such behaviour is not detected in IGZO devices, where mobility increases after $V_{GS} = -10$ V. The difference obtained amongst LA In_2O_3 and IGZO treated at 10 pulses can be associated to the higher carrier concentration found in In_2O_3. Physically, E_F is raised very quickly above CBM by V_{GS}, since the trap density is very low and very large μ_{FE} can be achieved when the small potential barriers associated with structural disorder are surpassed, which happens for $V_{GS} = 50$ V, where $\mu_{FE}$is maximum.

As V_{GS} gets higher than these values, the conductive channel is drawn closer to the semiconductor/dielectric interface, which contributes to increased scattering effects of the large density of induced carriers, resulting in the decrease of μ_{FE} (highlighted in a blue-shaded circle). An electron injection barrier may also contribute to this drop in mobility, as proposed by Dehuff et.al [291]. To compare IGZO and In_2O_3, two phenomena should be considered when understanding the change in μ_{FE}: the first one is carrier concentration N and the second one is the presence of grain boundaries. Starting from the unbiased state, the amount carrier traps located amongst the grain boundaries (both in IGZO and In_2O_3) can have a direct impact in the carrier movement. However, in In_2O_3, the high N can compensate to a greater extent for the trapped carriers within the grain boundaries (in comparison to IGZO). In this case, when V_{GS} is applied, this “excess” number of carriers can move easier across the channel, contributing to the increase in mobility. Similar behaviour is also obtained in In_2O_3 devices treated under 5 pulses (pink-shaded circle). Note that Hearings (1964) has also proposed a model where several mechanisms are contributing into mobility increase when V_{GS} is applied, including but not limited to the direct relation of mobility with N. No mobility decrease is exhibited in IGZO devices, possibly attributed to a difference in N. When N is lower, a larger fraction of the charges induced by V_{GS} must fill empty traps before E_F reaches CBM or above it, where mobility is maximised.

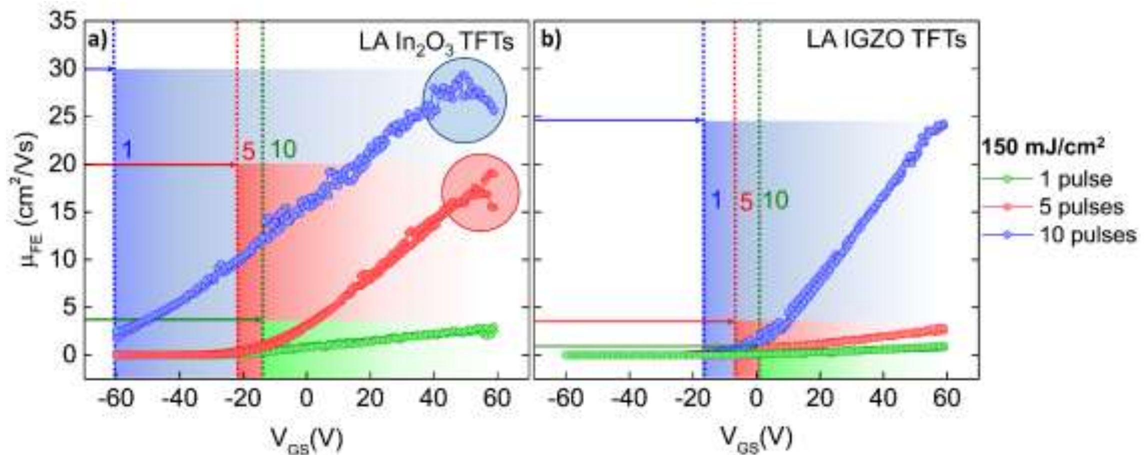

Figure 5-21. Mobility evolution versus gate voltage V_{GS} in Laser Annealed (a) In_2O_3 and (b) IGZO TFTs. Devices are treated at 150 mJ/cm^2 under 1 (green), 5 (red) and 10 (blue) pulses. Colour-shaded areas represent V_{GS} window where mobility starts to increase. Colour-coded arrows and colour-coded dotted vertical lines also highlight the corresponding V_{GS} threshold, above this point mobility starts to increase. Blue and pink shaded circles reveal areas of mobility decline.

5.5. Sol gel LA ZnO TFTs

The study of TFT devices based on sol-gel In_2O_3 and IGZO semiconductor films has revealed a significant change in crystal structure and carrier concentration because of laser annealing. The formation of In_2O_3 and IGZO was based on the use of nitrate-based precursors, the dissociation of which is known to occur at ~ 300 °C (also verified by I-V characteristics of thermally annealed devices, Figure 5-2). This temperature has also been cross examined in **Chapter 4**, where IRSE analysis of $In(NO_3)_3$ films annealed at 300 °C revealed the dissociation of precursor-related by-products. The second material studied by IRSE was sol-gel ZnO, based on $Zn(CH_3COO)_2$ conversion. The complex crystal structure of ZnO (wurtzite) has been often associated to changes in electronic behaviour of TFTs, as the presence of grain boundaries in ZnO dominates the carrier transport mechanism in the device channel. Also, for sol-gel ZnO -based TFTs, the choice of precursor plays a crucial role into the material's crystal structure thus device performance. Various studies involving the use of ZnO in TFT applications have demonstrated the carrier transport- crystal structure association, along with a plethora of applications. Especially for sol-gel ZnO, $Zn(NO_3)_2$ and $Zn(CH_3COO)_2$ have constituted the most prominent candidates towards the metal oxide formation. As our IRSE analysis has focused on the thermal annealing effect on $Zn(CH_3COO)_2$, this precursor was thus employed towards TFT fabrication. $Zn(CH_3COO)_2$ was dissolved in 2-Methoxyethanol (30 mg/ml), while Monoethanolamine (molar ratio 1: 1) was added to ensure acetate dissolution. The solution deposition (spin coating), substrate (200 nm SiO_2/Si) and electrode fabrication conditions remained similar to In_2O_3 and IGZO. Prior to electrode deposition, films were Laser Annealed at various fluences and pulses

aiming for the formation of ZnO. Since the analysis in Chapter 4 has revealed the demand in higher temperature treatments towards the complete conversion of $Zn(CH_3COO)_2$ into ZnO, (associated to the dissociation of acetate-related by-products) the laser fluence window was increased to $250 - 350\ mJ/cm^2$. Also, the laser pulse window was increased, varying from 1 to 20 pulses. To the best of our knowledge, this is the first reported study of Laser Annealed sol-gel ZnO TFTs based on the Laser-assisted conversion of $Zn(CH_3COO)_2$ into ZnO. The temperature of thermally annealed (Reference) devices remained at 300 °C, to cross examine the IRSE results.

Figure 5-22 shows the transfer characteristics of Laser Annealed sol-gel ZnO TFT devices, treated at 250 (**Figure 5-22a**), 300 (**Figure 5-22b**) and $350\ mJ/cm^2$ (**Figure 5-22c**). Gate voltage ($-60 < V_{GS} < 60\ V$) and Drain voltage ($V_{DS} = 5V$) values remained similar to In_2O_3 and IGZO TFT analysis. For the devices treated at $250\ mJ/cm^2$(**Figure 5-22a**), non-ideal TFT behaviour is revealed. Laser Annealing at 1 pulse is not exhibiting any increase in I_{DS} current even at the highest V_{GS} ($60\ V$), with the device remaining always switched off. An increase in I_{DS} is manifested at devices treated with 5 pulses, however some hysteresis as well as low I_{ON} values ($10^{-9}\ A$) are reported. An increase in pulses provokes improvement in transfer characteristics. At 10 pulses, a I_{DS} increase along with V_{ON} shift towards zero is exhibited, however a larger hysteresis is reported. For 15 and 20 pulses the elimination of hysteresis along with I_{ON} increase to $\sim 10^{-6}\ A$ indicates an improvement in device performance, with V_{ON} shifting towards highly negative values. An increase in I_{OFF} is also manifested for devices treated at 15 and 20 pulses. Generally, despite the improvement in performance with respect to pulse number, a non-ideal TFT behaviour is obtained in the set of devices based on ZnO treated at $250\ mJ/cm^2$.

TFTs processed at $350\ mJ/cm^2$ (**Figure 5-22c**) display clear deviation from **Figure 5-22a**, as devices treated at higher laser fluence perform always in ON state, regardless of the applied highly negative ($-60\ V$) V_{GS} values. This switch-on behaviour is obtained at all laser pulses, while I_{DS} increases with respect to pulse number. No hysteresis is shown, with I_{ON} exceeding $10^{-4}\ A$ at 20 pulses. In both cases (**Figure 5-22a-c**), the Laser Annealing conditions are leading to poor device performance: At $250\ mJ/cm^2$ low I_{DS}, hysteresis and high V_{ON} values are exhibited, while at $350\ mJ/cm^2$ the use of devices is limited as no switch-off region is obtained. The performance window corresponding to the used laser annealing parameters does not allow for a clear view of the fluence or pulse effect on ZnO, as the extreme TFT performances obtained could be attributed to either low (high) fluences or low (high) number of pulses.

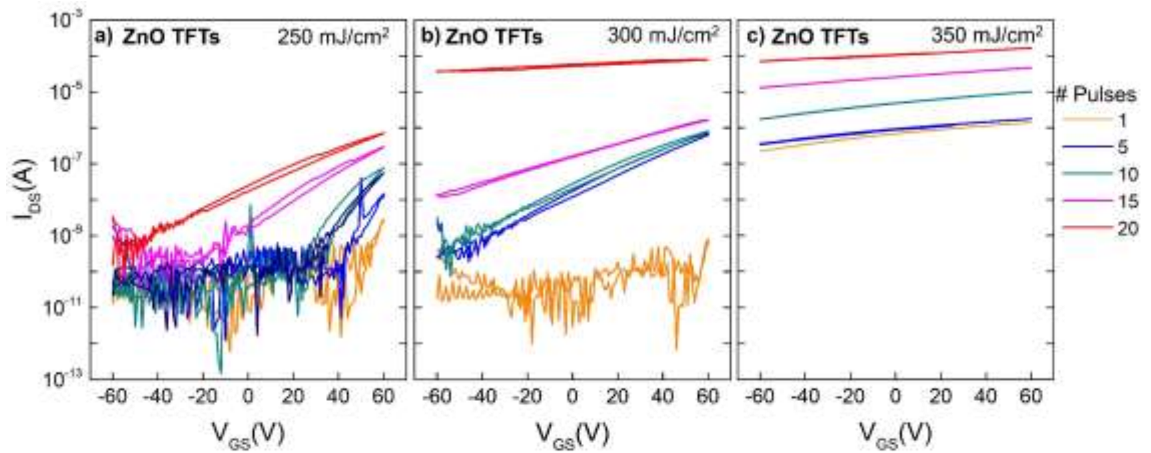

Figure 5-22. Transfer characteristics of laser annealed sol-gel ZnO TFT devices, treated at (a) $250\ \mathrm{mJ/cm^2}$, (b) $300\ \mathrm{mJ/cm^2}$ and (c) $350\ \mathrm{mJ/cm^2}$. $\mathrm{V_{DS}}$ was set at 5 V to ensure operation at the linear region.

To explore an association between fluence and pulse effect on ZnO formation, $300\ \mathrm{mJ/cm^2}$ were added to the laser annealed fluences employed in this work. **Figure 5-22b** displays the transfer characteristics of the corresponding ZnO TFT devices treated at $300\ \mathrm{mJ/cm^2}$, at $1, 5,10,15$ and 20 pulses. At this fluence, a "broader" window of TFT performances is obtained. At 1 pulse, similar behaviour to $250\ \mathrm{mJ/cm^2}$ is obtained: the device exhibits poor $\mathrm{I_{DS}}$ values as no clear ON state is displayed. However, as pulses increase, a gradual enhancement in $\mathrm{I_{DS}}$ is shown, followed by shift of $\mathrm{V_{ON}}$ towards more negative values. At 20 pulses, the device remains always switched on, with similar behaviour to the corresponding one at $350\ \mathrm{mJ/cm^2}$. Evidently, the use of $300\ \mathrm{mJ/cm^2}$ allows for the detection of a wide range in device performance thus offering a detailed view of the pulse effect.

The extraction of mobility $\mathrm{\mu_{FE}}$, as well as $\mathrm{V_{ON}}$ values of LA ZnO TFTs is presented in **Figure 5-23**. The low $\mathrm{I_{DS}}$ obtained from devices treated at $250\ \mathrm{mJ/cm^2}$ has a direct impact on mobility values (**Figure 5-23**, black solid line) where $\mathrm{\mu_{FE}} \sim 10^{-3}\ \mathrm{cm^2/Vs}$. As fluence increases, a monotonic increase with respect to number of pulses is obtained. For $300\ \mathrm{mJ/cm^2}$ (red solid line), $\mathrm{\mu_{FE}}$ reaches the maximum value of $1.1\ \mathrm{cm^2/Vs}$, while at $350\ \mathrm{mJ/cm^2}$ (blue solid line) it exceeds $3\ \mathrm{cm^2/Vs}$. However, the higher mobility values at $350\ \mathrm{mJ/cm^2}$ are not associated to improved TFT performance, as the devices are not suitable for switch-related applications. This is also confirmed by $\mathrm{V_{ON}}$ (blue dotted line), which remains constant at $-60\ \mathrm{V}$ (lowest applied $\mathrm{V_{GS}}$). A monotonic decrease in $\mathrm{V_{ON}}$ is obtained for devices treated at $250\ \mathrm{mJ/cm^2}$ (black dotted lines), while the decrease appears more abrupt for the devices annealed at $300\ \mathrm{mJ/cm^2}$ (red dotted line). As ZnO crystallinity has been widely correlated to the material's carrier transport mechanism, an investigation to surface morphology of LA ZnO was performed. Since $300\ \mathrm{mJ/cm^2}$ showed the most interesting results, 3 pulse conditions associated to different

device performances were chosen: 5, 15 and 20 pulse. The condition of 1 pulse was excluded as no TFT transfer characteristics were obtained. **Figure 5-24** displays the AFM images obtained from the channel area of ZnO TFTs treated at the abovementioned Laser Annealing conditions, alongside their corresponding electrical characterisation (transfer and output curves). AFM analysis and electrical characterisation of thermally annealed devices is also shown for comparison purposes. Surface morphology of stabilised $Zn(CH_3COO)_2$ is shown in **Figure 5-3c**. A comparison amongst stabilised, thermally annealed and Laser Annealed ZnO thin films reveals a dramatic change in ZnO crystal structure promoted by Laser Annealing, as the small grains observed in stabilised annealed films are dramatically increasing in size, forming large-sized grain boundaries [183,292]. The obtained AFM images present large grain features which dominate the height scale which can be misleading to the actual grain structure of ZnO.. An increase in grain size with respect to pulse increase is confirmed in **Figure 5-24**, in agreement to Oh *et al.* [293]. In addition, several structural defects, such as surface hillocks, pits or holes are observed due to a three-dimensional (3D) grain growth instead of 2D lateral growth.

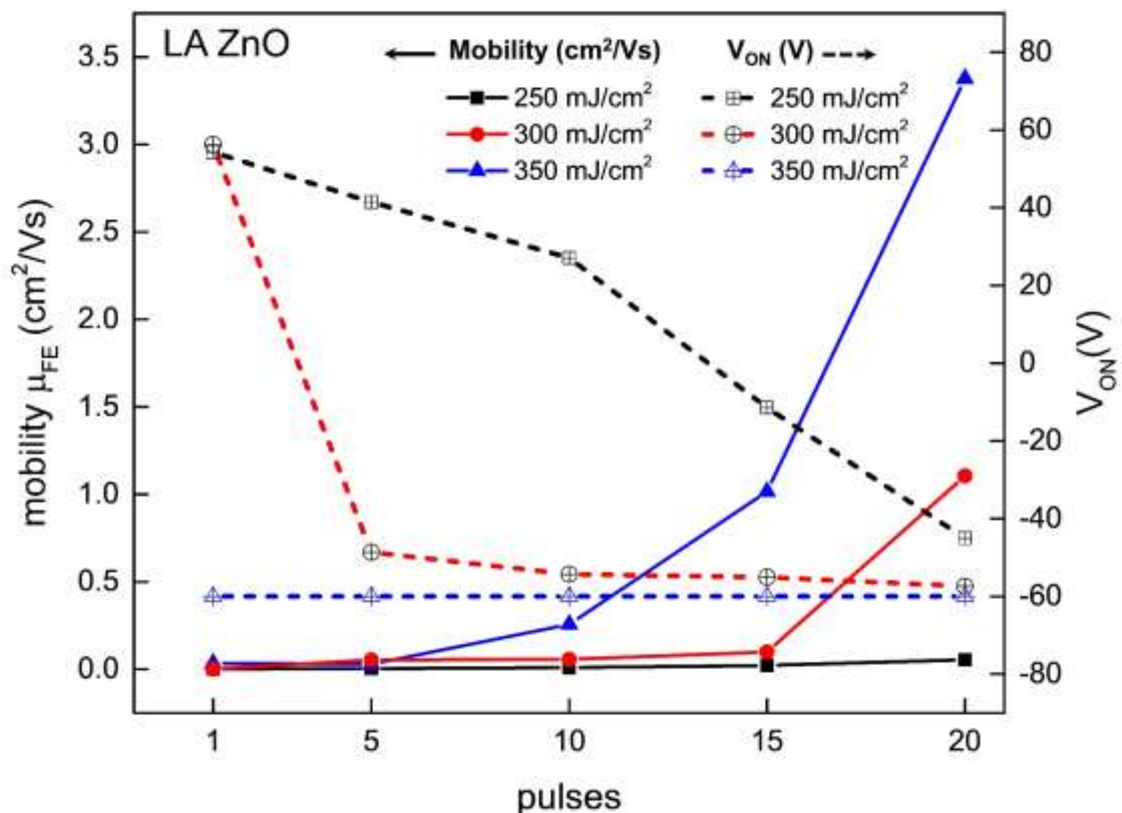

Figure 5-23. Field effect mobility μ_{FE} (solid lines) and V_{ON} values (dotted lines) of sol-gel ZnO TFTs, Laser annealed at 250 (black), 300 (red) and 350 mJ/cm^2 (blue).

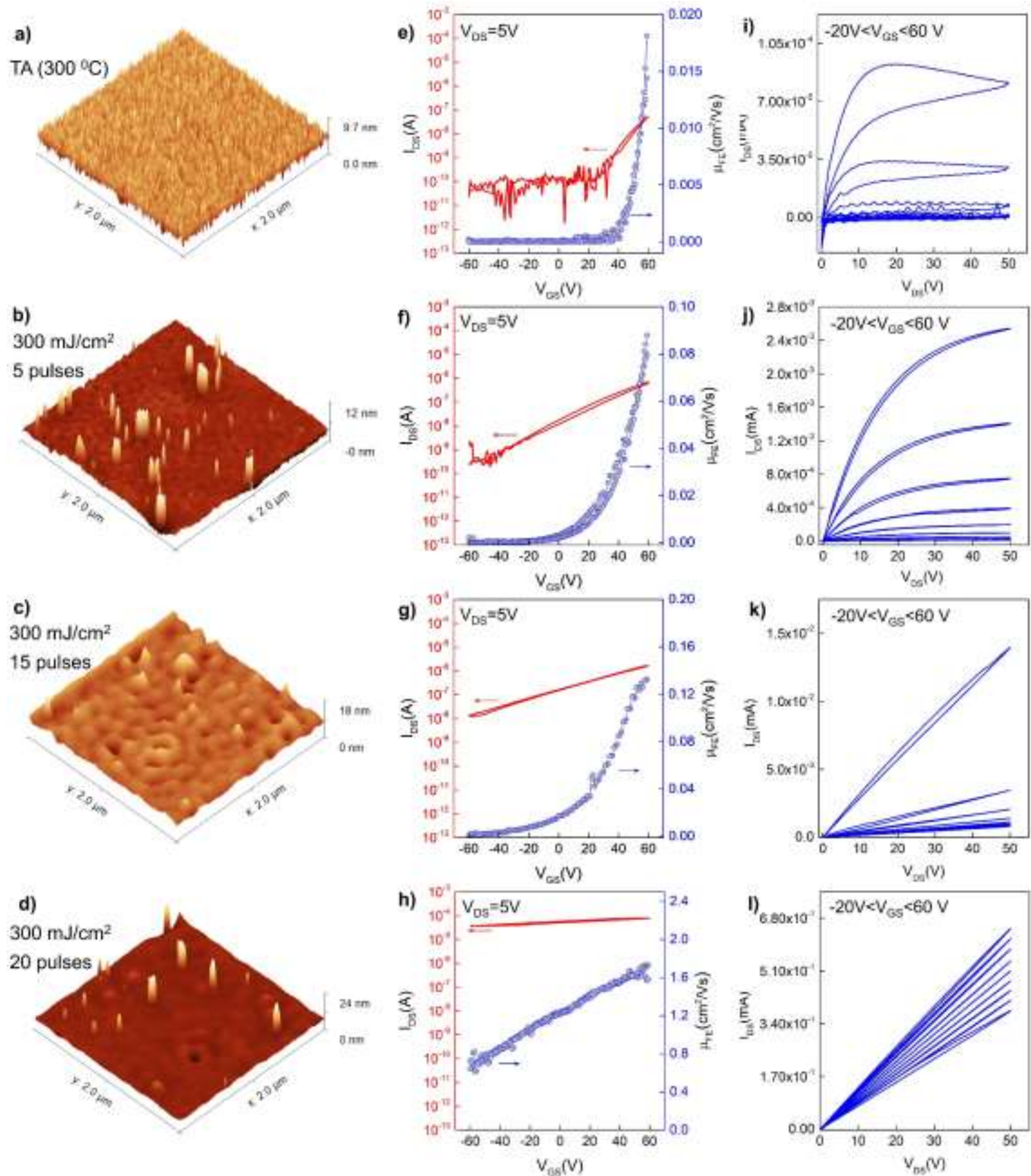

Figure 5-24. AFM images (a-d), transfer (e-h) and output (i-l) plots of thermally ($300\ ^{\circ}\text{C}, 60\ \text{min}$) and Laser Annealed ZnO TFTs, treated at $300\ \text{mJ/cm}^2$, at 5,15 and 20 pulses.

AFM analysis indicates a distinct surface phenomenon occurring from laser annealing, *i.e.,* the rapid melt-mediated re-crystallisation of ZnO. As grain growth is conducted laterally, we assume this is the preferred re-crystallisation direction. Vyasz *et al*. [294] have set the temperature gradient as the origin of lateral re-crystallisation after Laser Annealing, as thermal energy flows laterally more than vertically, before the impingement of the grains occurs, thus enhancing the grain growth. To examine the effect of ZnO morphological changes into the electrical performance of TFTs, the associated transfer and output characteristics are also presented in Figure 5-24e-l. For devices treated at 5 pulses, a switch-off region is detected, with

I_{DS} (red line) reporting a minimum value (I_{OFF}) at 10^{-10} A. Also the highest $\frac{I_{ON}}{OFF}$ amongst these devices is reported ($\sim 10^5$). Interestingly, I_{DS} increases monotonically with gate voltage without signs of saturation at high V_{GS}. Also, according to the output plot (**Figure 5-24j**), no current crowding effect is recorded, possibly due to low resistance ohmic contact between S-D electrodes and Laser Annealed ZnO . A clear transition from linear to saturation region is recorded, without any present hysteresis (as opposed to the thermally annealed device). As the number of pulses increases to 15 and 20 pulses, the change in crystal structure of ZnO is accompanied by a shift of V_{ON} into more negative values. Also, a gradual improvement in ON current is achieved with pulse increase. As seen in **Figure 5-24h** ($300\ mJ/cm^2$, 20 pulses), the device is always switched on, exhibiting high I_{OFF} ($\sim 10^{-5}A$) and poor $\frac{I_{ON}}{OFF}$. The abrupt increase in I_{OFF} can be attributed to an increase in carrier concentration in Laser Annealed ZnO films, particularly at the surface of ZnO films, which remains unaffected by the application of V_{GS}. The increase in carrier concentration has been previously associated to changes in crystal structure induced by Laser Annealing by Nakata *et al.* [295], suggesting that free carriers can be trapped in trap states amongst small grains, which is related to ZnO films with increased resistivity. As crystal grain growth is induced (in our case *via* the increase in LA pulses), current paths are easily formed by larger crystal grains thus I_{DS} is increased, thus suggesting the significant effect of LA on the improvement in ZnO transfer characteristics. The output characteristics of devices treated at ≥ 15 pulses (shown in **Figure 5-24k-l**) reveal a dramatic change in carrier transport – compared to devices treated at 5 pulses. For 15 and 20 pulses, no saturation region is obtained, with devices clearly not exhibiting pinch-off. Particularly for 15 pulses, a jump in I_{DS} is recorded when $V_{GS} = 60$ V is applied. A comparison amongst **Figure 5-23** and **Figure 5-24**, can lead to a correlation between μ_{FE} and changes in I_{ON}. As Laser Annealing induces an increase in I_{ON}, μ_{FE} increases, influenced by the crystalline quality of ZnO films. As many grain boundaries in the ZnO channel cause overlaps of double Schottky barriers and carrier scattering resulting in interference with carrier transport under V_{DS}. μ_{FE} increase is obtained by a reduction in defect concentration over increased pulse number [296].

5.5.1. Melting and Recrystallisation Mechanism

The improvement of electrical characteristics obtained in ZnO TFTs after Laser Annealing is attributed to the change in crystallisation in ZnO films and can be explained as following (**Figure 5-25**): prior to Laser Annealing, as deposited $Zn(CH_3COO)_2$ is presented as a stack of small, closely packed spherical grains. During LA, temperature increase over the grain contact points form hot spots where surface melting occurs, thus merging the spherical grains together. This process leads to grain size enlargement while the grain geometry is changed and any internal gaps in between grains are compacted.

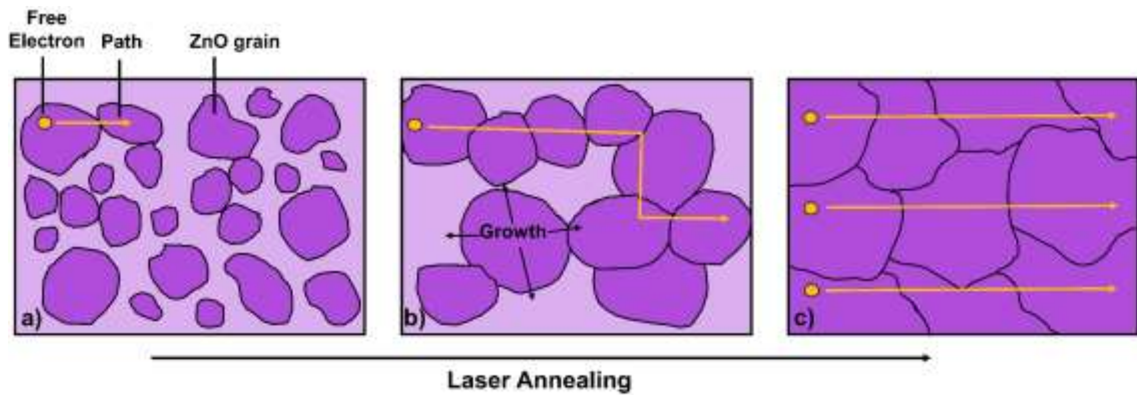

Figure 5-25. Re-crystallisation mechanism of ZnO films due to Laser Annealing effect. As Number of pulses increases, ZnO grains (a) agglomerate into larger grain structures (b), gradually forming a dense (c) film including large ZnO grains. Yellow arrows indicate the electron path during V_{GS} sweep.

The films become denser, where facetted large grains are impinged on each other. During this "grain merging", since the grain shape changes to facetted and impinged on each other, the inter grain defects (like voids and gaps) decrease, along with a drop in film discontinuity. Note that such defects may originally create energy levels in the band gap that tend to trap the free electrons and decrease their lifetime. Consequently, since the initially deposited small size grains are merging after LA thus forming large grains, it is evident to conclude that this effect causes a decrease in grain boundary density (also supported by Kim *et al*. [297]). This decrease along with the reduction in carrier traps at boundaries can shrink the initial grain boundary barrier scattering sites which may lead to degradation in field effect mobility as well as higher V_{ON} values [298]. This mechanism has also been verified theoretically by Nian *et al.* [299] where theoretical and experimental examination of Laser Annealing effect on solution processed AZO films was performed. The above results show that LA annealing can entirely transform the crystal structure of ZnO, which has a direct impact on electrical characteristics of TFT devices, leading to significant improvements in device performance.

Aside from crystal structure transformation during Laser Annealing, the carrier generation mechanism constitutes a point of interest. According to **Figure 5-23**, ZnO carrier concentration N continuously increases over Laser Annealing, as transfer plots indicate the transition of V_{ON} into more negative values. The change in crystal structure can adequately associate to this shift however a correlation to studies focusing on carrier generation in ZnO must also be made. Nagase *et al*. [183] demonstrated a correlation amongst crystal structure and oxygen vacancy formation in Laser Annealed ZnO films. They suggest an increase in oxygen vacancy formation with respect to laser fluence increase as oxygen atoms dissipate easier from the zinc oxide matrix due to induced higher temperatures. Zhang *et al*. [300] have also investigated the formation of oxygen vacancies (V_O) in ZnO during annealing in O_2 − rich

environment. According to their study, three antagonistic effects are occurring during annealing at high temperatures: i) V_O formation due to high temperature, ii) passivation of V_O due to the presence of O_2 and iii) production of defects specific to O_2-rich conditions in the form of peroxide-like diatomic oxygen. despite the presence of O_2 during annealing, a competition between the generation and passivation of oxygen vacancies occurs. This is also demonstrated by Drouilly *et al*. [301], according to which formation and filling of oxygen vacancies are competing processes under oxygenated atmosphere. However, oxygen pressure and temperature have antagonistic roles; under oxygen-rich environment, V_O formation prevails on the latter one at high temperatures (the critical point is defined by O_2 pressure), whereas a filling up process is favoured at below this critical temperature.

In addition to transfer and output plots, **Figure 5-24e-h** presents the mobility evolution of thermally and laser annealed ZnO TFTs. As previously seen in this work, a deconvolution of channel formation can be achieved *via* $\mu_{FE} - V_{GS}$ plots while shedding light to the contribution crystal structure into carrier transport mechanism along the channel. In the case of In_2O_3 and $IGZO$ devices, high concentration N contributed into a mobility increase at early stages of V_{GS} sweep, regardless of the formation of nanocrystals (inducing grain boundaries) as a result of LA. A considerably different $\mu_{FE} - V_{GS}$ trend is observed for ZnO. For thermally annealed and Laser Annealed devices (where ZnO presents a polycrystalline structure with small grains) the increase of mobility with V_{GS} is achieved in much higher V_{GS}, essentially due to the polycrystalline structure of ZnO with small grain sizes, hence large density of grain boundaries. Once the V_{GS} threshold (needed to surpass the grain boundary "barrier"), carriers can travel across the carrier and get collected by drain electrode – hence increase in mobility.

A few models have been proposed to describe quite well the behaviour of polycrystalline TFTs, namely the one demonstrated by Levinson in 1982 [302] and more recently the one of Hossain [303], specifically oriented for ZnO TFTs. From these models the barrier height associated with the depletion regions at the grain boundaries is modulated by the total N, which has contributions both background N and of the charges induced by V_{GS}. Furthermore, for smaller grain sizes the width of the depletion regions can extend deep inside the crystallites and even overlap with adjacent depletion regions, resulting in high resistivity. This comes in excellent agreement with our results, as the increase in crystal size shifts mobility increase towards lower V_{GS}. After Laser Annealing at 20 pulses, the formation of ZnO into large grains has a direct effect on mobility evolution (

Figure 5-24h), as a gradual increase in μ_{FE} is manifested, starting at low V_{GS}.

5.6. Concluding Remarks

The analysis performed in this chapter involved a detailed presentation on Laser Annealing implementation towards fabrication of TFTs based on sol-gel semiconductor films. The principal goal of this work was to explore the association between Laser Annealing and TFT performance beyond the conventional "process optimization" route; hence a holistic approach on the study of performance-associated parameters (i.e. dielectric and semiconductor thickness, air-exposure effect) was performed, with In_2O_3 accounting for the primary material of interest. In fact, a direct impact of dielectric thickness on device electrical performance was manifested, while $200\ nm\ SiO_2$ were associated to the optimum device features (μ_{FE}, V_{ON}, $I_{ON/OFF}$) in accord to laser processing conditions used in this study.

In addition, In_2O_3 thickness increase and long air-exposure also contributed in deconvoluting the Laser Annealing effect on In_2O_3 films. In detail, increase in In_2O_3 thickness revealed a rise in I_{DS} and a shift of V_{ON} towards more negative values (device always on). This result was attributed to the difficulty in formation of depletion region when semiconductor thickness increases. Furthermore, exposure of devices in ambient conditions showed a gradual decrease in I_{DS}, accompanied by a shift of V_{ON} towards more positive values (more effective device switch-off). This effect was assigned to the gradual decrease in carrier concentration N, as Oxygen is adsorbed in the semiconductor interface and fills the oxygen vacancies.

IGZO was also included in materials of study, aiming to elevate the impact of this work by introducing the compositional factor as a parameter of study. Indeed, the role of Ga prevailed a decrease in N, while the high In content ($In: Zn: Ga = 5: 3: 1$) induced similar crystal structure to In_2O_3. As a last material of study, $Zn(CH_3COO)_2$ was employed as starting material towards fabricating TFTs based on Laser Annealed ZnO films. Despite the plethora of reported studies on ZnO TFTs based on $Zn(CH_3COO)_2$ as well as Laser Annealing on vacuum-processed ZnO, no studies have been so far employed Laser Annealing as a manufacturing route of ZnO TFTs based on $Zn(CH_3COO)_2$ to the best of our knowledge. A correlation amongst structural change and electrical performance was conducted, revealing a direct impact of ZnO crystallisation on TFT performance upon Laser Annealing.

This chapter provides insights on the effect of Laser Annealing into the formation of sol-gel MO films, to consolidate the establishment of Laser Annealing as a go-to technique into manufacturing metal-oxide based electronics [112]. In addition, Laser Annealing can be considered as an excellent route towards the optimum merging of metal oxides and flexible substrates – especially when considering the localised (surface) heating effect of this technique while maintaining the substrate unaltered [55]. Therefore, the deconvolution of Laser Annealing

effect on crystal structure and conductivity of infamous metal oxides (such as In_2O_3, IGZO, ZnO), as well as the control of Laser Annealing effect *via* dielectric thickness tuning (studied in this chapter) is essential.

6. Laser Annealed Sol-Gel Thin Film Capacitors

This chapter focuses on the work conducted towards the investigation of Laser Annealed sol-gel metal oxide dielectric films. The principal material involved in this study is ZrO_2, with the corresponding thin films constituting the point of focus when used as dielectric in Capacitor and TFT devices. Despite the outstanding performance of ZrO_2 as a dielectric (high dielectric constant, amorphous nature), no studies involving sol-gel LA ZrO_2 thin films as active materials in electronic devices have been yet reported. Therefore, this study could introduce a novel route towards fabrication of advance performance dielectric films. In this work all films – similarly to semiconductor films of previous chapter- were fabricated *via* sol-gel process, with the precursor conversion being conducted *via* Laser Annealing (LA). To extract information regarding the ZrO_2 precursor conversion, a set of optical characterisation techniques have been employed: first, IRSE analysis of stabilised ($150\,°C$) and thermally treated ($300℃$) ZrO_2 precursor films is employed, aiming to investigate the temperature effect on ZrO_2 precursor. The thermal annealing conditions remain identical to those presented in Chapter 4 and Chapter 5 in order to associate our findings in precursor related by-product removal through the scope of IRSE. As a next step, Optical Reflection Spectroscopy (ORS) of LA treated ZrO_2 films is employed, in order to extract information on the thickness of laser treated films - as thickness is of high importance on the implementation of thin film dielectrics as electrical components. Following the optical characterisation, MOS capacitors based on ultra-thin ZrO_2 films were fabricated *via* Al deposition on top of LA ZrO_2 films, with p-doped Si in the role of substrate. Electrical characterisation ($C-V, C-f$, Breakdown voltage) on the MOS-Capacitor devices followed, aiming to explore the dielectric properties of Laser treated sol-gel ZrO_2 thin films. In addition, surface morphology of ZrO_2 thin films is studied *via* AFM analysis, focusing on the Laser annealing effect on the film roughness. As a final step, laser annealed sol-gel ZrO_2 and In_2O_3 thin films are incorporated into BGTC TFT devices, followed by the associated electrical characterisation (Transfer, Output and Capacitance). This final step constitutes the first reported attempt to incorporate laser annealing towards the fabrication of both dielectric and semiconductor layer based on sol-gel metal oxide films. In addition to ZrO_2, LA sol-gel Al_2O_3 is also incorporated as an active component of TFT devices in the final section of this chapter, aiming to enable a performance comparison amongst two dielectrics as well as highlight the key points during fabrication and characterisation of metal oxide dielectrics.

6.1. IRSE Analysis of ZrO_2 Precursor-Temperature Effect

The fabrication of ZrO_2 thin films based on sol-gel technique primarily requires deep understanding of the chemical paths during transformations of zirconium precursors into the oxide. To do that, one must first choose an appropriate metal salt – in our work Zirconium Acetylacetonate ($Zr(AcAc)_4$) was chosen as a starting material towards ZrO_2 formation. In general, acetoacetonates (beta-di-ketonates) are coordination compounds containing bidentate ligands which are often thermally stable [304] and can be easily prepared for a wide range of metals [305]. The stability constant of the acetoacetonate complex is notably high, which implies that the acetoacetonate is capable of abstracting metals from media in which its concentration is low [306]. Therefore, acetoacetonates can be used in rare metal isolation and use in many applications. For instance, they may be used in the preparation of supported metals or metal oxide catalysts [307].

To explore the thermal effect on ZrO_2 precursor, zirconium acetylacetonate (0.1 M) ($Zr(AcAc)_4$) dissolved in $2-ME$ was used as a precursor solution. The solution was deposited on top of p-Si wafers *via* spin coating, followed by a stabilisation step ($150^0C, 15\ min$) to evaporate the solvent. As a second step, films were thermally annealed at 300^0C for 60 mins to promote the conversion of $Zr(AcAc)_4$ into ZrO_2. IRSE measurements were performed at each thermal treatment step (stabilisation and thermal annealing), aiming to investigate the chemical composition of the $Zr(AcAc)_4$ films as well as gain an understanding of the temperature effect on precursor conversion (which can act as a guide to the LA conditions used later). **Figure 6-1** displays the IRSE measurements (Ψ and Δ) of stabilised (red and blue) and thermally annealed (pink and cyan) $Zr(AcAc)_4$ films. Psi and Delta were fitted (black solid lines, see fitting process in **Chapter 3**) by a set of Gaussian oscillators, presented in **Table 6-1**, aiming to extract the complex permittivity e(w) of $Zr(AcAc)_4$ as per treatment step. **Figure 6-2** presents ε_1 and ε_2 values of stabilised and thermally annealed $Zr(AcAc)_4$, as extracted from Ψ and Δ fittings. A set of absorption peaks are identified in the stabilised $Zr(AcAc)_4$ films (**Figure 6-2**, cyan line), corresponding to precursor related by-products. A set of two peaks at 284 and 396 cm^{-1} are assigned to $Zr-O$ phonon modes. Also, at 617 cm^{-1}, a peak representing propyne ($CH_3-C\equiv CH$) is detected [308]. However, considering the gaseous form of propyne (thus the difficulty in propyne detection during an ellipsometric measurement), this peak entails further investigation. The presence of propyne is indicative of the decomposition process of $Zr(AcAc)_4$, which involves the formation of a zirconium acetate-acetoacetonate complex:

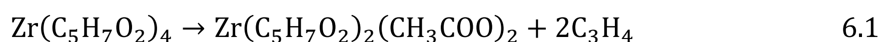

$$Zr(C_5H_7O_2)_4 \rightarrow Zr(C_5H_7O_2)_2(CH_3COO)_2 + 2C_3H_4 \qquad 6.1$$

In addition, absorption peaks at $1016\ cm^{-1}$ (ρCH_3), $1403\ cm^{-1}$ ($\delta_s CH_3$), $1548\ cm^{-1}$($\nu_{c-o}+\nu_{c-c}$) reveal the presence of acetate (CH_3COO) [309], where ν is stretching, δ in plane bending

or deformation and ρ rocking mode [137]. The Subscript s denotes degenerate symmetric modes.

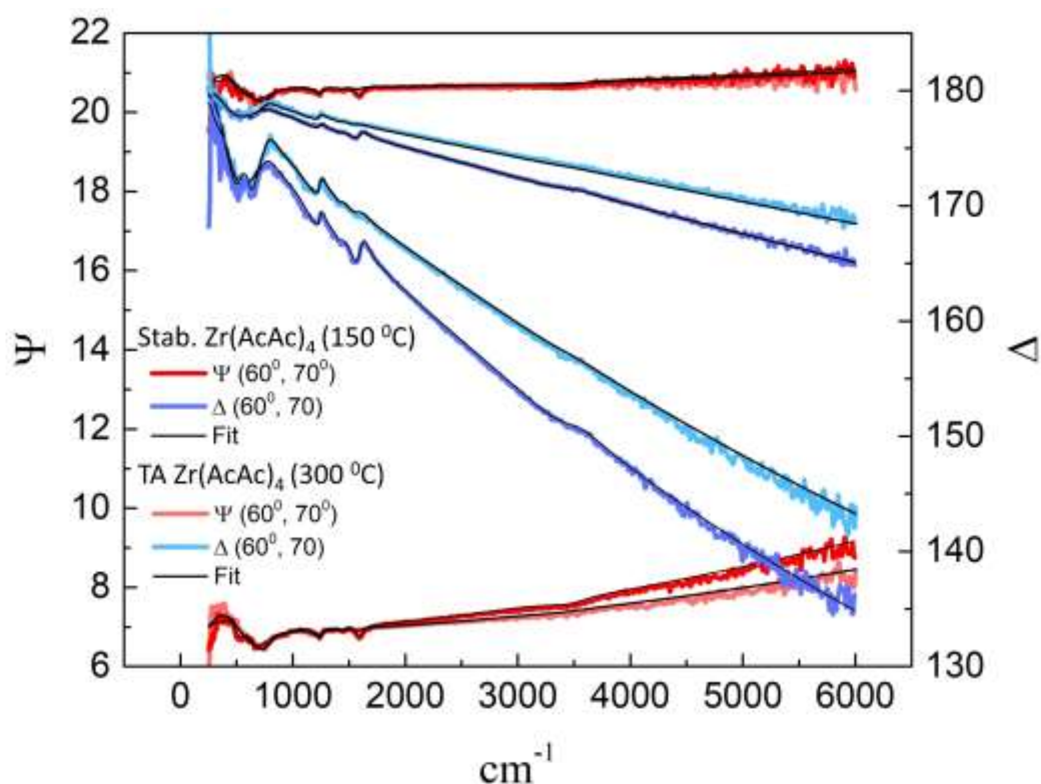

Figure 6-1. IRSE (Ψ and Δ) measurements, at 60^0 and 70^0 of incidence, of stabilised ($150\ °\mathrm{C}, 15\ \mathrm{min}$) and thermally annealed ($300\ °\mathrm{C}, 60\ \mathrm{min}$) $\mathrm{Zr(AcAc)_4}$ thin films. Ψ values are presented in red (stabilised) and light pink lines (thermally annealed). Δ is displayed in blue (stabilised) and cyan (thermally annealed). Alongside Ψ and Δ, the corresponding fitting is shown in black solid lines. The fitted values are associated to the corresponding opto-geometric model that includes a stack of Si substrate, a native SiO2 and $\mathrm{Zr(AcAc)_4}$.

A peak at $3323\ \mathrm{cm}^\wedge - 1$ is detected, associated to $-\mathrm{OH}$ molecules found in the zirconium acetate-acetoacetonate complex. Particularly for the peak at $1548\ \mathrm{cm}^{-1}$ ($\nu_{\mathrm{c-o}} + \nu_{\mathrm{c-c}}$), the confirmation of the presence of acetate after treatment of $\mathrm{Zr(AcAc)_4}$ at $100 - 200^0\mathrm{C}$ (in our case, $150^0\mathrm{C}$) reportedly indicates that the presence of the oxygen bonded to zirconium introduces a strain in one of the two acetonates [304], which makes the complex decomposition easier – a precious finding for the choice of laser annealing conditions. A clear change on the complex permittivity of $\mathrm{Zr(AcAc)_4}$ films is observed after thermal annealing (**Figure 6-2**, pink and blue lines). The most prominent detected peak is located at $350\ \mathrm{cm}^{-2}$, associated to $\mathrm{Zr-O}$ phonon mode [137,310]. During fitting, two Gaussian oscillators were employed for the corresponding feature, the wavelengths of which are presented in **Table 6-1**. Also, the peaks associated to $\delta_{\mathrm{s}}\mathrm{CH_3}$ [311], $-\mathrm{OH}$ and $\nu_{\mathrm{c-o}} + \nu_{\mathrm{c-c}}$ are detected, however the peak intensity drops significantly compared to the stabilised film, thus indicating the promotion

of by-product removal. An absorption peak at $1080\ \mathrm{cm^{-1}}$ is also detected, which has been previously associated to the presence $\mathrm{ZrO(CH_3COO)_2}$ [311].

The presence of a $\mathrm{ZrO(CH_3COO)_2}$ associated peak manifests the decomposition of $\mathrm{Zr(C_5H_7O_2)_2(CH_3COO)_2}$ through the following reaction:

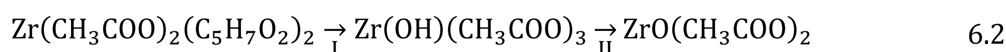

$$\mathrm{Zr(CH_3COO)_2(C_5H_7O_2)_2} \underset{\mathrm{I}}{\rightarrow} \mathrm{Zr(OH)(CH_3COO)_3} \underset{\mathrm{II}}{\rightarrow} \mathrm{ZrO(CH_3COO)_2} \qquad 6.2$$

The absorption peaks observed in **Figure 6-2** after thermal annealing at 300 °C manifest a "freeze" in transformation of $\mathrm{Zr(AcAc)_4}$ into $\mathrm{ZrO_2}$, at the stage of acetate formation. This has already been reported by Ismail et.al [304] , where annealing of $\mathrm{Zr(AcAc)_4}$ at $250-350^0\mathrm{C}$ led in detection of almost all of the characteristics of acetate anions (at $1560-600\ \mathrm{cm^{-1}}$). This result has already been observed in Chapter 4, where acetate-related by-products were detected during thermal annealing of $\mathrm{Zn(CH_3COO)_2}$ at 300 °C.

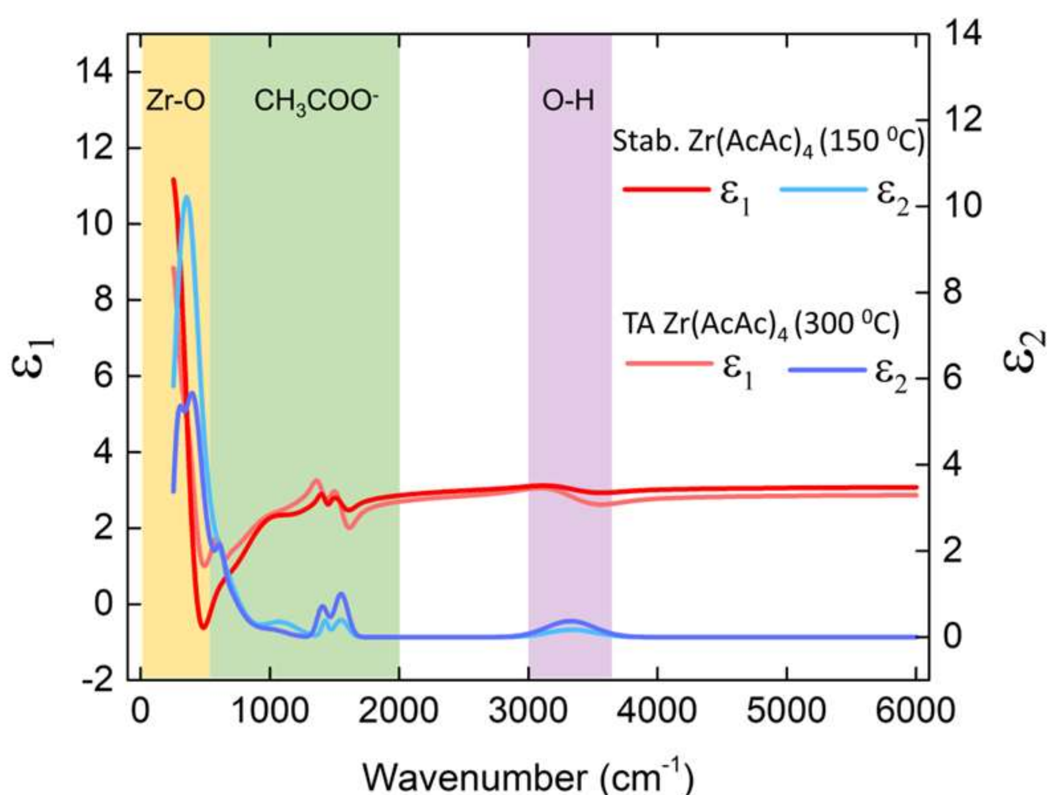

Figure 6-2. Real (ε_1) and imaginary (ε_2) parts of complex permittivity of stabilised ($150^0\mathrm{C}, 15\ \mathrm{min}$) and thermally annealed ($300^0\mathrm{C}, 60\ \mathrm{min}$) $\mathrm{Zr(AcAc)_4}$. ε_1 and ε_2 of stabilised $\mathrm{Zr(AcAc)_4}$ are presented in red and blue lines, while ε_1 and ε_2 of thermally annealed $\mathrm{Zr(AcAc)_4}$ is shown in light pink and cyan, respectively. The extraction of ε_1 and ε_2 was conducted *via* fitting of Ψ and Δ, shown in **Figure 6-1** in black lines. The graph is divided in 4 colour-coded regions: yellow area where $\mathrm{Zr-O}$ associated phonon modes are detected, green area for acetate-associated phonons modes, lilac area for hydroxyl ($-\mathrm{OH}$) phonon modes and white area where no spectral features are detected. The wavelength where individual phonon modes are located is presented in **Table 6-1**.

Table 6-1. ε_2 peaks of stabilised ($150\ °C$, $15\ min$) and thermally annealed (TA) ($300\ °C, 60\ min$) $Zr(AcAc)_4$ films, along with their corresponding interpretations and references.

Stabilised $Zr(AcAc)_4$ (cm^{-1})	TA $Zr(AcAc)_4$ (cm^{-1})	Interpretation	References
284	350	$Zr - O$	[309][137] [310]
396	388	$Zr - O$	[309][137] [310]
617	$-$	$CH_3 - C = CH$	[308] [309] [310]
1016	1080	ρCH_3	[309] [311]
1403	1427	$\delta_s CH_3$	[309]
1548	1548	$\nu_{c-o} + \nu_{c-c}$	[309]
3323	3339	$-OH$	[309][137]

6.2. Electrical Performance of ZrO_2 MOS Capacitors

IRSE analysis on stabilised and thermally annealed $Zr(AcAc)$ films revealed the initiation of precursor decomposition under treatment at 300^0C, where the $Zr - O$ associated absorption peak intensity increases with concurrent decrease of the corresponding acetate peaks. However, by-product removal at this temperature is not complete, as the dissolution of acetate complexes demands higher temperature treatments. This observation stands in good agreement with results presented in **Chapter 4** where acetate by-product analysis was performed through the scope of $Zn(CH_3COO)_2$, under similar thermal treatment conditions. Following the IRSE investigation regarding the behaviour of $Zr(AcAc)_4$ under thermal treatment, fabrication of LA sol-gel ZrO_2 thin films was conducted, for the purpose of use as a dielectric layer in metal oxide capacitor devices. This step constitutes a move towards the goal of this chapter, as the optimisation of LA sol-gel ZrO_2 thin films would enable their use as a dielectric in TFT devices. Since the point of attention is concentrated in the electrical performance of ZrO_2 films, a set of electrical measurements were performed ($C - V, C - f$, dielectric breakdown), aiming to verify the use of LA ZrO_2 as a dielectric. In addition, the dielectric film thickness was also investigated with respect to fabrication parameters, due to the importance of dielectric thickness in device performance. After the extraction of optimum fabrication parameters which led to best electrical performance, surface morphology investigation was also performed, to investigate the dielectric surface, as it constitutes a key-point towards the channel formation in BGTC TFTs.

The first step towards optimisation of ZrO_2 thin films involved the use of 0.1 M $Zr(AcAc)_4$, dissolved in $2 - ME$. Precursor films were deposited in p^{++} Si substrates *via* spin coating ($4000\ rpm, 30\ sec$), with stabilisation conditions of 150^0C for 15min, similarly to Chapter 4 and Chapter 5. LA fluence conditions varied from $200 - 275\ mJ/cm^2$, while films were treated under 1,2 and 3 pulses. To monitor the thickness effect in electrical performance, films of 1, 2 and 3 layers (i.e. successive spin coatings) were deposited. After each spin coating step, films underwent stabilisation ($150\ °C$) for a few seconds (for solvent removal), to avoid "uneven" stabilisation time amongst 1, 2 and 3-layered films. Alongside LA films, thermally annealed films are also used as a reference. Figure 6-3 displays the change in thickness with

respect to laser fluence and pulses for ZrO_2 films where 1, 2 and 3 layers are deposited during spin coating. Thickness measurements were performed with Optical Reflection Spectroscopy (ORS) and VIS-UV Spectroscopic Ellipsometry (see **Chapter 3** for details on thickness extraction and data fitting). Evidently, the LA effect is highly dependent on the initial film thickness, as different trends are observed in LA films of 1, 2 and 3 layers. In 1 layer, LA causes a significant decrease in thickness, reaching values close to zero. A thickness decrease is well expected during annealing, due to film densification, however in the case of 1 layer this decrease has proved inappropriate the use of 1 layer LA ZrO_2 when accounting for the objective of this work, namely the use of ZrO_2 as gate dielectric in TFTs.

At such low thicknesses (close to $0\ \mathrm{nm}$), thin film discontinuities as well as tunnelling effects prevail, therefore the dielectric role is questioned. The transition to 2-layered ZrO_2 films, however, displays a different behaviour in thickness variation. For 200 and $250\ \mathrm{mJ/cm^2}$ (red and orange lines, respectively), thickness shows a slight decrease, while this set of fluences presents almost identical resulting thicknesses. However, a fluence increase at $275\ \mathrm{mJ/cm^2}$ is accompanied with thickness decrease to $< 10\ \mathrm{nm}$ (dark yellow line). This implies the presence of a "fluence threshold", above which the film thickness drops significantly. For 3 layer films, a thickness decrease is observed with fluence increase, with thickness values of films treated at 250 and $275\ \mathrm{mJ/cm^2}$ varying from $15 - 19\ \mathrm{nm}$.

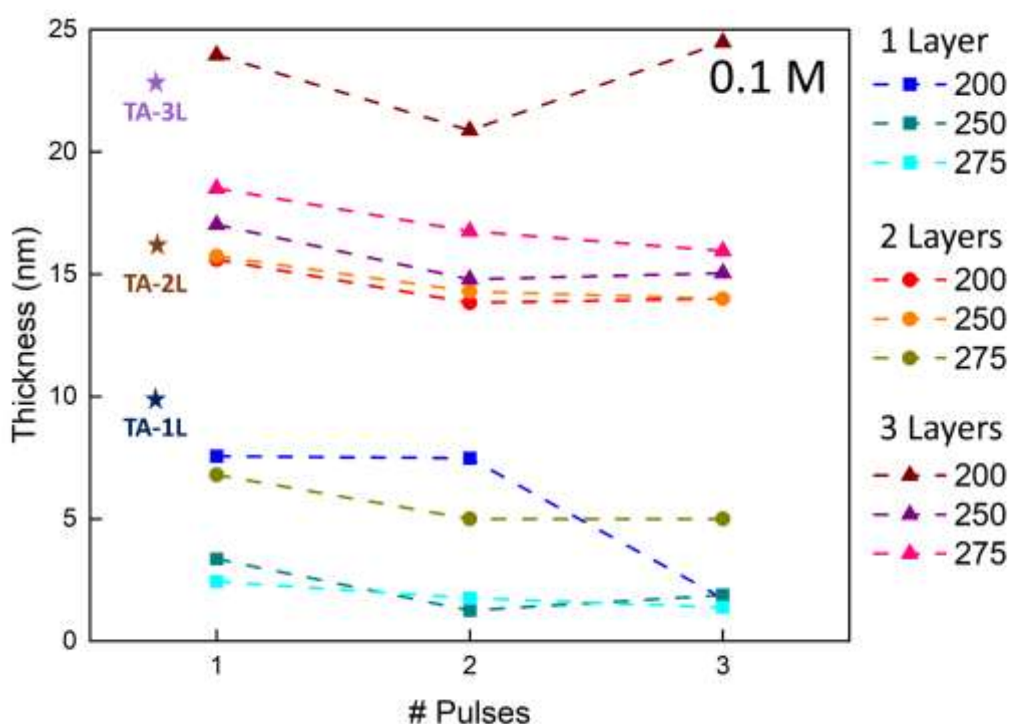

Figure 6-3. Thickness values of LA sol-gel ZrO_2 thin films, based on 1, 2 and 3-layered stacks. The solution concentration was kept constant at $0.1\ \mathrm{M}$, with $\mathrm{Zr(AcAc)_4}$ as metal oxide precursor and $2-\mathrm{ME}$ as a solvent. Films were deposited *via* spin coating ($4000\ \mathrm{rpm}, 30\ \mathrm{s}$). As LA parameters, 3 sets of laser fluence ($200, 250, 275\ \mathrm{mJ/cm^2}$) and

number of pulses (1,2 and 3) were used. Stars denote thicknesses of TA samples (TA-1L, TA-2L and TA-3L correspond to thermally annealed 1,2 and 3 layered films).

Following the thickness analysis, electrical characterisation of the corresponding films was employed. To realise this, Al electrodes of $1\ \mathrm{mm}$ in diameter were deposited *via* thermal evaporation atop of LA areas, thus forming MOS capacitor devices. **Figure 6-4** displays the $\mathrm{C-V}$ characteristics based on $\mathrm{ZrO_2}$ thin films of 1, 2 and 3 layers. For all 3 sets, an increase in capacitance values is observed with respect to laser fluence increase. This can be directly associated to thickness decrease (**Figure 6-3**), due to:

$$\mathrm{C} = \frac{\mathcal{E}_0 \mathrm{kA}}{\mathrm{d}} \qquad 6.3$$

where C is the capacitance, k is the dielectric constant, A is the electrode area and d is the dielectric thickness. Note that **Eq.6.3** is used to extract k values later in the text. For devices based on 1 layer $\mathrm{ZrO_2}$, the highest Capacitance values are observed, reaching $0.95\ \mathrm{\mu F/cm^2}$. Dual voltage scanning is employed during the $\mathrm{C\text{-}V}$ measurements, to identify any hysteresis during reverse bias. The results show a well-defined accumulation region under negative bias of the top electrode, as the negative voltage increases the formation of carrier accumulation at the $\mathrm{ZrO2-Si}$ interface, thus increasing the capacitance values. When a positive bias is applied, the depletion region is induced, therefore the capacitance decreases [312]. No presence of hysteresis is observed, indicating the absence of potential charge trapping sites in dielectric/substrate (or electrode) interface, as well as incomplete precursor conversion (where precursor-related by-products can also act as charge trapping sites). The same behaviour is seen in devices based on 2 layers of $\mathrm{ZrO_2}$, where Capacitance values drop significantly – possibly due to thickness increase. However, for 3-layered films, the corresponding behaviour is dominated by the presence of hysteresis, possibly due to film non-uniformities due to the multiple coatings. To further investigate the device performance, $\mathrm{C-f}$ measurements were additionally performed. Since the ultimate purpose of $\mathrm{ZrO_2}$ optimisation is its use as a dielectric layer in TFT devices, note that field effect devices (such as TFTs) work in accumulation based on channel formation in the dielectric-semiconductor interface. Therefore, $\mathrm{C-f}$ measurements are performed in accumulation region ($\mathrm{V_{ac} = -3V}$). **Figure 6-5** displays the associated capacitance values of MOS capacitors based on 1, 2 and 3 layers of $\mathrm{ZrO_2}$. For 1 layer, apparent frequency dispersion can be detected, regardless of LA parameters. This dispersion can be attributed to two phenomena: the low thickness and charge trapping sites. In the case of 1 layered dielectric, the significantly low thickness values are suggested to be the dominant origin of frequency dispersion. This argument is supported by the elimination of frequency dependency in 2-layered dielectrics, where thickness increases. However, at fluences higher than $250\ \mathrm{mJ/cm^2}$,

frequency dispersion reappears (the same LA condition where a significant drop in thickness is manifested – see **Figure 6-3**).

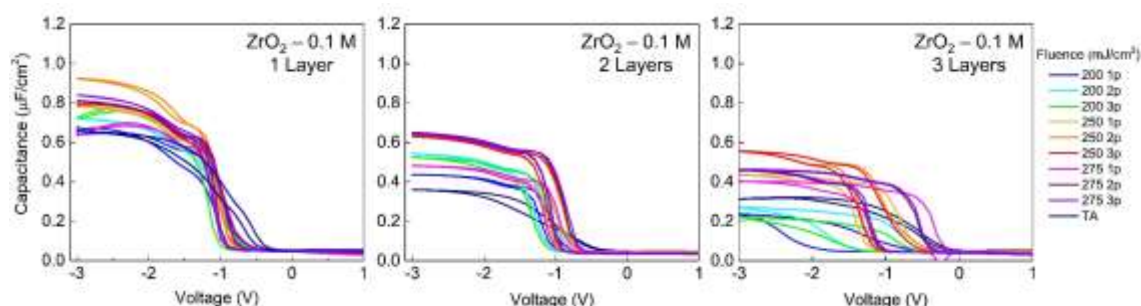

Figure 6-4. Capacitance- voltage $(\mathrm{C-V})$ measurements of MOS-Capacitor devices, with sol-gel Laser Annealed $\mathrm{ZrO_2}$ as a dielectric. The solution concentration was chosen at $0.1\ \mathrm{M}$. C-V characteristics are divided in 3 panels, corresponding to the number of deposited precursor $(\mathrm{Zr(AcAc)_4})$ layers *via* spin coating deposition. Laser fluences varied from $200-275\ \mathrm{mJ/cm^2}$. The number of pulses selected for each laser fluence was set to $1, 2$ and 3. Highly doped Silicon $(\mathrm{p-Si^{++}})$ is used as a substrate to $\mathrm{ZrO_2}$ films, therefore, accumulation region is formed in negative voltage values. The Voltage sweep window was set at $-3 < \mathrm{V} < 1\ \mathrm{V}$ to examine the device operation regions. Thermally evaporated Al constitutes the bottom and top electrode material. Device performance of thermally annealed (TA) $\mathrm{ZrO_2}$ dielectric films is also depicted in navy blue.

Interestingly, in 3-layered $\mathrm{ZrO_2}$ MOS devices, frequency dependency re-appears regardless of LA conditions; considering the increase in thickness, one could consider the presence of charge carrier traps thus the response of trap charges to signal frequency. At low frequencies, some of the traps can easily follow the change in gate bias voltage and thus contribute to the capacitance values (which are similar to the corresponding maximum values in $\mathrm{C-V}$ measurements). However, as frequency increases, the slow trapping and de-trapping processes cannot respond rapidly to the gate bias change, therefore the capacitance in accumulation region decreases. Nevertheless, due to the use of low thickness dielectric films in this work $(< 50\ \mathrm{nm})$ one must always consider the frequency dispersion based on conduction mechanisms through a metal oxide insulator such as Schottky emission, Fowler – Nordheim tunnelling as well as direct tunnelling [313]. Since MOS devices based on 2-layered $\mathrm{ZrO_2}$ thin films exhibited the best performance based on $\mathrm{C-V}$ and $\mathrm{C-f}$ characteristics, a deeper investigation on the dielectric constant k of these films was performed. **Figure 6-6** displays the extracted k values of 2-layered $\mathrm{ZrO_2}$ film, based on $\mathrm{C-V}$ graph shown in **Figure 6-5** and thicknesses shown in **Figure 6-3**. This graph can be divided in three (colour-coded) regions; region 1 (light yellow) where lowest k values and slight frequency dispersion are seen, region 2 (light blue) where the lowest frequency dispersion is observed and region 3 (lilac) where highest dispersion and k values are shown. Starting from region 1, the lowest k values correspond to films treated at the highest laser fluence values $(275\ \mathrm{mJ/cm^2})$.

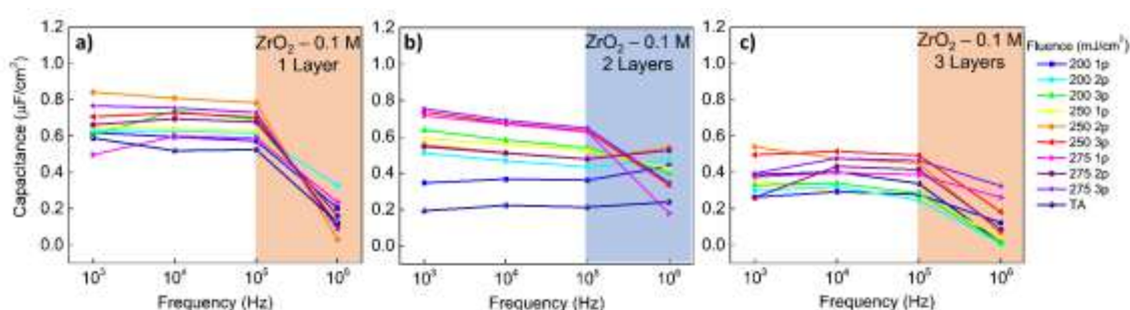

Figure 6-5. Capacitance- frequency measurements of MOS-Capacitor devices, with LA $\mathrm{ZrO_2}$ as a dielectric. The solution concentration was chosen at $0.1\ \mathrm{M}$. C-V measurements are divided in 3 panels, corresponding to the number of deposited precursor ($\mathrm{Zr(AcAc)_4}$) layers *via* spin coating deposition. Laser fluences varied from $200 - 275\ \mathrm{mJ/cm^2}$ The number of pulses selected for each laser fluence was set to 1, 2 and 3. Frequency is swept from $1\ \mathrm{kHz}$ to $1\ \mathrm{MHz}$ while stress voltage is kept at $-3\ \mathrm{V}$. Each panel contains a shaded area where the highest Capacitance – frequency dispersion is detected. For $\mathrm{C - f}$ measurements corresponding to 2 Layers of deposited $\mathrm{ZrO_2}$ precursor (b), the shaded area is presented in blue to highlight the improved device performance in comparison to (a) and (c).

Despite the lack of frequency dependence in devices annealed at 1 pulse (magenta), dispersion is observed in 2 and 3 pulses, possibly due to the decrease in film thickness which promotes the tunnelling phenomena (thus deteriorating the ability of dielectric to store charge – a qualitative description of dielectric constant). Low k values (< 4) along with the presence of frequency dispersion in region 1 indicate the unsuitability of such high fluences, rendering $250\ \mathrm{mJ/cm^2}$ as a fluence threshold towards optimisation of LA conditions used in $\mathrm{ZrO_2}$. Region 2 (light blue) includes k values corresponding to $\mathrm{ZrO_2}$ films treated at the lowest fluence values, along with thermally annealed (navy blue) films. For films treated at 1 pulse (200 and $250\ \mathrm{mJ/cm^2}$), dielectric constant does not show any frequency dispersion. However, as pulses increase, a slight drop in dielectric constant appears at higher fluences (green and turquoise lines), thus indicating a deterioration of device performance. Since no significant drop in thickness is manifested under these LA conditions, a possible reasoning would be the enhancement in crystallisation which leads to the introduction of grain boundaries resulting in leakage current paths [314]. Region 3 displays dielectric constant evolution of $\mathrm{ZrO_2}$ films ($250\ \mathrm{mJ/cm^2}$, 2 and 3 pulses) presenting the highest frequency dispersion. At low frequencies, k values reach a maximum value of 12, while a significant drop is reported at $1\ \mathrm{MHz}$.

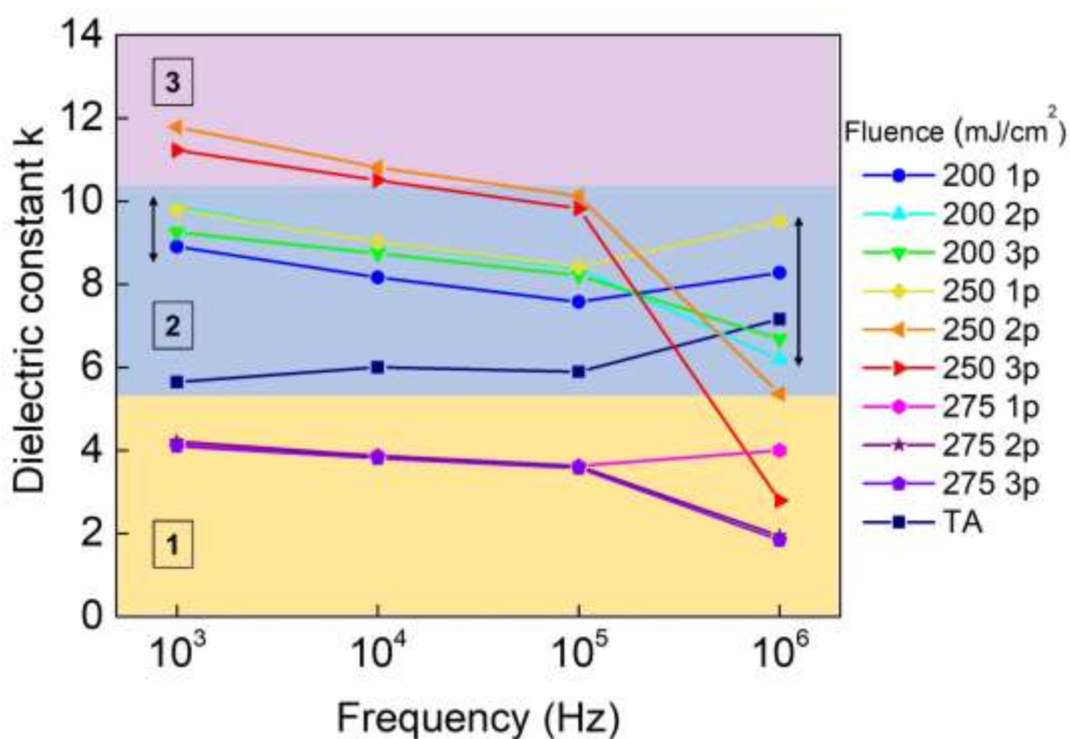

Figure 6-6. Dielectric constant values (k) along with the corresponding frequency dependence of MOS-Capacitor devices with Laser annealed $\mathrm{ZrO_2}$ as a dielectric. The solution concentration was chosen at $0.1\ \mathrm{M}$ while the number of layers was chosen at 2. The extraction of k values was based on Capacitance values presented in Figure 6-5, with corresponding thicknesses shown in Figure 6-3. Three colour coded regions are presented. Region 1 (light yellow) corresponds to devices with low k and high frequency dispersion, region 3 (light blue) includes the optimum capacitor behaviour and region 3 (lilac) corresponds to devices exhibiting high k alongside high frequency dispersion. In region 2, black arrows on left and right highlight the change in k with frequency increase.

Considering no significant changes in thickness amongst these LA conditions, this behaviour could be attributed to crystallisation enhancement as well as impurity content. In both cases, the presence of interface states (other induced by increased roughness in high crystalline $\mathrm{ZrO_2}$ or carbon-related trap charges) may be an essential reason for capacitance (and thus k) variation at different frequencies. At low frequencies, a frequency-dependent interface capacitance ($\mathrm{C_{it}}$) is created due to the modulation of interface states by the AC signal. At high frequencies, these states cannot follow the change in AC signal, therefore the contribution of $\mathrm{C_{it}}$ to the total capacitance is almost zero [315]. According to the analysis above, the performance of MOS capacitors based on LA $\mathrm{ZrO_2}$ thin films is highly dependent on the annealing conditions used during precursor conversion. For fluences above $275\ \mathrm{mJ/cm^2}$, frequency dispersion is apparent in all devices, with tunnelling effects becoming the most dominant conduction mechanism within the insulator. This can also be cross referenced with a significant thickness decrease. Therefore the next step towards optimisation of $\mathrm{ZrO_2}$ is a re-

adjustment of laser fluence window to lower fluences. In addition, the number of layers comprising the final film has a strong effect on the final performance, as layer increase may introduce interface traps amongst the layers, which may act as leakage paths. However, the choice of multiple layers constitutes an effective way to increase the thickness, a parameter quite significant for the insulator properties. To obtain thickness increase, the second step towards ZrO_2 film optimisation was the increase in solution concentration to $0.15\ M$. A new set of samples based on this solution concentration was fabricated, with laser fluences dropping to $200/225/250\ mJ/cm^2$, while the number of pulses was identical to the previous set. Figure 6-7 displays the $C-V$ characteristics of MOS capacitors based on the new solution concentration ($0.15\ M$). Similarly to $0.1\ M$, devices based on 1 layer display large Capacitance values, possibly due to the decreased film thickness. This behaviour is not present in 2-layered films, where maximum capacitance values (in accumulation region) drop significantly. Especially for 2 layers, most LA conditions lead to similar capacitance values, with only exception the film annealed at $250\ mJ/cm^2$ with 3 pulses. Aside this condition, the rest characteristics show well-defined accumulation region at negative voltages applied at the top contact. This is due to a fast accumulation rate of electrons at the $Si-ZrO_2$ interface, which acts as a parallel-plate capacitor with capacitance equal to ZrO_2 capacitance.

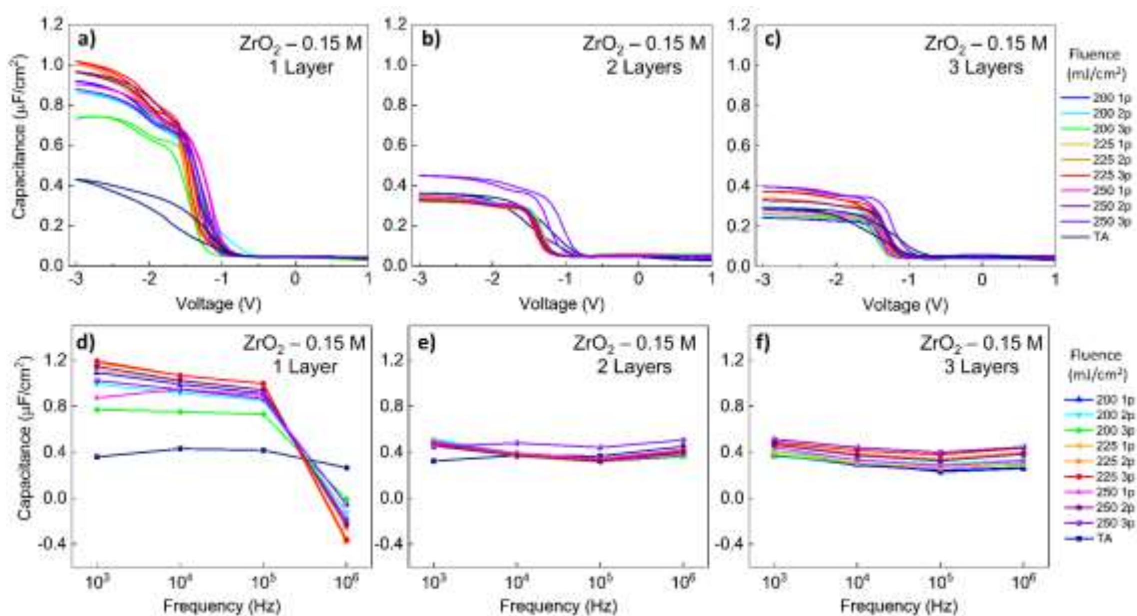

Figure 6-7. (a-c) Capacitance – Voltage ($C-V$) and (d-f) Capacitance- Frequency ($C-f$) measurements of MOS-Capacitor devices, with LA ZrO_2 as a dielectric. The solution concentration was chosen at $0.15\ M$. $C-V$ and $C-f$ measurements are divided in 3 panels, corresponding to the number of deposited precursor ($Zr(AcAc)_4$) layers *via* spin coating deposition. Laser fluences varied from $200-250\ mJ/cm^2$ The number of pulses selected for each laser fluence was set to 1, 2 and 3. Frequency is swept from $1\ kHz$ to $1\ MHz$ while stress voltage is kept at $-3\ V$. Thermally annealed (TA) measurements are also presented in navy blue.

Under positive bias, a depletion region is formed, leading to the $\mathrm{ZrO_2}$ capacitance and the depletion region capacitance being in series, resulting in a decrease of the total capacitance. The curves corresponding to LA films show the typical MOS-Capacitor characteristics without hysteresis, indicating a good quality dielectric-Si interface. In contrast, TA device (navy line) shows hysteresis which may be related to the presence of charge trapping, possibly due to the presence of carbon-related by-products. In addition, TA device presents a less abrupt transition to accumulation (in comparison to LA devices), which is reportedly correlated to charge trapping sites in the dielectric-Si interface [316]. For 3-layered $\mathrm{ZrO_2}$ based capacitors, a broader window in Capacitance values is manifested, with a direct dependence of $\mathrm{C_{max}}$ values upon laser fluence and number of pulses. Capacitance-frequency characteristics (**Figure 6-7**) presents the effect of multiple layers on device performance. For 1 layer of $\mathrm{ZrO_2}$, significant frequency dispersion is observed in all LA devices, in contrast to the thermally annealed one, where capacitance remains almost constant. This significant deterioration in device performance at high frequencies led us to discard any further investigation of 1-layered devices, thus continuing our investigation based on 2 and 3 layers of dielectric. For 2 layers, no dispersion was detected, with most devices presenting almost similar C values versus frequency.

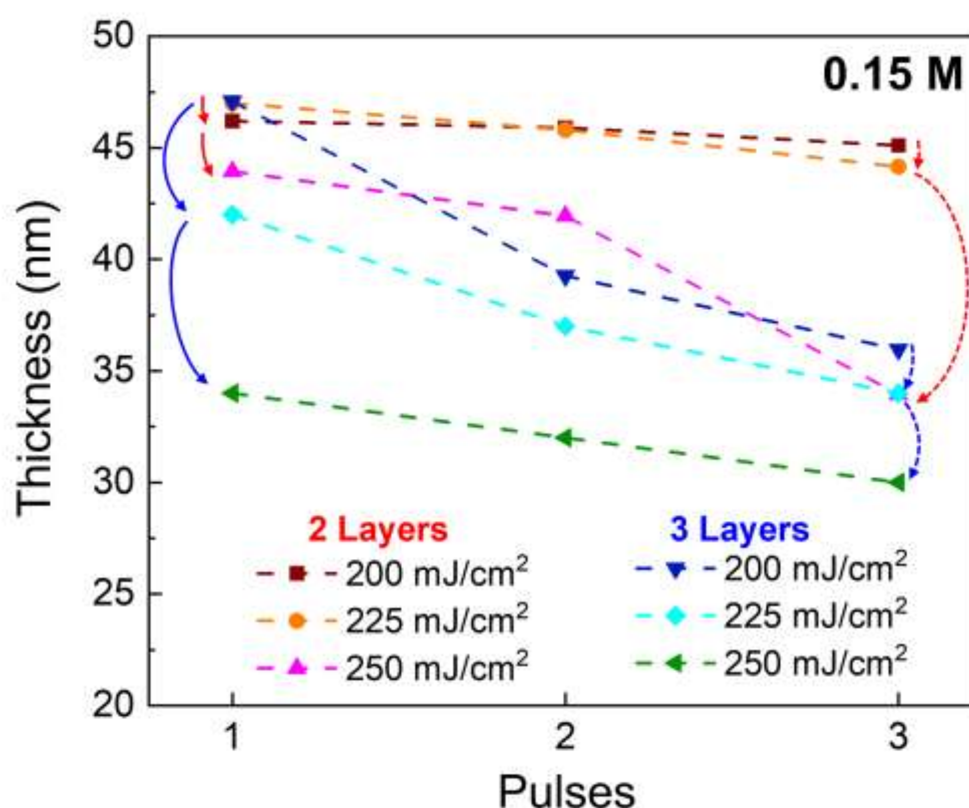

Figure 6-8. Thickness values of LA sol-gel $\mathrm{ZrO_2}$ thin films, based on 2 and 3-layered stacks. The solution concentration was kept constant at $0.15\ \mathrm{M}$, with $\mathrm{Zr(AcAc)_4}$ as metal oxide precursor and $2-\mathrm{ME}$ as a solvent. Films were deposited *via* spin coating ($4000\ \mathrm{rpm}, 30\ \mathrm{s}$). As LA parameters, 3 sets of laser fluence ($200, 225, 250\ \mathrm{mJ/cm^2}$) and number of pulses (1,2 and 3) were used.

At high frequencies, 3-layered ZrO_2 devices treated at lower fluences exhibit the lowest Capacitance values, possibly due to remaining carbon-related by-products. **Figure 6-8** present the thickness values of 2 and 3 layered ZrO_2 films, after LA. Interestingly, for 2-layered films, similar thickness values are observed for films treated at 200 and $225\ \mathrm{mJ/cm^2}$. The effect of LA on thickness becomes more apparent in films treated at $250\ \mathrm{mJ/cm^2}$ (magenta line), where the role of pulses also prevails. Especially for 3 pulses, thickness drops significantly, an effect that can be correlated to the increase in capacitance values in **Figure 6-7**. In contrast to 2-layered films, a significant LA effect on thickness of 3-latered films is seen. For $200\ \mathrm{mJ/cm^2}$ and 1 pulse, thickness is similar to 2 layers, however a dramatic decrease is seen as fluence and pulses increase, leading to films $< 35\ \mathrm{nm}$ when treated at $250\ \mathrm{mJ/cm^2}$. This deviation amongst thicknesses can be associated to the larger window of Capacitance values seen in **Figure 6-7**. One possible explanation on the deviation observed amongst 2 and 3 layered ZrO_2 thicknesses could arise from the role of LA towards film densification. As films are deposited during subsequent spin coatings, a set of interface defects are formed, such as free $-OH$ radicals, H_2O molecules (spin coatings take place in ambient conditions) and discontinuities on the surface of each layer. During LA, the elimination of such interface defects (accompanied by removal of precursor-related by-products) promotes film compactness to a great extent. This phenomenon occurs in all multi-layered films; however, it could appear more significant in 3-layered films. Based on the above thicknesses, dielectric constant values were then calculated with respect to frequency change (**Figure 6-9**). The highest k values are reported for 2-layered ZrO_2 films, reaching values of 27. No large deviation is observed in k values of 2-layered ZrO_2, with films treated at $250\ \mathrm{mJ/cm^2}$ exhibiting the lowest dielectric constant values. For 3-layered films, k is highly dependent on LA parameters, as a notable decrease is observed with fluence increase. Especially for $250\ \mathrm{mJ/cm^2}$, k drops to ~ 8.

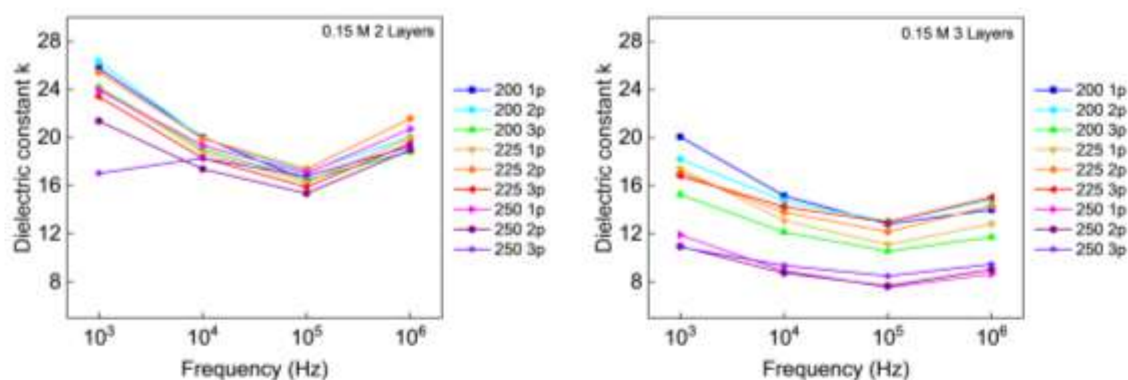

Figure 6-9. Dielectric constant values (k) along with the corresponding frequency dependence of MOS-Capacitor devices with Laser annealed ZrO_2 as a dielectric. The solution concentration was chosen at $0.15\ \mathrm{M}$ while the number of deposited layers varied between 2 and 3. The extraction of k was based on Capacitance values presented in **Figure 6-7**, with corresponding thicknesses shown in **Figure 6-8**.

The final step to complete the electrical characterisation of LA $\mathrm{ZrO_2}$ MOS Capacitors involved the study of dielectric breakdown. **Figure 6-10** displays the breakdown fields for 2-layered and 3-layered $\mathrm{ZrO_2}$ MOS capacitors, treated at $200{,}225$ and $250\ \mathrm{mJ/cm^2}$ (1,2 and 3 pulses), along with the corresponding characteristic of thermally annealed samples (green line) for comparison. Dashed lines of the associated colour are extrapolated from the breakdown region towards x-axis, aim to extract the corresponding breakdown field values. For 2-layered $\mathrm{ZrO_2}$ treated at $200\ \mathrm{mJ/cm^2}$, a comparison amongst thermally and laser annealed samples reveals higher breakdown field values for samples treated at 2 and 3 pulses, thus outperforming the corresponding reference. However, treatment at a single pulse deteriorates the device operation limit, with breakdown occurring at similar values as the TA reference. For $225\ \mathrm{mJ/cm^2}$, 1 pulse exhibits the highest breakdown field, however 2 and 3 pulses lead to a decrease in breakdown field values. In all cases, treatment at 2 pulses performs always better than thermal annealing. This instability of performance amongst 1 and 3 pulses may originate from two competing parameters associated to laser pulse number: at low numbers of pulses, incomplete conversion may occur, leading to formation of leakage paths (higher chance of dielectric collapse) while at high numbers of pulses the decrease in thickness may promote dielectric damages due to tunnelling effects.

Despite the superior breakdown performance seen in LA devices of 2-layered $\mathrm{ZrO_2}$ samples, a notably different pattern is manifested in 3-layered samples treated at similar LA conditions. Most of LA treated devices (excluding the one treated at lowest LA conditions ($200\ \mathrm{mJ/cm^2}$, 1 pulse) display a notably worse performance compared to thermally annealed device which exhibits the highest breakdown fields. So far in this work, significant discrepancies amongst 2 and 3-layered $\mathrm{ZrO_2}$ films were met in device performance, with 2-layered films exhibiting higher dielectric constant values, as well as higher breakdown field values in comparison to thermally annealed samples. A set of suggestions have been suggested to explain this behaviour, including the LA effect in film densification, as well as film discontinuities amongst layers which can occur during subsequent spin coatings. During MOS-Capacitor operation, the charge storage depends heavily on three parameters: dielectric thickness, dielectric constant and dielectric-semiconductor interface. The presence of roughness or surface non-uniformities can significantly affect the creation of carrier traps/paths across the dielectric, accompanied by changes in device performance. Also, the presence of surface roughness in dielectric-semiconductor interface of TFTs may have a detrimental effect on performance, where interface traps deteriorate the channel formation. For the abovementioned reasons, an investigation on surface morphologies of 2 and 3-layered $\mathrm{ZrO_2}$ films was employed. The chosen

LA fluence was set at $225\ \mathrm{mJ/cm^2}$, as this constitutes the condition with the optimal results, based on the device performance analysis conducted so far.

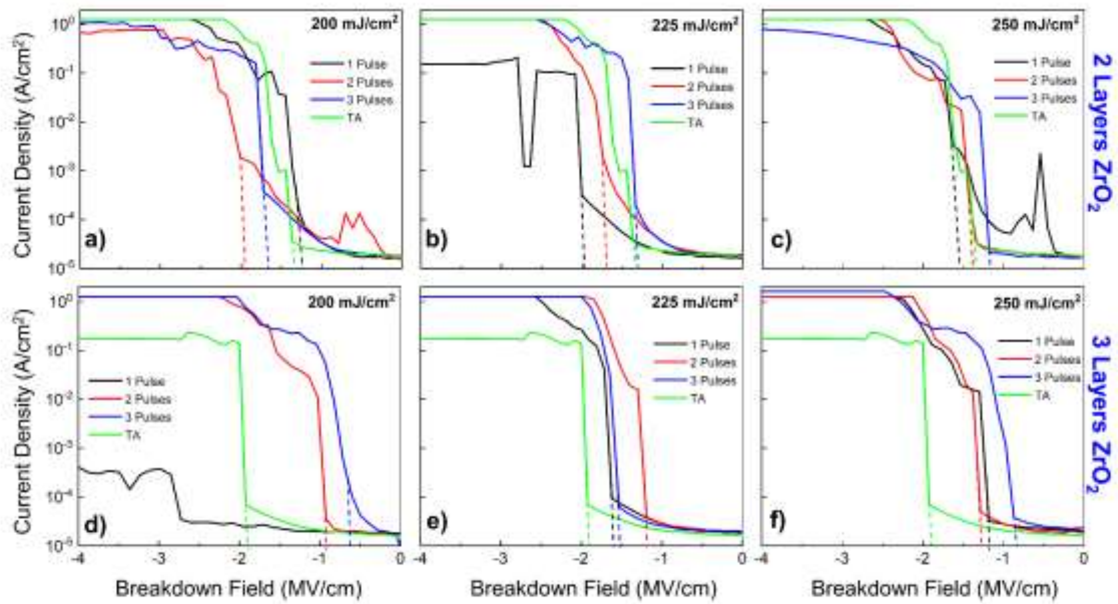

Figure 6-10. Dielectric breakdown of 2 and 3-layered LA ZrO_2 thin films, treated at $200, 225$ and $250\ \mathrm{mJ/cm^2}$, under 1 (black), 2 (red) and 3 (blue) pulses. Green line also represents the performance of reference (TA) samples. The extrapolation of breakdown region into the associated breakdown field ($\mathrm{MV/cm}$) is represented by corresponding dotted lines.

Figure 6-11 presents the surface morphology results of 2 and 3-ayered ZrO_2 films treated at $225\ \mathrm{mJ/cm^2}$ under 1,2 and 3 pulses, as extracted from AFM analysis. Results of thermally annealed (TA) samples are also provided for reference. A significant difference in surface topology is observed amongst the films. For 2-layered ZrO_2, a smooth surface is obtained regardless of pulse number, with roughness values remaining at a notably low level, similarly to the reference sample. However, the surface morphology of 3-layered ZrO_2 films depicts the formation of a crystalline material, dominated by spherulite-shaped crystals. As number of pulses increases, the film becomes denser, while crystal size increases and nanocrystals merge. This topography is significantly different to the reference TA sample, where a smooth surface of low roughness is obtained, similarly to 2-layered ZrO_2 films.

The association amongst film thickness and nucleation process has frequently gathered scientific interest in the past. Boscke et. Al [317] explored the crystallisation temperature barrier with film thickness in ZrO_2 and HfO_2 thin films. According to this study, a general trend is an increase of crystallization temperature with reduction of film thickness, which can be explained by a higher nucleation barrier if the film thickness approaches the critical radius for nucleation. According to this mechanism, the crystallisation of ZrO_2 should occur above a certain, critical,

thickness. The crystallisation initiation above a temperature threshold is a two-step process which involves formation of nuclei and subsequent crystal growth [318]. The formation of crystalline nuclei leads to the formation of an energetically unfavourable interface. Small nuclei with large specific surface area are instable, so that a minimum size is required to form stable nuclei. Due to this, an energy barrier exists between the amorphous and the crystalline state. The second step, the crystal growth, is mediated by diffusion of atoms to the crystal nuclei. The crystallization temperature is defined by the energy required to overcome the nucleation barrier and by the activation energy of the diffusion process. If the film thickness is reduced to the nm range, the nuclei become two dimensionally constrained and the energy gain of the crystalline phase over the amorphous phase is reduced. This results in an increase of the crystallization temperature. Yu *et al*. [319] have also investigated the thickness-nucleation rate dependency, according to which the homogeneous nucleation and subsequent crystal growth can be controlled by tuning the annealing duration as well as the "seed" substrate (*i.e.* the surface where the film grows). According to the classical nucleation theory (CNT), the effective rate of homogeneous nucleation is proportional to the volume of material. The crystallization behaviour of amorphous films is thus shown to be entirely controllable by introducing thickness variations, which locally change the volume of material. Crystalline domains formed early in thick regions can seed the lateral epitaxial growth of directional and textured domains, even on disordered surfaces. Polycrystalline films are thus produced with an entirely programmed microstructure, including the location, size, shape, texture, and in-plane crystallographic orientation of domains, as well as the location and orientation of domain boundaries. Their investigation on thin films with various thicknesses revealed that upon thermal annealing for a short duration, nucleation, and growth of crystalline spherulites was only observed in the thicker part of the sample, whereas the thinner section remained amorphous and did not exhibit any evidence of nucleation in the thin section even after the thick region has fully crystallized. Similar experiments have also been performed in the past on vacuum-deposited inorganic metal oxide films of molybdenum oxide ($\mathrm{MoO_x}$) prepared with different thicknesses [320]. The thinner films required more time to crystallize and exhibited a substantially smaller nucleation density than the thicker films. These experiments confirm qualitatively that the onset of nucleation of the crystalline phase in amorphous thin films is thickness dependent. Therefore, to quantify this thickness-nucleation rate process, one can consider [319]:

$$\mathrm{R} = \frac{\mathrm{N}}{\mathrm{dV} \times \mathrm{dt}} \qquad 6.4$$

where R is a volumetric term defined as the number of nuclei (N) formed per unit volume (dV) in given time (dt). When this formula is applied to a film of finite thickness (ignoring heterogeneous nucleation at interfaces), the number of atoms available to form critical nuclei

per unit area (dA) of film scales with thickness d. An effective homogeneous nucleation rate per unit area and time can thus be described as R_A:

$$R_A = \frac{N}{dt \times dA} = R \times d \qquad 6.5$$

The above equation can quantitively explain the difference amongst nucleation status of 2-layered and 3-layered ZrO_2 films, treated under identical LA conditions.

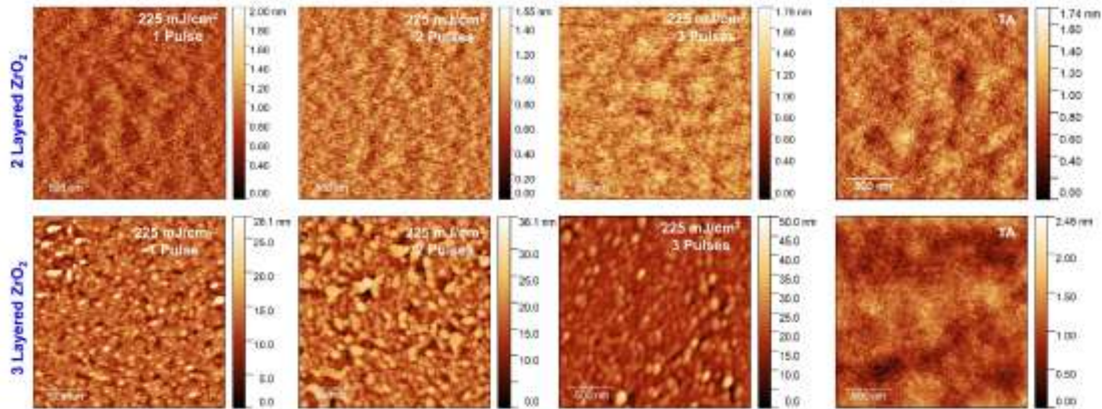

Figure 6-11. Atomic Force Microscopy (AFM) analysis of 2 and 3-layered ZrO_2 thin films, treated at $225\ mJ/cm^2$, under 1, 2 and 3 pulses. The corresponding TA samples are also presented for reference.

6.3. Electrical Characterisation of TFTs Based on a Sol-Gel Laser Annealed Dielectric and Semiconductor

One of the key objectives of this work concerned the development of TFT devices based on sol gel LA dielectric and semiconductor layers. This section investigates such an implementation. To the best of our knowledge, this constitutes the first attempt of TFT fabrication with sol-gel LA for a bilayer of metal oxides (as the gate dielectric and the active semiconductor). To achieve this, the findings involving the dielectric layer optimisation (presented in this chapter) were combined with the research on sol-gel LA semiconductors outlined in **Chapter 5**. ZrO_2 and In_2O_3 served as the two key materials of interest. In addition, Al_2O_3 (a well-known high-k dielectric material) was employed as an alternative for the dielectric material in the TFT devices. Al_2O_3 was selected for 2 reasons. Firstly, there was an opportunity to utilise our in-house atomic layer deposition (ALD) facilities to grow atomically smooth Al_2O_3 thin films with a thickness of $20\ nm$. This enabled the elimination of any sol-gel related "matching" issues of the underlying film and allowed for direct observation of how sol-gel LA of In_2O_3 films can be combined with ultra-thin dielectrics in a TFT. The second reason for also employing Al_2O_3 as a dielectric layer was the existing expertise in sol-gel LA Al_2O_3 thin films and their use as dielectrics. Recent studies performed by E. Carlos *et al.* [54], using the same research facilities used in this project, verified the use of Al_2O_3 as a dielectric in TFTs based on Al_2O_3 and In_2O_3. However, this work

involved the use of sputter-deposited In_2O_3 films on top of sol-gel LA Al_2O_3 thin films. To complete this research, an attempt was made to fabricate sol-gel, laser processed In_2O_3 on top of a sol-gel laser processed Al_2O_3 thin film. Three combinations of materials and the deposition processes were tested, including but not limited to:

i. ALD Al_2O_3 followed by sol gel LA In_2O_3,
ii. Sol-gel LA Al_2O_3 followed by sol gel LA In_2O_3,
iii. Sol-gel LA ZrO_2 followed by sol gel LA In_2O_3.

The deposition conditions chosen for sol-gel Al_2O_3 were based on the findings of E. Carlos [54]: Aluminium Nitrate Nonahydrate ($Al(NO_3)_3 \cdot 9H_2O$) was dissolved in $2-ME$ in a concentration of 0.1 M. Urea was also added to the solution, with molar ratio $2.5:1$ to induce a combustion reaction. The solution was then deposited *via* spin coating at 2000 rpm, for 35 s in Si substrates, followed by stabilisation at 150 °C for 15 mins. The LA conditions were set at $175\ mJ/cm^2$, based on the optimum results reported by E. Carlos [54]. Regarding ZrO_2, the concentration chosen during the fabrication of the solution was 0.15 M (2 Layers). According to our abovementioned results, this value provides the best balance amongst thin film thickness and film morphology. An overview of the LA conditions and annealing steps towards BGTC TFT fabrication is presented in Table 6-2. It is important to note that in **Chapter 5**, Si substrates with an additional $100-400$ nm SiO_2 were utilised. This was done to focus on the formation of sol-gel In_2O_3 during LA. The use of thick dielectric films (SiO_2 in our case) prevented dielectric breakdown issues and allowed for the use of very high (or low) V_{GS} values. This provided the option to observe the performance of sol-gel LA In_2O_3 across a broader V_{GS} range. Once this study was completed, the next step was the implementation of this film in devices based on ultra-thin, high-k dielectrics.

Table 6-2: LA conditions employed in fabrication of fully sol-gel TFT devices.

Batch No	Dielectric	Semiconductor
1	ZrO_2 - $225\ mJ/cm^2$, 1 pulse	In_2O_3 – $150-250\ mJ/cm^2$, 1-3 pulses
2	ZrO_2 – 300^0 C, 60 min	In_2O_3 - 300^0 C, 60 min
3	Al_2O_3 - $175\ mJ/cm^2$, 1 pulse	In_2O_3 – $150-250\ mJ/cm^2$, 1-3 pulses
4	Al_2O_3 – 300^0 C, 60 min	In_2O_3 - 300^0 C, 60 min
5	One-step Al_2O_3/In_2O_3 bilayer – $150-250\ mJ/cm^2$, 1-3 pulses	
6	One-step ZrO_2/In_2O_3 bilayer – $150-250\ mJ/cm^2$, 1-3 pulses	

Following fabrication, each batch presented in Table 6-2 was electrically characterised, aiming to correlate the device performance to LA effect on dielectric and semiconductor films. Electrical characterisation involved transfer and output curves, followed by leakage current investigation as well as capacitance measurements. Transfer and output characteristics provide essential insights regarding the semiconductor film formation *via* sol-gel, as well as the dielectric-semiconductor interface (where the channel is formed). In addition, leakage current investigation along with capacitance measurements is indicative of the dielectric quality. The

first attempt towards fabrication of fully sol-gel LA TFTs involved the combination of laser processed sol-gel ZrO_2 with In_2O_3 thin films to form a BGTC TFT structure. For comparison, TFTs based on thermally annealed sol-gel ZrO_2 and In_2O_3 thin films were additionally fabricated. **Figure 6-12** displays a comparison between electrical behaviour of thermally annealed and laser annealed devices (see Table 6- for LA conditions) through the scope of transfer and output curves, along with $I_{GS} - V_{GS}$ and capacitance plots. For thermally annealed devices, high I_{DS} current is exhibited, with I_{ON} exceeding 10^{-3} A. Arrows display a clockwise direction in current sweep. V_{ON} is located at 0 V while I_{OFF} is maintained at high current values at switch-off state thus degrading $I_{ON/OFF}$. In comparison to thermally annealed devices, a significant drop in I_{ON} is revealed for LA TFTs (**Figure 6-12e**), exhibiting I_{ON} ~ $(10^{-6}A)$. Moreover, sawtooth waveform is detected at $-1\ V_{GS} < 1\ V$, a phenomenon previously attributed to extreme instability in device performance. In contrast to **Figure 6-12a**, the presence of hysteresis is manifested in I_{DS} with regards to reverse V_{GS} sweep. This can be attributed to the dominance of carrier traps along the device channel. In this case, traps may be allocated to precursor-associated organic residuals due to incomplete $In(NO_3)_3$ conversion, or ZrO_2/In_2O_3 interface discontinuities. A comparison between output curves (**Figure 6-12c** and **g**) provides complementary information regarding the channel formation mechanism.

For thermally annealed devices **Figure 6-12c** indicates a clear transition from linear to saturation region, with a slight current crowding at low V_{DS}. However, LA TFTs (**Figure 6-12g**) exhibit a more deteriorated output plot. Significant drain current hysteresis is observed despite its general outline is still in accord with output characteristics. The detection of noise at low V_{DS} comes in agreement with device instability, as seen in the corresponding transfer curve. Such hysteresis may be contributed to the presence of carrier traps along the channel. Also, no clear transition to saturation is shown, with I_{DS} increasing continuously. **Figure 6-12b** and f display the leakage currents of the corresponding devices. For thermally annealed TFTs, high leakages are detected, exhibiting values comparable to I_{DS} (**Figure 6-12a**).

Similar behaviour is seen in **Figure 6-12f** with $I_{GS} \sim 10^{-6}$ A. The leakage current increase shown in thermally annealed TFTs could be attributed to incomplete conversion of $Zr(AcAc)_4$, where remaining organic residuals contribute to additional charges [312]. However, such behaviour is not observed in LA TFTs. This, along with the presence of high hysteresis (compared to thermally annealed devices) and the difference in I_{ON} in transfer curves can be explained as follows: In thermally annealed devices, a sufficient conversion of $In(NO_3)_3$ into In_2O_3 is exhibited – in agreement to our previous findings on thermally annealed In_2O_3 on Si, as well as our IRSE analysis. However, this temperature (300^0C) is not effective towards promoting the

full conversion of $\mathrm{Zr(AcAc)_4}$ into $\mathrm{ZrO_2}$ – in agreement to IRSE results shown in **Figure 6-2**. This leads to devices exhibiting high current values ($\mathrm{In_2O_3}$ complete conversion) along with high leakages ($\mathrm{ZrO_2}$ incomplete conversion). This "mismatch" is also associated to the difference in precursor salts (nitrate/acetylacetonate), which convert into metal oxides *via* different chemical pathways thus demanding different temperature windows. For LA TFTs, the mechanism is reversed: LA $\mathrm{ZrO_2}$ precursor under $225\ \mathrm{mJ/cm^2}$ provides a dielectric film that can adequately prevent high leakage current, possibly due to a better precursor conversion (compared to thermally annealed $\mathrm{ZrO_2}$). However, semiconductor-associated carrier traps are deteriorating the device performance (hysteresis, low $\mathrm{I_{ON}}$).

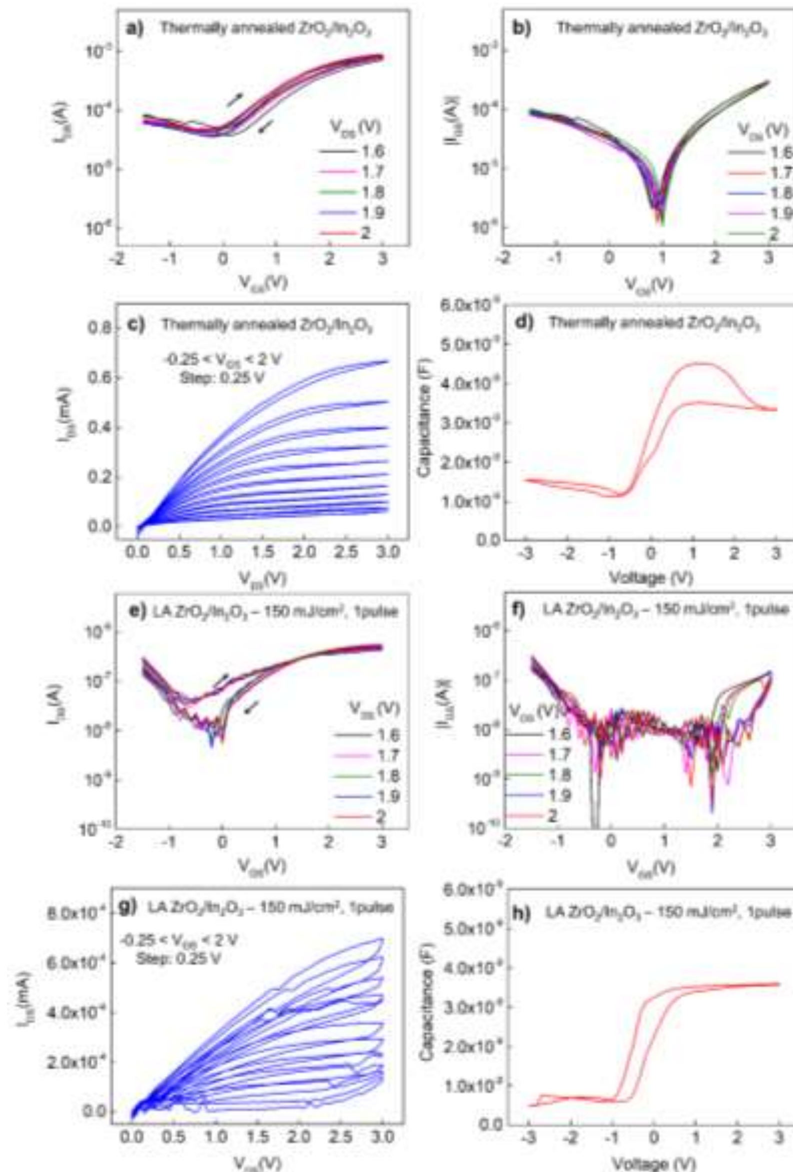

Figure 6-12. $\mathrm{I-V}$ and $\mathrm{C-V}$ characterisation of TFT devices based on sol-gel thermally (a-d) and Laser annealed (e-h) $\mathrm{ZrO_2}$ and $\mathrm{In_2O_3}$ thin films. The thermal annealing conditions chosen here are $300^0\mathrm{C}, 60$ mins. Panels (e-h) represent devices annealed at two stages; $\mathrm{ZrO_2}$ is annealed at $225\ \mathrm{mJ/cm^2}$ (1 pulse), followed by $\mathrm{In_2O_3}$ precursor deposition and additional annealing at $150\ \mathrm{mJ/cm^2}$ (1 pulse). (a and e) represent the

transfer curves, (b-f) leakage currents, (c-g) output curves and (d-h) C-V measurements of thermally and laser annealed TFT devices, respectively. V_{DS}Output curves (c-g) are extracted at $-0.25 < V_{GS} < 2$ V. Arrows in (e) indicate the I_{DS} direction during V_{GS} sweep.

The presence of carrier traps can be attributed to incomplete conversion of In_2O_3 precursor or a damage in dielectric/semiconductor interface after the additional LA treatment of the semiconductor. Both scenarios can hinder channel formation in the interface, which can explain the large hysteresis during the return sweep in output curves. Current crowding at low V_{DS} is also present in LA devices. Despite the deteriorated performance in LA TFTs, a transistor-like behaviour is clearly exhibited, constituting an insightful finding of our work. **Figure 6-13** displays the electrical performance of batches 3&4 in **Table 6-2**, TFTs based on thermally (a-d) and LA (e-h) Al_2O_3 and In_2O_3 sol-gel thin films. In contrast to the corresponding ZrO_2-based TFTs, devices based on thermally annealed Al_2O_3 fail to perform accordingly. Transfer and leakage curves (**Figure 6-13a** and **b**) present similar V_{GS} dependence, thus indicating operation under breakdown. In such case, carriers injected through gate electrode are directly collected by drain electrode, as dielectric fails to exhibit any carrier storage and perform as a capacitor. Dielectric damage is also illustrated in **Figure 6-13d**, where carrier overflow is presented at 2 V. Also, output curves in **Figure 6-13c** show the inability of channel formation (thus I_{DS} dependency on V_{GS}), as I_{DS} increases exponentially indicating performance in breakdown region.

Despite the device failure (dominated by Al_2O_3 damage), LA devices exhibit a significantly different performance. Transfer curve shown in **Figure 6-13e** reveals signs of TFT performance, with I_{DS} exhibiting a slight increase at V_{GS} sweeping. Note the decreased V_{DS} steps employed over this measurement to prevent device from breakdown. I_{DS} increase is only delivered at the highest V_{DS} (0.6 V, pink line), while current values are comparable to I_{OFF}, followed by large hysteresis during reverse V_{GS} sweeping (arrow direction). Assuming a $V_{ON} \sim -0.2$ V (where a slight I_{DS} increase starts to appear), $I_{ON/OFF}$ is significantly poor. Leakages (**Figure 6-13f**) present similar current values to I_{DS} (10^{-4}A), indicating the dielectric failure to prevent gate carrier tunnelling. Interestingly, output plot at **Figure 6-13g** manifests the performance of a device based on highly conductive semiconductor, as I_{DS} continuously increases monotonically with V_{DS}. An increase in I_{DS} is also dominated by V_{GS} increase, however no significant dependence of I_{DS} on V_{GS} is manifested as output curves corresponding to different V_{GS} are difficult to distinguish. Capacitance-Voltage measurements reveal dielectric failure, with carrier overflow at 2.5 V. A comparison amongst output and Capacitance plots manifests a contradictory device behaviour, as despite the successful channel formation during V_{DS} (output), a dielectric damage is revealed over the capacitance measurement. This behaviour

may be attributed to the device irreversible damage over output or capacitance measurements, due to dielectric sensitivity. The device behaviour presented in **Figure 6-13e-h** reveals a contradictory laser annealing effect on devices based on Al_2O_3/In_2O_3: starting from the performance of Al_2O_3 as a dielectric, the initial treatment at $175\ mJ/cm^2$, followed by 1 pulse of $150\ mJ/cm^2$ (during LA of In_2O_3), leads to a significant deterioration of the dielectric performance.

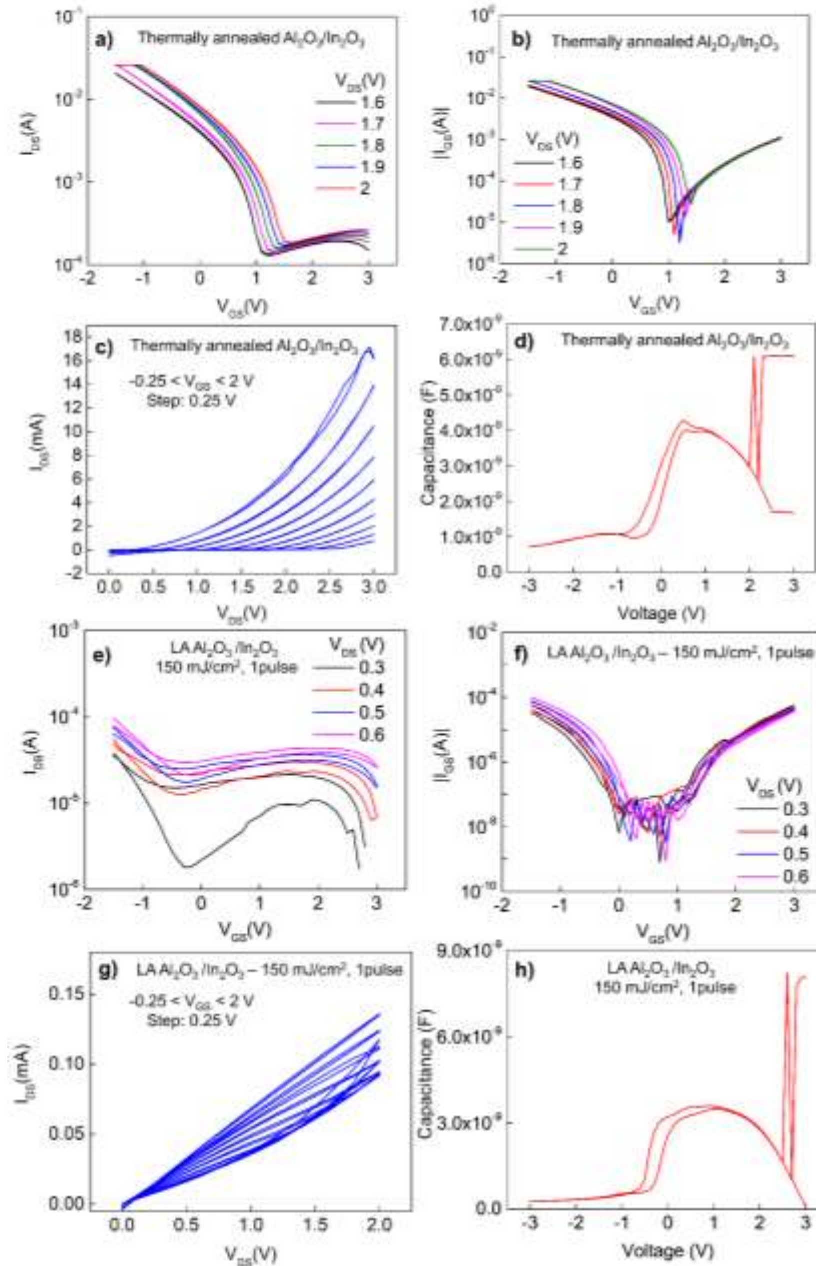

Figure 6-13. $I-V$ and $C-V$ characterisation of TFT devices based on sol-gel thermally (a-d) and Laser annealed (e-h) Al_2O_3 and In_2O_3 thin films. The thermal annealing conditions chosen here are 300^0 C, 60 mins. Panels (e-h) represent devices annealed at two stages; Al_2O_3 is annealed at $175\ mJ/cm^2$ (1 pulse), followed by In_2O_3 precursor deposition and additional annealing at $150\ mJ/cm^2$ (1 pulse). a) and e) represent the transfer curves, (b-f) leakage currents, (c-g) output curves and (d-h) $C-V$

measurements of thermally and laser annealed TFT devices, respectively. Output curves (c-g) are extracted at $-0.25\ \mathrm{V} < \mathrm{V_{GS}} < 2\ \mathrm{V}$. Arrows in e) indicate the $\mathrm{I_{DS}}$ direction during $\mathrm{V_{GS}}$ sweep. Drain voltage values at e) range from $0.3\mathrm{V}$ to $0.6\ \mathrm{V}$, to prevent device from damage due to dielectric malfunction.

This can be observed in the Capacitance performance (**Figure 6-13d-h**), where dielectric breakdown occurs at $2\ \mathrm{V}$ (capacitance breakdown). Concurrently, the poor performance of the corresponding thermally annealed film indicates issues during the manufacturing process. For LA $\mathrm{In_2O_3}$, however, treatment at $150\ \mathrm{mJ/cm^2}$ appears to convert the precursor into a highly conductive semiconductor, with the device performing constantly in linear region (output plot) without reaching pinch-off. For thermally annealed $\mathrm{In_2O_3}$ on top of $\mathrm{Al_2O_3}$, no results can be obtained as the dielectric failure prevents the extraction of channel-associated formation. These results reveal an opposite pattern compared to $\mathrm{ZrO_2/In_2O_3}$ based TFTs, where thermally annealed devices exhibited the best behaviour. **Figure 6-14** shows the electrical characterisation of TFTs based on one-step laser annealed sol-gel $\mathrm{ZrO_2}$ (dielectric) and $\mathrm{In_2O_3}$ (semiconductor) films (batches 5 and 6).

As can be seen in plot a), no current increase is obtained following $\mathrm{V_{GS}}$ sweeping, while the device remains in OFF state regardless of $\mathrm{V_{DS}}$ increase. Similar behaviour is obtained in $\mathrm{I_{GS}}$-$\mathrm{V_{GS}}$ (**Figure 6-14b**), where leakage current is not relative to sweeping gate voltage, remaining at low current values despite $\mathrm{V_{DS}}$ increase. A poor device performance is also depicted in the corresponding output curve in **Figure 6-14c**, where $\mathrm{I_{DS}}$ remains independent of $\mathrm{V_{GS}}$ while not exhibiting the characteristic transition from linear to saturation region. Transfer and output plots clearly indicate a failure towards channel formation in the dielectric/semiconductor interface, as no carrier collection can be achieved with respect to $\mathrm{V_{DS}}$ and $\mathrm{V_{GS}}$ sweeping. When accounting for the fabrication routine followed in this case (one-step laser annealing of stabilised $\mathrm{ZrO_2/In_2O_3}$), two assumptions can be made to interpret transfer and output characteristics: Once $\mathrm{ZrO_2}$ precursor film is deposited *via* spin coating, the stabilisation treatment at $150^0\mathrm{C}$ (15 mins) is effectively removing the remaining solvent, however no precursor conversion occurs; therefore a following deposition of $\mathrm{In_2O_3}$ precursor (based on the same solvent, $2-\mathrm{ME}$) could create a blend of $\mathrm{ZrO_2/In_2O_3}$, preventing the formation of a uniform $\mathrm{ZrO_2/In_2O_3}$ interface (after LA) where a carrier channel can be formed. The second assumption is associated to LA effect on $\mathrm{ZrO_2/In_2O_3}$ interface; the heat induction involved under treatment of 1 pulse can create an intermediate phase between $\mathrm{ZrO_2}$ and $\mathrm{In_2O_3}$, thus affecting the formation of a distinct $\mathrm{In_2O_3}$ film. Despite poor device performance, the decreased leakage current along with capacitance behaviour illustrated in **Figure 6-14d** manifest the formation of $\mathrm{ZrO_2}$ dielectric layer, similarly to **Figure 6-13**.

Despite the similarities over fabrication, TFTs based on one-step processed LA sol-gel Al_2O_3/In_2O_3 films exhibit a deviation in device performance, in comparison to ZrO_2/In_2O_3 structure. **Figure 6-14e-g** display the corresponding transfer and output curves, where breakdown characteristics are observed. Also, a similarity amongst I_{DS} and I_{GS} dependence on V_{GS} sweep is illustrated, indicating the dielectric's failure to prevent the drain collection of carriers injected directly from gate electrode. The dielectric damage is also displayed in the output plot (**Figure 6-14g**), where the device performs directly in breakdown region, revealing the gate to source junction due to the avalanche effect. Capacitance-voltage plot illustrates as a sharp overflow at 2 V indicating the device failure as an MOS- Capacitor component, in accord with the output and transfer characteristics.

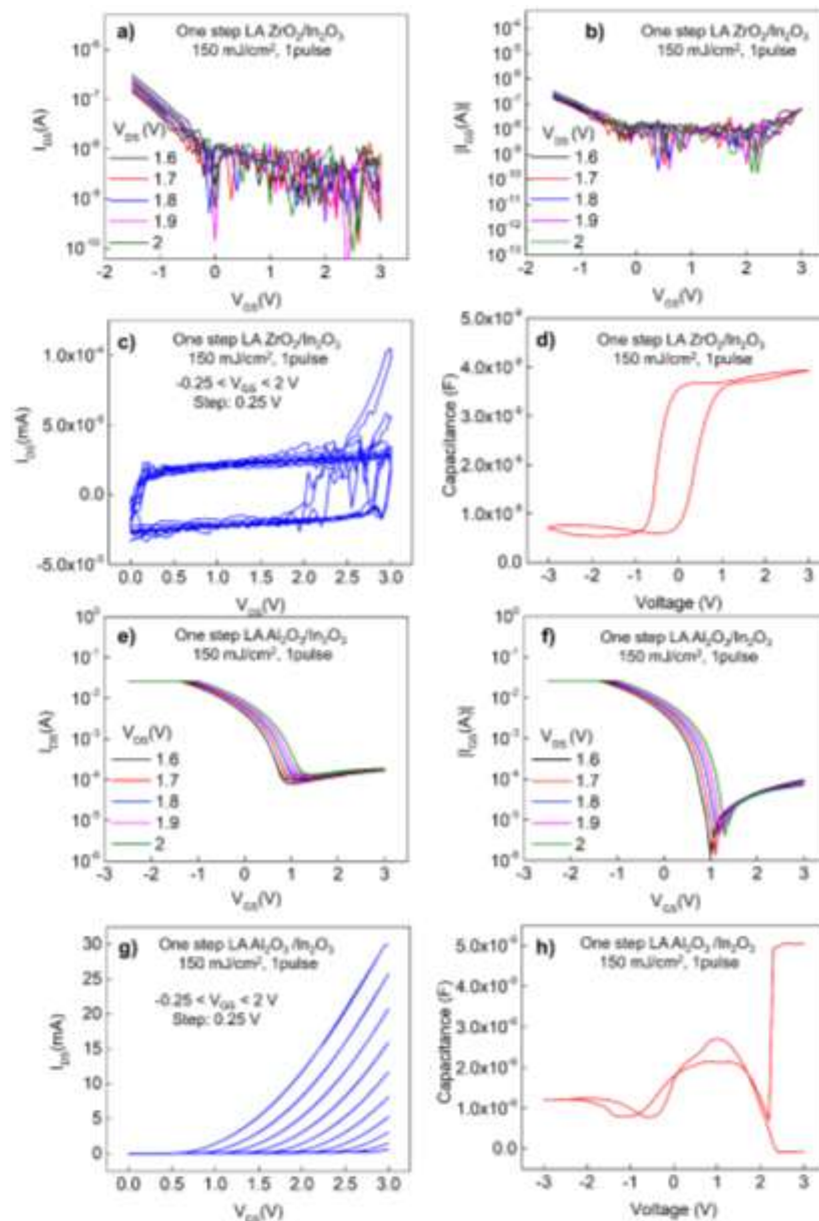

Figure 6-14. $I-V$ and $C-V$ characterisation of TFT devices based on one step sol-gel Laser annealed ZrO_2/In_2O_3 (a-d) and Al_2O_3/In_2O_3 (e-h) thin films. Dielectric precursor solutions were initially spin coated and stabilised ($150^0C, 15$ min), followed by the

corresponding In_2O_3 precursor deposition and stabilisation; A single laser annealing step ($150\ mJ/cm^2, 1$ pulse) was afterwards conducted. (a-e) represent the transfer curves, (b-f) leakage currents, (c-g) output curves and (d-h) C-V measurements, of thermally and laser annealed TFT devices, respectively. Output curves (c-g) are extracted at -$0.25V < V_{GS} < 2$ V.

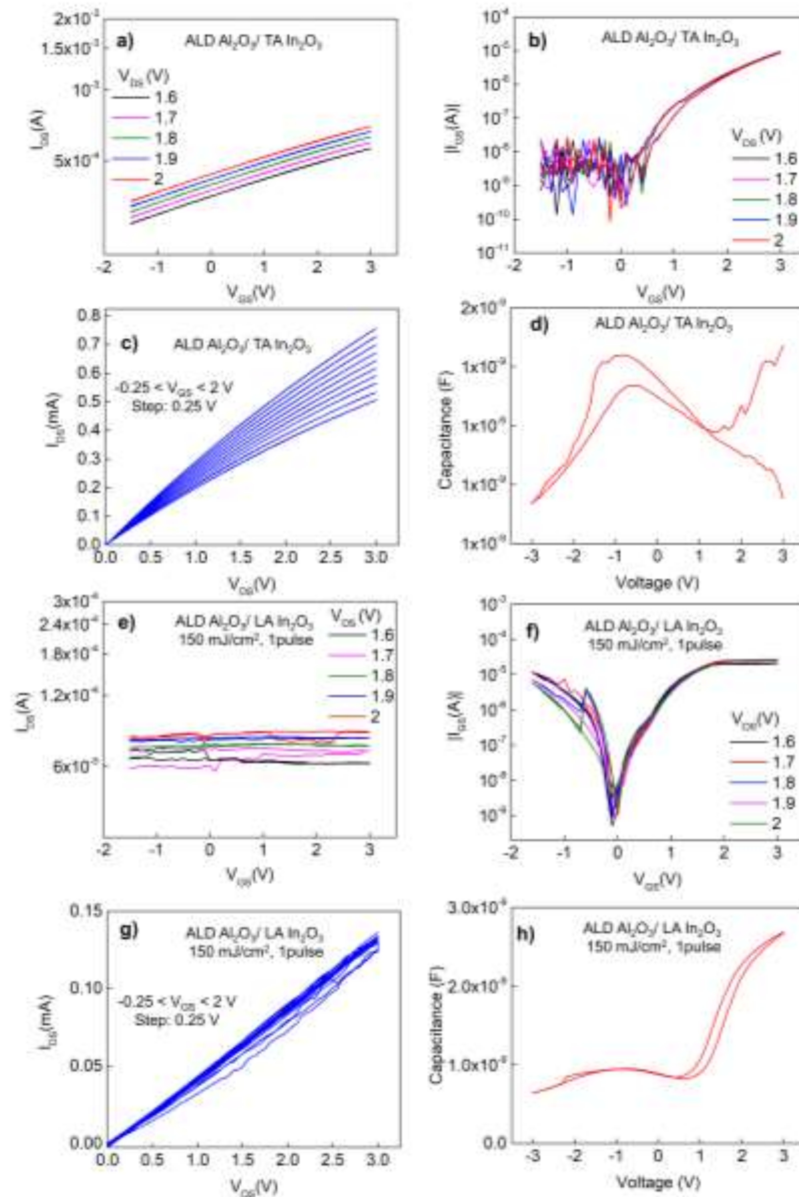

Figure 6-15. $I - V$ and $C - V$ characterisation of TFT devices based on ALD fabricated Al_2O_3 with sol-gel thermally annealed In_2O_3 (a-d) and ALD fabricated Al_2O_3 with sol-gel LA In_2O_3 (e-h) thin films. (a-e) represent the transfer curves, (b-f) leakage currents, (c-g) output curves and (d-h) $C - V$ measurements of thermally and laser annealed TFT devices, respectively. Output curves (c-g) are extracted at $-0.25V < V_{GS} < 2$ V. Arrows

in e) indicate the I_{DS} direction during V_{GS} sweep. Drain voltage values at a) and e) range from $1.6V$ to $2V$.

The electrical characterisation of TFT devices based on sol-gel Al_2O_3/In_2O_3 thin films revealed a problematic Al_2O_3 behaviour as a dielectric layer, which raised concerns on Al_2O_3 formation as well as prevented any In_2O_3-associated information extraction- since dielectric failure hindered any TFT-related feature. Therefore, to extract information on In_2O_3 formation on top of Al_2O_3 surface, Atomic Layer Deposition (ALD) was employed as an alternative technique towards the formation of Al_2O_3, which would constitute the TFT dielectric. Thickness was chosen at 20 nm, to match the corresponding thickness of sol-gel LA Al_2O_3. The use of ALD Al_2O_3 would eliminate the scenario of a dielectric failure due to incomplete precursor conversion, as well as provide a uniform, smooth surface on which In_2O_3 could be deposited. The smooth surface can be directly correlated to the device performance as it promotes a successful channel formation in Al_2O_3/In_2O_3 interface. After obtaining Al_2O_3 thin films (*via* ALD), In_2O_3 precursor was deposited on top using the same spin coating parameters as before. After deposition (and stabilisation) In_2O_3 were either thermally or laser annealed ($150\ mJ/cm^2$).

Figure 6-15 represents the electrical characterisation of TFTs based on ALD Al_2O_3/sol-gel In_2O_3 thin films. For thermally annealed In_2O_3 (**Figure 6-15a-d**), transfer plot (**Figure 6-15a**) reveals a device behaviour corresponding to a highly conductive In_2O_3 film. V_{DS} and V_{GS} remain similar to the rest of this analysis to compare the device performance amongst batches. The device exhibits high I_{ON} values, approaching 10^{-3} A at the highest V_{DS}. Also, device remains always switched ON while a clear dependence of I_{DS} on V_{DS} is reported thus indicating the dominance of free carriers. Also, no hysteresis is observed for the first time in this work, indicating a potential absence of free carrier traps along the channel. This could also be associated to the use of ALD Al_2O_3 as a dielectric with smooth film surface, which eliminates any presence of carrier traps due to surface roughness. On-off ratio values remain poor, in accord to the constant ON-state of the device. The highly conductive nature of thermally annealed In_2O_3 is also confirmed by the corresponding output plot shown in **Figure 6-15c**. A small dependence of I_{DS} on V_{GS} is manifested, with output curves remaining in linear mode without reaching pinch-off state. Leakage currents (shown in **Figure 6-15b**) are kept at low levels, approaching 10^{-5}A. Also, C-V measurements confirm the valid performance of ALD Al_2O_3 as a dielectric, with favourable capacitor features which involve a clear increase in capacitance with respect to voltage along with elimination of hysteresis. For ALD Al_2O_3/LA In_2O_3 based TFTs (treated at $150\ mJ/cm^2$, 1 pulse), the electrical performance appears as a more deteriorated version of the corresponding thermally annealed ones. As seen in transfer curve (**Figure 6-15e**),

the device remains constantly in ON state (similarly to **Figure 6-15a**), exhibiting $I_{DS}\sim10^{-4}A$. I_{ON}/I_{OFF} remains extremely poor, possibly due to the formation of a highly conductive In_2O_3. However, significant noise is detected along measurement, indicating instability at channel formation along V_{GS} sweeping. The constantly ON state of the device is also manifested in the output plot (**Figure 6-15g**). As can be seen, no V_{GS} dependence is observed in the output curves, with I_{DS} current constantly increasing with respect to V_{DS}. No transition to saturation is achieved, in accord to transfer results. Also, the presence of noise along V_{DS} sweep is observed, similarly to **Figure 6-15e**.

6.4. Concluding Remarks

This chapter explored the potential use of sol-gel LA ZrO_2 as a dielectric in TFT devices. This was conducted in 3 steps; at first, a study in precursor ($Zr(AcAc)_4$) conversion mechanism was employed through the scope of IRSE, to gain preliminary knowledge on the LA conditions to be used. According to these results, $Zr(AcAc)_4$ does not fully dissociate after thermal treatment at 300^0 C, as acetate-related by-products are detected ($\delta_s CH_3$, $\rho CH_3 \nu_{c-o} + \nu_{c-c}$). This result is in accordance with the associated analysis in Chapter 4 on zinc acetate.

Afterwards, the fabrication of MOS capacitors based on sol-gel LA ZrO_2 thin films was realised, with varying solution concentrations and LA conditions. The optimisation process involved optical, electrical, and morphological characterisation of ZrO_2 thin films, thus providing information regarding thickness, electrical performance, and surface morphology of the corresponding thin films. To optimise the fabrication conditions of ZrO_2 thin films, 2 solution concentrations were tested (0.1 M, 0.15 M), along with deposition of 1,2 and 3 layered films. A LA process window of $200-275$ mJ/cm^2 was also chosen, with 1,2 and 3 pulses per film. From that work, the optimum LA and deposition conditions were chosen, namely 225 mJ/cm^2 and 2 layers of ZrO_2. These conditions were later employed towards developing sol-gel LA sol-gel BGTC TFTs, where sol-gel LA In_2O_3 was employed as the semiconductor layer. Despite the poor electrical performance observed in TFTs, insightful knowledge was extracted, principally related to fine tuning of LA conditions of subsequent layers in a stack. This can be summarised in **Figure 6-16**:

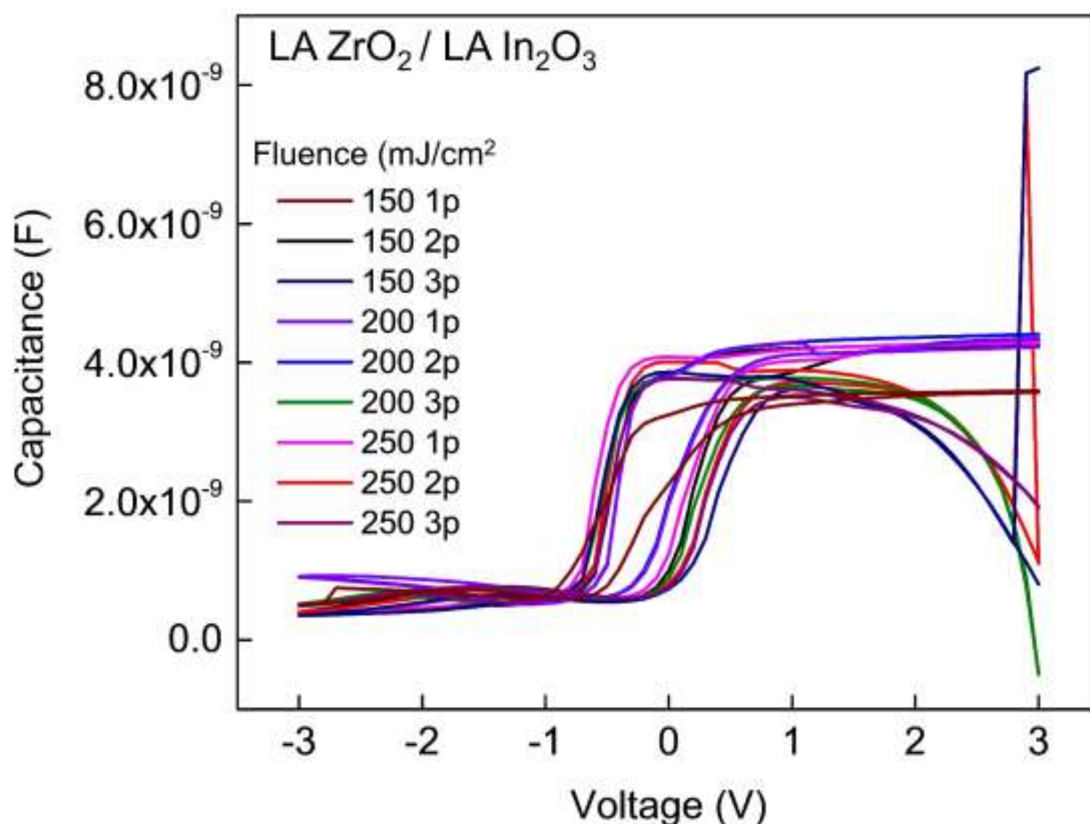

Figure 6-16. C-V characteristics of LA ZrO_2/In_2O_3 TFTs. LA was employed in a two-step process; initially, ZrO_2 was formed *via* LA of $Zr(AcAc)_4$ at $225\ mJ/cm^2$. Afterwards, $In(NO_3)_3$ precursor deposition was conducted, following LA at conditions shown in figure legend ($150 - 250\ mJ/cm^2$, 1-3 pulses).

Figure 6-16 shows the Capacitance-Voltage characteristics of LA ZrO_2/In_2O_3 TFTs of batch no 1 (see **Table 6-2** for more info on LA conditions). n-type Si is now used as a device substrate. Therefore, accumulation region is formed in positive Voltage values. For devices treated at 1 pulse, a capacitance characteristic with clear transition from depletion to accumulation is observed. An increase in laser fluence is accompanied by increase in maximum capacitance values, possibly due to film densification (thus decrease in film thickness). However, as number of pulses increase, a significant deterioration in capacitance curves is obtained. Despite the transition from depletion to accumulation (at $0.5\ V$), a large decrease in capacitance values is obtained at higher voltages, due to the high tunnelling rate through ZrO_2, thus hindering the accumulation of electrodes. Interestingly, the pulse effect plays a significant role in this case, in contrast to the results of MOS Capacitors, where fluence was the dominant LA parameter. However, one must consider the annealing process followed in TFT production, with ZrO_2 undergoing laser treatment twice. **Figure 6-16** can effectively summarise another key-point of this chapter; the optimisation in fabrication process of individual layers of sol-gel LA thin films (in our case ZrO_2) is of highly importance in TFT fabrication. Especially for the dielectric in

BGTC devices, this is the layer which withstands two sets of treatment (one for the dielectric and one for the semiconductor on top). For this reason, fine tuning on LA conditions of the dielectric must always account for a transition of the fluence (and pulse) window towards lower values, which will simultaneously convert the precursor as well as provide space for the subsequent LA of the semiconductor on top.

In this chapter, the challenges in manufacturing fully sol-gel, laser annealed TFT devices are addressed, following the optimisation of individual layers (dielectric in this chapter, semiconductor in Chapter 5). Despite the realisation of optimum laser processing conditions per layer, the interface amongst dielectric and semiconductor may require additional optimisation. Therefore, to avoid the "over-processing" of $\mathrm{ZrO_2}$ with LA, films were treated at 1 pulse, followed by subsequent deposition of $\mathrm{In_2O_3}$ and LA treatment at 150 $\mathrm{mJ/cm^2}$ (lower fluence values compared to the individual optimisations). This "fine tuning" constitutes one of the highlights of this chapter as it pinpoints the critical steps needed to integrate Laser Annealing into high volume manufacturing schemes of electronics.

7. Conclusions and Future Perspectives

7.1. Conclusions

The work conducted in this Ph.D. programme elaborated on unravelling the photochemically assisted conversion of metalorganic thin film precursors into metal oxides (MOs), followed by their subsequent use in thin film electronic devices. An initial investigation involving the use of IRSE was conducted, with In_2O_3 and ZnO precursor salts as materials of interest. In detail, $In(NO_3)_3$ and $Zn(CH_3COO)_2$ thin films underwent several thermal annealing treatments, with IRSE providing a detailed mapping of the temperature effect into In_2O_3 and ZnO formation. Since the principal goal of MO thin films is their use in electronic devices, an additional challenge was included during IRSE investigation. Specifically, the fabrication and study of ultra-thin metal oxide precursor films. This challenge was accompanied by the difficulty in extracting a detailed absorption profile (*via* IRSE) when films were deposited on Si (due to IRSE sensitivity limitations). To further explore this substrate effect, a set of substrates were added to the research alongside Si, with various reflectivities in the IR spectrum (where absorption peaks of In_2O_3 and ZnO and their precursors are located). The set of 4 different substrates (Si, Al, Au, and TiN) upon which thermally treated $In(NO_3)_3$ and $Zn(CH_3COO)_2$ thin films were examined, provided vital information upon the precursor conversion into a MO as well as the correlation of IRSE sensitivity to substrate reflectivity. In detail, analysis of $In(NO_3)_3$ on highly reflective substrates like Al and Au revealed a set of nitrate-related by-products on the film, after stabilisation. Their removal was manifested after thermal annealing at 300 °C. In contrast to $In(NO_3)_3$, thermal annealing of $Zn(CH_3COO)_2$ did not lead to the full conversion into ZnO, as acetate by-products demand higher annealing temperatures to dissociate. To the best of our knowledge, this is the first time IRSE is employed to provide this information profile in ultra-thin ($10 - 15$ nm) films. Importantly, a figure of merit was proposed to associate the substrate's optoelectronic properties to IRSE sensitivity enhancement.

Following the IRSE investigation, where an overview of the precursor's conversion mechanism was obtained, the next step of this research was conducted involving the introduction of a laser annealing (LA) step to the film fabrication process. This technique substituted thermal annealing towards the formation of In_2O_3 and ZnO films, based on the same precursors studied during IRSE investigation ($In(NO_3)_3$ and $Zn(CH_3COO)_2$). In this part of the research the MO films were deposited atop SiO_2, aiming to develop a dielectric – semiconductor bilayer that, after the deposition of metal contacts, was transformed into a bottom-gate top-contact (BGTC) thin-film transistor (TFT) device. IGZO was also included in the list of materials of interest, the fabrication route of which was similar to In_2O_3 and ZnO (sol gel, LA). A set of laser fluences and number of pulses represented the principal parameters of

interest towards the formation of semiconductor films, the quality of which was examined through the scope of device electrical performance. A critical parameter of study was the dielectric thickness, which affected the LA parameter window. In detail, different thicknesses of SiO_2 have an impact in the absorption profile of the surface film. This parameter directly affected the electrical device performance, where the use of $200\ nm\ SiO_2$ was found to be the optimum choice (amongst $100, 200$ and $400\ nm\ SiO_2$). This SiO_2 thickness was later used to study the effect of LA on more sol-gel MO semiconductors, such as IGZO and ZnO. Also, surface morphology investigation of sol-gel LA In_2O_3, ZnO and IGZO films revealed a significant change in thin film morphology in comparison to thermal annealing, which was additionally correlated to device performance (charge transport mechanism).

Finally, fabrication of sol-gel deposited, laser processed MO dielectrics formed a completing step of this research work, where ZrO_2 constituted the material of study. A set of optical (IRSE and ORS), morphological (AFM) and electrical (I-V, C-V, C-f) characterisation studies were performed aiming to optimise the fabrication of ZrO_2 thin film as a dielectric, with a set of fluences and pulses applied on 1, 2 and 3 spin coated layers of ZrO_2. An initial IRSE investigation revealed the incomplete conversion of $Zr(AcAc)_4$ into ZrO_2 at $300\ °C$ (the temperature used for the reference samples), with detected acetate by-products, which require temperatures above $300\ °C$ to dissociate (a finding in accordance with the initial IRSE study of $Zn(CH_3COO)_2$). The electrical performance of 1-layered ZrO_2 was found inappropriate for use in TFT devices, as large frequency dispersion was detected (possibly due to decreased film thickness). The optimum electrical performance of ZrO_2 thin films was obtained at 2-layered films, which combined the best C-V, C-f, and dielectric breakdown results along with the smoothest film surface. The criticality of smooth surface was particularly highlighted in BGTC TFTs, as the dielectric – semiconductor interface (which can be tremendously deteriorated by dielectrics with high roughness) defines the channel formation mechanism. Finally, 3-layered ZrO_2 films showed increased crystallisation (thus roughness), a parameter which renders them inferior to smooth 2 – layered ZrO_2 films. Following ZrO_2 thin film optimisation, TFT devices based on sol-gel deposited, laser processed In_2O_3 and ZrO_2 were fabricated. In addition to ZrO_2, Al_2O_3 was also used as a reference dielectric layer. Electrical characterisation of devices revealed TFT behaviour in ZrO_2/In_2O_3 thin films when In_2O_3 was thermally annealed. However, in devices where both dielectric and semiconductor layers were laser annealed, the device performance was poor, with reported dielectric breakdown due to the subsequent LA step in In_2O_3 (which inevitably affects dielectric as well). Therefore, further investigations would be required to better capitalise on the apparent benefits of the LA approach. Devices based on Al_2O_3/In_2O_3 did not show the desirable TFT performance features.

7.2. Future Perspectives

As in most Ph.D. research programmes, the obtained results of this work have revealed several pathways of new research work of high interest. These are listed below:

1. **IRSE investigation of sol gel deposited, laser processed MO thin films:** The IRSE analysis conducted in this work shall constitute a guideline into precise fitting of metalorganic precursor thin films which convert into metal oxides *via* LA. The existing knowledge on substrate importance should define the optimum film-substrate combinations, with potential in expanding the precursor palette into new materials of interest. However, an important limitation should be first resolved, namely the role of substrate in LA. To resolve the first limitation, theoretical and experimental investigation on substrate's reflectivity at $248\ \mathrm{nm}$ (KrF Laser wavelength) should be conducted, to reveal the absorption profile of thin films deposited atop of the substrate (similarly to the investigation conducted in this work with the $\mathrm{SiO_2}$ thicknesses).
2. **Optimisation on $\mathbf{ZrO_2 - In_2O_3}$ LA conditions when both layers are formed using LA**: In devices based on sol-gel deposited, laser processed dielectric and semiconductor layers, the annealing of semiconductor highly affects the dielectric layer. A potential solution would involve the "under-annealing" of dielectric at the time of its fabrication. However, a potential dissolving of the unconverted dielectric precursor could occur during semiconductor deposition. To tackle this problem, a set of changes in solution fabrication and deposition, such as an appropriate choice of precursors and solvents that do not dissolve each other during film stacking. Note that the solvent used in this work was 2-ME for both dielectric and semiconductor layers. In case of change in solvent, re-optimisation of deposition and LA conditions should be conducted.
3. **Use of dielectric bilayer:** Investigation of dielectric combinations, such as $\mathrm{Al_2O_3/ZrO_2}$ bilayers. This can potentially combine the advantages of metal oxides (such as high dielectric constant of $\mathrm{Al_2O_3}$ and smoothness of $\mathrm{ZrO_2}$ on top).
4. **Substitution of $\mathbf{2\text{-}ME}$ with $\mathbf{H_2O}$ towards environmentally friendly device fabrication:** minimisation of solvent waste (in our case 2-ME) which, however, requires re-optimisation of LA conditions.
5. **Exploration of p-type sol-gel deposited, laser processed semiconductors:** p-type materials such as CuO: IRSE and LA could be combined to optimise the fabrication route of CuO thin films, with potential implementation in p-type semiconductor TFT devices.
6. **Substitution of spin coating with printing-based deposition techniques:** Inkjet printing, slot-die and spray coating could be implemented (instead of spin coating) towards dielectric and semiconductor thin film deposition. This fabrication route, combined with LA (large-

scale compatible annealing technique), can constitute the next step in fabrication of high-performance electronics, while exhibiting perfect compatibility with large-scale fabrication schemes.

7. **Exploration of sol-gel deposited, laser processed transparent conductive oxides (TCOs):** The presented research involved the investigation of semiconductor and dielectric materials, however an expand into conductive metal oxides will allow for the substitution of metal contact with metal oxides of tuneable optoelectronic properties (such as ITO and AZO).
8. **Transition to flexible substrates:** The most challenging and promising step of this research work is the implementation of sol-gel and LA expertise into fabricating flexible devices. The transition from Si would require re-optimisation of deposition parameters, theoretical study on the change in absorption profiles of sol-gel films at the laser's wavelength ($248\ \mathrm{nm}$) and re-optimisation of LA conditions for each film.

8. References

1. D. Zhang, T. Huang, and L. Duan, "Emerging Self-Emissive Technologies for Flexible Displays," Adv. Mater. **32**(15), 1902391 (2020).
2. Y. S. Rim, "Review of metal oxide semiconductors-based thin-film transistors for point-of-care sensor applications," J. Inf. Disp. **21**(4), 203–210 (2020).
3. A. Kumar, A. K. Goyal, and N. Gupta, "Review—Thin-Film Transistors (TFTs) for Highly Sensitive Biosensing Applications: A Review," ECS J. Solid State Sci. Technol. **9**(11), 115022 (2020).
4. A. Sebastian, M. Le Gallo, R. Khaddam-Aljameh, and E. Eleftheriou, "Memory devices and applications for in-memory computing," Nat. Nanotechnol. **15**(3), 529–544 (2020).
5. A. H. Elsheikh, S. W. Sharshir, M. K. Ahmed Ali, J. Shaibo, E. M. A. Edreis, T. Abdelhamid, C. Du, and Z. Haiou, "Thin film technology for solar steam generation: A new dawn," Sol. Energy **177**(1), 561–575 (2019).
6. S. Lauzurica, M. Lluscà, D. Canteli, M. I. Sánchez-Aniorte, J. López-Vidrier, S. Hernández, J. Bertomeu, and C. Molpeceres, "New strategies in laser processing of TCOs for light management improvement in thin-film silicon solar cells," Laser Process. Fabr. Solar, Displays, Optoelectron. Devices III **9180**(1), 918006 (2014).
7. S. Heo, M. Chang, Y. Ju, S. Jung, and H. Hwang, "The effect of KrF laser annealing within an ultrashort time on metal-alumina-nitride-oxide-silicon-type flash memory devices," Appl. Phys. Lett. **93**(17), 172115 (2008).
8. G.-R. Lin and C.-J. Lin, "CO2 laser rapid-thermal-annealing SiOx based metal-oxide-semiconductor light emitting diode," Appl. Phys. Lett. **91**(7), 072103 (2007).
9. G. Dubourg and M. Radović, "Multifunctional Screen-Printed TiO 2 Nanoparticles Tuned by Laser Irradiation for a Flexible and Scalable UV Detector and Room-Temperature Ethanol Sensor," ACS Appl. Mater. Interfaces **11**(6), 6257–6266 (2019).
10. M. Li, W. Anderson, N. Chokshi, R. L. DeLeon, and G. Tompa, "Laser annealing of laser assisted molecular beam deposited ZnO thin films with application to metal-semiconductor-metal photodetectors," J. Appl. Phys. **100**(5), 053106 (2006).
11. A. La Magna, P. Alippi, V. Privitera, S. Scalese, S. Pannitteri, G. Fortunato, L. Mariucci, and M. Camalleri, "Material modifications induced by laser annealing in two-dimensional structures," Appl. Phys. Lett. **84**(23), 4738–4740 (2004).
12. A. Turak, "Interfacial degradation in organic optoelectronics," RSC Adv. **3**(18), 6188–6225 (2013).
13. Y.-H. Yang, S. S. Yang, and K.-S. Chou, "Characteristic Enhancement of Solution-Processed In–Ga–Zn Oxide Thin-Film Transistors by Laser Annealing," IEEE Electron Device Lett. **31**(9), 969–971 (2010).
14. H. Yu, H. Lee, J. Lee, H. Shin, and M. Lee, "Laser-assisted patterning of solution-processed oxide semiconductor thin film using a metal absorption layer," Microelectron. Eng. **88**(1), 6–10 (2011).
15. C. Chen, G. Chen, H. Yang, G. Zhang, D. Hu, H. Chen, and T. Guo, "Solution-processed metal oxide arrays using femtosecond laser ablation and annealing for thin-film transistors," J. Mater. Chem. C **5**(36), 9273–9280 (2017).
16. K. M. Yu, H. M. Ji, M. C. Nguyen, A. H. T. Nguyen, S. J. Choi, J. G. Cheon, J. H. Kim, S. W. Kim, S. Y. Cho, and R. Choi, "Low-Temperature Fabrication of High Quality Gate Insulator in Metal-Oxide-Semiconductor Capacitor Using Laser Annealing," IEEE Electron Device Lett. **40**(2), 167–170 (2019).
17. X. Yu, T. J. Marks, and A. Facchetti, "Metal oxides for optoelectronic applications," Nat. Mater. **15**, 383–396 (2016).
18. J. Livage, M. Henry, and C. Sanchez, "Sol-gel chemistry of transition metal oxides," Prog. Solid State Chem. **18**(4), 259–341 (1988).
19. K. Nishio and T. Tsuchiya, "Sol-gel processing of thin films with metal salts," in *Handbook of Sol-Gel Science and Technology: Processing, Characterization and Applications*

(Springer Cham, 2018), pp. 133–154.

20. Y.-H. Kim, J.-S. Heo, T.-H. Kim, S. Park, M.-H. Yoon, J. Kim, M. S. Oh, G.-R. Yi, Y.-Y. Noh, and S. K. Park, "Flexible metal-oxide devices made by room-temperature photochemical activation of sol-gel films," Nature **489**, 128–132 (2012).
21. A. E. Danks, S. R. Hall, and Z. Schnepp, "The evolution of “sol-gel” chemistry as a technique for materials synthesis," Mater. Horizons **3**(2), 91–112 (2016).
22. M. E. Díaz-García and R. B. Laíño, "Molecular imprinting in sol-gel materials: Recent developments and applications," Microchim. Acta **149**(2), 19–36 (2005).
23. G. Neri, "Non-conventional sol-gel routes to nanosized metal oxides for gas sensing: From materials to applications," Sci. Adv. Mater. **2**(1), 3–15 (2010).
24. S. Dellis, I. Isakov, N. Kalfagiannis, K. Tetzner, T. D. Anthopoulos, and D. C. Koutsogeorgis, "Rapid laser-induced photochemical conversion of sol-gel precursors to In2O3 layers and their application in thin-film transistors," J. Mater. Chem. C **5**(15), 3673–3677 (2017).
25. R. A. John, N. A. Chien, S. Shukla, N. Tiwari, C. Shi, N. G. Ing, and N. Mathews, "Low-temperature chemical transformations for high-performance solution-processed oxide transistors," Chem. Mater. **28**(22), 8305–8313 (2016).
26. W. Seiler, M. Nistor, C. Hebert, and J. Perrière, "Epitaxial undoped indium oxide thin films: structural and physical properties," Sol. Energy Mater. Sol. Cells **116**(1), 34–42 (2013).
27. M. Feneberg, J. Nixdorf, C. Lidig, R. Goldhahn, Z. Galazka, O. Bierwagen, and J. S. Speck, "Erratum: Many-electron effects on the dielectric function of cubic In2O3: Effective electron mass, band nonparabolicity, band gap renormalization, and Burstein-Moss shift," Phys. Rev. B **94**(4–15), 239905 (2016).
28. O. Bierwagen, "Indium oxide - A transparent, wide-band gap semiconductor for (opto)electronic applications," Semicond. Sci. Technol. **30**(2), 024001 (2015).
29. H. Pan, D. Lee, S. H. Ko, C. P. Grigoropoulos, H. K. Park, and T. Hoult, "Fiber laser annealing of indium-tin-oxide nanoparticles for large area transparent conductive layers and optical film characterization," Appl. Phys. A Mater. Sci. Process. **104**(1), 29–38 (2011).
30. M. Noh, I. Seo, J. Park, J. S. Chung, Y. S. Lee, H. J. Kim, Y. J. Chang, J. H. Park, M. G. Kang, and C. Y. Kang, "Spectroscopic ellipsometry investigation on the excimer laser annealed indium thin oxide sol-gel films," Curr. Appl. Phys. **16**(2), 145–149 (2016).
31. C. W. Cheng, W. C. Shen, C. Y. Lin, Y. J. Lee, and J. S. Chen, "Fabrication of micro/nano crystalline ITO structures by femtosecond laser pulses," Appl. Phys. A Mater. Sci. Process. **101**(6), 243–248 (2010).
32. S. Sanctis, R. C. Hoffmann, M. Bruns, and J. J. Schneider, "Direct Photopatterning of Solution–Processed Amorphous Indium Zinc Oxide and Zinc Tin Oxide Semiconductors—A Chimie Douce Molecular Precursor Approach to Thin Film Electronic Oxides," Adv. Mater. Interfaces **5**(15), 1–8 (2018).
33. J. Doménech and A. Prieto, "Stability of ZnO particles in aqueous suspensions under UV illumination," J. Phys. Chem. **90**(6), 1123–1126 (1986).
34. J. Zhou, N. Xu, and Z. L. Wang, "Dissolving behavior and stability of ZnO wires in biofluids: A study on biodegradability and biocompatibility of ZnO nanostructures," Adv. Mater. **18**(18), 2432–2435 (2006).
35. D. Mora-Fonz, T. Lazauskas, M. R. Farrow, C. R. A. Catlow, S. M. Woodley, and A. A. Sokol, "Why Are Polar Surfaces of ZnO Stable?," Chem. Mater. **29**(12), 5306–5320 (2017).
36. M. F. Khan, A. H. Ansari, M. Hameedullah, E. Ahmad, F. M. Husain, Q. Zia, U. Baig, M. R. Zaheer, M. M. Alam, A. M. Khan, Z. A. Alothman, I. Ahmad, G. M. Ashraf, and G. Aliev, "Sol-gel synthesis of thorn-like ZnO nanoparticles endorsing mechanical stirring effect and their antimicrobial activities: Potential role as nano-Antibiotics," Sci. Rep. **6**(1), 27689 (2016).
37. I. Hölken, M. Hoppe, Y. K. Mishra, S. N. Gorb, R. Adelung, and M. J. Baum, "Complex shaped ZnO nano- and microstructure based polymer composites: Mechanically stable and environmentally friendly coatings for potential antifouling applications," Phys. Chem. Chem. Phys. **18**(10), 7114–7123 (2016).

38. W. W. Rudolph, D. Fischer, M. R. Tomney, and C. C. Pye, "Indium(III) hydration in aqueous solutions of perchlorate, nitrate and sulfate. Raman and infrared spectroscopic studies and ab-initio molecular orbital calculations of indium(III)-water clusters," Phys. Chem. Chem. Phys. **6**(22), 5145–5155 (2004).
39. J. Chandradass, D. S. Bae, and K. H. Kim, "A simple method to prepare indium oxide nanoparticles: Structural, microstructural and magnetic properties," Adv. Powder Technol. **22**(3), 370–374 (2011).
40. M. I. Ivanovskaya, E. A. Ovodok, and D. A. Kotsikau, "Sol-gel synthesis and features of the structure of Au-In2O 3 nanocomposites," Glas. Phys. Chem. **37**(1), 560–567 (2011).
41. Y. C. Yoon, K. S. Park, and S. D. Kim, "Effects of low preheating temperature for ZnO seed layer deposited by sol-gel spin coating on the structural properties of hydrothermal ZnO nanorods," Thin Solid Films **597**(12), 125–130 (2015).
42. N. B. Patil, A. R. Nimbalkar, and M. G. Patil, "ZnO thin film prepared by a sol-gel spin coating technique for NO2 detection," Mater. Sci. Eng. B Solid-State Mater. Adv. Technol. **227**(1), 53–60 (2018).
43. S. Logothetidis, D. Georgiou, A. Laskarakis, C. Koidis, and N. Kalfagiannis, "In-line spectroscopic ellipsometry for the monitoring of the optical properties and quality of roll-to-roll printed nanolayers for organic photovoltaics," Sol. Energy Mater. Sol. Cells **112**(1), 144–156 (2013).
44. A. Liu, H. Zhu, Z. Guo, Y. Meng, G. Liu, E. Fortunato, R. Martins, and F. Shan, "Solution Combustion Synthesis: Low-Temperature Processing for p-Type Cu:NiO Thin Films for Transparent Electronics," Adv. Mater. **29**(34), (2017).
45. E. Carlos, R. Branquinho, A. Kiazadeh, J. Martins, P. Barquinha, R. Martins, and E. Fortunato, "Boosting Electrical Performance of High-κ Nanomultilayer Dielectrics and Electronic Devices by Combining Solution Combustion Synthesis and UV Irradiation," ACS Appl. Mater. Interfaces **9**(46), 40428–40437 (2017).
46. K. H. Wang, H. W. Zan, and O. Soppera, "The zinc-loss effect and mobility enhancement of DUV-patterned sol-gel IGZO thin-film transistors," Semicond. Sci. Technol. **33**(3), (2018).
47. H.-W. Zan, W.-T. Chen, C.-W. Chou, C.-C. Tsai, C.-N. Huang, and H.-W. Hsueh, "Low Temperature Annealing with Solid-State Laser or UV Lamp Irradiation on Amorphous IGZO Thin-Film Transistors," Electrochem. Solid-State Lett. **13**(5), 144 (2010).
48. W. T. Park and Y. Y. Noh, "A self-aligned high resolution patterning process for large area printed electronics," J. Mater. Chem. C **5**(26), 6467–6470 (2017).
49. K. Tetzner, Y.-H. Lin, A. Regoutz, A. Seitkhan, D. J. Payne, and T. D. Anthopoulos, "Sub-second photonic processing of solution-deposited single layer and heterojunction metal oxide thin-film transistors using a high-power xenon flash lamp," J. Mater. Chem. C **5**(45), 11724–11742 (2017).
50. T. Y. Eom, C. H. Ahn, J. G. Kang, M. S. Salman, S. Y. Lee, Y. H. Kim, H. J. Lee, C. M. Kang, and C. Kang, "Investigation of the evolution of nitrogen defects in flash-lamp-annealed InGaZnO films and their effects on transistor characteristics," Appl. Phys. Express **11**(6), (2018).
51. B. Pécz, L. Dobos, D. Panknin, W. Skorupa, C. Lioutas, and N. Vouroutzis, "Crystallization of amorphous-Si films by flash lamp annealing," Appl. Surf. Sci. **242**(1–2), 185–191 (2005).
52. S. H. Jeong, B. S. Bae, J. Y. Kim, S. J. Moon, K. M. Yu, B. K. Kim, H. J. Kim, and E. J. Yun, "Flash Lamp Annealing Effect on Stability of Oxide TFT," ECS Trans. **64**(10), 109–113 (2014).
53. J. Lehmann, R. Hübner, J. V. Borany, W. Skorupa, T. Mikolajick, A. Schäfer, J. Schubert, and S. Mantl, "Millisecond flash lamp annealing for LaLuO3 and LaScO 3 high-k dielectrics," Microelectron. Eng. **109**(9), 381–384 (2013).
54. E. Carlos, S. Dellis, N. Kalfagiannis, L. Koutsokeras, D. C. Koutsogeorgis, R. Branquinho, R. Martins, and E. Fortunato, "Laser induced ultrafast combustion synthesis of solution-based AlOX for thin film transistors," J. Mater. Chem. C **8**(18), 6176–6184 (2020).

55. E. Yarali, C. Koutsiaki, H. Faber, K. Tetzner, E. Yengel, P. Patsalas, N. Kalfagiannis, D. C. Koutsogeorgis, and T. D. Anthopoulos, "Recent Progress in Photonic Processing of Metal-Oxide Transistors," Adv. Funct. Mater. **30**(20), 1906022 (2019).
56. J. P. S. Bermundo, C. Kulchaisit, D. C. Corsino, A. Syairah, M. N. Fujii, H. Ikenoue, Y. Ishikawa, and Y. Uraoka, "30-3: High Performance All Solution Processed Oxide Thin-Film Transistor via Photo-induced Semiconductor-to-Conductor Transformation of a-InZnO," SID Symp. Dig. Tech. Pap. **50**(1), 422–425 (2019).
57. N. T. Nguyen, *Micromixers*, 2nd ed. (William Andrew Publishing, 2012).
58. M. S. Brown and C. B. Arnold, "Fundamentals of Laser-Material Interaction and Application to Multiscale Surface Modification," in *Springer Series in Materials Science* (2010), pp. 91–120.
59. D. Basting, *Excimer Laser Technology*, 1st ed. (Springer-Verlag Berlin, 2006).
60. A. Toropov and T. Shubina, "Plasmonic effects in metal–semiconductor nanostructures," Acta Crystallogr. Sect. B Struct. Sci. **71**(5), 579–581 (2015).
61. M. Fox, *Optical Properties of Solids*, 2nd ed. (Oxford University Press, 2011).
62. D. J. Griffiths and C. Inglefield, *Introduction to Electrodynamics*, 4th ed. (Pearson, 2005).
63. V. Barcilon and N. Bleistein, *Mathematical Methods for Wave Phenomena.*, 1st ed. (Academic Press, 1984).
64. M. Campanelli, *Classical Mechanics: A Professor–Student Collaboration* (IOP Publishing Ltd, 2020).
65. T. M. Atanackovic and A. Guran, *Theory of Elasticity for Scientists and Engineers*, 1st ed. (bIRKHAUSER, 2000).
66. C. C. Murdock, "Coulomb’s Law and the Dielectric Constant," Am. J. Phys. **12**, 201–203 (1944).
67. L. E. Sutton, "Electric dipole moments and resonance in molecules," Trans. Faraday Soc. **30**, 789–801 (1934).
68. A. F. J. Levi, "The Lorentz oscillator model," in *Essential Classical Mechanics for Device Physics* (2016).
69. S. Kumar, P. Tiwari, and M. Zymbler, "Internet of Things is a revolutionary approach for future technology enhancement: a review," J. Big Data **6**(1), 111 (2019).
70. S. B. K. Moorthy, *Thin Film Structures in Energy Applications* (Springer Cham, 2015).
71. C. Garlisi, E. Trepci, X. Li, R. Al Sakkaf, K. Al-Ali, R. P. Nogueira, L. Zheng, E. Azar, and G. Palmisano, "Multilayer thin film structures for multifunctional glass: Self-cleaning, antireflective and energy-saving properties," Appl. Energy **264**(1), 114697 (2020).
72. P. Yianoulis and M. Giannouli, "Thin solid films and nanomaterials for solar energy conversion and energy saving applications," J. Nano Res. **2**(2), 49–60 (2008).
73. Y. E. Firat and A. Peksoz, "Efficiency enhancement of electrochromic performance in NiO thin film via Cu doping for energy-saving potential," Electrochim. Acta **295**(1), 645–654 (2019).
74. W. A. MacDonald, "Engineered films for display technologies," J. Mater. Chem. **14**(1), 4–10 (2004).
75. K. Myny, "The development of flexible integrated circuits based on thin-film transistors," Nat. Electron. **1**, 30–39 (2018).
76. A. N. Hanna, A. T. Kutbee, R. C. Subedi, B. Ooi, and M. M. Hussain, "Wavy Architecture Thin-Film Transistor for Ultrahigh Resolution Flexible Displays," Small **14**(1), 1703200 (2018).
77. J. K. Jeong, "The status and perspectives of metal oxide thin-film transistors for active matrix flexible displays," Semicond. Sci. Technol. **26**(3), 034008 (2011).
78. M. Salamati, G. Kamyabjou, M. Mohamadi, K. Taghizade, and E. Kowsari, "Preparation of TiO2@W-VO2 thermochromic thin film for the application of energy efficient smart windows and energy modeling studies of the produced glass," Constr. Build. Mater. **218**(9), 477–482 (2019).
79. C. G. Granqvist, "Electrochromics for smart windows: Oxide-based thin films and

devices," Thin Solid Films **564**, 1–38 (2014).

80. M. Aburas, V. Soebarto, T. Williamson, R. Liang, H. Ebendorff-Heidepriem, and Y. Wu, "Thermochromic smart window technologies for building application: A review," Appl. Energy **255**(12), 113522 (2019).
81. Y. Ke, C. Zhou, Y. Zhou, S. Wang, S. H. Chan, and Y. Long, "Emerging Thermal-Responsive Materials and Integrated Techniques Targeting the Energy-Efficient Smart Window Application," Adv. Funct. Mater. **28**(22), 1800113 (2018).
82. A. J. More, R. S. Patil, D. S. Dalavi, S. S. Mali, C. K. Hong, M. G. Gang, J. H. Kim, and P. S. Patil, "Electrodeposition of nano-granular tungsten oxide thin films for smart window application," Mater. Lett. **134**(1), 298–301 (2014).
83. P. Heremans, A. K. Tripathi, A. de Jamblinne de Meux, E. C. P. Smits, B. Hou, G. Pourtois, and G. H. Gelinck, "Mechanical and Electronic Properties of Thin-Film Transistors on Plastic, and Their Integration in Flexible Electronic Applications," Adv. Mater. **28**(22), 4266–4282 (2016).
84. X. Jia, C. Fuentes-Hernandez, C. Y. Wang, Y. Park, and B. Kippelen, "Stable organic thin-film transistors," Sci. Adv. **4**(1), 1–7 (2018).
85. J. W. Borchert, U. Zschieschang, F. Letzkus, M. Giorgio, R. T. Weitz, M. Caironi, J. N. Burghartz, S. Ludwigs, and H. Klauk, "Flexible low-voltage high-frequency organic thin-film transistors," Sci. Adv. **6**(21), 1–8 (2020).
86. T. D. Lee and A. U. Ebong, "A review of thin film solar cell technologies and challenges," Renew. Sustain. Energy Rev. **70**(1), 1286–1297 (2017).
87. Y. Li, G. Xu, C. Cui, and Y. Li, "Flexible and Semitransparent Organic Solar Cells," Adv. Energy Mater. **8**(7), 1701791 (2018).
88. J. Y. Kim, J. W. Lee, H. S. Jung, H. Shin, and N. G. Park, "High-Efficiency Perovskite Solar Cells," Chem. Rev. **120**(15), 7867–7918 (2020).
89. R. Kubota, Y. Sasaki, T. Minamiki, and T. Minami, "Chemical Sensing Platforms Based on Organic Thin-Film Transistors Functionalized with Artificial Receptors," ACS Sensors **4**(10), 2571–2587 (2019).
90. N. Wang, A. Yang, Y. Fu, Y. Li, and F. Yan, "Functionalized Organic Thin Film Transistors for Biosensing," Acc. Chem. Res. **52**(2), 277–287 (2019).
91. L. Venema, "Silicon electronics and beyond," Nature **479**, 309 (2011).
92. P. Siffert and E. Krimmel, *Silicon: Evolution and Future of a Technology* (Springer, 2010).
93. K. Jousten, *Handbook of Vacuum Technology*, 2nd ed. (John Wiley & Sons, 2016).
94. R. W. Keyes, "Fundamental limits of silicon technology," Pro. IEEE **89**(3), 227–239 (2001).
95. J. D. Meindl, Q. Chen, and J. A. Davis, "Limits on silicon nanoelectronics for terascale integration," Science (80-.). **293**(5537), 2044–2049 (2001).
96. R. W. Keyes, "Physical limits of silicon transistors and circuits," Reports Prog. Phys. **68**(12), 2701 (2005).
97. K. C. Saraswat, "(Invited) How Far Can We Push Conventional Silicon Technology and What are the Future Alternatives?," ECS Trans. **98**(5), 69 (2020).
98. L. C. Andreani, A. Bozzola, P. Kowalczewski, M. Liscidini, and L. Redorici, "Silicon solar cells: Toward the efficiency limits," Adv. Phys. X **4**(1), 126–148 (2019).
99. P. Kumbhakar, C. Chowde Gowda, P. L. Mahapatra, M. Mukherjee, K. D. Malviya, M. Chaker, A. Chandra, B. Lahiri, P. M. Ajayan, D. Jariwala, A. Singh, and C. S. Tiwary, "Emerging 2D metal oxides and their applications," Mater. Today **45**(1), 142–168 (2021).
100. M. Lira-Cantú, *The Future of Semiconductor Oxides in Next-Generation Solar Cells* (Elsevier, 2018).
101. A. A. Odeh and Y. Al-Douri, "Metal oxides in electronics," in *Metal Oxide Powder Technologies* (Elsevier, 2020), pp. 263–278.
102. H. Takagi and H. Y. Hwang, "An emergent change of phase for electronics," Science (80-.). **327**(5973), 1601–1602 (2010).
103. D. H. Lee, Y. J. Chang, G. S. Herman, and C. H. Chang, "A general route to printable high-mobility transparent amorphous oxide semiconductors," Adv. Mater. **19**(6), 843–847

(2007).

104. Y. N. Zhuravlev and O. S. Obolonskaya, "Structure, mechanical stability, and chemical bond in alkali metal oxides," J. Struct. Chem. **51**(1), 1005–1013 (2010).
105. M. A. Timmerman, R. Xia, P. T. P. Le, Y. Wang, and J. E. ten Elshof, "Metal Oxide Nanosheets as 2D Building Blocks for the Design of Novel Materials," Chem. - A Eur. J. **26**(42), 9084–9098 (2020).
106. Z. Sun, T. Liao, Y. Dou, S. M. Hwang, M. S. Park, L. Jiang, J. H. Kim, and S. X. Dou, "Generalized self-assembly of scalable two-dimensional transition metal oxide nanosheets," Nat. Commun. **5**, 3813 (2014).
107. J. Mei, T. Liao, L. Kou, and Z. Sun, "Two-Dimensional Metal Oxide Nanomaterials for Next-Generation Rechargeable Batteries," Adv. Mater. **29**(48), 1700146 (2017).
108. S. Calnan and A. N. Tiwari, "High mobility transparent conducting oxides for thin film solar cells," Thin Solid Films **518**(7), 1839–1849 (2010).
109. Y. S. Rim, H. Chen, X. Kou, H. S. Duan, H. Zhou, M. Cai, H. J. Kim, and Y. Yang, "Boost up mobility of solution-processed metal oxide thin-film transistors via confining structure on electron pathways," Adv. Mater. **26**(25), 4273–4278 (2014).
110. X. Wang and A. Dodabalapur, "Trapped Carrier Scattering and Charge Transport in High-Mobility Amorphous Metal Oxide Thin-Film Transistors," Ann. Phys. **530**(12), 1800341 (2018).
111. W. Xu, H. Li, J. Bin Xu, and L. Wang, "Recent Advances of Solution-Processed Metal Oxide Thin-Film Transistors," ACS Appl. Mater. Interfaces **10**(31), 25878–25901 (2018).
112. J. W. Park, B. H. Kang, and H. J. Kim, "A Review of Low-Temperature Solution-Processed Metal Oxide Thin-Film Transistors for Flexible Electronics," Adv. Funct. Mater. **30**(20), 1904632 (2020).
113. A. Liu, H. Zhu, H. Sun, Y. Xu, and Y. Y. Noh, "Solution Processed Metal Oxide High-κ Dielectrics for Emerging Transistors and Circuits," Adv. Mater. **30**(33), 1–39 (2018).
114. S. R. Thomas, P. Pattanasattayavong, and T. D. Anthopoulos, "Solution-processable metal oxide semiconductors for thin-film transistor applications," Chem. Soc. Rev. **42**(16), 6910–6923 (2013).
115. R. Abbel, Y. Galagan, and P. Groen, "Roll-to-Roll Fabrication of Solution Processed Electronics," Adv. Eng. Mater. **20**(8), 1701190 (2018).
116. H. Sato, T. Minami, S. Takata, and T. Yamada, "Transparent conducting p-type NiO thin films prepared by magnetron sputtering," Thin Solid Films **236**(2), 27–31 (1993).
117. H. Kawazoe, M. Yasukawa, H. Hyodo, M. Kurita, H. Yanagi, and H. Hosono, "P-type electrical conduction in transparent thin films of CuAlO2," Nature **389**, 939–942 (1997).
118. P. M. Cândido Barquinha, "transparent oxide thin film transistors: production, characterisation and integration," Universidade Nova de Lisboa (2010).
119. K. Ellmer, "Resistivity of polycrystalline zinc oxide films: Current status and physical limit," J. Phys. D. Appl. Phys. **34**(21), 3097 (2001).
120. M. Okude, K. Ueno, S. Itoh, M. Kikuchi, A. Ohtomo, and M. Kawasaki, "Effect of in situ annealed SnO2 buffer layer on structural and electrical properties of (0 0 1) SnO2/TiO2 heterostructures," J. Phys. D. Appl. Phys. **41**(12), 125309 (2008).
121. J. R. Bellingham, W. A. Phillips, and C. J. Adkins, "Electrical and optical properties of amorphous indium oxide," J. Phys. Condens. Matter **2**(28), 6207 (1990).
122. K. Nomura, H. Ohta, K. Ueda, T. Kamiya, M. Hirano, and H. Hosono, "Thin-film transistor fabricated in single-crystalline transparent oxide semiconductor," Science (80-.). **300**(5623), 1269–1272 (2003).
123. K. Nomura, H. Ohta, A. Takagi, T. Kamiya, M. Hirano, and H. Hosono, "Room-temperature fabrication of transparent flexible thin-film transistors using amorphous oxide semiconductors," Nature **432**, 488–492 (2004).
124. R. L. Weiher, "Electrical properties of single crystals of indium oxide," J. Appl. Phys. **33**(9), 2834–2839 (1962).
125. P.-M. F. smith william, Hashemi Javad, *Foundations of Materials Science and Engineering*,

6th ed. (McGraw-Hill Education, 2019).

126. Schroeder H, "Properties and applications of oxide layers deposited on glass from organic solutions," in *Opt.Acta 9* (1962), p. 249.
127. J. Robertson, "High dielectric constant gate oxides for metal oxide Si transistors," Reports Prog. Phys. **69**(2), 327 (2006).
128. J. S. Park, W.-J. Maeng, H.-S. Kim, and J.-S. Park, "Review of recent developments in amorphous oxide semiconductor thin-film transistor devices," Thin Solid Films **520**(6), 1679–1693 (2012).
129. E. Fortunato, P. Barquinha, and R. Martins, "Oxide semiconductor thin-film transistors: A review of recent advances," Adv. Mater. **24**(22), 2945–2986 (2012).
130. S. T. Meyers, J. T. Anderson, C. M. Hung, J. Thompson, J. F. Wager, and D. A. Keszler, "Aqueous inorganic inks for low-temperature fabrication of ZnO TFTs," J. Am. Chem. Soc. **130**(51), 17603–17609 (2008).
131. S. Park, K.-H. Kim, J. Jo, S. Sung, K.-T. Kim, W. Lee, J. Kim, H. J. Kim, G. Yi, Y. Kim, M. Yoon, and S. K. Park, "In-Depth Studies on Rapid Photochemical Activation of Various Sol-Gel Metal Oxide Films for Flexible Transparent Electronics," Adv. Funct. Mater. **25**(19), 2807–2815 (2015).
132. D. H. Kim, J. W. Park, Y. M. Chang, D. Lim, and H. Chung, "Electrical properties and structure of laser-spike-annealed hafnium oxide," Thin Solid Films **518**(10), 2812–2815 (2010).
133. C. H. Lee, S. H. Hur, Y. C. Shin, J. H. Choi, D. G. Park, and K. Kim, "Charge-trapping device structure of Si O2 SiNhigh-k dielectric Al2 O3 for high-density flash memory," Appl. Phys. Lett. **86**(15), 152908 (2005).
134. S. K. Kim, S. W. Lee, J. H. Han, B. Lee, S. Han, and C. S. Hwang, "Capacitors with an equivalent oxide thickness of <0.5 nm for nanoscale electronic semiconductor memory," Adv. Funct. Mater. **20**(18), 2989–3003 (2010).
135. S. Takeda, Y. Ikuta, M. Hirano, and H. Hosono, "Modification of sol–gel-derived amorphous Al2O3 thin films by F2 excimer laser irradiation at ambient temperature," J. Mater. Res. **16**(4), 1003–1009 (2001).
136. J. H. Kim, Y. S. Rim, and H. J. Kim, "Homojunction solution-processed metal oxide thin-film transistors using passivation-induced channel definition," ACS Appl. Mater. Interfaces **6**(7), 4819–4822 (2014).
137. T. López, F. Tzompantzi, J. Hernández-Ventura, R. Gómez, X. Bokhimi, G. Pecchi, and P. Reyes, "Effect of zirconia precursor on the properties of ZrO2-SiO2 sol-gel oxides," J. Sol-Gel Sci. Technol. **24**(2), 207–219 (2002).
138. Y. M. Park, A. Desai, A. Salleo, and L. Jimison, "Solution-processable zirconium oxide gate dielectrics for flexible organic field effect transistors operated at low voltages," Chem. Mater. **25**(13), 2571–2579 (2013).
139. C. Zhu, A. Liu, G. Liu, G. Jiang, Y. Meng, E. Fortunato, R. Martins, and F. Shan, "Low-temperature, nontoxic water-induced high-: K zirconium oxide dielectrics for low-voltage, high-performance oxide thin-film transistors," J. Mater. Chem. C **4**(45), 10715–10721 (2016).
140. J. Li, Y. Pan, C. Xiang, Q. Ge, and J. Guo, "Low temperature synthesis of ultrafine α-Al2O3 powder by a simple aqueous sol-gel process," Ceram. Int. **32**(5), 587–591 (2006).
141. S. Park, C.-H. Kim, W.-J. Lee, S. Sung, and M.-H. Yoon, "Sol-gel metal oxide dielectrics for all-solution-processed electronics," Mater. Sci. Eng. R Reports **114**(1), 1–22 (2017).
142. M. Parashar, V. K. Shukla, and R. Singh, "Metal oxides nanoparticles via sol–gel method: a review on synthesis, characterization and applications," J. Mater. Sci. Mater. Electron. **31**(3), 3729–3749 (2020).
143. C. Glynn and C. O'Dwyer, "Solution Processable Metal Oxide Thin Film Deposition and Material Growth for Electronic and Photonic Devices," Adv. Mater. Interfaces **4**(2), 1600610 (2017).
144. M. Ebelman, "On the composition," Ann. Chim. Phys **16**, 129 (1846).

145. Y. Dimitriev, Y. Ivanova, and R. Iordanova, "History of Sol-Gel Science and Technology," J. Univ. Chem. Technol. Metall. **43**(2), 181–192 (2008).
146. B. E. Yoldas, "Monolithic glass formation by chemical polymerization," J. Mater. Sci. **14**(8), 1843–1849 (1979).
147. E. A. Cochran, K. N. Woods, D. W. Johnson, C. J. Page, and S. W. Boettcher, "Unique chemistries of metal-nitrate precursors to form metal-oxide thin films from solution: Materials for electronic and energy applications," J. Mater. Chem. A **7**(42), 24124–24149 (2019).
148. G. W. Scherer, "Aging and drying of gels," J. Non. Cryst. Solids **100**(1–3), 77–92 (1988).
149. S. L. Isley and R. L. Penn, "Titanium dioxide nanoparticles: Effect of sol-gel pH on phase composition, particle size, and particle growth mechanism," J. Phys. Chem. C **112**(12), 4469–4474 (2008).
150. C. De Coelho Escobar and J. H. Z. Dos Santos, "Effect of the sol-gel route on the textural characteristics of silica imprinted with Rhodamine B," J. Sep. Sci. **37**(7), 868–875 (2014).
151. M. M. Collinson, H. Wang, R. Makote, and A. Khramov, "The effects of drying time and relative humidity on the stability of sol-gel derived silicate films in solution," J. Electroanal. Chem. **519**(1–2), 65–71 (2002).
152. I. Bretos, R. Jiménez, J. Ricote, and M. L. Calzada, "Low-temperature crystallization of solution-derived metal oxide thin films assisted by chemical processes," Chem. Soc. Rev. **47**(2), 291–308 (2017).
153. K. H. Lim, J. Lee, J. E. Huh, J. Park, J. H. Lee, S. E. Lee, and Y. S. Kim, "A systematic study on effects of precursors and solvents for optimization of solution-processed oxide semiconductor thin-film transistors," J. Mater. Chem. C **5**(31), 7768–7776 (2017).
154. S. Jeong, J. Y. Lee, S. S. Lee, Y. Choi, and B. H. Ryu, "Impact of metal salt precursor on low-temperature annealed solution-derived Ga-doped In2O3 semiconductor for thin-film transistors," J. Phys. Chem. C **115**(23), 11773–11780 (2011).
155. Y. H. Kim, J. S. Heo, T. H. Kim, S. Park, M. H. Yoon, J. Kim, M. S. Oh, G. R. Yi, Y. Y. Noh, and S. K. Park, "Flexible metal-oxide devices made by room-temperature photochemical activation of sol gel films," Nature **489**(7414), 128–132 (2012).
156. K. N. Woods, P. N. Plassmeyer, D. H. Park, L. J. Enman, A. K. Grealish, B. L. Kirk, S. W. Boettcher, D. A. Keszler, and C. J. Page, "Low - temperature steam annealing of metal oxide thin films from aqueous precursors: Enhanced counterion removal, resistance to water absorption, and dielectric constant," Chem. Mater. **29**(19), 8531–8538 (2017).
157. W. J. Scheideler, R. Kumar, A. R. Zeumault, and V. Subramanian, "Low-Temperature-Processed Printed Metal Oxide Transistors Based on Pure Aqueous Inks," Adv. Funct. Mater. **27**(4), 1606062 (2017).
158. Y. S. Rim, H. Chen, T. Bin Song, S. H. Bae, and Y. Yang, "Hexaaqua Metal Complexes for Low-Temperature Formation of Fully Metal Oxide Thin-Film Transistors," Chem. Mater. **27**(16), 5808–5812 (2015).
159. G. Liu, A. Liu, H. Zhu, B. Shin, E. Fortunato, R. Martins, Y. Wang, and F. Shan, "Low temperature, nontoxic water-induced metal-oxide thin films and their application in thin-film transistors," Adv. Funct. Mater. **25**(17), 2564–2572 (2015).
160. A. Liu, G. X. Liu, H. H. Zhu, F. Xu, E. Fortunato, R. Martins, and F. K. Shan, "Fully solution-processed low-voltage aqueous In2O3 thin-film transistors using an ultrathin ZrOx dielectric," ACS Appl. Mater. Interfaces **6**(20), 17364–17369 (2014).
161. P. N. Plassmeyer, K. Archila, J. F. Wager, and C. J. Page, "Lanthanum aluminum oxide thin-film dielectrics from aqueous solution," ACS Appl. Mater. Interfaces **7**(3), 1678–1684 (2015).
162. K. N. Woods, T. H. Chiang, P. N. Plassmeyer, M. G. Kast, A. C. Lygo, A. K. Grealish, S. W. Boettcher, and C. J. Page, "High-κ Lanthanum Zirconium Oxide Thin Film Dielectrics from Aqueous Solution Precursors," ACS Appl. Mater. Interfaces **9**(12), 10897–10903 (2017).
163. R. M. Pasquarelli, D. S. Ginley, and R. O'hayre, "Solution processing of transparent conductors: From flask to film," Chem. Soc. Rev. **40**(11), 5406–5441 (2011).

164. A. Nadarajah, M. E. Carnes, M. G. Kast, D. W. Johnson, and S. W. Boettcher, "Aqueous solution processing of F-doped SnO2 transparent conducting oxide films using a reactive tin(II) hydroxide nitrate nanoscale cluster," Chem. Mater. **25**(20), 4080–4087 (2013).
165. Carl friedrich Gauss, *Carl Friedrich Gauss: Werke* (Springer-Verlag Berlin, 1900).
166. Ali Hajimiri, *Analog: Inexact Science, Vibrant Art* (2021).
167. S. D. Brotherton, *Introduction to Thin Film Transistors*, 1st ed. (Springer Cham, 2013).
168. W. Shockley, "A unipolar “field-effect” transistor," Proc. IRE **40**(11), 1365–1376 (1952).
169. M. Marinkovic, R. Takata, A. Neumann, D. V. Pham, R. Anselmann, J. Maas, J. L. Van Der Steen, G. Gelinck, and L. Katsouras, "Large-area processing of solution type metal-oxide in TFT backplanes and integration in highly stable OLED displays," Dig. Tech. Pap. - SID Int. Symp. **48**(1), 169–172 (2017).
170. S. Jeong, Y. G. Ha, J. Moon, A. Facchetti, and T. J. Marks, "Role of gallium doping in dramatically lowering amorphous-oxide processing temperatures for solution-derived indium zinc oxide thin-film transistors," Adv. Mater. **22**(12), 1346–1350 (2010).
171. E. A. Cochran, D. H. Park, M. G. Kast, L. J. Enman, C. K. Perkins, R. H. Mansergh, D. A. Keszler, D. W. Johnson, and S. W. Boettcher, "Role of Combustion Chemistry in Low-Temperature Deposition of Metal Oxide Thin Films from Solution," Chem. Mater. **29**(21), 9480–9488 (2017).
172. E. Carlos, R. Branquinho, A. Kiazadeh, P. Barquinha, R. Martins, and E. Fortunato, "UV-Mediated Photochemical Treatment for Low-Temperature Oxide-Based Thin-Film Transistors," ACS Appl. Mater. Interfaces **8**(45), 31100–31108 (2016).
173. S. C. Park, D. Kim, H. Shin, D. K. Lee, X. Zhang, J. Park, and J. S. Choi, "Advanced photo-annealing of indium zinc oxide films for thin-film transistors using pulse UV light," J. Inf. Disp. **17**(1), 1–7 (2016).
174. J. Kim, J.-H. Ji, S.-W. Min, G.-H. Jo, M.-W. Jung, M.-J. Park, S.-K. Lee, and J.-H. Koh, "Enhanced conductance properties of UV laser/RTA annealed Al-doped ZnO thin films," Ceram. Int. **43**(4), 3900–3904 (2017).
175. J. M. Fairfield and G. H. Schwuttke, "Silicon diodes made by laser irradiation," Solid. State. Electron. **11**(12), 1175-IN6 (2002).
176. J. C. Bean, H. J. Leamy, J. M. Poate, G. A. Rozgonyi, J. P. Van Der Ziel, J. S. Williams, and G. K. Celler, "Substrate and doping effects upon laser-induced epitaxy of amorphous silicon," J. Appl. Phys. **50**(2), 881–885 (1979).
177. M. Hatano, S. Moon, M. Lee, K. Suzuki, and C. P. Grigoropoulos, "In situ and ex situ diagnostics on melting and resolidification dynamics of amorphous and polycrystalline silicon thin films during excimer laser annealing," J. Non. Cryst. Solids **266**–**269**(1), 654–658 (2003).
178. Y. Tamminga, G. E. J. Eggermont, W. K. Hofker, D. Hoonhout, R. Garrett, and F. W. Saris, "Differences between ruby and Nd:YAG laser annealing of ion implanted silicon," Phys. Lett. A **69**(6), 436–438 (1979).
179. T. Sameshima, S. Usui, and M. Sekiya, "XeCl Excimer laser annealing used in the fabrication of poly-Si TFT’s," IEEE Electron Device Lett. **7**(5), 276–278 (1986).
180. M. Cervera, B. J. Garcia, J. Martinez, J. Garrido, and J. Piqueras, "Electronic defect levels in continuous wave laser annealed silicon metal oxide semiconductor devices," J. Appl. Phys. **64**(6), 3079–3084 (1988).
181. H. Hosono, M. Kurita, and H. Kawazoe, "Excimer laser crystallization of amorphous indium-tin oxide thin films and application to fabrication of Bragg gratings," Thin Solid Films **351**(1–2), 137–140 (1999).
182. H. Hosono, M. Kurita, and H. Kawazoe, "Excimer laser crystallization of amorphous indium-tin-oxide and its application to fine patterning," Japanese J. Appl. Physics, Part 2 Lett. **37**(10), 1119 (1998).
183. T. Nagase, T. Ooie, and J. Sakakibara, "Novel approach to prepare zinc oxide films: Excimer laser irradiation of sol-gel derived precursor films," Thin Solid Films **357**(2), 151–158 (1999).

184. S. Cha, S. Lee, J. Eun Jang, A. Jang, J. Pyo Hong, J. Lee, J. Inn Sohn, D. Joon Kang, and J. Min Kim, "Ultrafast and low temperature laser annealing for crystalline TiO 2 nanostructures patterned by electro-hydrodynamic lithography," Appl. Phys. Lett. **103**(5), 053114 (2013).
185. H. I. Shin, K. H. Kim, T. W. Kim, and H. K. Kim, "Fiber laser annealing of brush-painted ITO nanoparticles for use as transparent anode for organic solar cells," Ceram. Int. **42**(12), 13983–13989 (2016).
186. B. J. Li, L. J. Huang, N. F. Ren, X. Kong, Y. L. Cai, and J. L. Zhang, "Improving the performance of nickel-coated fluorine-doped tin oxide thin films by magnetic-field-assisted laser annealing," Appl. Surf. Sci. **351**(1), 113–118 (2015).
187. R. Molaei, R. Bayati, and J. Narayan, "Crystallographic characteristics and p -type to n -type transition in epitaxial Nio thin film," Cryst. Growth Des. **13**(12), 5459–5465 (2013).
188. H. Pan, N. Misra, S. H. Ko, C. P. Grigoropoulos, N. Miller, E. E. Haller, and O. Dubon, "Melt-mediated coalescence of solution-deposited ZnO nanoparticles by excimer laser annealing for thin-film transistor fabrication," Appl. Phys. A Mater. Sci. Process. **94**(10), 111–115 (2009).
189. C. N. Chen and J. J. Huang, "Effects of excimer laser annealing on low-temperature solution based indium-zinc-oxide thin film transistor fabrication," J. Appl. Res. Technol. **13**(2), 170–176 (2015).
190. L. E. Scriven, "Physics and Applications of DIP Coating and Spin Coating," MRS Proc. **121**, 717–729 (1988).
191. A. G. Emslie, F. T. Bonner, and L. G. Peck, "Flow of a viscous liquid on a rotating disk," J. Appl. Phys. **29**(5), 858–862 (1958).
192. D. M. Mattox, *The Foundations of Vacuum Coating Technology*, 1st ed. (Springer-Verlag Berlin, 2003).
193. F. Lévy, "Film Growth and Epitaxy: Methods," in *Reference Module in Materials Science and Materials Engineering* (2016).
194. J. A. Hillier, P. Patsalas, D. Karfaridis, S. Camelio, W. Cranton, A. V Nabok, C. J. Mellor, D. C. Koutsogeorgis, and N. Kalfagiannis, "Photo-engineered optoelectronic properties of indium tin oxide via reactive laser annealing," Sci. Rep. **12**, 14986 (2022).
195. N. Kalfagiannis, D. C. Koutsogeorgis, E. Lidorikis, and P. Patsalas, "Laser Annealing as a Platform for Plasmonic Nanostructuring," in *Nanoplasmonics - Fundamentals and Applications*, G. Barbillon, ed. (2017).
196. R. A. Ganeev, *Laser - Surface Interactions*, 1st ed. (Springer Dordrecht, 2014).
197. E. Carpene, D. Höche, and P. Schaaf, "Fundamentals of Laser-Material Interactions," in *Springer Series in Materials Science* (2010), pp. 91–120.
198. D. Bäuerle, "Laser processing and chemistry: recent developments," Appl. Surf. Sci. **186**(1–4), 1–6 (2002).
199. M. von Allmen and A. Blatter, *Laser-Beam Interactions with Materials: Physical Principles and Applications*, 2nd ed. (Springer-Verlag Berlin, 1995).
200. G. H. Jo, J. H. Ji, K. Masao, J. G. Ha, S. K. Lee, and J. H. Koh, "CO2 laser annealing effects for Al-doped ZnO multilayered films," Ceram. Int. **44**(S1), S211–S215 (2018).
201. M. Lluscà, J. López-Vidrier, S. Lauzurica, M. I. Sánchez-Aniorte, A. Antony, C. Molpeceres, S. Hernández, B. Garrido, and J. Bertomeu, "Activation of visible up-conversion luminescence in transparent and conducting ZnO:Er:Yb films by laser annealing," J. Lumin. **167**(1), 101–105 (2015).
202. H. Palneedi, J. H. Park, D. Maurya, M. Peddigari, G. T. Hwang, V. Annapureddy, J. W. Kim, J. J. Choi, B. D. Hahn, S. Priya, K. J. Lee, and J. Ryu, "Laser Irradiation of Metal Oxide Films and Nanostructures: Applications and Advances," Adv. Mater. **30**(14), 1705148 (2018).
203. A. Siozios, N. Kalfagiannis, D. V Bellas, C. Bazioti, G. P. Dimitrakopulos, G. Vourlias, W. M. Cranton, E. Lidorikis, D. C. Koutsogeorgis, and P. Patsalas, "Sub-surface laser nanostructuring in stratified metal/dielectric media: a versatile platform towards flexible, durable and large-scale plasmonic writing," Nanotechnology **26**(15), 155301 (2015).

204. D. V. Bellas, D. Toliopoulos, N. Kalfagiannis, A. Siozios, P. Nikolaou, P. C. Kelires, D. C. Koutsogeorgis, P. Patsalas, and E. Lidorikis, "Simulating the opto-thermal processes involved in laser induced self-assembly of surface and sub-surface plasmonic nano-structuring," Thin Solid Films **630**, 7–24 (2017).
205. G. H. Jo, S. H. Kim, and J. H. Koh, "Enhanced electrical and optical properties based on stress reduced graded structure of Al-doped ZnO thin films," Ceram. Int. **44**(1), 735–741 (2018).
206. V. S. Teodorescu, A. V. Maraloiu, M. G. Blanchin, T. Yamada, C. S. Sandu, P. Delaporte, and M. Zaharescu, "Structure and dielectric properties of low fluence excimer laser annealing of sol-gel HfO2thin films deposited on Si wafer," in *Proceedings of the International Semiconductor Conference, CAS* (2013), pp. 77–80.
207. G. Jo and J.-H. Koh, "Laser annealing effects on Ga dopants for ZnO thin films for transparent conducting oxide applications," Ceram. Int. **45**(5), 6190–6197 (2019).
208. G. Friedbacher and H. Bubert, *Surface and Thin Film Analysis: A Compendium of Principles, Instrumentation, and Applications, Second Edition* (2011).
209. M. Born, E. Wolf, and E. Hecht, *Principles of Optics: Electromagnetic Theory of Propagation, Interference and Diffraction of Light*, 7th ed. (Cambridge University Press, 2013).
210. H. Fujiwara, *Spectroscopic Ellipsometry* (John Wiley & Sons, Ltd, 2007).
211. H. Wöhler, G. Haas, M. Fritsch, and D. A. Mlynski, "Faster 4 × 4 matrix method for uniaxial inhomogeneous media," J. Opt. Soc. Am. A **5**(9), 1554 (1988).
212. O. S. Heavens, "Optical properties of thin films," Rep. Prog. Phys. **23**(1), 2–62 (1960).
213. J. A. Hillier, "Photo-engineered Optoelectronic Properties of Transparent Conductive Oxides via Reactive Laser Annealing (ReLA): The Consequence of Defects.," Nottingham Trent University (2021).
214. H. P. Gavin, *The Levenburg-Marqurdt Algorithm For Nonlinear Least Squares Curve-Fitting Problems* (2022).
215. P. H. Lissberger, "Ellipsometry and polarised light," Nature **269**, 270 (1977).
216. S. Amador-Alvarado, J. M. Flores-Camacho, A. Solís-Zamudio, R. Castro-García, J. S. Pérez-Huerta, E. Antúnez-Cerón, J. Ortega-Gallegos, J. Madrigal-Melchor, V. Agarwal, and D. Ariza-Flores, "Temperature-dependent infrared ellipsometry of Mo-doped VO2 thin films across the insulator to metal transition," Sci. Rep. **10**, 8555 (2020).
217. J. B. Baxter and C. A. Schmuttenmaer, "Conductivity of ZnO nanowires, nanoparticles, and thin films using time-resolved terahertz spectroscopy," J. Phys. Chem. B **110**(50), 25229–25239 (2006).
218. J. Z. Chen, H. Ahn, S. C. Yen, and Y. J. Tsai, "Thermally induced percolational transition and thermal stability of silver nanowire networks studied by THz spectroscopy," ACS Appl. Mater. Interfaces **6**(23), 20994–20999 (2014).
219. G. M. Turner, M. C. Beard, and C. A. Schmuttenmaer, "Carrier localization and cooling in dye-sensitized nanocrystalline titanium dioxide," J. Phys. Chem. B **106**(45), 11716–11719 (2002).
220. N. V. Smith, "Classical generalization of the Drude formula for the optical conductivity," Phys. Rev. B - Condens. Matter Mater. Phys. **64**(15), 155106 (2001).
221. L. E. Brus, "Electron-electron and electron-hole interactions in small semiconductor crystallites: The size dependence of the lowest excited electronic state," J. Chem. Phys. **80**(9), 4403–4409 (1984).
222. N. Kalfagiannis, J. L. Stoner, J. Hillier, I. Vangelidis, and E. Lidorikis, "Mid- to far-infrared sensing: SrTiO3, a novel optical material," J. Mater. Chem. C **7**(26), 7851–7857 (2019).
223. J. A. Hillier, S. Camelio, W. Cranton, A. V. Nabok, C. J. Mellor, D. C. Koutsogeorgis, and N. Kalfagiannis, "When ellipsometry works best: A case study with transparent conductive oxides," ACS Photonics **7**(10), 2692–2702 (2020).
224. H. G. Tompkins, T. Tiwald, C. Bungay, and A. E. Hooper, "Use of Molecular Vibrations to Analyze Very Thin Films with Infrared Ellipsometry," J. Phys. Chem. B **108**(12), 3777–3780

(2004).

225. S. Dhanasingh, D. Nallasamy, S. Padmanapan, and V. C. Padaki, "Cetyltrimethylammonium bromide- and ethylene glycol-assisted preparation of mono-dispersed indium oxide nanoparticles using hydrothermal method," Chem. Pap. **68**(2), 1079–1086 (2014).
226. A. Yahia, A. Attaf, H. Saidi, M. Dahnoun, C. Khelifi, A. Bouhdjer, A. Saadi, and H. Ezzaouia, "Structural, optical, morphological and electrical properties of indium oxide thin films prepared by sol gel spin coating process," Surfaces and Interfaces **14**(1), 158–165 (2019).
227. H. Xuemei, S. Yukun, and B. Bo, "Fabrication of Cubic p-n Heterojunction-Like NiO/In2O3 Composite Microparticles and Their Enhanced Gas Sensing Characteristics," J. Nanomater. **2016**, 7589028 (2016).
228. A. Taufiq, H. N. Ulya, J. Utomo, Sunaryono, N. Hidayat, H. Susanto, N. Mufti, Munasir, and S. Soontaranon, "Structural, Optical, and Antifungal Characters of Zinc Oxide Nanoparticles Prepared by Sol-gel Method," J. Phys. Conf. Ser. **1093**, 012001 (2018).
229. G. Nagaraju, Udayabhanu, Shivaraj, S. A. Prashanth, M. Shastri, K. V. Yathish, C. Anupama, and D. Rangappa, "Electrochemical heavy metal detection, photocatalytic, photoluminescence, biodiesel production and antibacterial activities of Ag–ZnO nanomaterial," Mater. Res. Bull. **94**(1), 54–63 (2017).
230. A. Top and H. Çetinkaya, "Zinc oxide and zinc hydroxide formation via aqueous precipitation: Effect of the preparation route and lysozyme addition," Mater. Chem. Phys. **167**, 77–87 (2015).
231. A. Hasanpour, M. Niyaifar, M. Asan, and J. Amighian, "Synthesis and characterization of Fe3O4 and ZnO nanocomposites by the sol-gelmethod," J. Magn. Magn. Mater. **334**, 41–44 (2013).
232. A. Koodziejczak-Radzimska, E. Markiewicz, and T. Jesionowski, "Structural characterisation of ZnO particles obtained by the emulsion precipitation method," J. Nanomater. **2012**, 656353 (2012).
233. Q. Zhu, J. Chen, Q. Zhu, Y. Cui, L. Liu, B. Li, and X. Zhou, "Monodispersed hollow microsphere of ZnO mesoporous nanopieces: Preparation, growth mechanism and photocatalytic performance," Mater. Res. Bull. **45**, 2024–2030 (2010).
234. Z. Luo, W. Cheng, H. Chen, X. Fu, X. Peng, F. Luo, and L. Nie, "Preparation and properties of enzyme-modified cassava starch-zinc complexes," J. Agric. Food Chem. **61**(19), 4631–4638 (2013).
235. D. Wu, Y. Jiang, J. Liu, Y. Yuan, J. Wu, K. Jiang, and D. Xue, "Template Route to Chemically Engineering Cavities at Nanoscale: A Case Study of Zn(OH) 2 Template," Nanoscale Res. Lett. **5**(5), 1779 (2010).
236. E. Kandare and J. M. Hossenlopp, "Thermal degradation of acetate-intercalated hydroxy double and layered hydroxy salts," Inorg. Chem. **45**(9), 3766–3773 (2006).
237. S. Wang and E. Iglesia, "Experimental and theoretical assessment of the mechanism and site requirements for ketonization of carboxylic acids on oxides," J. Catal. **345**, 183–206 (2017).
238. S. Pathiranage, S. D. Gunapala, and M. Premaratne, "Tunable plasmonic resonator using conductivity modulated Bragg reflectors," J. Phys. Condens. Matter **33**(24), 245301 (2021).
239. S. Randhawa, M. U. González, J. Renger, S. Enoch, and R. Quidant, "Design and properties of dielectric surface plasmon Bragg mirrors," Opt. Express **18**(14), 14496–14510 (2010).
240. H. G. Tompkins and J. N. Hilfiker, *Spectroscopic Ellipsometry: Practical Application to Thin Film Characterization (Materials Characterization and Analysis Collection)* (Momentum Press Engineering, 2015).
241. K. J. Baeg and J. Lee, "Flexible Electronic Systems on Plastic Substrates and Textiles for Smart Wearable Technologies," Adv. Mater. Technol. **5**(7), 2000071 (2020).
242. Z. Zhao, A. Rose, S. J. Kwon, Y. Jeon, and E. S. Cho, "Rapid photonic curing effects of xenon flash lamp on ITO–Ag–ITO multilayer electrodes for high throughput transparent

electronics," Sci. Rep. **13**, 1042 (2023).

243. P. K. Weimer, "The TFT—A New Thin-Film Transistor," Proc. IRE **50**(6), 1462–1469 (1962).
244. T. Saidani, M. Zaabat, M. S. Aida, R. Barille, M. Rasheed, and Y. Almohamed, "Influence of precursor source on sol–gel deposited ZnO thin films properties," J. Mater. Sci. Mater. Electron. **28**(6), 9252–9257 (2017).
245. J. Y. Kim, S. Noh, D. Lee, P. K. Nayak, Y. Hong, and C. Lee, "Solution-processable zinc oxide for the polymer solar cell based on P3HT:PCBM," in *Journal of Nanoscience and Nanotechnology* (2011), pp. 5995–6000.
246. A. Pimentel, S. H. Ferreira, D. Nunes, T. Calmeiro, R. Martins, and E. Fortunato, "Microwave synthesized ZnO nanorod arrays for UV sensors: A seed layer annealing temperature study," Materials (Basel). **9**(4), 299 (2016).
247. Y. Y. Zhengxu Wang, Guangwei Xu, Zhiyu Zhao, Le Cai, Quantan, Wu, Pei Cheng, Yepin Zhao, Jingjing Xue, Rui Wang, Chong Liu, "Cluster Size Control toward High Performance Solution Processed InGaZnO Thin Film Transistors," ACS Appl. Electron. Mater. **1**(12), 2483–2488 (2019).
248. Y. T. Saravanan Kumaran, Meng-Tieh Liu, Kung-Yen Lee, "The Impact of Solvents on the Performances of Solution- Processed Indium Gallium Zinc Oxide Thin-Film Transistors Using Nitrate Ligands," Adv. Eng. Mater. **22**(2), 1901053 (2020).
249. M. S. Grover, P. A. Hersh, H. Q. Chiang, E. S. Kettenring, J. F. Wager, and D. A. Keszler, "Thin-film transistors with transparent amorphous zinc indium tin oxide channel layer," J. Phys. D. Appl. Phys. **40**(5), 1335 (2007).
250. L. Liu, C. C. He, J. Zeng, Y. H. Peng, W. Y. Chen, Y. J. Zhao, and X. B. Yang, "Theoretical Study of Oxygen-Vacancy Distribution in In2O3," J. Phys. Chem. C **125**(13), 7077–7085 (2021).
251. S. Pearton, *GAN and ZNO-Based Materials and Devices*, 1st ed. (Springer-Verlag Berlin, 2012).
252. D. Kang, H. Lim, C. Kim, I. Song, J. Park, Y. Park, and J. Chung, "Amorphous gallium indium zinc oxide thin film transistors: Sensitive to oxygen molecules," Appl. Phys. Lett. **90**(19), 192101 (2007).
253. Z. Fan, D. Wang, P. C. Chang, W. Y. Tseng, and J. G. Lu, "ZnO nanowire field-effect transistor and oxygen sensing property," Appl. Phys. Lett. **85**(24), 5923–5925 (2004).
254. J. Lagowski, E. S. Sproles, and H. C. Gatos, "Quantitative study of the charge transfer in chemisorption; Oxygen chemisorption on ZnO," J. Appl. Phys. **48**(8), 3566–3575 (1977).
255. P. Barquinha, A. Pimentel, A. Marques, L. Pereira, R. Martins, and E. Fortunato, "Influence of the semiconductor thickness on the electrical properties of transparent TFTs based on indium zinc oxide," J. Non. Cryst. Solids **352**(9–20), 1749–1752 (2006).
256. C. E. Kim, E. N. Cho, P. Moon, G. H. Kim, D. L. Kim, H. J. Kim, and I. Yun, "Density-of-states modeling of solution-processed InGaZnO thin-film transistors," IEEE Electron Device Lett. **31**(10), 1131–1133 (2010).
257. T. Morimoto, Y. Yang, Y. Ochiai, N. Fukuda, and Y. Ohki, "Effects of metal content on electrical and physical properties in solution-processed IGZO thin films," Appl. Phys. A Mater. Sci. Process. **126**(5), 388 (2020).
258. H. W. Lee and W. J. Cho, "Effects of vacuum rapid thermal annealing on the electrical characteristics of amorphous indium gallium zinc oxide thin films," AIP Adv. **8**(1), 015007 (2018).
259. H. J. Kim, K. Park, and H. J. Kim, "High-performance vacuum-processed metal oxide thin-film transistors: A review of recent developments," J. Soc. Inf. Disp. **28**(7), 591–622 (2020).
260. A. C. Tickle, *Thin-Film Transistors: A New Approach to Microelectronics* (Wiley, 1969).
261. A. Dixit, C. Sudakar, R. Naik, V. M. Naik, and G. Lawes, "Undoped vacuum annealed In2O3 thin films as a transparent," Appl. Phys. Lett. **95**(19), 192105 (2009).
262. A. Walsh and C. R. A. Catlow, "Structure, stability and work functions of the low index surfaces of pure indium oxide and Sn-doped indium oxide (ITO) from density functional theory," J. Mater. Chem. **20**(46), 10438–10444 (2010).

263. T. Minami, "Transparent conducting oxide semiconductors for transparent electrodes," Semicond. Sci. Technol. **20**(4), S35 (2005).
264. H. Yabuta, M. Sano, K. Abe, T. Aiba, T. Den, H. Kumomi, K. Nomura, T. Kamiya, and H. Hosono, "High-mobility thin-film transistor with amorphous InGaZnO4 channel fabricated by room temperature rf-magnetron sputtering," Appl. Phys. Lett. **89**(11), 112123 (2006).
265. C. Tsakonas, V. L. Kuznetsov, W. M. Cranton, N. Kalfagiannis, K. M. Abusabee, D. C. Koutsogeorgis, N. Abeywickrama, and P. P. Edwards, "Low temperature sputter-deposited ZnO films with enhanced Hall mobility using excimer laser post-processing," J. Phys. D. Appl. Phys. **50**(48), 485306 (2017).
266. J. Y. Lee, F. Shan, H. S. Kim, and S. J. Kim, "Effect of Femtosecond Laser Postannealing on a-IGZO Thin-Film Transistors," IEEE Trans. Electron Devices **68**(7), 3371–3378 (2021).
267. H. Y. Kim, E. A. Jung, G. Mun, R. E. Agbenyeke, B. K. Park, J. S. Park, S. U. Son, D. J. Jeon, S. H. K. Park, T. M. Chung, and J. H. Han, "Low-Temperature Growth of Indium Oxide Thin Film by Plasma-Enhanced Atomic Layer Deposition Using Liquid Dimethyl(N-ethoxy-2,2-dimethylpropanamido)indium for High-Mobility Thin Film Transistor Application," ACS Appl. Mater. Interfaces **8**(40), 26924–26931 (2016).
268. I. N. Reddy, C. V. Reddy, M. Cho, J. Shim, and D. Kim, "Structural, optical and XPS study of thermal evaporated In2O3 thin films," Mater. Res. Express **4**(8), 086406 (2017).
269. S. Cho, "Effects of rapid thermal annealing on the properties of In 2O3 thin films grown on glass substrate by rf reactive magnetron sputtering," Microelectron. Eng. **89**, 84–88 (2012).
270. Ian J McColm; N J Clark, *Forming, Shaping and Working of High-Performance Ceramics* (New York : Chapman and Hall, 1990).
271. T. O. L. Sunde, M. A. Einarsrud, and T. Grande, "Solid state sintering of nano-crystalline indium tin oxide," J. Eur. Ceram. Soc. **33**(3), 565–574 (2013).
272. B. C. Kim, J. H. Lee, J. J. Kim, H. Y. Lee, and J. S. Lee, "Densification of nanocrystalline ITO powders in fast firing: Effect of specimen mass and sintering atmosphere," Mater. Res. Bull. **40**(2), 395–404 (2005).
273. L. Abello, B. Bochu, A. Gaskov, S. Koudryavtseva, G. Lucazeau, and M. Roumyantseva, "Structural characterization of nanocrystalline SnO2 by X-ray and Raman spectroscopy," J. Solid State Chem. **135**(1), 78–85 (1998).
274. G. Korotcenkov, V. Brinzari, M. Ivanov, A. Cerneavschi, J. Rodriguez, A. Cirera, A. Cornet, and J. Morante, "Structural stability of indium oxide films deposited by spray pyrolysis during thermal annealing," Thin Solid Films **479**(1–2), 38–51 (2005).
275. I. Choudhary and Deepak, "Investigation of time-dependent stability and surface defects in sol–gel derived IGZO and IZO thin films," J. Sol-Gel Sci. Technol. **100**(3), 132–146 (2021).
276. H. Jeon, S. Na, M. R. Moon, D. Jung, H. Kim, and H.-J. Lee, "The Effects of Zn Ratio on the Microstructure Electrical Properties of InGaZnO Films," J. Electrochem. Soc. **13**(9), 1310 (2011).
277. H. E. Silva-Lopez, B. S. Marcelino, A. Guillen-Cervantes, O. Zelaya-Angel, and R. Ramirez-Bon, "Physical Properties of Sputtered Indium-doped ZnO Films Deposited on Flexible Transparent Substrates," Mater. Res. **21**(6), (2018).
278. D. H. Yoon, S. J. Kim, D. L. Kim, S. Jin Heo, and H. J. Kim, "Quenching effects on the solution-processed In-Ga-Zn-O system," Electrochem. Solid-State Lett. **14**(9), E28 (2011).
279. C. Y. Tsay and T. T. Huang, "Improvement of physical properties of IGZO thin films prepared by excimer laser annealing of sol-gel derived precursor films," Mater. Chem. Phys. **140**(1), 365–372 (2013).
280. X. Huang, C. Wu, H. Lu, F. Ren, D. Chen, Y. Liu, G. Yu, R. Zhang, Y. Zheng, and Y. Wang, "Large-swing a-igzo inverter with a depletion load induced by laser annealing," IEEE Electron Device Lett. **35**(10), 1034–1036 (2014).
281. K. Nomura, T. Kamiya, M. Hirano, and H. Hosono, "Origins of threshold voltage shifts in room-temperature deposited and annealed a-In-Ga-Zn-O thin-film transistors," Appl.

Phys. Lett. **95**(1), 013502 (2009).

282. D. Hyung Kim, D. Youn Yoo, H. Kwang Jung, D. Hwan Kim, and S. Yeol Lee, "Origin of instability by positive bias stress in amorphous Si-In-Zn-O thin film transistor," Appl. Phys. Lett. **99**(17), 172106 (2011).
283. C. Chen, H. Yang, Q. Yang, G. Chen, H. Chen, and T. Guo, "Low-temperature solution-processed flexible metal oxide thin-film transistors via laser annealing," J. Phys. D. Appl. Phys. **52**(1), 385105 (2019).
284. C. Chen, G. Chen, H. Yang, G. Zhang, D. Hu, H. Chen, and T. Guo, "Solution-processed metal oxide arrays using femtosecond laser ablation and annealing for thin-film transistors," J. Mater. Chem. C **5**(36), 9273–9280 (2017).
285. S. K. Sundaram and E. Mazur, "Inducing and probing non-thermal transitions in semiconductors using femtosecond laser pulses," Nat. Mater. **1**, 217–224 (2002).
286. E. G. Gamaly and A. V. Rode, "Physics of ultra-short laser interaction with matter: From phonon excitation to ultimate transformations," Prog. Quantum Electron. **37**(5), 215–323 (2013).
287. D. H. Lee, S. M. Park, D. K. Kim, Y. S. Lim, and M. Yi, "Effects of Ga composition ratio and annealing temperature on the electrical characteristics of solution-processed IGZO thin-film transistors," J. Semicond. Technol. Sci. **53**(2), 197–202 (2013).
288. G. H. Kim, B. Du Ahn, H. S. Shin, W. H. Jeong, H. J. Kim, and H. J. Kim, "Effect of indium composition ratio on solution-processed nanocrystalline InGaZnO thin film transistors," Appl. Phys. Lett. **94**(23), 233501 (2009).
289. C. C. Lo and T. E. Hsieh, "Preparation of IGZO sputtering target and its applications to thin-film transistor devices," Ceram. Int. **38**(5), 3977–3983 (2012).
290. M. Moreira, E. Carlos, C. Dias, J. Deuermeier, M. Pereira, P. Barquinha, R. Branquinho, R. Martins, and E. Fortunato, "Tailoring IGZO composition for enhanced fully solution-based thin film transistors," Nanomaterials **9**(9), 1273 (2019).
291. N. L. Dehuff, E. S. Kettenring, D. Hong, H. Q. Chiang, J. F. Wager, R. L. Hoffman, C. H. Park, and D. A. Keszler, "Transparent thin-film transistors with zinc indium oxide channel layer," J. Appl. Phys. **97**(6), 064505 (2005).
292. R. J. Winfield, L. H. K. Koh, S. O'Brien, and G. M. Crean, "Excimer laser processing of ZnO thin films prepared by the sol-gel process," Appl. Surf. Sci. **254**(4), 855–858 (2007).
293. M. S. Oh, R. Nirmala, and R. Navamathavan, "Improved Structural and Electrical Properties of ZnO-Based Thin Film Transistors by Using Pulsed KrF Excimer Laser Irradiation," J. Electron. Mater. **48**(5), 3137–3144 (2019).
294. S. Vyas, "A short review on: Optimization techniques of ZnO based thin film transistors," Chinese J. Phys. **56**(1), 117–124 (2018).
295. M. Nakata, K. Takechi, T. Eguchi, E. Tokumitsu, H. Yamaguchi, and S. Kaneko, "Effects of thermal annealing on ZnO thin-film transistor characteristics and the application of excimer laser annealing in plastic-based ZnO thin-film transistors," Jpn. J. Appl. Phys. **48**(1), 081608 (2009).
296. J.-J. Kim, J.-Y. Bak, J.-H. Lee, H. S. Kim, N.-W. Jang, Y. Yun, and W.-J. Lee, "Characteristics of laser-annealed ZnO thin film transistors," Thin Solid Films **518**(11), 3022–3025 (2010).
297. K. Kim, S. Kim, and S. Y. Lee, "Effect of excimer laser annealing on the properties of ZnO thin film prepared by sol-gel method," Curr. Appl. Phys. **12**(2), 585–588 (2012).
298. J. Robertson, "Disorder, band offsets and dopability of transparent conducting oxides," Thin Solid Films **516**(7), 1419–1425 (2008).
299. Q. Nian, M. Callahan, M. Saei, D. Look, H. Efstathiadis, J. Bailey, and G. J. Cheng, "Large scale laser crystallization of solution-based alumina-doped zinc oxide (AZO) Nanoinks for highly transparent conductive electrode," Sci. Rep. **5**, 15517 (2015).
300. M. Zhang, F. Averseng, F. Haque, P. Borghetti, J. M. Krafft, B. Baptiste, G. Costentin, and S. Stankic, "Defect-related multicolour emissions in ZnO smoke: From violet, over green to yellow," Nanoscale **11**(11), 5102–5115 (2019).
301. C. Drouilly, J. M. Krafft, F. Averseng, S. Casale, D. Bazer-Bachi, C. Chizallet, V. Lecocq, H.

Vezin, H. Lauron-Pernot, and G. Costentin, "ZnO oxygen vacancies formation and filling followed by in situ photoluminescence and in situ EPR," J. Phys. Chem. C **116**(40), 21297–21307 (2012).

302. J. Levinson, F. R. Shepherd, P. J. Scanlon, W. D. Westwood, G. Este, and M. Rider, "Conductivity behavior in polycrystalline semiconductor thin film transistors," J. Appl. Phys. **53**(2), 1193–1202 (1982).
303. F. M. Hossain, J. Nishii, S. Takagi, A. Ohtomo, T. Fukumura, H. Fujioka, H. Ohno, H. Koinuma, and M. Kawasaki, "Modeling and simulation of polycrystalline ZnO thin-film transistors," J. Appl. Phys. **94**(12), 7768–7777 (2003).
304. H. M. Ismail, "Characterization of the decomposition products of zirconium acetylacetonate: nitrogen adsorption and spectrothermal investigation," Powder Technol. **85**(3), 253–259 (1995).
305. K. Nakamoto, *Infrared and Raman Spectra of Inorganic and Coordination Compounds: Part A: Theory and Applications in Inorganic Chemistry: Sixth Edition* (w, 2008).
306. "CRC Handbook of Chemistry and Physics, 86th Edition Edited by David R. Lide (National Institute of Standards and Technology). CRC Press (an imprint of Taylor and Francis Group): Boca Raton, FL. 2005. 2544 pp. $125.96. ISBN 0-8493-0486-5.," J. Am. Chem. Soc. **128**(16), 5585 (2006).
307. J. C. Védrine, "Metal Oxides in Heterogeneous Oxidation Catalysis: State of the Art and Challenges for a More Sustainable World," ChemSusChem **12**(3), 577–588 (2019).
308. A. Ortiz, J. C. Alonso, and E. Haro-Poniatowski, "Spray deposition and characterization of zirconium-oxide thin films," J. Electron. Mater. **34**(1), 150–155 (2005).
309. S. Li, W. Li, Q. Zhang, R. Shu, H. Wang, H. Xin, and L. Ma, "Lignin-first depolymerization of native corn stover with an unsupported MoS2 catalyst," RSC Adv. **8**(3), 1361–1370 (2018).
310. I. Georgieva, N. Danchova, S. Gutzov, and N. Trendafilova, "DFT modeling, UV-Vis and IR spectroscopic study of acetylacetone-modified zirconia sol-gel materials," J. Mol. Model. **18**(1), 2409–2412 (2012).
311. R. M. Mahfouz, G. A. W. Ahmed, A. I. Al-Wassil, M. R. H. Siddiqui, and A. M. Al-Otaibi, "Radiation-induced synthesis of ZrO 2 nanoparticles by thermal decomposition of zirconium acetylacetonate," Radiat. Eff. Defects Solids **168**(11–12), 950–958 (2013).
312. O. Obregon, S. Alcantara, S. Soto, and Dominguez, "Effects of Electrical Stress in Solution-Processed Spin-On Glass Dielectric Films: Frequency Dependence," MDPI Eng. Proc. **4**(1), 2 (2021).
313. K. Jensen, *Introduction to the Physics of Electron Emission* (Wiley, 2017).
314. J. H. Park, Y. B. Yoo, K. H. Lee, W. S. Jang, J. Y. Oh, S. S. Chae, and H. K. Baik, "Low-temperature, high-performance solution-processed thin-film transistors with peroxo-zirconium oxide dielectric," ACS Appl. Mater. Interfaces **5**(2), 410–417 (2013).
315. S. Kaya, R. Lok, A. Aktag, J. Seidel, and E. Yilmaz, "Frequency dependent electrical characteristics of BiFeO3 MOS capacitors," J. Alloys Compd. **583**(1), 476–480 (2014).
316. M. A. Dominguez, O. Obregon, and J. A. Luna-Lopez, "Study of stability of solution-processed dielectric film under electrical stress," J. Alloys Compd. **688**(Part A), 893–896 (2016).
317. T. Boscke, "Crystalline Hafnia and Zirconia Based Dielectrics for Memory Applications," Technischen Universitat Hamburg-Harburg (2010).
318. J. Bohm, D. Klimm, M. Muhlberg, and B. Winkler, *Introduction to Crystallography* (Boston: De Gruyter, 2021).
319. L. Yu, M. R. Niazi, G. O. Ngongang Ndjawa, R. Li, A. R. Kirmani, R. Munir, A. H. Balawi, F. Laquai, and A. Amassian, "Programmable and coherent crystallization of semiconductors," Sci. Adv. **3**(3), 1602462 (2017).
320. M. Anwar and C. A. Hogarth, "Structural investigations and colour centres in MoO3 films deposited by vacuum evaporation," Int. J. Electron. **67**(4), 567–576 (1989).

9. Appendix

Table 9-1. Fitting parameters of IRT measurements.

2-ME			$In(NO_3)_3$ solution			$In(NO_3)_3$ dried		
ε_∞=1.273±0.0005			ε_∞=6.23±0.07			ε_∞=4.83±0.08		
$E(cm^{-1})$	A	γ	$E(cm^{-1})$	A	γ	$E(cm^{-1})$	A	γ
573.0±24.2	3±2	0.024±0.005	280.8±1.6	8.2±0.2	0.104±0.0008	290.5±8.1	8.7±0.2	0.0087±0.0004
726.4±322.8	0.6±0.6	0.04±0.006	403.5±8.1	3.7±0.4	0.023±0.002	403.5±24.2	3±3	0.012±0.005
831.3±0.8	2.5±0.2	0.0026±0.0003	553.6±5.6	2.6±0.6	0.01±0.002	516.5±161.4	3.7±0.7	0.02±0.04
887.8±0.72	2.9±0.2	0.0023±0.0002	646.5±1.6	1±0.3	0.0017±0.0007	589.2±8.1	2±1	0.007±0.0005
968.5±1.6	1.2±0.2	0.0031±0.0006	677.9±8.1	3±0.6	0.018±.004	644.1±6.4	2±1	0.005±0.03
1016.9±0.8	2.3±0.2	0.0026±0.0003	831.3±16.1	2±1	0.018±0.008	694.1±48.4	3±3	0.009±0.002
1065.3±0.4	6.7±0.2	0.004±0.0002	832.9±0.6	3±0.2	0.0023±0.0002	766.7±56.5	3±1	0.01±0.002
1121.8±0.4	5.5±0.2	0.0029±0.0001	887.8±0.7	2.7±0.2	0.0024±0.0002	823.2±8.1	3±2	0.006±0.004
1162.2±40.3	1.1±0.1	0.041±0.009	968.5±3.2	0.9±0.4	0.004±0.001	879.7±16.1	2.1±0.6	0.009±0.008
1194.5±0.7	2.0±0.2	0.0019±0.0002	1016.9±0.4	4.7±0.5	0.0029±0.0002	944.3±16.1	0.6±0.3	0.05±0.009
1331.7±7.2	0.3±0.1	0.004±0.003	1065.3±03	8.3±0.4	0.0047±0.0002	968.5±7.3	0.4±0.07	0.003±0.003
1372.1±2.4	0.9±0.2	0.003±0.0009	1121.8±0.3	7.1±0.2	0.0035±0.0001	1033.1±0.8	3.1±0.5	0.009±0.001
1412.4±4.0	1.0±0.1	0.006±0.002	1194.5±0.4	2.4±0.2	0.0021±0.0002	1113.8±6.5	1.4±0.3	0.0052±0.0007
1460.8±2.4	1.9±0.2	0.0043±0.0005	1210.6±4.8	1.5±0.2	0.1±0.05	1202.6±7.3	0.7±0.4	0.01±0.004
1646.5±4.0	0.29±0.09	0.003±0.001	1234.8±1.6	0.8±0.1	0.0026±0.0006	1307.5±0.7	5.9±0.5	0.0082±0.0004
2066.2±48.4	0.06±0.02	0.003±0.01	1291.3±1.6	2.6±0.6	0.0035±0.0006	1404.3±3.2	5±0.3	0.02±0.002
2728.0±24.2	0.15±0.08	0.007±0.005	1307.5±2.4	3.8±0.6	0.0077±0.0008	1517.3±0.8	2.7±0.3	0.0076±0.0006
2800.6±32.2	0.26±0.04	0.069±0.009	1404.3±4.8	3.7±0.5	0.021±0.004	1638.4±2.4	1.66±0.09	0.0126±0.0006
2824.8±80.7	0.4±0.3	0.004±0.002	1460.8±1.6	1.2±0.2	0.0034±0.0006	1694.9±56.4	0.32±0.03	0.2±0.2
2832.9±80.7	1.1±0.7	0.01±0.002	1517.3±0.7	3.4±0.3	0.0051±0.0003	2421.3±7.2	0.6±0.1	0.044±0.005
2881.4±4.0	0.7±0.7	0.005±0.003	1646.4±4.8	0.9±0.1	0.09±0.002	3066.9±8.1	3±0.1	0.073±0.003
2929.8±5.6	0.1±0.2	0.002±0.002	1711.1±16.1	0.2±0.1	0.005±0.003	3438.3±3.2	1.32±0.08	0.036±0.001
2937.8±2.4	1.2±0.9	0.007±0.004	1977.4±40.3	0.13±0.08	0.02±0.01	4382.6±40.3	0.21±0.003	0.31±0.02
2986.3±3.2	0.32±0.09	0.03±0.009	2114.6±48.4	0.1±0.07	0.01±0.01			
3309.1±2.4	1.2±0.2	0.03±0.005	2469.7±32.2	0.7±0.1	0.05±0.01			
3446.3±8.1	0.8±0.4	0.02±0.002	2824.8±161.4	1±4	0.03±0.03			
			2841.0±3.2	0.9±0.1	0.006±0.001			
			2881.3±2.4	0.8±0.2	0.004±0.001			
			2937.8±4.0	1.5±0.2	0.01±0.001			
			3228.4±807.1	0.18±0.06	0.4±0.1			
			3066.9±80.7	3±2	0.05±0.09			
			3309.1±80.7	3±2	0.04±0.04			
			3486.6±56.5	1±1	0.03±0.01			

$Zn(CH_3COO)_2$ solution			$Zn(CH_3COO)_2$ dried		
ε_∞=5.69±0.09			ε_∞=5.7±0.1		
$E(cm^{-1})$	A	γ	$E(cm^{-1})$	A	γ
507.6±7.3	1±1	0.001±0.002	492.3±8.1	0.3±0.1	0.005±0.003
540.7±8.1	2±1	0.006±0.005	510.1±2.4	0.5±0.3	0.001±0.0008
548.8±32.3	3.6±0.9	0.06±0.01	654.5±3.2	1.74±0.07	0.03±0.002
621.4±40.3	2±1	0.02±0.01	654.8±3.2	0.8±0.3	0.0023±0.0008
831.3±0.8	4.4±0.7	0.0022±0.0004	677.2±6.5	0.7±0.1	0.004±0.002
887.3±0.8	5±0.7	0.0021±0.0003	823.6±3.2	0.3±0.1	0.0021±0.0009
968.5±3.2	1.5±0.5	0.0022±0.0009	871.6±2.4	0.46±0.07	0.004±0.0008
1025.0±0.8	6±0.8	0.0021±0.0003	928.2±16.1	0.01±0.3	0.0001±0.00005
1065.4±0.8	6.8±0.9	0.0047±0.0003	1033.1±0.7	2.55±0.07	0.0052±0.0002
1081.5±16.1	2.3±0.4	0.029±0.006	1073.4±0.5	2.89±0..09	0.0032±0.0001

1121.8±0.7	7±1	0.0031±0.0002	1162.2±2.4	0.81±0.04	0.106±0.0007
1194.5±0.8	3.8±0.5	0.0018±0.0003	1323.6±0.8	1.04±0.07	0.0056±0.0005
1234.8±4.0	0.7±0.3	0.002±0.001	1404.4±0.6	1.94±0.08	0.0048±0.0002
1331.7±8.1	0.4±0.4	0.002±0.001	1477.0±2.4	2.8±0.04	0.345±0.0005
1372.1±3.2	0.9±0.5	0.002±0.003	1573.8±05	3.21±0.06	0.0079±0.0001
1396.3±16.1	1.9±0.5	0.03±0.009	2171.1±48.4	0.49±0.01	0.2±0.01
1412.4±4.8	1.2±0.5	0.005±0.003	2881.3±5.6	0.39±0.03	0.011±0.002
1460.8±2.4	2.7±0.4	0.0036±0.0006	2897.5±24.2	0.71±0.05	0.067±0.005
1581.9±4.0	1.1±0.5	0.005±0.002	2954.0±3.2	0.37±0.05	0.0069±0.0009
1614.2±161.5	0.5±0.2	0.3±0.1	3147.7±6.5	0.09±0.03	0.005±0.002
1630.3±24.2	0.8±0.2	0.013±0.005	3284.9±4.8	2.14±0.08	0.0491±0.0007
1961.2±24.2	0.1±0.2	0.003±0.007			
2130.7±48.4	0.1±0.1	0.01±0.02			
2728.0±16.1	0.2±0.2	0.005±0.006			
2832.9±8.1	1.7±0.2	0.004±0.003			
2905.6±403.5	0.4±0.8	0.05±0.08			
2881.3±4.8	2±1	0.005±0.008			
2897.5±24.2	2±1	0.016±0.002			
2937.8±16.1	2±2	0.0054±0.0007			
2986.3±6.4	0.6±0.4	0.004±0.003			
3228.4±807.1	0.22±0.07	0.1±0.1			
3309.1±161.4	3±2	0.04±0.01			
3389.8±48.4	2.5±0.1	0.03±0.01			
4382.6±56.5	0.028±.04	0.01±0.002			

Table 9-2. IRSE fitting parameters for stabilised $In(NO_3)_3$.

Stab $In(NO_3)_3$ on Si			Stab $In(NO_3)_3$ on TiN		
ε_∞=2.26±0.02			ε_∞=2.96±0.006		
$E(cm^{-1})$	A	γ	$E(cm^{-1})$	A	γ
469±80.7	1.3±0.3	0.14±0.02	371±32.2	4.7±0.6	0.019±0.003
1049±2.4	0.78±0.05	0.75±0.04	403.5±16.1	4±2	0.11±0.04
			388±16.1	0.3±0.3	0.1±0.1
			1024±80.7	0.69±0.07	0.0061±0.0007
			1306±2.4	0.99±0.09	0.028±0.002
			1355±6.4	0.5±0.09	0.524±0.005
			1613±5.6	0.16±0.02	0.011±0.002
			3193±16.1	0.33±0.01	0.051±0.005
			3443±4.0	0.35±0.04	0.025±0.002
Stab $In(NO_3)_3$ on Au			**Stab $In(NO_3)_3$ on Al**		
ε_∞=3.126±0.004			ε_∞=3.292±0.003		
$E(cm^{-1})$	A	γ	$E(cm^{-1})$	A	γ
415±5.6	9.1±0.6	0.013±0.002	366±16.1	9±4	0.01±0.004
552±24.2	2.2±0.2	0.024±0.007	423±64.5	4±2	0.022±0.009
800±24.2	0.7±0.1	0.02±0.01	685±32.2	1.49±0.07	0.05±0.01
1008±40.3	0.7±0.1	0.027±0.007	1032±4.8	0.9±0.1	0.018±0.002
1314±2.4	1.5±0.2	0.0076±0.0009	1306±1.6	2.8±0.1	0.0065±0.0004
1411±8.1	1.02±0.05	0.018±0.002	1371±4.0	1.71±0.03	0.0262±0.0007
1614±161.4	0.5±0.5	0.6±0.1	1637±4.0	0.22±0.03	0.009±0.001
1596±5.6	0.31±0.05	0.008±0.002	2397±40.3	0.27±0.007	0.16±0.01

3121±32.3	0.42±0.02	0.061±0.007	3193±8.1	0.74±0.03	0.057±0.004
3419±5.6	0.5±0.06	0.029±0.002	3452±3.2	0.56±0.05	0.027±0.001

Table 9-3. IRSE fitting parameters for stabilised $Zn(CH_3COO)_2$.

Stab $Zn(CH_3COO)_2$ on Si			Stab $Zn(CH_3COO)_2$ on TiN		
ε_∞=1.744±0.002			ε_∞=1.72±0.05		
$E(cm^{-1})$	A	γ	$E(cm^{-1})$	A	γ
467±1.61	1.71±0.07	0.0183±0.0007	483±4.8	2.1±0.2	0.0126±0.0006
			838±8.1	0.38±0.04	0.059±0.003
			1387±4.8	0.24±0.02	0.025±0.002
			1605±4.0	0.17±0.02	0.012±0.001
			3347±8.1	0.061±0.007	0.042±0.003

Stab $Zn(CH_3COO)_2$ on Au			Stab $Zn(CH_3COO)_2$ on Al		
ε_∞=2.5±0.1			ε_∞=2.0±0.1		
$E(cm^{-1})$	A	γ	$E(cm^{-1})$	A	γ
479±4.8	3.1±0.4	0.0127±0.005	438±8.1	3.0±0.5	0.018±0.001
701±40.3	0.19±0.02	0.067±0.009	838±16.1	0.04±0.05	0.054±0.003
1330±5.6	0.15±0.06	0.006±0.002	1387±8.1	0.096±0.002	0.22±0.03
1411±8.1	0.32±0.04	0.016±0.002	1605±8.0	0.17±0.03	0.019±0.003
1613±3.2	0.25±0.03	0.0146±0.0009	3347±16.1	0.08±0.01	0.055±0.004
3298±5.6	0.15±0.02	0.076±0.002			

Table 9-4. IRSE fitting parameters for thermally annealed $In(NO_3)_3$ $(300°C)$.

TA $In(NO_3)_3$ on Si			TA $In(NO_3)_3$ on TiN		
ε_∞=5.69±0.09			ε_∞=2.1±0.03		
$E(cm^{-1})$	A	γ	$E(cm^{-1})$	A	γ
461±24.2	1.4±0.1	0.036±0.004	338±48.4	10±6	0.01±0.002
			490±64.5	4±2	0.02±0.01
			685±64.5	1.2±0.4	0.04±0.01
			1040±242.1	0.29±0.07	0.09±0.04

TA $In(NO_3)_3$ on Au			TA $In(NO_3)_3$ on Al		
ε_∞=1.89±0.06			ε_∞=3.02±0.07		
$E(cm^{-1})$	A	γ	$E(cm^{-1})$	A	γ
301±16.1	16±5	0.010±0.004	412±7.2	9.2±0.7	0.015±0.003
338±32.2	2.6±0.4	0.038±0.004	552±24.2	2.7±0.3	0.021±0.004
589±0.8	0.59±0.03	0.006±0.0004	823±5.6	2.42±0.07	0.0254±0.0008
975±1.6	0.45±0.006	0.132±0.004	911±3.2	0.78±0.09	0.0084±0.0007

Table 9-5. IRSE fitting parameters for thermally annealed $Zn(CH_3COO)_2$ $(300°C)$.

TA $Zn(CH_3COO)_2$ on Si			TA $Zn(CH_3COO)_2$ on TiN		
ε_∞=1.83±0.09			ε_∞=1.57±0.04		
Drude-Smith ω_p= n/a c =n/a γ =n/a			Drude-Smith ω_p=0.113±0.004 c =-0.89±0.06 γ =0.135±0.003		
$E(cm^{-1})$	A	γ	$E(cm^{-1})$	A	γ
492±8.1	2.4±0.3	0.013±0.001	414±16.1	3.6±0.5	0.018±0.001
			762±5.6	0.23±0.02	0.023±0.002
			1395±24.2	0.026±0.007	0.021±0.007
			1572±16.1	0.022±0.009	0.008±0.004
			3363±16.1	0.016±0.003	0.036±0.006

TA $Zn(CH_3COO)_2$ on Au			TA $Zn(CH_3COO)_2$ on Al		
ε_∞=2.3±0.1			ε_∞=1.66±0.03		
Drude-Smith ω_p=0.128±0.008 c =-0.9±0.1 γ =0.18±0.02			Drude-Smith ω_p=0.146±0.004 c =-0.87±0.03 γ =0.166±0.003		
$E(cm^{-1})$	A	γ	$E(cm^{-1})$	A	γ
412±24.2	5±1	0.02±0.003	406±16.1	4.8±0.6	0.018±0.001
959±56.5	0.13±0.05	0.06±0.02	806±7.2	0.19±0.02	0.024±0.002
1379±2.2	0.08±0.03	0.015±0.008	1395±16.1	0.048±0.009	0.016±0.005
1548±56.5	0.05±0.02	0.02±0.02	1572±24.2	0.039±0.007	0.018±0.006
3169±64.5	0.023±0.006	0.08±0.02	3306±16.1	0.018±0.003	0.031±0.005

Table 9-6. IRSE fitting parameters for thermally annealed $In(NO_3)_3$ and $Zn(CH_3COO)_2$ on Al$(450\ °C)$.

TA $In(NO_3)_3$ on Al (450^0C)			TA $Zn(CH_3COO)_2$ on Al (450^0C)		
ε_∞=3.08±0.01			ε_∞=1.854±0.001		
			Drude-Smith ω_p=0.123±0.001 c =-0.783±0.005 γ =0.124±0.005		
$E(cm^{-1})$	A	γ	$E(cm^{-1})$	A	γ
392±16.1	13±2	0.013±0.003	397±5.64	9.5±0.4	0.014±0.001
473±40.35	2.4±0.2	0.078±0.005			